UNIVERSITAT DE BARCELONA

Structural organization of model membranes:
a complementary approach combining atomic force microscopy and X-ray techniques

Berta Gumí Audenis

UNIVERSITAT DE BARCELONA

Programa de doctorat:
BIOTECNOLOGIA

Structural organization of model membranes:

a complementary approach combining atomic force microscopy and X-ray techniques

Memòria que presenta **Berta Gumí Audenis** per optar
al títol de Doctor per la Universitat de Barcelona.

Directora:

Dr. Marina Inés Giannotti

Centro de investigación Biomèdica en red (CIBER). Institut de Bioenginyeria de Catalunya (IBEC). Departament de Ciència dels Materials i Química Física de la Universitat de Barcelona.

Co-director i tutor:

Prof. Fausto Sanz Carrasco

Departament de Ciència dels Materials i Química Física de la Universitat de Barcelona. Institut de Bioenginyeria de Catalunya (IBEC).

Barcelona, març de 2018

UNIVERSITAT DE BARCELONA

Programa de doctorat:
BIOTECNOLOGIA

Structural organization of model membranes:

a complementary approach combining atomic force microscopy and X-ray techniques

Berta Gumí Audenis

Directora:

Dr. Marina Inés Giannotti

Co-director i tutor:

Prof. Fausto Sanz Carrasco

Barcelona, març de 2018

Als meus pares
i a l'Anna

Index

Outline **11**

1. Introduction **13**

1.1. Biological membranes 14

1.1.1. The composition of biological membranes 14

1.1.1.1. Cholesterol 15

1.1.1.2. Sphingolipids 16

1.1.2. The mechanics of biological membranes 16

1.2. Model membrane systems 17

1.3. Physical and structural characterization of lipid bilayers 18

1.3.1. AFM: topographical and mechanical characterization 19

1.3.2. X-Ray grazing incidence techniques: structural characterization 21

1.3.2.1. XRR: vertical structure 22

1.3.2.2. GIXD: in-plane lateral organization 23

1.3.2.3. Coupling AFM and XR techniques 24

1.4. Objectives 25

1.5. References 27

2. From simple to complex bilayers: AFM and AFM-FS study **31**

2.1. Introduction 32

2.2. Experimental 33

2.3. Results and discussions 35

2.3.1. Vesicles characterization 35

2.3.2. AFM and AFM-FS study: membrane structural and nanomechanical properties 37

2.3.2.1. From pure to binary SLBs: GalCer and Chol effect. 37

2.3.2.2. Ternary SLBs 41

2.3.3. Dynamic Force Spectroscopy (DFS): SLB rupture activation energy 43

2.4. Conclusions 45

2.5. References 46

3. Quatsome membranes: AFM and AFM-FS study **49**

3.1. Introduction 50

3.2. Experimental 51

3.3. Results and discussions 53

3.3.1. QT vesicles: Structural characterization 53

3.3.2. QT membranes on mica: AFM topographical characterization. 54

3.3.3. QT membranes on mica: AFM mechanical characterization. 56

3.3.4. Effect of the ions on the SQM topography and mechanics. 58

3.3.5. Effect of the temperature on the SQMs structure. 59

3.3.6. Elasticity measurement on QT vesicles 63
3.4. Conclusions 65
3.5. References 66
4. Pulling lipid tubes from model membranes 67
4.1. Introduction 68
4.2. Experimental 70
4.3. Results and discussions 71
4.3.1. Phospholipid headgroup and phase state 71
4.3.2. Effect of the underlying substrate 75
4.3.3. F_{tube} does not depend on the AFM tip 77
4.4. Conclusions 77
4.5. References 78
5. Effect of HNP1 defensin on model supported lipid bilayers 81
5.1. Introduction 82
5.2. Experimental 84
5.3. Results and discussions 87
5.3.1. HNP1 defensin and phosphocholine (PC) bilayers 87
5.3.1.1. HNP1 on DOPC SLBs. 88
5.3.1.2. HNP1 on DPPC SLBs. 91
5.3.2. HNP1 defensin and phosphoethanolamine (PE):phosphatidylglycerol (PG) bilayers 93
5.3.2.1. HNP1 on DOPE SLBs. 93
5.3.2.2. HNP1 on DOPE:DOPG and DOPE:DPPG SLBs. 94
5.4. Conclusions 98
5.5. References 98
6. In-plane molecular organization of hydrated single lipid bilayers: DPPC:Cholesterol 101
6.1. Introduction 102
6.2. Experimental 103
6.3. Results and discussions 105
6.3.1. Strategy of the setup 105
6.3.2. GIXD on DPPC:Chol bilayers 108
6.3.3. AFM and fluorescence on DPPC:Chol bilayers 111
6.4. Conclusions 113
6.5. References 113
7. Custom AFM for X-Ray beamlines 115
7.1. Introduction 116
7.2. Experimental 118

7.3. Results and discussions 119
7.3.1. Design and development of the custom AFM 119
7.3.2. Commissioning of the custom AFM 123
7.3.3. Radiation damage on phospholipid bilayers 126
7.3.4. Dynamic processes: phase transitions on phospholipid bilayers 129
7.4. Conclusions 131
7.5. References 132
8. General conclusions 135
Appendix 1: Resum en català 139
Appendix 2: Symbols and acronyms 163
Appendix 3: Publications and communications 169
Acknowledgments 173

Outline

This thesis has been organized in eight chapters:

Chapter 1 is dedicated to a general introduction to biological membranes and model bilayer systems, such as supported lipid bilayers (SLBs) used as simplified models. This chapter also describes the capabilities of atomic force microscopy and spectroscopy tools (AFM and AFM-FS, respectively), as well as X-ray (XR) techniques, to address the physicochemical, mechanical and structural study on SLBs. The objectives of the thesis are included at the end of this chapter.

Chapters 2 to **7** include the vast majority of this thesis, as they contain the experimental results. Each chapter is treated individually and comprises a brief specific introduction to the matter, an experimental section, results and discussion and conclusions.

Chapter 2 presents the use of AFM and AFM-FS techniques to study the physical properties of SLBs. This chapter includes the evaluation of the phase behavior and nanomechanics of SLBs containing first a single component, to then increase the complexity by incorporating up to three components; a phospholipid, cholesterol (Chol) and a glycosphingolipid.

Chapter 3 describes the use of AFM and AFM-FS techniques to study the morphology and nanomechanics of the membrane of vesicular systems that have a technological application in drug delivery: quatsomes. This chapter includes also the study of the ions and temperature effect on these membranes.

Chapter 4 presents a novel approach based on AFM-FS to study mechanics of SLBs. This includes the evaluation of the membrane composition as well as the influence of the supporting substrate on membrane mechanics by studying the growing force of a lipid tube pulled out from an SLB with the AFM tip.

Chapter 5 details the effect of small defensin peptides on the membrane structural and mechanical properties. This chapter includes the characterization of SLBs of different composition by means of AFM and XR techniques before and after incubating a human neutrophil peptide.

Chapter 6 describes a novel setup that allows for grazing incidence XR diffraction (GIXD) characterization of hydrated individual SLBs. This chapter includes GIXD recordings on 1,2-dipalmitoyl-*sn*-glycero-3-phosphoCholine (DPPC):Chol SLBs providing new insights on the structure of this binary system.

Chapter 7 presents the development of a custom AFM to be used as a sample holder for synchrotron XR beamlines, that aims to simultaneously evaluate the AFM morphology and mechanics with the structural information gathered with grazing incidence X-ray experiments. The instrument allows a wide range of possible investigations, such as the

evaluation of radiation damage effects induced by the X-ray beam on SLBs the study of membrane phase transitions included in this chapter.

Chapter 8 is reserved for the general conclusions of this thesis.

Finally, there are three appended sections. **Appendix I** summarizes this thesis in Catalan. **Appendix II** comprises a list of symbols and acronyms that have been used throughout the thesis. **Appendix III** lists the publications and communications related to this thesis.

Chapter 1

Introduction

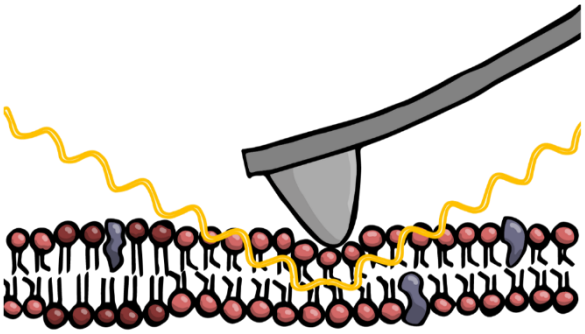

1.1. Biological membranes

1.1.1. The composition of biological membranes

Biological membranes (BMs) are self-sealing boundaries, which confine the permeability barriers of cells and organelles and provide the means to compartmentalize functions. Apart from being crucial for the cell structure, they provide a support matrix for all the proteins inserted in the cell, acting as channels to exchange mass, energy and information with the environment.[1-3]

In 1972, Singer and Nicolson proposed the *fluid mosaic model*,[4] assigning the concept of fluidity to the membrane (figure 1.1). They defined the cell membrane as a two-dimensional liquid where all the membrane-associated lipids and proteins present lateral mobility, being this an essential property for their function. Knowing the complex composition of cell membranes, lipids are the main component of BMs together with all the proteins and carbohydrates, building the bilayer structure.[5] Thousands of lipid species are found in BMs, including phospholipids, sterols and sphingolipids (SLs). The chemical structures of some lipids are exemplified in figure 1.2. It has been experimentally shown that the BMs are able to laterally segregate its constituents, subcompartmentalizing them in small domains (10-200 nm) generally known as "lipid rafts".[6, 7] These "lipid rafts" are fluctuating nanoscale assemblies of lipids enriched in cholesterol (Chol) and SLs, the formation of which is driven by lipid-lipid and protein-lipid interactions.[8] They are present in both leaflets of an asymmetric cell membrane and seem to play significant biological roles by regulating cellular processes, such as in membrane signaling and trafficking.[6, 8, 9]

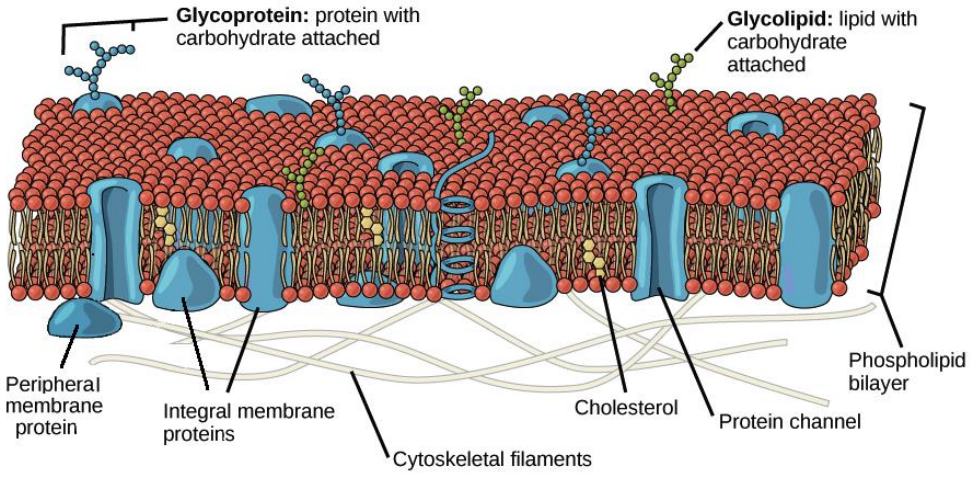

Figure 1.1 The *fluid mosaic model* of the cell membrane. Reproduced with permission from OpenStax College. Copyright © 2013.

1.1.1.1. Cholesterol

Chol (figure 1.2(c)) is a fundamental component of eukaryotic cells and it can even locally reach concentrations up to 50 mol % of the overall lipid contained in cell plasma membranes. Certainly, Chol plays an essential role modulating membrane physical properties, being highly important on the function and evolution of the BM.[5, 10] It regulates the membrane fluidity and controls the lipid organization and phase behavior, as well as it increases the mechanical stability of the membrane.[11-13] From the molecular point of view, Chol produces a condensing effect by ordering the fluid phase lipids in the membrane, which leads to an increment on the bilayer thickness and a decrease on its permeability.[14, 15]

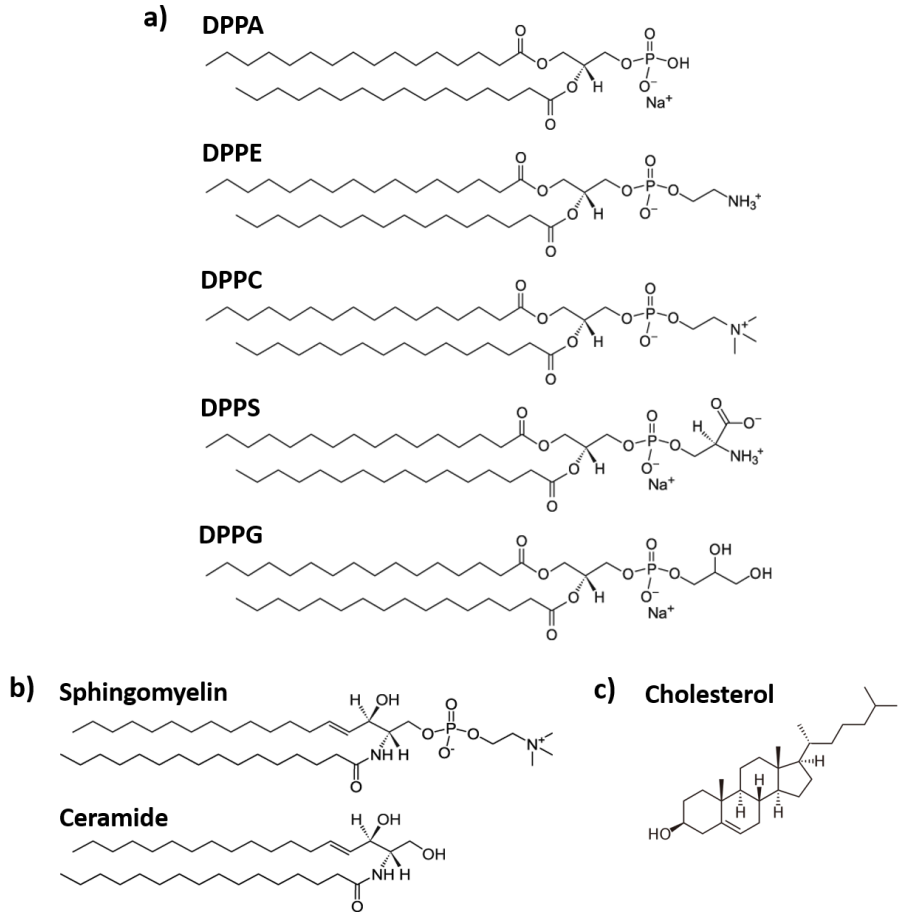

Figure 1.2 Chemical structures of some lipids common in BMs: a) Phospholipids: 1,2-dipalmitoyl-*sn*-glycero-3-phosphate (DPPA), 1,2-dipalmitoyl-*sn*-glycero-3-phosphoethanolamine (DPPE), 1,2-dipalmitoyl-*sn*-glycero-3-phosphocholine (DPPC), 1,2-dipalmitoyl-*sn*-glycero-3-phospho-L-serine (DPPS) and 1,2-dipalmitoyl-*sn*-glycero-3-phospho-(1'-*rac*-glycerol) (DPPG). b) SLs: sphingomyelin and ceramide. c) Sterol: Chol.

Nevertheless, many studies highlight that the effect of Chol into the lipid bilayer depends on the molecular structure of the neighboring lipids, especially on the degree of chain unsaturation, the length of the hydrophobic tails and the chemical composition of the headgroup. [11, 16, 17] However, as previously mentioned, Chol is generally accompanied by SLs in rafts, playing a conjunct effect on the physical properties of the lipid bilayer.

1.1.1.2. Sphingolipids

SLs comprise a large family of membrane lipids, including phosphosphingolipids (PSLs) and glycosphingolipids (GSLs), and they are composed of a hydrophobic ceramide (Cer) (figure 1.2(b)) and a hydrophilic headgroup.[18] Free Cer is a major component of the stratum corneum and it is found in smaller proportions in cell membranes, in which they occur as intermediate in the metabolism of more complexes SLs, and where they play an important role in cell signaling.[19, 20] PSLs exhibit similar amphipathic features as phospholipids, being the core structure of Cer combined with a phosphocholine headgroup. Sphingomyelin (SM) (figure 1.2(b)) is the most prevalent membrane PSLs and, because of its structural similarities with phosphocholines (PCs), it is able to form lipid bilayers as well.[21] When the hydrophilic group is a sugar these are the GSLs, which have chemical structures in general much more complex than PSLs. Examples of GSLs are cerebrosides, when the sugar is glucose (glucosylceramide, GlcCer) or galactose (galactosylceramide, GalCer), or those with higher number of sugar moieties like globosides and gangliosides. In particular, cerebrosides are commonly found in the central nervous system, primarily localized in the neuronal tissues.[22, 23] In general, SLs are known to have a significant impact on membrane properties, enhancing the ordering of the phospholipid molecules and producing lateral phase segregation as well as domain formation.[19]

1.1.2. The mechanics of biological membranes

BMs mediate several biological functions, such as trafficking, cell division, endocytosis and exocytosis, demanding hard conformational changes of the lipid membrane like fusion, fission or tubes growth.[5] These mechanical requirements are only possible due to the organization of the chemical composition of the lipids into the membrane of each organelle, which is directly linked to the organelle function.[24] For instance, in-plane membrane tension and curvature changes, and consequently the membrane shape control, are mechanical parameters governed by the lipid composition of the membrane together with the proteins localized in it. Thanks to the dynamic behavior of the membrane, lateral and transverse forces within the membrane are significant and change rapidly as the membrane is bent or stretched, and as new constituents are added, removed or chemically modified. Differences in structure between the two leaflets and between different areas of the bilayer can be associate to membrane deformation to alter the activities of membrane binding proteins.[5, 25]

In addition, the lipids in the membrane act as physical support for the transmembrane integrins, connecting the extracellular matrix with the cytoskeleton.[26] In this way, transmission of the mechanical signals from the exterior of cells to their interior occurs though the plasma membrane, determining the behavior of these cells.[27] It is then the correlation between the composition and the packing of the lipids what essentially governs the membrane physicochemical and mechanical properties.[28]

1.2. Model membrane systems

Considering the complex chemical diversity of BMs, model bilayers systems are frequently used to study membrane properties and biological processes. For instance, giant unilamellar vesicles (GUVs) have become an essential model to mimic BMs, when studying domains dynamics and the influence of composition changes to the physical properties of the overall GUV, or its interactions with DNA and proteins.[29-31] However, the simple composition allowed for GUVs model systems is usually a limitation, since it does not fully comprises the complex composition of cell membranes. Similar to GUVs are the giant plasma membrane vesicles (GPMVs), which are obtained from cell membranes and maintain the lipid complexity and the large amount of transmembrane proteins.[8, 32]

Nevertheless, due to the micro and nanoscale range of domains in BMs, and the consequent need of local techniques to explore BMs at the nanometric level, supported bilayer systems are then very manageable platforms, since they retain two-dimensional order and lateral mobility and offer excellent environments for the insertion of membrane proteins. Nowadays, a wide range of supported bilayer systems have emerged as suitable approaches for biological studies, like self-assembled monolayer-monolayer systems or bilayer coated microfluidics, within others. However, supported lipid bilayers (SLBs) -or supported planar bilayers (SPBs)- facilitate the use of surface analytical techniques. SLBs are ideal platforms to study the lipid lateral interactions, the growth of lipid domains, as well as interactions between the lipid membrane and proteins, peptides and drugs, cell signaling, etc.[33-36]

Among the several methods to obtain SLBs, the most widely used are the Langmuir-Blodgett (LB) technique, to prepare mono and bilayers, the hydration of spin-coated films and the liposome rupture or fusion method, to prepare bilayers.[37-39] The liposome rupture method, the most popular and simple, consists on the fusion of small unilamellar vesicles (SUVs) from a suspension as soon as they get in contact with a flat substrate (figure 1.3). Then, the SUVs will start fusing between them, deforming, flattening and finally rupturing to form a continuous SLB.[37] In any case, the mechanism to obtain bilayers from SUVs is not fully understood. Variables concerning the lipid vesicles (composition, concentration and size), the physicochemical environment (pH, temperature and ionic strength) as well as related to

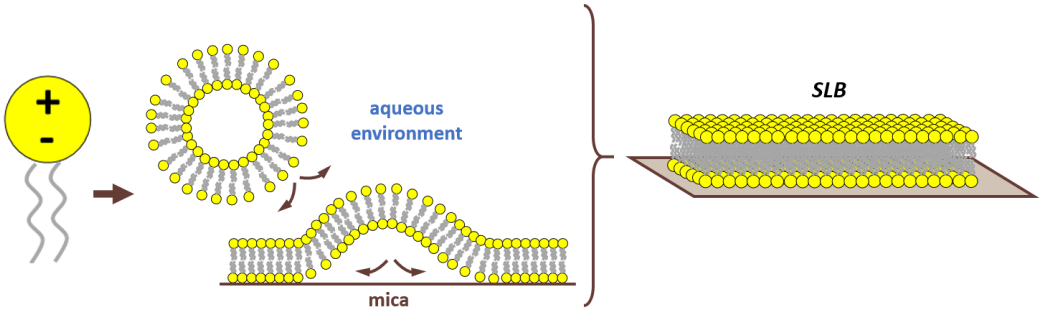

Figure 1.3 Schematic diagram showing the formation of SLBs via the liposome rupture method.

the surface (roughness and charge density) have been reported to highly influence the final SLB structure.[40] Mica is the most common material used as substrate, since it is easy to cleave and so to get a clean surface, atomically flat and hydrophilic. Apart from mica, other alternative substrates can be used, i.e. borosilicate glass, silicon oxide or even gold surfaces.[41]

The impossibility of decoupling the bilayer properties from the supporting substrate and of measuring the bilayer curvature due to its two-dimensional confinement are limitations of the SLB's approach. In this context, other bilayer systems, such as polymer-cushioned phospholipid bilayers[42, 43] and pore spanning bilayers,[44] are proposed to overcome these limitation, since they allow the physical characterization of the bilayer decoupling the effect of the substrate. In addition, stacks of lipid bilayer are also emerging as alternative approaches to mimic multilamellar membranes.[45, 46]

1.3. Physical and structural characterization of lipid bilayers

Several reports demonstrate the wide variety of useful techniques to study supported and non-supported lipid membranes, including fluorescence microscopy,[47] fluorescence recovering after photobleaching (FRAP),[48] Brewster angle microscopy (BAM),[49] as well as ellipsometry, among others. Focusing on investigating the physical properties of lipid bilayers, micropipette aspiration has proven to be remarkable on the determination of elastic modulus of the membrane in GUVs.[30] This technique allows to measure the overall mechanical response of a GUVs after small changes in the composition.[50] Nevertheless, due to the complex composition and diversity of the membranes, mostly comprising submicrometric domains, the use of local characterization techniques is required.

Thanks to the possibility of working under controlled environment and with distance and force resolution at the nanoscale, atomic force microscopy (AFM) is nowadays a well-established technique for both imaging the morphology and probing the local physical and

mechanical properties of SLBs by means of force spectroscopy.[12, 51-54] However, the resolution given by AFM might be inferior to the one achievable with X-ray (XR) and neutron techniques.[55-58] In particular, XR techniques such as XR reflectivity (XRR) and grazing incidence XR diffraction (GIXD) are powerful tools to characterize surfaces below the nanoscale, providing structural information in the reciprocal space through the interaction between XR and the sample electronic structure.[59-63] Still, since these techniques do not involve any mechanical interaction with the specimen, mechanical properties cannot be evaluated with XR.

1.3.1. AFM: topographical and mechanical characterization

Since AFM was born in 1986,[64] it has been an essential technique to explore a wide range of samples at the nanoscale. The main advantage of AFM relies on the possibility of controlling the environmental conditions (medium composition and temperature) while applying and sensing minimal forces (pN to nN range). This consequently enables to operate in a liquid environment on a large variety of biological samples; from single molecules, i.e. DNA or proteins, to macromolecular assemblies such as SLBs or even whole cells.[65, 66] AFM has become a well-established technique for imaging the lateral organization of lipid membranes that show homogeneous or phase separated morphology.[51, 54] Comparing with other techniques, AFM allows for the structure of biological samples to be imaged in real time – with the possible use of high speed AFM (HS-AFM)[67-69] – and with (sub)nanometer resolution.[70] Figure 1.4 shows two examples. In the first one, the HS-AFM is used to track the motion dynamics of the myosin-V molecular motor when walking along an actin filament (figure 1.4(a)).[71] The second example shows that the acquisition of topographical images with a HS-AFM (figure 1.4(b), right) is approximately three orders of magnitude faster compared with a conventional AFM (figure 1.4(b), left), allowing the capture of single molecule dynamics.[72] The conventional AFM image corresponds to the photosynthetic apparatus of *Rhodospirillum photometricum*, whereas the HS-AFM topographies show OmpF trimers.

Thanks to the ability of AFM to sense and apply forces with high accuracy, AFM-based force spectroscopy (AFM-FS) has become an excellent tool to study molecular interactions at the single molecule level.[73] Therefore, during the last decades AFM-FS has been used to perform nanomechanical studies on a wide range of systems, such as indenting hard materials with the AFM tip[74] or pulling individual macromolecules – polysaccharides,[73, 75] proteins[76-78] and DNA[79] – during the retract of the AFM tip away from the surface. In the case of lipid bilayers, AFM-FS has become very valuable to probe the mechanical properties at the nanoscale with high spatial and force resolution.[13, 52, 53, 80]

Experimentally, an SLB patch is first located by AFM imaging the sample (figure 1.5(a)). Then, the AFM tip away from the surface is approached and maintained at constant force

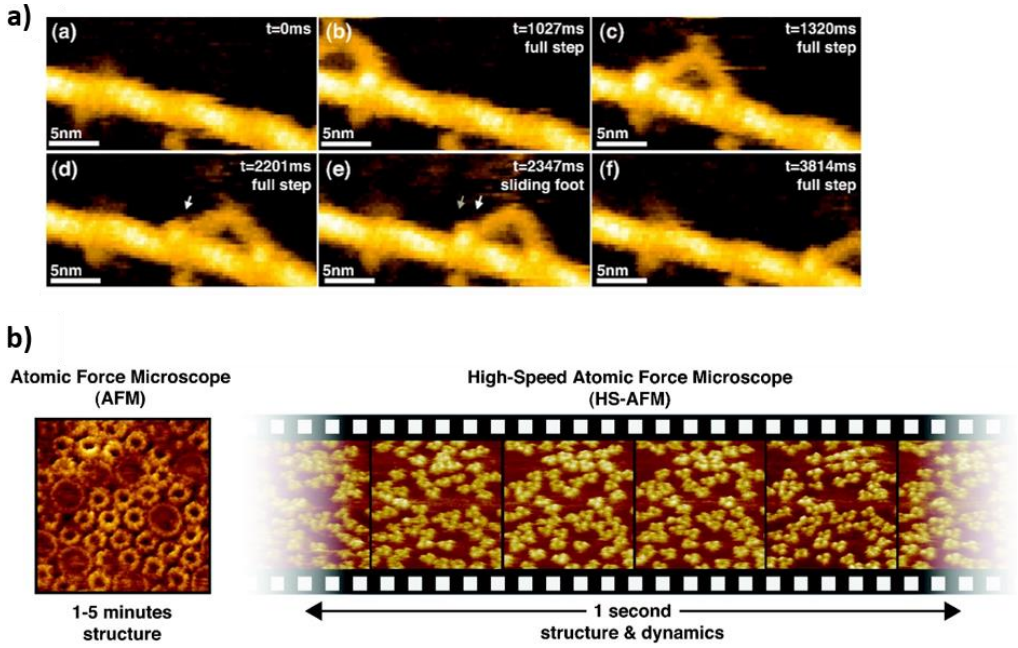

Figure 1.4 a) Molecular motor motion dynamics of myosin-V walking along an actin filament. (a) – (d) and (f) Full step of myosin-V motor. (e) Sliding of trailing head (arrows in (d) and (e)). Adapted with permission from refs.[71-72]. Copyright © 2010, Springer Nature. b) Left: conventional AFM image of the photosynthetic apparatus of *Rhodospirillum photometricum*. Right: HS-AFM images series of OmpF trimers. Adapted with permission from ref.[72]. Copyright © 2011, Elsevier.

onto the SLB (AFM-based force clamp),[45, 46] or approached and retracted at constant velocity.[12, 52, 81] Upon mechanical contact, the cantilever deflection increases and the SLB is elastically compressed by the AFM probe until the tip suddenly breaks through the bilayer, getting in direct contact with the substrate (figure 1.6). The penetration of the AFM tip through the bilayer appears as a discontinuity in the approaching force-separation curve (red curve in figure 1.6). The step observed in the separation correlates with the thickness of the SLB. The vertical force at which this discontinuity happens corresponds to the maximum force the bilayer is able to stand before breaking and it is defined as breakthrough force (F_b). F_b usually occurs at several nN and it is considered as a direct measurement of the lateral interactions between the lipid molecules. Previous reports show that F_b is significantly altered due to variations in the chemical structure of the phospholipid molecules[34, 82] and in the physicochemical environment (temperature, pH or ionic strength).[12, 82-84] Therefore, F_b is considered as the fingerprint of the mechanical stability of a certain lipid bilayer under specific environmental conditions. In multicomponent SLBs (figure 1.5- bottom), the F_b value can be directly associated to the membrane composition of homogeneous systems or phase-segregated domains.[13, 85, 86] Hence, force spectroscopy

measurements helps to better understand the nature of the different phases observed in the AFM topographical images, thanks to what is called F_b map (figure 1.5(b)). After imaging the selected area, several force-distance curves are performed by following a grid in the same scanned region. Extracting the values of the desired mechanical parameters, an F_b map correlating with the topography can be built, as well as the corresponding distribution in order to get the mean values for each variable (figure 1.5(c)). For instance, values of F_b, adhesion forces a nd height obtained from force-distance curves can be associated to the different gel and liquid domains observed in the topography of phase-segregated SLBs. This phase segregation is exemplified in figure 1.5-bottom for a DPPC (1,2-dipalmitoyl-*sn*-glycero-3-phosphocholine) SLB that contains 20 mol % of Chol. We observe the domains of different composition in the topographical image (figure 1.5(a), bottom) that display different mechanical resistance, as shown in the F_b map (figure 1.5(b), bottom) and bimodal F_b distribution (figure 1.5(c), bottom).

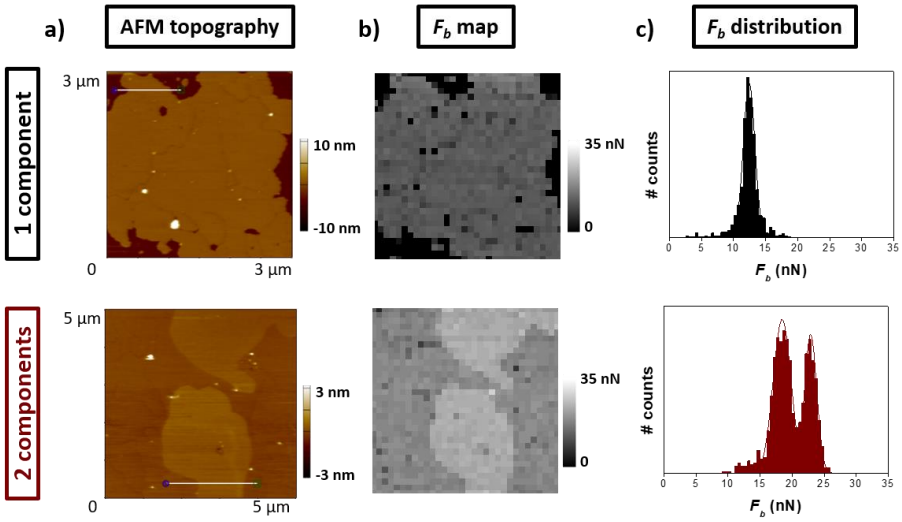

Figure 1.5 AFM-FS experiments performed on SLBs of 1 (top) and 2 (bottom) components. a) AFM topographical images. b) F_b maps. c) F_b distributions.

1.3.2. X-Ray grazing incidence techniques: structural characterization

X-Ray (XR) grazing incidence (GI) techniques have been employed to study a large variety of samples from many different fields like biology, chemistry, physics, among others. Indeed, techniques such as reflectometry (XRR), GI small-angle XR scattering (GISAXS) and GI XR diffraction (GIXD), have been widely used to characterize the structural properties of biological surfaces at the nanoscale.[61, 87, 88] They provide information about the sample structure in the reciprocal space, by means of the interaction between the XR and the sample. In these experiments, the information is usually averaged over the area illuminated by the beam footprint, ranging from hundreds of microns to several millimeters depending

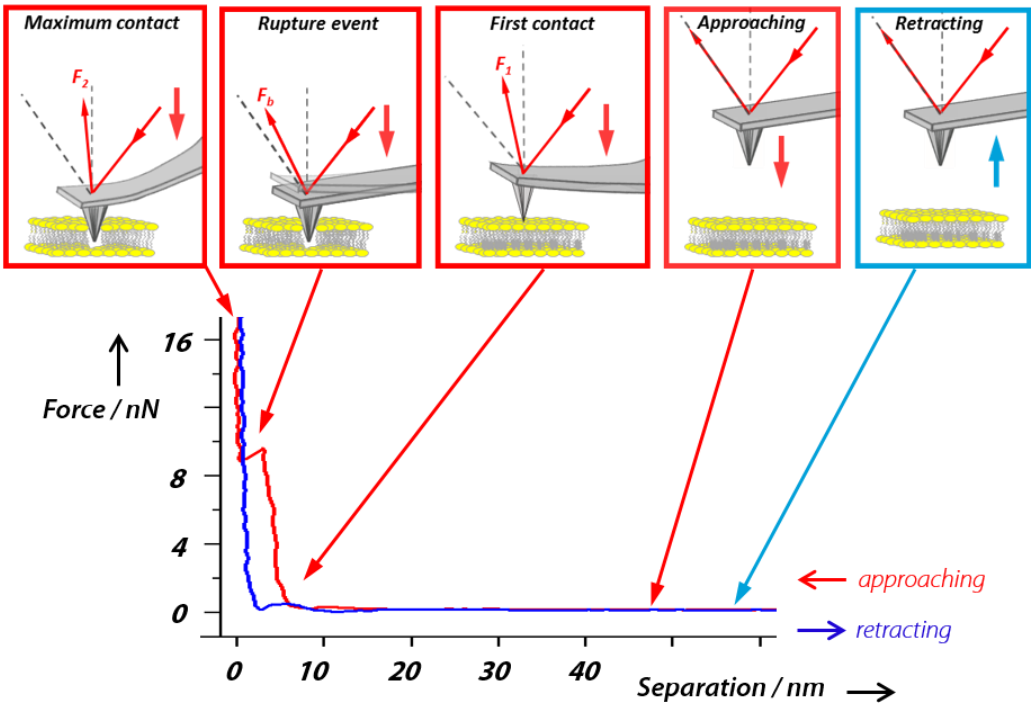

Figure 1.6 Schematics of the SLB indentation process using AFM-based force spectroscopy (AFM-FS), displaying a force–separation typical curve, showing the discontinuity in the approach curve when the bilayer is punctured.

on the beam size and the experimental conditions. Data are usually collected in synchrotrons, large-scale facilities providing XR beams with high brilliance. Synchrotron radiation permits to investigate the structure of materials by providing the electronic density at high resolution, allowing to probe length scales ranging from angstroms to microns.

1.3.2.1. XRR: vertical structure

XRR is a surface analytical technique for studying the detailed surface properties of thin films and multilayer-based materials, obtaining information about the film thickness, the surface roughness and the density. XRR has been applied to a wide range of research areas including soft matter (polymers and biological systems, within others), semiconductors or metals. In fact, there is already a large amount of XRR experiments that have focused on determining the electronic vertical structure of lipid monolayers, bilayers and stacks of bilayers (or multi-bilayers), at the liquid/air and solid/liquid interfaces, respectively, considering XRR as a well-established technique in the field.[59, 62, 63] However, in the study of

biological samples with XRR, radiation damage due to the high beam energy and exposure time remains an unresolved issue.

In XRR, the intensity of the reflected XR beam is measured over a range of angles in the specular direction* (figure 1.7) during the interaction between the XR beam with a sample area that has variations in the electronic density (figure 1.8(a)), and so representing the different layers of the sample. Above the critical angle for total reflection, the XRR intensity (figure 1.8(b)) decreases in a way that is dependent on the structural properties of the interface. Therefore, each sample layer scatters a certain XR reflected beam (figure 1.8(a)). The constructive and destructive interference between the XR beams reflected at the different sample layers provides the interference pattern, and so the fringes characteristic from a typical XRR curve (figure 1.8(b)). These interferences depend on the film thickness and the energy (or wavelength) of the XR beam. Finally, the XRR curves need to be fitted with a specific model that provides the scatering length density (SLD) profile, from where we get the information about the structural parameters of the films.

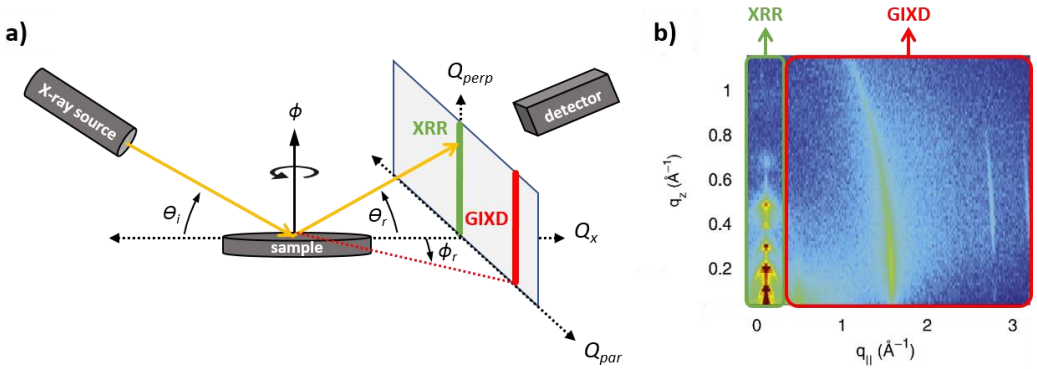

Figure 1.7 a) Diagram of XR specular (θ_i and θ_r are symmetric) and off-specular (θ_i and θ_r are asymmetric) reflection, for XRR and GIXD acquisitions, respectively. b) Diffracted intensity 2D contour plot for multilamellar DMPC membrane stacks, with the specular (XRR) and off-specular (GIXD) regions highlighted. Adapted from ref.[92]. Copyright © 2015, Elsevier.

1.3.2.2. GIXD: in-plane lateral organization

GIXD is an analytical surface technique for studying the atomic structure of materials, obtaining information about the in-plane *d*-spacing between atoms or molecules. Concerning lipid membranes, most of the GIXD reported studies have been extrapolated from experiments conducted on multi-bilayers[89, 90] or on monolayers at the water/air interface.[91] This is due to the requirement of a wetting preservation to guarantee the

* In specular conditions the incident (θ_i) and reflected (θ_r) angles are symmetric.

stability of BMs at the solid/liquid interface, which makes the in-plane structural characterization of a single lipid bilayer extremely challenging.†

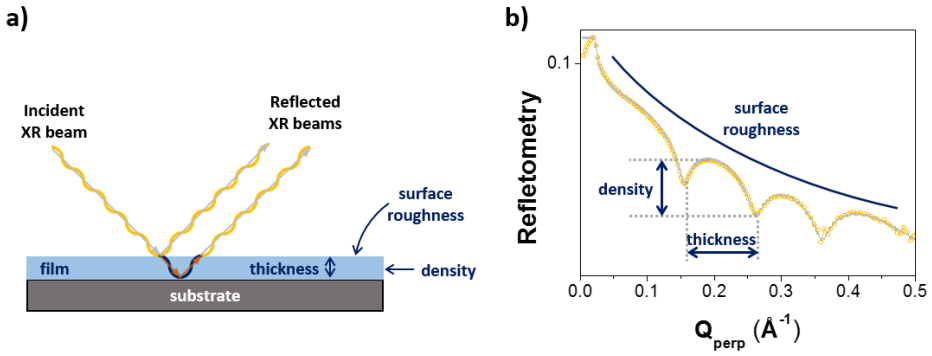

Figure 1.8 a) Scheme of the incident and reflected XR beams from a thin film. b) XRR curve of a thin film, in this case an SLB.

After exposing the incident XR beam to the sample in GI conditions, the diffracted intensity two-dimensional pattern is acquired, such as the one presented in figure 1.7(b) corresponding to stacks of multilamellar DMPC (1,2-dimyristoyl-*sn*-glycero-3-phosphocholine) membranes.[92] Integrating the diffraction pattern over $Q_{perpendicular}$ (Q_{perp}) in the off-specular region (figure 1.7(a)),‡ the position of the diffraction peaks along $Q_{parallel}$ (Q_{par}) are determined. Finally, these positions are used to calculate the *d*-spacing between the atoms or molecules considering the equations for the corresponding sample packing.

1.3.2.3. Coupling AFM and XR techniques

Due to the fact that mechanical properties cannot be evaluated with XR techniques because of the non-mechanical interaction with the specimen, the combination of XR with the local –nanometer scale- and mechanical information by AFM has become attractive during the last decade.[93-98] So far, *in situ* correlative XR-AFM has give insights of dynamic processes,[99] such as phase transitions or chemical reactions, as well as to use the AFM tip to apply an external force or employ it to align a nano-object with the XR beam. In addition, the AFM can also be used to evaluate the radiation damage induced by the XR beam in real time.[99] Limiting radiation damage is a major challenge when using very intense XR beams on soft and biological samples. For instance, the formation of micrometric holes produced by an intense XR nanobeam on a semiconducting organic thin film has been lately observed *in situ* by means of HS-XR-AFM.[100]

† See chapter 6 for further details.
‡ In off-specular conditions the incident and reflected angles are asymmetric.

1.4. Objectives

The general objective of this thesis is to investigate the physicochemical and structural properties of model lipid membranes combining atomic force microscopy (AFM) and spectroscopy (AFM-FS) and X-Ray techniques. The AFM provides the morphological and mechanical information of the SLBs, whereas the XR gives more understandings on the electronic structure of the bilayers. We also propose advanced methodologies based on AFM and XR as well as the coupling of both techniques for local *in situ* experiments. These technical progresses allow us to study not only the diversity on the chemical composition of the bilayers, but also the effect of small molecules or peptides to the membrane physical and structural properties. In addition, by means of AFM and AFM-FS we also characterize vesicular systems that are not composed by phospholipid molecules, which have a technological application: to act as nanocarriers for drug delivery.

Based on this general objective, the specific objectives are:

- Study of the nanomechanics by means of AFM and AFM-FS of SLBs of different composition (chapter 2) as well as on membranes of vesicles used for biomedical applications (chapter 3).

  To this end, we study the phase behavior and mechanical properties of pure PC SLBs, and membranes of increased complexity by incorporating a specific content of Chol and galactosylceramides (GalCer) (chapter 2). GalCer are glycosphingolipids mainly found in neuronal tissues, being involved in a very wide range of biological activities such as cell-cell interaction, intracellular communication, cellular development, and antitumor/cytotoxic effects. In addition, they are known to be aligned in a compact manner and accumulated in the outer leaflet of the membrane together with Chol. It is known that specific amounts of GalCer can lead to separation of domains in some PC membranes. However, the mechanics of these bilayers has still not been evaluated. For this reason, it is of great significance to study the nanomechanical behavior of these components into model PC SLBs to better understand their physical function.

  We also characterize for the first time the membrane morphology and nanomechanics of Quatsome (QT) membranes (chapter 3). QTs are recently discovered unilamellar nanovesicles constituted by quaternary ammonium surfactants and sterols, which fulfill the structural and physicochemical requirements to be a potential platform for the encapsulation of both therapeutic and diagnostic actives for site specific delivery. According to the cationic surfactant and sterol, as well as the suspension media used to prepare the QTs, it is possible to tune the mechanical properties of their bilayer and the flexibility of the entire QT vesicle, a property that is essential in several specific applications, like transdermal

drug delivery. For this reason, it is important to fully understand the interplay between the compositional structure and the physical and mechanical properties.

- Evaluation of the effect of small antimicrobial peptides on the structural and mechanical properties of model membranes using both AFM and XR based techniques (chapter 5).

  We assess the effect of a human neutrophil peptide (HNP) defensin on the physical and structural properties of model membranes with different composition (chapter 5). The mechanisms by which microorganisms are killed by defensins are not fully understood, although in general it is believed that killing is a consequence of disruption of the microbial membrane. In the case of the HNP1, several reports have shown the lipid specificity of these peptides, which have been mostly studied on model vesicular systems or on extracts of bacterial membranes. Here, we study the morphological, mechanical and structural changes observed on model SLBs of different phospholipid composition, before and upon the incubation of HNP1. This can provide a better understanding on the HNP1 activity towards mammalian or bacterial cells.

- Establishment of advanced methodologies based on AFM-FS (chapter 4) and XR (chapter 6) techniques to study mechanics and lateral organization of SLBs, including the development of an AFM to be used *in situ* with synchrotron XR measurements (chapter 7).

  We propose an advanced AFM-FS approach to explore the nanomechanics of SLBs by pulling out lipid tubes with an AFM tip (chapter 4). It is known that several cellular processes involve conformational changes such as bending, vesiculation and tubulation. Elasticity and mechanical measurements have been reported using different techniques on a wide range of model membrane systems. However, the heterogeneous composition of the membranes as well as the complex sample preparation protocols made more difficult the membrane mechanics characterization. Hence, our methodological approach, combines the advantages of the AFM to locally probe a sample with lateral resolution at the nanoscale and apply and sense force in the pN range, with the simplicity of the SLB approach.

  We further present a novel and simple setup that allows for straightforward GIXD characterization of hydrated individual SLBs (chapter 6). The structural characterization of single hydrated bilayers by GIXD is an extremely challenging task, and only few successful GIXD studies have been reported so far using complex setups. This is due to the need of a wetting layer to guarantee the integrity of the BMs, which then requires high energy XR to increase the transmission through the liquid. Thus, the detection of the signal scattered by the bilayer structure gets more

complicated because of the resultant enhancement of the background level. The exposed setup is designed to minimize the scattering from the liquid and to allow the detection of the extremely weak diffracted signal from the lipid bilayer. This enables the differentiation of coexisting domains in phase-segregated membranes, such as the ones studied in this work composed of DPPC and different contents of Chol.

Finally, we developed a custom AFM that can be installed in a synchrotron radiation beamline, allowing *in situ* AFM and XR measurements (chapter 7). As mentioned before, the resolution obtained by AFM is usually inferior to the one achievable with XR techniques. On the other hand, XR do not involve any mechanical interaction with the sample, preventing the evaluation of its mechanical properties. Hence, it is usually a multimodal and correlative approach the requirement to better understand the mechanisms that govern, in our case, the structure of biological membranes. Here, the instrument allows a wide range of possible investigations by means of AFM and grazing incidence XR techniques, including soft and biological samples under physiological conditions.

Part of the work reported in this thesis was performed at the ESRF, the European Synchrotron in Grenoble (France).

1.5. References

1. W. Dowhan, *Annu. Rev. Biochem.*, 1997, **66**, 199-232.
2. O. Mouritsen and L. Bagatolli, "Life - As a Matter of Fat", *Springer International Publishing AG*, 2015.
3. P. L. Yeagle, "The Membranes of Cells", *Academic Press*, Boston, 2016, pp. 1-25.
4. S. J. Singer and G. L. Nicolson, *Science*, 1972, **175**, 720.
5. G. van Meer, D. R. Voelker and G. W. Feigenson, *Nat. Rev. Mol. Cell Bio.*, 2008, **9**, 112-124.
6. D. Lingwood and K. Simons, *Science*, 2010, **327**, 46-50.
7. K. Simons and W. L. C. Vaz, *Annu. Rev. Biophy. Biom.*, 2004, **33**, 269-295.
8. E. Sezgin, I. Levental, S. Mayor and C. Eggeling, *Nat. Rev. Mol. Cell Bio.*, 2017, **18**, 361.
9. S. Chiantia, N. Kahya and P. Schwille, *Langmuir*, 2007, **23**, 7659-7665.
10. J. Henriksen, A. C. Rowat, E. Brief, Y. W. Hsueh, J. L. Thewalt, M. J. Zuckermann and J. H. Ipsen, *Biophys. J.*, 2006, **90**, 1639-1649.
11. J. J. Pan, T. T. Mills, S. Tristram-Nagle and J. F. Nagle, *Phys. Rev. Lett.*, 2008, **100**.
12. L. Redondo-Morata, M. I. Giannotti and F. Sanz, *Mol. Membr. Biol.*, 2014, **31**, 17-28.
13. L. Redondo-Morata, M. I. Giannotti and F. Sanz, *Langmuir*, 2012, **28**, 12851-12860.
14. T. Rog, M. Pasenkiewicz-Gierula, I. Vattulainen and M. Karttunen, *BBA - Biomembranes*, 2009, **1788**, 97-121.
15. W.-C. Hung, M.-T. Lee, F.-Y. Chen and H. W. Huang, *Biophys. J.*, 2007, **92**, 3960-3967.
16. J. J. Pan, S. Tristram-Nagle and J. F. Nagle, *Phys. Rev. E*, 2009, **80**.
17. N. Kucerka, J. D. Perlmutter, J. Pan, S. Tristram-Nagle, J. Katsaras and J. N. Sachs, *Biophys. J.*, 2008, **95**, 2792-2805.
18. P. L. Yeagle, "The Membranes of Cells", *Academic Press*, Boston, 2016, pp. 27-56.
19. F. M. Goni and A. Alonso, *BBA-Biomembranes*, 2006, **1758**, 1902-1921.
20. C. R. Bollinger, V. Teichgraber and E. Gulbins, *BBA - Mol. Cell Res.*, 2005, **1746**, 284-294.

21. F. Guyomarc'h, M. Chen, O. Et-Thakafy, S. Zou and C. Lopez, *BBA - Biomembranes*, 2017, **1859**, 949-958.
22. M. L. Longo and C. D. Blanchette, *BBA - Biomembranes*, 2010, **1798**, 1357-1367.
23. X. L. Han and H. Cheng, *J. Lipid Res.*, 2005, **46**, 163-175.
24. J. C. M. Holthuis and T. P. Levine, *Nat. Rev. Mol. Cell Bio.*, 2005, **6**, 209.
25. P. A. Janmey and P. K. J. Kinnunen, *Trends Cell Biol.*, 2006, **16**, 538-546.
26. E. Hohenester, *Curr. Opin. Struc. Biol.*, 2014, **29**, 10-16.
27. P. Roca-Cusachs, T. Iskratsch and M. P. Sheetz, *J. Cell Sci.*, 2012, **125**, 3025.
28. A. E. M. Beedle, A. Williams, J. Relat-Goberna and S. Garcia-Manyes, *Curr. Opin. Chem. Biol.*, 2015, **29**, 87-93.
29. O. Wesolowska, K. Michalak, J. Maniewska and A. B. Hendrich, *Acta Biochim. Pol.*, 2009, **56**, 33-39.
30. E. Evans, V. Heinrich, F. Ludwig and W. Rawicz, *Biophys. J.*, 2003, **85**, 2342-2350.
31. N. Kahya, D. Scherfeld, K. Bacia and P. Schwille, *J. Struct. Biol.*, 2004, **147**, 77-89.
32. E. Sezgin, H.-J. Kaiser, T. Baumgart, P. Schwille, K. Simons and I. Levental, *Nat. Protoc.*, 2012, **7**, 1042.
33. E. T. Castellana and P. S. Cremer, *Surf. Sci. Rep.*, 2006, **61**, 429-444.
34. S. Garcia-Manyes, L. Redondo-Morata, G. Oncins and F. Sanz, *J. Am. Chem. Soc.*, 2010, **132**, 12874-12886.
35. M. C. Giocondi, D. Yamamoto, E. Lesniewska, P. E. Milhiet, T. Ando and C. Le Grimellec, *BBA - Biomembranes*, 2010, **1798**, 703-718.
36. M. C. Giocondi, V. Vie, E. Lesniewska, P. E. Milhiet, M. Zinke-Allmang and C. Le Grimellec, *Langmuir*, 2001, **17**, 1653-1659.
37. M.-P. Mingeot-Leclercq, M. Deleu, R. Brasseur and Y. F. Dufrene, *Nat. Protoc.*, 2008, **3**, 1654-1659.
38. D. R. Talham, T. Yamamoto and M. W. Meisel, *J. Phys.-Condens. Mat.*, 2008, **20**.
39. U. Mennicke and T. Salditt, *Langmuir*, 2002, **18**, 8172-8177.
40. E. Reimhult, F. Hook and B. Kasemo, *Langmuir*, 2003, **19**, 1681-1691.
41. L. K. Tamm and H. M. McConnell, *Biophys. J.*, 1985, **47**, 105-113.
42. J. Majewski, J. Y. Wong, C. K. Park, M. Seitz, J. N. Israelachvili and G. S. Smith, *Biophys. J.*, 1998, **75**, 2363-2367.
43. H. L. Smith, M. S. Jablin, A. Vidyasagar, J. Saiz, E. Watkins, R. Toomey, A. J. Hurd and J. Majewski, *Phys. Rev. Lett.*, 2009, **102**.
44. I. Mey, M. Stephan, E. K. Schmitt, M. M. Mueller, M. Ben Amar, C. Steinem and A. Janshoff, *J. Am. Chem. Soc.*, 2009, **131**, 7031-7039.
45. L. Redondo-Morata, M. I. Giannotti and F. Sanz, *Langmuir*, 2012, **28**, 6403-6410.
46. J. Relat-Goberna, A. E. M. Beedle and S. Garcia-Manyes, *Small*, 2017, **13**, 1700147-n/a.
47. J. P. Slotte, *BBA - Lipid Lipid Met.*, 1995, **1259**, 180-186.
48. V. Schram, H. N. Lin and T. E. Thompson, *Biophys. J.*, 1996, **71**, 1811-1822.
49. D. Honig and D. Mobius, *J. Phys. Chem.*, 1991, **95**, 4590-4592.
50. W. Rawicz, K. C. Olbrich, T. McIntosh, D. Needham and E. Evans, *Biophys. J.*, 2000, **79**, 328-339.
51. L. Redondo-Morata, M. I. Giannotti and F. Sanz, "Atomic Force Microscopy in Liquid", *Wiley-VCH Verlag GmbH & Co.KGaA*, Weinheim, Germany, 2012.
52. S. Garcia-Manyes and F. Sanz, *BBA - Biomembranes*, 2010, **1798**, 741-749.
53. L. Picas, P. E. Milhiet and J. Hernandez-Borrell, *Chem. Phys. Lipids*, 2012, **165**, 845-860.
54. K. El Kirat, S. Morandat and Y. F. Dufrene, *BBA - Biomembranes*, 2010, **1798**, 750-765.
55. G. Fragneto, T. Charitat and J. Daillant, *Eur. Biophys. J. Biophy.*, 2012, **41**, 863-874.
56. G. Fragneto, *Eur. Phys. J. – Spec. Top.* , 2012, **213**, 327-342.
57. N. Kucerka, F. A. Heberle, J. J. Pan and J. Katsaras, *Membranes*, 2015, **5**, 454-472.
58. J. F. Nagle and S. Tristram-Nagle, *BBA – Rev. Biomembranes*, 2000, **1469**, 159-195.
59. F. Evers, C. Jeworrek, K. Weise, M. Tolan and R. Winter, *Soft Matter*, 2012, **8**, 2170-2175.
60. C. E. Miller, J. Majewski, T. Gog and T. L. Kuhl, *Phys. Rev. Lett.*, 2005, **94**, 238104.
61. C. E. Miller, J. Majewski, E. B. Watkins, D. J. Mulder, T. Gog and T. L. Kuhl, *Phys. Rev. Lett.*, 2008, **100**, 058103.
62. E. Novakova, K. Giewekemeyer and T. Salditt, *Phys. Rev. E*, 2006, **74**.

63. J. Daillant, E. Bellet-Amalric, A. Braslau, T. Charitat, G. Fragneto, F. Graner, S. Mora, F. Rieutord and B. Stidder, *P. Natl. Acad. Sci. USA*, 2005, **102**, 11639-11644.
64. G. Binnig, C. F. Quate and C. Gerber, *Phys. Rev. Lett.*, 1986, **56**, 930-933.
65. Y. F. Dufrene, T. Ando, R. Garcia, D. Alsteens, D. Martinez-Martin, A. Engel, C. Gerber and D. J. Muller, *Nat. Nano.*, 2017, **12**, 295-307.
66. P. Parot, Y. F. Dufrene, P. Hinterdorfer, C. Le Grimellee, D. Navajas, J. L. Pellequer and S. Scheuring, *J. Mol. Recognit.*, 2007, **20**, 418-431.
67. T. Ando, T. Uchihashi and N. Kodera, *Jpn. J. Appl. Phys.*, 2012, **51**.
68. T. Ando, T. Uchihashi and S. Scheuring, *Chem. Rev.*, 2014, **114**, 3120-3188.
69. F. Eghiaian, F. Rico, A. Colom, I. Casuso and S. Scheuring, *Febs Lett.*, 2014, **588**, 3631-3638.
70. S. Scheuring and Y. F. Dufrene, *Mol. Microbiol.*, 2010, **75**, 1327-1336.
71. N. Kodera, D. Yamamoto, R. Ishikawa and T. Ando, *Nature*, 2010, **468**, 72.
72. I. Casuso, F. Rico and S. Scheuring, *Curr. Opin. Chem. Biol.*, 2011, **15**, 704-709.
73. M. I. Giannotti and G. J. Vancso, *Chem. Phys. Chem*, 2007, **8**, 2290-2307.
74. S. G. Corcoran, R. J. Colton, E. T. Lilleodden and W. W. Gerberich, *Phys. Rev. B*, 1997, **55**, 16057-16060.
75. M. I. Giannotti, M. Rinaudo and G. J. Vancso, *Biomacromolecules*, 2007, **8**, 2648-2652.
76. M. I. Giannotti, I. C. de Vaca, J. M. Artes, F. Sanz, V. Guallar and P. Gorostiza, *J. Phys. Chem. B*, 2015, **119**, 12050-12058.
77. F. Rico, L. Gonzalez, I. Casuso, M. Puig-Vidal and S. Scheuring, *Science*, 2013, **342**, 741-743.
78. T. E. Fisher, A. F. Oberhauser, M. Carrion-Vazquez, P. E. Marszalek and J. M. Fernandez, *Trends Biochem. Sci.*, 1999, **24**, 379-384.
79. G. U. Lee, L. A. Chrisey and R. J. Colton, *Science*, 1994, **266**, 771.
80. A. Alessandrini and P. Facci, *Micron.*, 2012, **43**, 1212-1223.
81. B. Gumi-Audenis, L. Costa, F. Carla, F. Comin, F. Sanz and M. I. Giannotti, *Membranes*, 2016, **6**.
82. S. Garcia-Manyes, G. Oncins and F. Sanz, *Biophys. J.*, 2005, **89**, 1812-1826.
83. S. Garcia-Manyes, G. Oncins and F. Sanz, *Biophys. J.*, 2005, **89**, 4261-4274.
84. S. Garcia-Manyes, G. Oncins and F. Sanz, *Electrochim. Acta*, 2006, **51**, 5029-5036.
85. J. K. Li, R. M. A. Sullan and S. Zou, *Langmuir*, 2011, **27**, 1308-1313.
86. M. H. Abdulreda and V. T. Moy, *Biophys. J.*, 2007, **92**, 4369-4378.
87. C. E. Miller, J. Majewski, T. Gog and T. L. Kuhl, *Phys. Rev. Lett.*, 2005, **94**.
88. E. Nováková, K. Giewekemeyer and T. Salditt, *Phys. Rev. E*, 2006, **74**, 051911.
89. T. Salditt and G. Brotons, *Anal. Bioanal. Chem.*, 2004, **379**, 960-973.
90. M. A. Barrett, S. Zheng, L. A. Toppozini, R. J. Alsop, H. Dies, A. Wang, N. Jago, M. Moore and M. C. Rheinstadter, *Soft Matter*, 2013, **9**, 9342-9351.
91. A. Ivankin, I. Kuzmenko and D. Gidalevitz, *Phys. Rev. Lett.*, 2010, **104**, 108101.
92. H. Dies, B. Cheung, J. Tang and M. C. Rheinstädter, *BBA - Biomembranes*, 2015, **1848**, 1032-1040.
93. T. Scheler, M. Rodrigues, T. W. Cornelius, C. Mocuta, A. Malachias, R. Magalhaes-Paniago, F. Comin, J. Chevrier and T. H. Metzger, *Appl. Phys. Lett.*, 2009, **94**.
94. M. S. Rodrigues, O. Dhez, S. Le Denmat, J. Chevrier, R. Felici and F. Comin, *J. Instrum.*, 2008, **3**.
95. L. Costa and M. S. Rodrigues, *Synchrotron Radiat. News*, 2016, **29**, 3-7.
96. N. Pilet, J. Raabe, S. E. Stevenson, S. Romer, L. Bernard, C. R. McNeill, R. H. Fink, H. J. Hug and C. Quitmann, *Nanotechnology*, 2012, **23**.
97. Z. Ren, F. Mastropietro, A. Davydok, S. Langlais, M. I. Richard, J. J. Furter, O. Thomas, M. Dupraz, M. Verdier, G. Beutier, P. Boesecke and T. W. Cornelius, *J. Synchrotron Radiat.*, 2014, **21**, 1128-1133.
98. C. Leclere, T. W. Cornelius, Z. Ren, A. Davydok, J. S. Micha, O. Robach, G. Richter, L. Belliard and O. Thomas, *J. Appl. Crystallogr.*, 2015, **48**, 291-296.
99. B. Gumi-Audenis, F. Carla, M. V. Vitorino, A. Panzarella, L. Porcar, M. Boilot, S. Guerber, P. Bernard, M. S. Rodrigues, F. Sanz, M. I. Giannotti and L. Costa, *J. Synchrotron Radiat.*, 2015, **22**, 1364-1371.
100. M. V. Vitorino, Y. Fuchs, T. Dane, M. S. Rodrigues, M. Rosenthal, A. Panzarella, P. Bernard, O. Hignette, L. Dupuy, M. Burghammer and L. Costa, *J. Synchrotron Radiat.*, 2016, **23**, 1110-1117.

Chapter 2

From simple to complex bilayers: AFM and AFM-FS study*

The physicochemical properties of biological membranes (BMs) are sometimes more difficult to evaluate due to high complexity of the BMs regarding composition, including phospholipids, sphingolipids and cholesterol (Chol). Supported lipid bilayers (SLBs) are simplified model systems frequently used to mimic BMs, allowing to investigate biological processes occurring at the cellular and subcellular level. SLBs permit to increase the bilayer complexity, from bilayers of one component to multicomponent ones. In this work, we used the well-stablished atomic force microscopy (AFM) and AFM-based force spectroscopy (AFM-FS) techniques to characterize the physical properties of SLBs from simple pure phosphocholine (PC), to PC bilayers incorporating components, such as Chol or/and a surface glycosphingolipid, to increase the complexity of the systems. We evaluated the phase behaviour and nanomechanics.

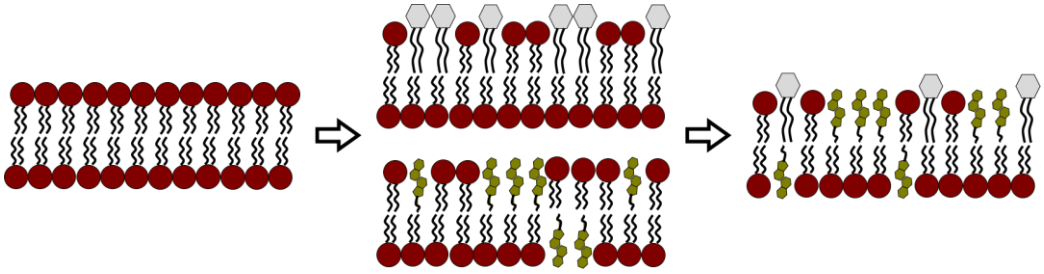

* This work has been published: B. Gumí-Audenis, F. Sanz and M. I. Giannotti. *Soft Matter*, 2015, **11**, 5447-5454;

2.1. Introduction

The physical properties of biological membranes (BMs) are sometimes difficult to evaluate, comprising those affecting the biological processes mediated by the membrane.[1] Moreover, the composition of BMs is of significant complexity, including large amounts of sphingolipids (SLs), together with cholesterol (Chol) and glycerophospholipids, complicating their physicochemical characterization. In fact, to coordinate its functions, the membrane is able to laterally segregate nanoscale assemblies of lipids enriched in Chol, SLs and proteins in the outer leaflet of the membrane.[2, 3] This is known as the "raft" concept of membrane subcompartmentalization, in which these domains are known to have an important influence on essential functions in membrane signalling and trafficking.[2, 4] Nanometric techniques are therefore become essential to explore the heterogeneous physical properties of BMs.

As explained in the introductory chapter, model bilayer systems, such as supported lipid bilayers (SLBs), are frequently used to mimic BMs, allowing to investigate biological processes occurring at the cellular and subcellular level.[5, 6] Hence, the use of these manageable bilayer platforms facilitates the physicochemical characterisation, giving the possibility of increasing the bilayer complexity, from pure phospholipid bilayers to multicomponent ones. Thanks to the possibility of working in a controlled environment, atomic force microscopy (AFM) is now a well-established technique for both imaging the morphology and probing the local nanomechanical properties of SLBs by means of force spectroscopy modes.[5, 7-10] In this chapter, we will focus on studying the physical properties of phosphocholine (PC) SLBs, before and after incorporating Chol or/and a glycosphingolipid (GSL), namely galactosylceramide (GalCer), increasing then the complexity of the membranes. The chemical structures of the different components are shown in figure 2.1.

Chol can reach concentrations up to 50 mol % of the overall lipid contained in cell plasma membranes. Certainly, Chol plays an essential role in modulating membrane physical properties, being highly important in the function and evolution of the BMs.[11, 12] It is involved in the regulation of membrane fluidity, control of the lipid organization and phase behavior, and increase of the mechanical stability of the membrane.[7, 13, 14]

Among the family of SLs, GSLs are important communication devices used by cells, as they function as receptors in signalling, microbial and cellular adhesion processes, and display immunological identity.[15, 16] It is believed that Chol plays an essential role in the mechanisms behind the receptor function of GSLs,[17-20] by regulating the GSL accessibility through direct conformational tuning of the headgroup. In particular, cerebrosides are a family of GSLs, specifically composed of a double-tailed ceramide (Cer), which is bound to a monosaccharide, either galactose (galactosylceramide, GalCer) or glucose (glucosylceramide, GlcCer), by a glycosidic linkage through the primary hydroxyl. They are

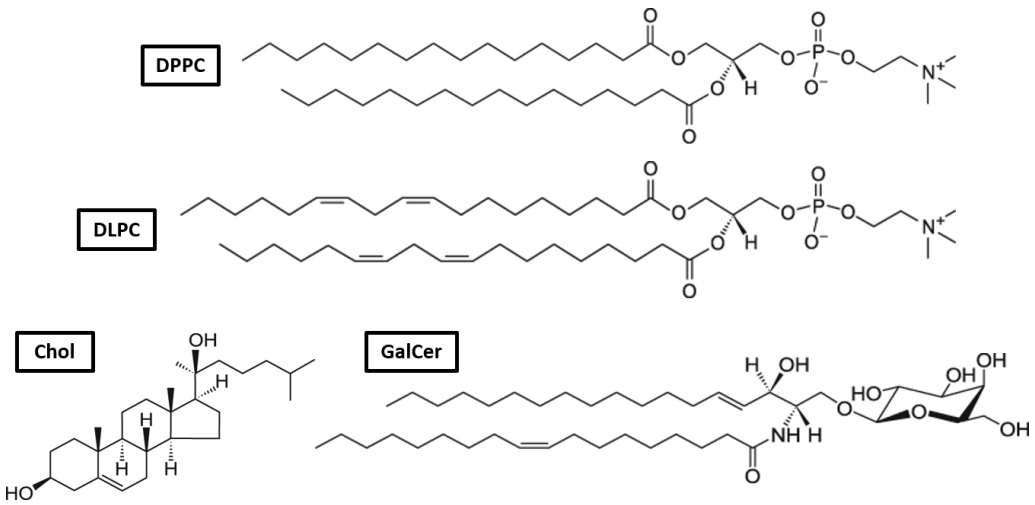

Figure 2.1 Chemical structures of DPPC (1,2-dipalmitoyl-*sn*-glycero-3-phosphocholine), DLPC (1,2-dilauroyl-*sn*-glycero-3-phosphocoline), Chol and GalCer.

commonly found to be highly saturated in natural sources.[21, 22] GalCer is found primarily in neuronal tissues and is the major GSL in the central nervous system, being the largest single component of the myelin sheath of nerves. GalCer is involved in cell-cell interaction, intracellular communication, cellular development, and antitumor/cytotoxic effects.[23] Its transition temperature (T_m) is well above physiological body temperature, due to the extensive hydrogen bonding capability by lateral interaction between the saccharide headgroup and the hydroxy and amide groups of the sphingosine base of the ceramide part.[24, 25] GalCer is aligned in a compact manner and tend to be accumulated in the outer leaflet of the membrane together with Chol.[22, 26] Therefore, it is of great significance to understand the nanomechanical behavior of lipid bilayers and the physical function of each membrane component.

In this work, we used the well-stablished atomic force microscopy (AFM) and AFM-based force spectroscopy (AFM-FS) techniques, including dynamic force spectroscopy (DFS) measurements, to characterize the physical properties of model SLBs. We evaluated the phase behaviour and nanomechanical properties of the pure PC bilayers, then incorporating components (GalCer or/and Chol) to increase the complexity of the systems.

2.2. Experimental

Materials. 1,2-dipalmitoyl-*sn*-glycero-3-phosphocholine (DPPC), 1,2-dilauroyl-*sn*-glycero-3-phosphocoline (DLPC) and cholesterol (Chol) were purchased from Sigma-Aldrich (St. Louis, MO) and galactosylceramides (Ceramide beta-*D*-galactose, GalCer, from bovine spinal cord -containing both hydroxy and non-hydroxy fatty acid side chains) from

Matreya LLC (Pleasant Gap, PA). All experiments were performed in buffer solution of 150 mM NaCl, 20 mM $MgCl_2$, 20 mM HEPES (4-(2-hydroxyethyl)-1-piperazineethanesulfonic acid) (pH 7.4) prepared with ultrapure water (Milli-Q reverse osmosis system, 18.2 mΩ·cm resistivity) and filtered before use with an inorganic membrane filter (0.22 μm pore size, Whatman International Ltd., England, U.K.).

Sample preparation.

Lipid vesicles. DPPC, DLPC, Chol and GalCer were individually dissolved in chloroform:methanol (3:1) to give a final concentration of 3 mM. Aliquots of phospholipid solutions were mixed and poured into a falcon tube to obtain different compositions. Next, the solvent was evaporated to dryness under nitrogen flow in order to achieve a thin film on the walls of the tube. Afterwards, the dried phospholipid films were hydrated with buffer solution, previously heated above the T_m of the lipid, until a final total concentration of 1 or 7 mM (stated) for vesicles characterization, and 0.25-0.35 mM to prepare SLBs. The falcon tubes were then subjected to cycles of vortex mixing (1 min) and heating (20 s) at a temperature above T_m. The vesicles suspensions were placed in an ultrasound bath for 30 min to finally obtain small unilamellar vesicles (SUVs).[27-30]

Supported lipid bilayers (SLBs). Circular mica surfaces (Ted Pella, Redding, CA) were used as substrates for AFM experiments. Before their use, mica surfaces were glued onto Teflon discs with epoxy-based mounting glue. To obtain SLBs, 100 μL of SUVs suspension were deposited onto freshly cleaved mica and heated for 20 min at a temperature above the T_m of the lipid mixture. After that, the samples were rinsed several times with buffer solution to avoid having unfused vesicles, but always kept hydrated on the mica substrates. During the sample preparation procedure, phospholipid-containing solutions were always protected from light.

Dynamic Light Scattering (DLS). Size distribution of DLPC and DPPC vesicles suspensions containing 20 mol % GalCer (1 mM) were analysed by DLS using a Zetasizer NanoS (Malvern Instruments, UK). Three independent runs were carried out for each sample. The measurements were performed at room temperature (*RT*).

Differential Scanning Calorimetry (DSC): DSC measurements were performed using a MicroCal VP-DSC (MicroCal, Northhampton, MA). Approximately 600 μL of liposome suspensions (7 mM) were placed in the sample cell and the same volume of buffer solution was used as reference. With 0.5 ºC·min^{-1} heating and cooling rate, the measurements were performed in the temperature range of 25 to 70 ºC.

Atomic force microscopy (AFM) and AFM-based force spectroscopy (AFM-FS). AFM images and AFM-FS measurements were performed with an MFP-3D atomic force microscope (Asylum Research, Santa Barbara, CA) using V-shaped Si_3N_4 cantilevers with sharp silicon tips and having a nominal spring constant of 0.35 N·m^{-1} (SNL, Bruker AFM

Probes, Camarillo, CA). After having measured the sensitivity of the piezo ($V \cdot m^{-1}$), the cantilever spring constants were individually calibrated using the equipartition theorem (thermal noise routine).[31]

AFM images were acquired in both contact and AC modes, at *RT* and under liquid conditions (buffer solution). After imaging an interesting area, force-distance curves were recorded by approaching and retracting the cantilever tip to the sample at constant velocity (1 $\mu m \cdot s^{-1}$, unless specifically stated). Force curves were acquired in the force map mode,[5] using an array of 32 x 32 (24 x 24 in the DFS experiments) points over a range of areas from 2 x 2 to 10 x 10 μm^2, depending on the observed phospholipid domain sizes in the scanned region.

2.3. Results and discussions

2.3.1. Vesicles characterization

The size of the liposomes in the suspension was first determined by DLS. Histograms of the number-weighted diameter for DPPC:GalCer (80:20 molar ratio) and DLPC:GalCer (80:20 molar ratio) (figure 2.2) show a unimodal distribution with mean values of 78 ± 13 nm and 65 ± 13 nm, respectively. These results confirm that the vesicles obtained by the method used are small and uniform in size. This may be of relevance when working in mixed bilayers, to ensure that the SLB composition is representative of the vesicles one, as vesicles composition and opening kinetics may vary with their size.

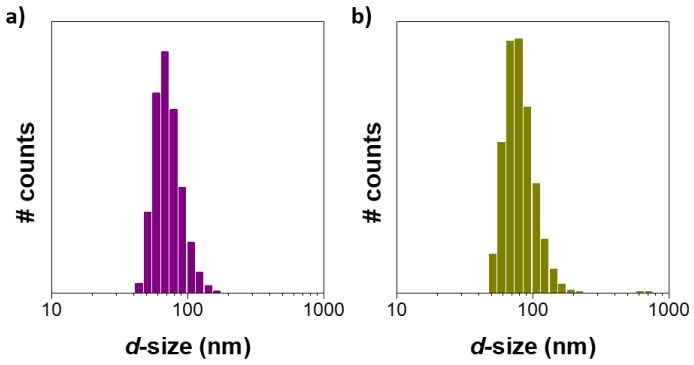

Figure 2.2 Number-weighted diameter distribution measured by DLS of vesicle suspensions, in 150 mM NaCl, 20 mM $MgCl_2$, 20 mM HEPES (pH 7.4). a) DLPC:GalCer (80:20 molar ratio). b) DPPC:GalCer (80:20 molar ratio).

Then, the thermal transition of the vesicles was assessed by DSC. Increasing temperature, DPPC vesicles undergo a sharp phase transition at 41.6 °C (see figure 2.3) from a solid-ordered (s_o) (gel phase) to a liquid-disordered (l_d) phase (fluid phase).[14, 32] Besides, a pretransition assigned to the change from a crystalline gel phase to a rippled gel phase (P_β)

is observed at 34.7 ºC. The order-disorder phase transition of GalCer vesicles is relatively broad, between 55 and 65 ºC, with a maximum at 60.1 ºC, as shown in figure 2.3. The high temperature transition is a result of the hydrogen bonding capability of the saccharide headgroup and of the amide and hydroxy groups in the ceramide.[24, 25] It has been reported that GalCer T_m is essentially independent of the acyl chain length, although the presence of a 2-OH group in the sequence lowers the temperature value.[22] The GalCer used in this work is from a natural source (bovine) and contains both hydroxy and non-hydroxy fatty acid chains, which explains the broad peak.

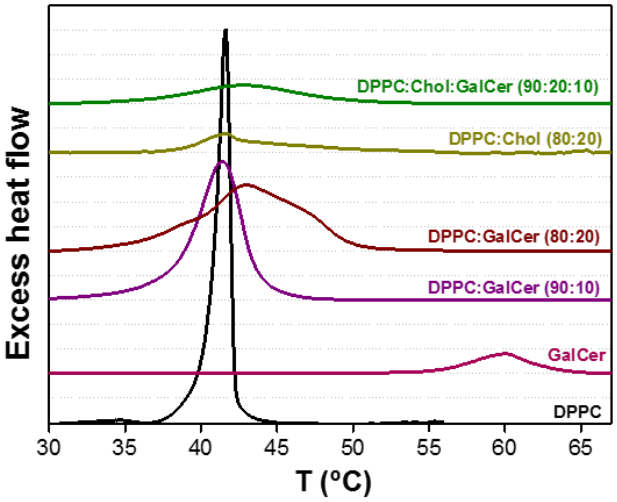

Figure 2.3 DSC thermograms of lipid vesicles: DPPC, GalCer, DPPC:GalCer (90:10 and 80:20 molar ratio), DPPC:Chol (80:20 molar ratio) and DPPC:Chol:GalCer (70:20:10 molar ratio). All suspensions in 150 mM NaCl, 20 mM $MgCl_2$, 20 mM HEPES (pH 7.4).

Upon addition of 10 mol % GalCer to the DPPC bilayer, a slight decrease in the main DPPC transition temperature to 41.4 ºC is observed, whereas the phospholipid pretransition is no longer detected (figure 2.3). Moreover, the peak width and asymmetry increased. This could be associated with the coexistence of more than one phase with similar T_m or to the dissolution of GalCer in the DPPC bilayer, since no peak is detected in the temperature range of the main transition of pure GalCer. When increasing the GalCer content up to 20 mol %, the main transition of the DPPC:GalCer vesicles occurs at a higher temperature, 43.0 ºC, with two shoulders that suggests the formation of different domains on the lipid bilayer.

The incorporation of Chol in DPPC bilayers has been extensively studied in a previous work of our group.[14] For Chol molar fractions higher than 10 mol %, Chol-rich and DPPC-rich phases coexist in the DPPC:Chol system. This occurs for compositions up to 35 mol % of Chol, displaying thermograms where a sharp peak is assigned to the main transition of DPPC-rich phase and a broader one corresponds to the melting of Chol-rich domains. In

accordance, we observe for DPPC:Chol (80:20 molar ratio) a broad transition (figure 2.3) that corresponds to the superimposition of a broad transition and a sharp one, close to the one of pure DPPC. For the ternary system DPPC:Chol:GalCer (70:20:10 molar ratio), a very broad transition is observed around 42.9 ºC (figure 2.3). Again, no transition at temperatures corresponding to pure GalCer is detected. This allows us to conclude that GalCer is dissolved within the different phases in the bilayer.

2.3.2. AFM and AFM-FS study: membrane structural and nanomechanical properties.

2.3.2.1. From pure to binary SLBs: GalCer and Chol effect.

As a first step, we evaluated the morphology and the nanomechanical properties by means of AFM and AFM-FS on pure phospholipid bilayers. We chose two phospholipids, representative of s_o and l_d SLBs, with their T_m well distant from *RT*: DPPC, an unsaturated PC with 16-carbon chains and T_m = 41.6 ºC, and DLPC, a saturated PC with 12-carbon chains and T_m = -2 °C. When deposited on mica, DPPC extends onto the surface to form bilayer patches, as displayed in the AFM topography of figure 2.4(a), while DLPC tends to completely cover the mica surface due to its fluid state at *RT* (figure 2.5(a)).

When performing AFM-FS measurements, the penetration of the AFM tip through the bilayer appears as a discontinuity in the approaching force-separation curve (figure 2.6). The vertical force at which this discontinuity happens corresponds to the maximum force the bilayer is able to stand before breaking, defined as breakthrough force (F_b).[5] This bilayer failure process for s_o and l_d SLBs is expected to occur at quite distant F_b values. While 11.1 ± 0.9 nN was obtained for pure DPPC SLBs (figure 2.4(b) and (c)), 2.7 ± 0.4 nN was obtained for pure DLPC SLBs (figure 2.5(b) and (c)). In addition, the typical force-separation curves were observed for both systems, detecting the compressibility effect for s_o SLBs (figure 2.6(a), DPPC) and the sudden break characteristic of l_d SLBs (figure 2.6(b), DLPC).

GalCer. We then prepared SLBs incorporating a second component, GalCer, and evaluated its effect on the phase behaviour and nanomechanical properties of the DPPC and DLPC SLBs. We used molar fractions of GalCer up to 20 %. For DPPC:GalCer SLBs with 10 mol % GalCer, a homogeneous bilayer was observed in the AFM topographical image (figure 2.4(a)), suggesting that GalCer is dissolved in the DPPC bilayer. When GalCer content is increased to 20 mol % (figure 2.4(a)), there is again no clear phase segregation in the form of domains. However, the SLB patches display certain heterogeneities in the form of groove-like features. This is also evidenced when performing AFM-FS: the determined F_b is homogeneous within the membrane, as observed in the F_b maps (figure 2.4(b)) and the unimodal F_b distributions (figure 2.4(c)). Nevertheless, the F_b histograms become wider and slightly asymmetric when increasing the GalCer content to 20 mol %, which may be associated to a certain heterogeneity degree, as suggested from the topography. The incorporation of GalCer to DPPC SLBs clearly increases the mechanical stability of the

bilayers, as the F_b changes to 13.0 ± 1.2 nN for 10 mol % GalCer, and to 21.2 ± 2.7 nN for 20 mol % GalCer (figure 2.7(a)). These results are in agreement with the DSC predictions. It is important to keep in mind that the presence of a hard substrate influence the lipid ordering and the interleaflet coupling[33†] compared to the vesicles suspension tested in the DSC experiments.

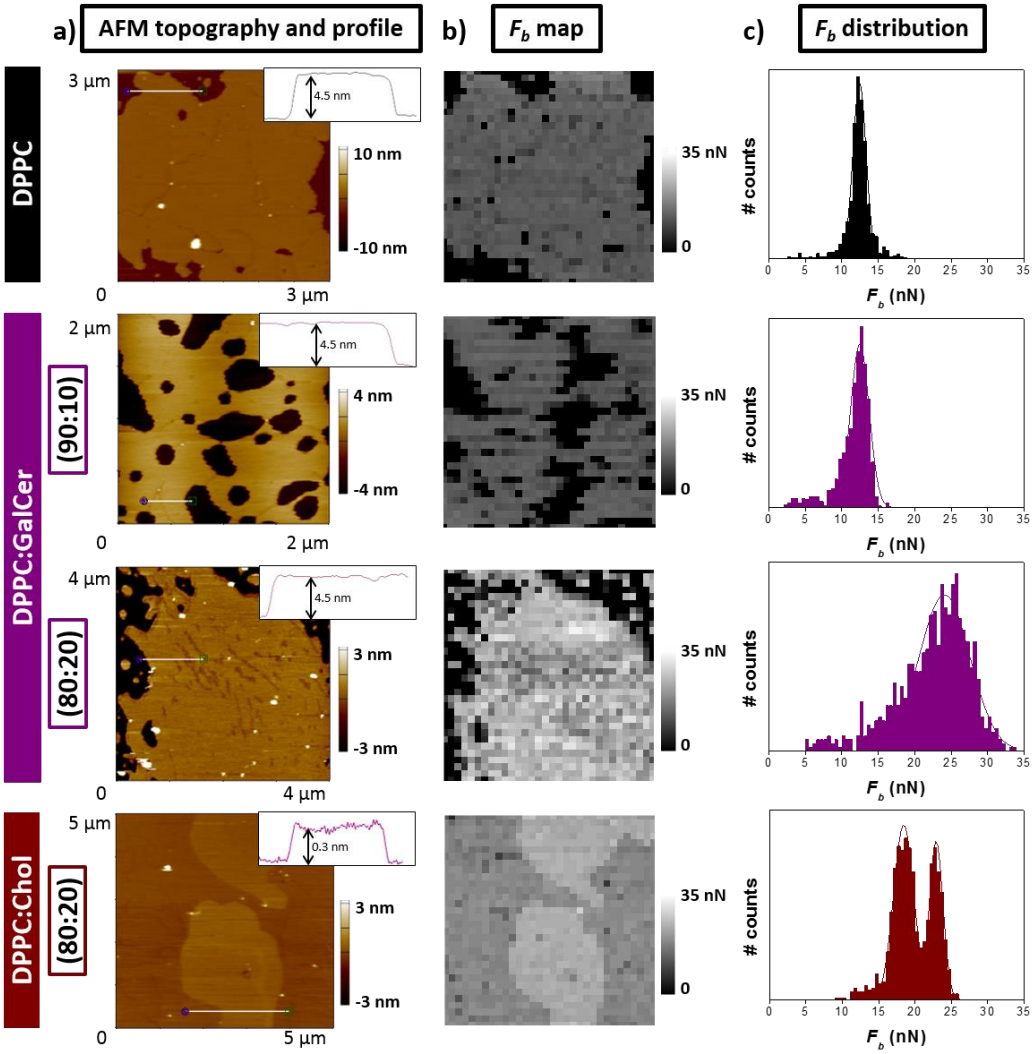

Figure 2.4 DPPC, DPPC:GalCer (90:10 and 80:20 molar ratio) and DPPC:Chol (80:20 molar ratio) SLBs on mica in 150 mM NaCl, 20 mM $MgCl_2$, 20 mM HEPES (pH 7.4) and *RT*. a) AC AFM topographical images and profiles. b) F_b maps. c) F_b distributions.

† See also chapter 3 and 7.

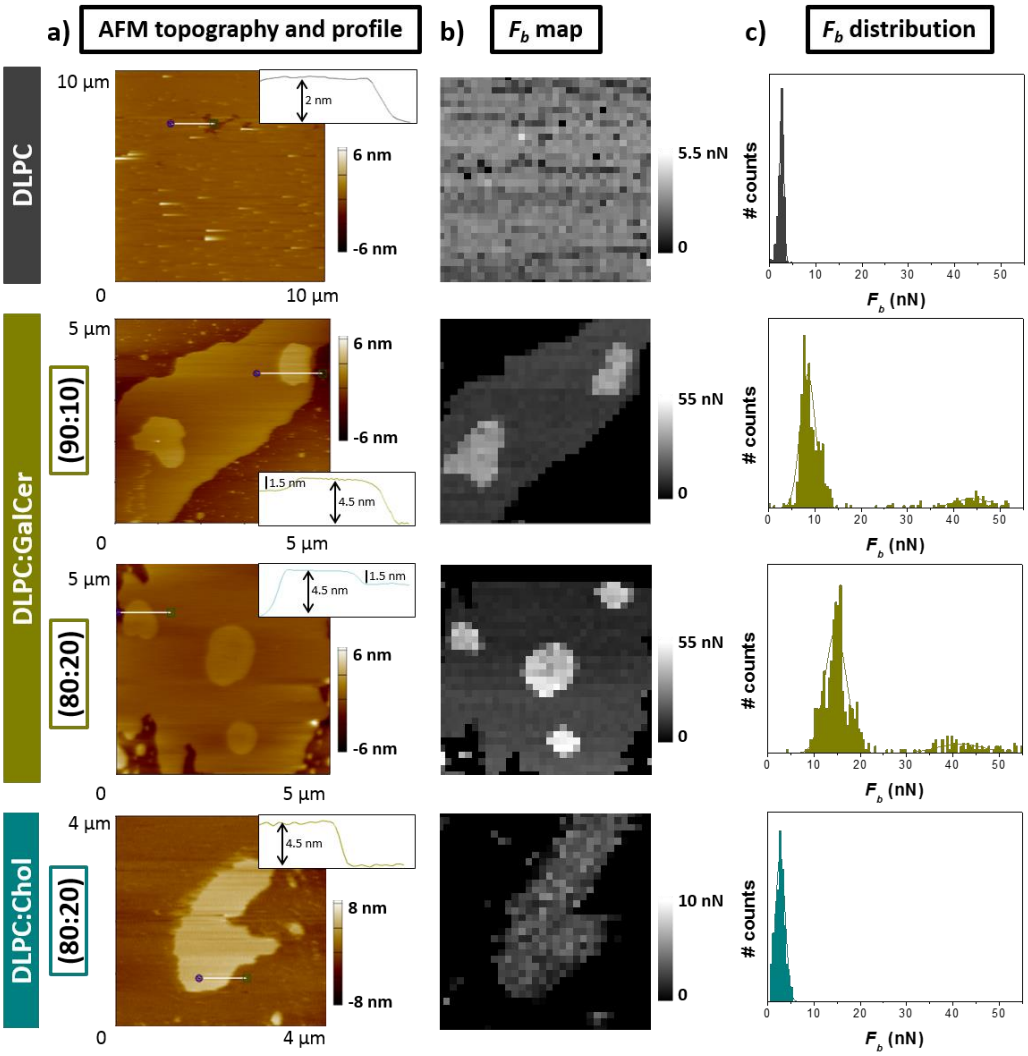

Figure 2.5 DLPC, DLPC:GalCer (90:10 and 80:20 molar ratio) and DLPC:Chol (80:20 molar ratio) SLBs on mica in 150 mM NaCl, 20 mM $MgCl_2$, 20 mM HEPES (pH 7.4) and *RT*. a) AC AFM topographical images and profiles. b) F_b maps. c) F_b distributions.

Upon incorporation of GalCer into the DLPC l_d bilayer, segregation into different domains is observed for both 10 and 20 mol % GalCer (figure 2.5(a)). The segregated domains (higher features in the topographical images) display similar thickness to the ones observed for s_o DPPC bilayers, which suggests the coexistence of fluid and gel-like phases. Besides, the difference in thickness between domains (~ 1.5 nm) is consistent with the GalCer being mainly on the upper leaflet. However, the different compressibility properties of fluid and gel-like phases calculated from AC mode AFM may lead overestimated values. It has been

reported that in DLPC:GalCer SLBs formed by vesicle fusion, the GalCer domains display transbilayer asymmetry, with a difference in height between domains of *ca*. 1 nm, as opposed to height differences of 1.75 nm for symmetric domains in SLBs obtained through Langmuir-Blodget deposition, when measured from contact mode AFM.[26]

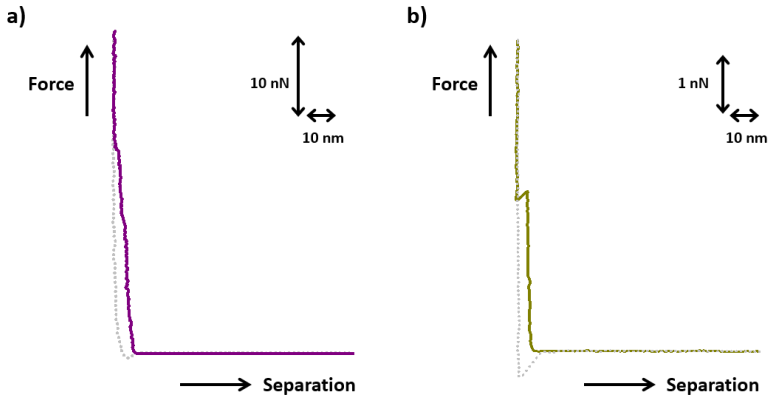

Figure 2.6 Typical force-separation curves. a) DPPC s_o bilayer. b) DLPC l_d bilayer.

From AFM-FS, two different populations are clearly distinguished in the F_b distributions (figure 2.5 (c)), with mean values of 7.6 ± 1.0 and 43.6 ± 4.6 nN for 10 mol %, and 14.7 ± 2.3 and 41.5 ± 5.0 nN for 20 mol %, that correspond to the different phases observed in the AFM images (figure 2.5(a)). According to the topography, the lower F_b value is associated to the continuous phase (DLPC-rich), whereas the higher F_b corresponds to the thicker domains, richer in GalCer (figure 2.5 (b)). This GalCer-rich phase seems to be already saturated for the

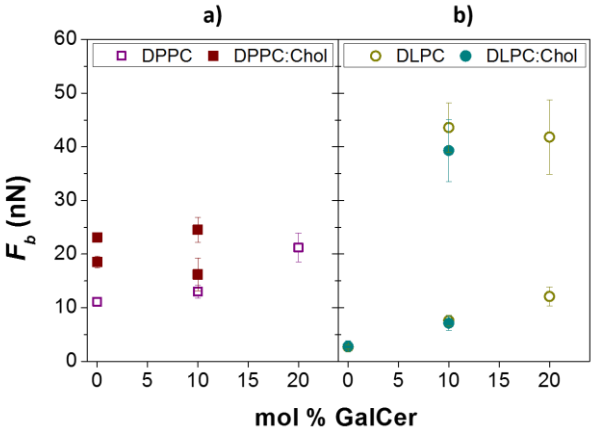

Figure 2.7 Mean F_b values of (a) DPPC and DPPC:Chol (20 mol % Chol) and (b) DLPC and DLPC:Chol (20 mol % Chol) systems as a function of the GalCer content. All the measurements in 150 mM NaCl, 20 mM $MgCl_2$, 20 mM HEPES (pH 7.4) and at *RT*.

DLPC:GalCer 90:10 bilayers, as for the DLPC:GalCer 80:20 SLBs the domains display similar properties and very high F_b values too. We consider then that this nanomechanical enhancement is mainly due to the well-known capacity of GSLs to form strong hydrogen bonding interactions. The mechanical stability of the DLPC-rich continuous phase increases linearly with the general GalCer content of the bilayer, arriving to F_b values of the order of an s_o SLB for DLPC:GalCer (80:20) (figure 2.7(b)).

Chol. The incorporation of Chol into the PC bilayers was also subject of study on this section, considering binary bilayers of PC:Chol 80:20 molar ratio. When 20 mol % Chol is introduced into the DPPC bilayers, the coexistence of two different phases with approximately 0.3 nm height difference occurs, as observed in the topography image corresponding to this system in figure 2.4(a). As formerly reported,[14] the higher domains are associated to a Chol-rich phase and the lower continuous domain corresponds to a DPPC-rich phase, results that are in agreement with those obtained in the DSC thermograms (figure 2.3). In accordance, this system shows a bimodal distribution of F_b when evaluated by AFM-FS, with mean values of 18.5 ± 1.1 and 23.1 ± 0.9 nN, associated to the DPPC-rich and Chol-rich phases, respectively (figure 2.4 and 2.7(a)).

Conversely, Chol is generally totally dissolved in l_d SLBs.[14] When 20 mol % Chol was incorporated into DLPC bilayers, a membrane patch of homogeneous topography and F_b map, as well as the corresponding F_b distribution are obtained, presenting a mean F_b value of 2.8 ± 1.0 nN (figure 2.5 and 2.7(b)).

Comparing both s_o and l_d model systems (DPPC and DLPC), significant differences in the topographical images as well as in the mechanical stability are observed when adding GalCer and Chol. Hence, the phospholipid state at the working temperature is an essential parameter which governs the general behaviour of the SLBs mixtures. In general, no clear domains are observed in DPPC systems, whereas in DLPC, GalCer induces a phase separation. Both in DPPC and DLPC bilayers, the incorporation of GalCer up to 20 mol % provokes an increase in F_b (figure 2.7). Nevertheless, when 20 mol % Chol is incorporated into the PC bilayers, segregation into different phases for the DPPC system and homogeneity for DLPC SLBs occurs. The mechanical stability is enhanced by the addition of Chol into DPPC membranes, whereas for DLPC, this Chol content seems not to modify the F_b (figure 2.7).

2.3.2.2. Ternary SLBs.

Knowing that GSLs and Chol may act together when tuning GSL functions as membrane receptors and communicators, we evaluated the influence of Chol on the distribution of GalCer in the membrane. For this, a specific content of Chol was incorporated to binary mixtures composed by PCs (DPPC or DLPC) and GalCer, increasing the complexity of the bilayers (figure 2.8).

The DPPC:Chol:GalCer (70:20:10 molar ratio) SLBs display phase segregation with a difference in height of approximately 0.5 nm between domains (figure 2.8(a)). Taking into account the previous results (figure 2.4), the thicker domains may correspond to Chol-rich phases, whereas the thinner ones may be associated to Chol-poor phases. Accordingly, the nanomechanical characterization for the DPPC:Chol:GalCer blend resulted in a bimodal F_b histogram (figure 2.8(c)), with mean values of 16.2 ± 3.1 and 24.5 ± 2.3 nN for each of the phases, as seen in the F_b map (figure 2.8(b)). These values are similar to the ones obtained with DPPC:Chol system (figure 2.7(a)), which raises the possibility of having the GalCer dissolved in both Chol-rich and Chol-poor domains. Still, a slight increase on the mechanical stability of the Chol-rich domains might be associated to a preferential distribution of GalCer towards the Chol-rich phase.

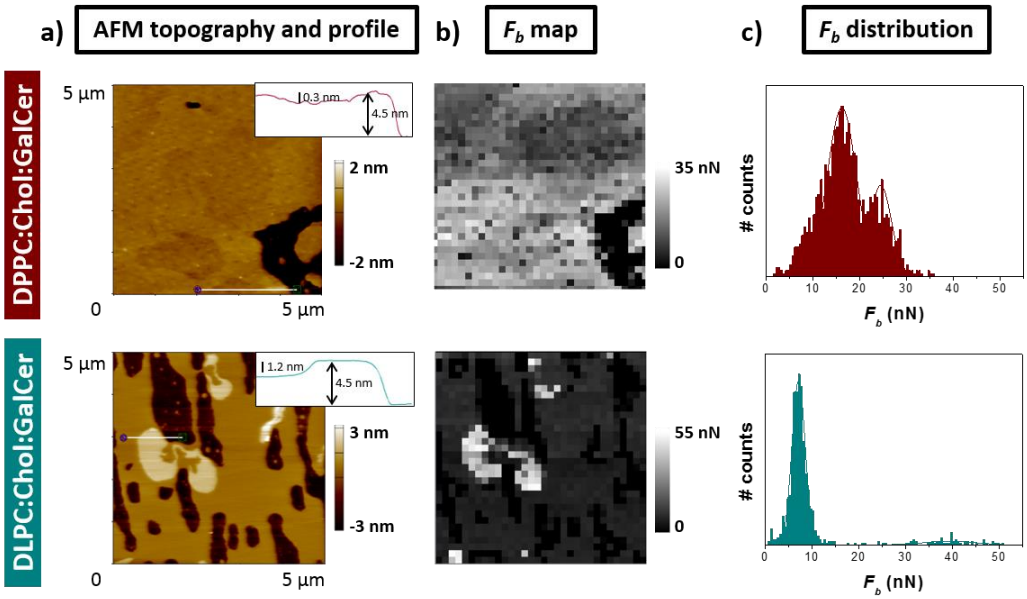

Figure 2.8 DPPC:Chol_GalCer (70:20:10 molar ratio) and DLPC:Chol:GalCer (70:20:10 molar ratio) SLBs on mica in 150 mM NaCl, 20 mM $MgCl_2$, 20 mM HEPES (pH 7.4) and *RT*. a) AC AFM topographical images and profiles. b) F_b maps. c) F_b distributions.

When introducing Chol to obtain DLPC:Chol:GalCer (70:20:10 molar ratio) SLBs, the system shows two separated domains with *ca.* 1.2 nm height difference (figure 2.8(a) and (b)). As can be seen in the F_b distribution (figure 2.8(c)), the mean F_b values for each domain are 7.1 ± 1.4 and 39.3 ± 5.8 nN. Both phases display considerably higher nanomechanical stability than DLPC:Chol (80:20 molar ratio) SLBs, although similar to bilayers of DLPC:GalCer (90:10) (figure 2.7(b)). For low GalCer contents, 20 mol % Chol barely affects pure DLPC bilayers and the GalCer distribution on them.

2.3.3. Dynamic Force Spectroscopy (DFS): SLB rupture activation energy

The mechanical rupture of lipid bilayers is of thermal-fluctuation nature and the application of an external force facilitates and directs the destructive action of those fluctuations. The penetration of the cantilever tip into the lipid bilayer has been modelled and widely conceived as a two-state activated process[34] with an associated energy barrier that follows the Arrhenius law (equation 2.1). The probability for a lipid bilayer rupture by thermal fluctuations is then proportional to the Boltzmann factor (k_B):

$$k(t) = A \cdot e^{-\left(\frac{\Delta E(t)}{k_B \cdot T}\right)} \qquad \text{(equation 2.1)}$$

where the pre-exponential factor A is defined as the frequency at which the AFM tip attempts to penetrate the bilayer, generally approximated to the resonance frequency of the cantilever, ΔE is the activation energy required for the formation of a hole in the bilayer that is large enough to initiate rupture and lead the tip breakthrough and T is the absolute temperature.

The thermomechanically activated nature of the bilayer rupture kinetics give rise to a loading-rate (r) dependence, which allows the calculation of the activation energy of the bilayer rupture in absence of an external force (ΔE_0). As the bilayer rupture and breakthrough of the AFM tip are here represented in terms of force rather than in terms of time (which occurs in AFM-based force clamp, AFM-FC[35]), and considering that the tip is moving at a constant velocity (v) towards the sample, the load increases according to $F=k_s v t$. k_s is the spring constant of the cantilever and F is the force applied at a time t. Using the relation between the force dependence of the activation energy ΔE and the force dependence of the velocity proposed by Butt *et al.*,[36] the activation energy of the bilayer failure can be calculated (equation 2.2):

$$\Delta E(F_b) = -k_B \cdot T \cdot ln\left[\left(\frac{0.693 k_s}{A}\right)\frac{dv}{dF_b}\right] \qquad \text{(equation 2.2)}$$

In DFS experiments on indentation of SLBs, it has been well-established that the mean F_b increases linearly with the logarithm of the loading rate[36-39] (equation 2.3). Combining equations 2.2 and 2.3 into equation 2.4 and extrapolating this relation to zero mean breakthrough force (F_b= 0) we calculate the ΔE_0.

$$F_b = a + b \cdot \log(v) \qquad \text{(equation 2.3)}$$

$$\Delta E(F_b) = -k_B \cdot T \cdot ln\left(\frac{1.6 k_s}{Ab} v\right) = k_B \cdot T\left[2.3\frac{a - F_b}{b} - ln\left(\frac{1.6 k_s}{Ab}\right)\right] \qquad \text{(equation 2.4)}$$

Following this approach, we collected data by means of DFS for the previously studied DPPC and DPPC:GalCer (80:20 molar ratio) SLBs (figure 2.4). In figure 2.9, the corresponding

F_b maps and F_b histograms at the different velocities, ranging from 0.5 and 6 μm·s^{-1}, are displayed, where we detected the tendency of F_b increasing with the approaching velocity of the tip. When plotting the obtained F_b values (figure 2.10), we clearly saw a linear behaviour

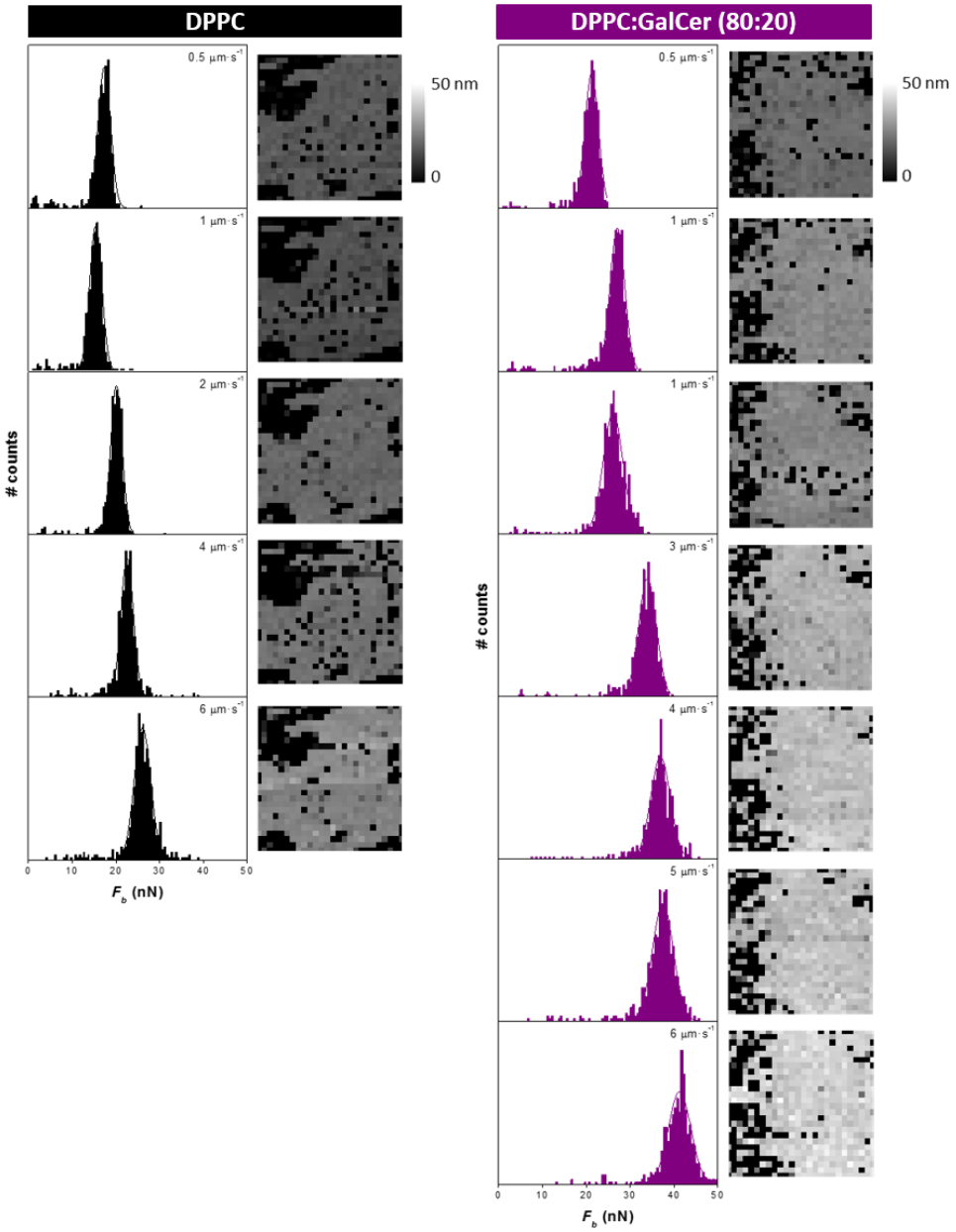

Figure 2.9 F_b distributions and maps obtained at different approaching velocities on DPPC and DPPC:GalCer (80:20 molar ratio) SLBs deposited on mica, in 150 mM NaCl, 20 mM $MgCl_2$, 20 mM HEPES (pH 7.4) and at *RT*.

with the logarithm of the velocity for both SLB systems. From the linear fitting we obtained a and b (equation 2.3) and calculated ΔE_0 using equation 2.4, considering F_b = 0, k_s = 0.35 N·m^{-1} and A = 8600 Hz.[34, 40] The resulting values were very similar for both systems: 9.9 ± 2.7 k_BT for pure DPPC and 9.1 ± 1.1 k_BT for DPPC:GalCer (80:20), in the range of reported ones.[35, 37]

The observed dependence of the F_b with the velocity, and so the loading rate, indicates that the higher the loading rate, the less time (less chances) for the bilayer to rupture in an interval of force increase (ΔF). This is a general behaviour observed for AFM tip indentation on SLBs. Although no differences in the activation energy values are observed for the two systems (DPPC and DPPC:GalCer), the rate at which F_b increases with the logarithm of the tip velocity is higher for the DPPC:GalCer than for DPPC SLBs. This suggests that GalCer, due to its extensive hydrogen bonding capability, directly affects the thermal fluctuations of the DPPC bilayer, yielding a higher chance for the SLB to remain intact than for pure DPPC, considering the same interval of force increase.

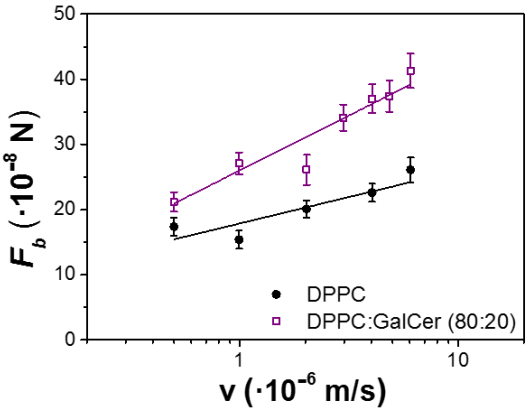

Figure 2.10 Dynamic F_b spectra: dependence of the mean F_b on the loading rate for DPPC and DPPC:GalCer (80:20 molar ratio) SLBs deposited on mica in 150 mM NaCl, 20 mM $MgCl_2$, 20 mM HEPES (pH 7.4) and at *RT*.

2.4. Conclusions

We presented the use of the well-stablished AFM and AFM-FS techniques to characterize the phase behaviour and nanomechanical properties of SLBs, for SLBs of composition ranging from pure phospholipids to more complex ternary mixtures. We confirm that the phospholipid state (s_o, for DPPC, or l_d, for DLPC) at the working temperature is a defining parameter governing the behaviour of lipid bilayer mixtures, including Chol and GalCer.

Upon the introduction of GalCer, phase segregation does not occur in DPPC SLBs, while separated domains are clearly manifested in DLPC SLBs. In general, amounts up to 20 mol

% GalCer provoke an increase in the nanomechanical stability for both systems. Interestingly, the segregated domains in DLPC:GalCer SLBs are of exceptionally high mechanical stability, while increasing amounts of GalCer confers characteristics typical of s_o SLBs on the continuous DLPC-rich phase. Conversely, 20 mol % Chol provokes segregation into different phases and nanomechanics enhancement for the DPPC system, whereas homogeneity and similar F_b values are obtained for DLPC SLBs.

When studying the 3-component bilayers, Chol appears to be determinant for the domain formation, GalCer distribution and enhanced nanomechanical properties of DPPC:Chol:GalCer (70:20:10) SLBs. On the other hand, for DLPC:Chol:GalCer SLBs, the phase behaviour and mechanical stability are dominated by the GalCer partial immiscibility, while Chol barely affects DLPC bilayers with low contents of GalCer.

By means of DFS, the lineal increment of the F_b with the logarithm of the loading rate was observed for DPPC and DPPC:GalCer SLBs. This effect is more pronounced (steeper slope) when GalCer is present in the SLB, due to GalCer extensive hydrogen bonding capability. The activation energy of the bilayer failure in absence of force calculated for both systems was in the range of the ones previously reported.

2.5. References

1. W. Dowhan, *Annu. Rev. Biochem.*, 1997, **66**, 199-232.
2. D. Lingwood and K. Simons, *Science*, 2010, **327**, 46-50.
3. K. Simons and W. L. C. Vaz, *Annu. Rev. Bioph. Biom.*, 2004, **33**, 269-295.
4. S. Chiantia, N. Kahya and P. Schwille, *Langmuir*, 2007, **23**, 7659-7665.
5. L. Redondo-Morata, M. I. Giannotti and F. Sanz, in *Atomic Force Microscopy in Liquid*, eds. A. M. Baró and R. G. Reifenberger, Wiley-VCH Verlag GmbH & Co.KGaA, Weinheim, Germany, 2012.
6. M.-P. Mingeot-Leclercq, M. Deleu, R. Brasseur and Y. F. Dufrene, *Nat. Protoc.*, 2008, **3**, 1654-1659.
7. L. Redondo-Morata, M. I. Giannotti and F. Sanz, *Mol. Membr. Biol.*, 2014, **31**, 17-28.
8. S. Garcia-Manyes and F. Sanz, *BBA-Biomembranes*, 2010, **1798**, 741-749.
9. L. Picas, P. E. Milhiet and J. Hernandez-Borrell, *Chem. Phys. Lipids*, 2012, **165**, 845-860.
10. K. El Kirat, S. Morandat and Y. F. Dufrene, *BBA-Biomembranes*, 2010, **1798**, 750-765.
11. G. van Meer, D. R. Voelker and G. W. Feigenson, *Nat. Rev. Mol. Cell Bio.*, 2008, **9**, 112-124.
12. J. Henriksen, A. C. Rowat, E. Brief, Y. W. Hsueh, J. L. Thewalt, M. J. Zuckermann and J. H. Ipsen, *Biophys. J.*, 2006, **90**, 1639-1649.
13. J. J. Pan, T. T. Mills, S. Tristram-Nagle and J. F. Nagle, *Phys. Rev. Lett.*, 2008, **100**.
14. L. Redondo-Morata, M. I. Giannotti and F. Sanz, *Langmuir*, 2012, **28**, 12851-12860.
15. S. Hakomori, *BBA – Gen. Subjects*, 2008, **1780**, 325.
16. R. Malhotra, *Biochem. Anal. Biochem.* , 2012, **1**, 1000108.
17. D. Lingwood, B. Binnington, T. Róg, I. Vattulainen, M. Grzybek, Ü. Coskun, C. A. Lingwood and K. Simons, *Nat. Chem. Biol.*, 2011, **7**, 260.
18. N. Yahi, A. Aulas and J. Fantini, *PLoS ONE*, 2010, **5**, e9079.
19. J. Fantini, N. Yahi and N. Garmy, *Front. Physiol.*, 2013, **4**, 120.
20. T. Róg and I. Vattulainen, *Chem. Phys. Lipids*, 2014, **184**, 82.
21. X. L. Han and H. Cheng, *J. Lipid Res.*, 2005, **46**, 163-175.
22. M. L. Longo and C. D. Blanchette, *BBA-Biomembranes*, 2010, **1798**, 1357-1367.
23. X. Zhou, L. Tang and Y. Liu, *Lipids*, 2009, **44**, 759-763.
24. J. M. Boggs, *BBA – Rev. Biomembranes*, 1987, **906**, 353.

25. P.-G. Nyholm, I. Pascher and S. Sundell, *Chem. Phys. Lipids*, 1990, **52**, 1.
26. C. D. Blanchette, W. C. Lin, T. V. Ratto and M. L. Longo, *Biophys. J.*, 2006, **90**, 4466-4478.
27. S. J. Attwood, Y. Choi and Z. Leonenko, *Int. J. Mol. Sci.*, 2013, **14**, 3514-3539.
28. L. Bagatolli and P. B. Sunil Kumar, *Soft Matter*, 2009, **5**, 3234.
29. D. M. Carter Ramirez, Y. A. Kim, R. Bittman and L. J. Johnston, *Soft Matter*, 2013, **9**, 4890.
30. M.-P. Mingeot-Leclercq, M. Deleu, R. Brasseur and Y. F. Dufrene, *Nat. Protoc.*, 2008, **3**, 1654.
31. R. Proksch, T. E. Schaffer, J. P. Cleveland, R. C. Callahan and M. B. Viani, *Nanotechnology*, 2004, **15**, 1344-1350.
32. D. Marsh, *Chem. Phys. Lipids*, 1991, **57**, 109-120.
33. S. Garcia-Manyes, G. Oncins and F. Sanz, *Biophys. J.*, 2005, **89**, 4261-4274.
34. H. J. Butt and V. Franz, *Phys. Rev. E*, 2002, **66**.
35. L. Redondo-Morata, M. I. Giannotti and F. Sanz, *Langmuir*, 2012, **28**, 6403-6410.
36. H.-J. Butt and V. Franz, *Phys. Rev. E*, 2002, **66**, 031601.
37. S. Loi, G. Sun, V. Franz and H.-J. Butt, *Phys. Rev. E*, 2002, **66**, 031602.
38. V. Franz, S. Loi, H. Müller, E. Bamberg and H.-J. Butt, *Colloid. Surfaces B*, 2002, **23**, 191.
39. R. M. A. Sullan, J. K. Li, C. Hao, G. C. Walker and S. Zou, *Biophys. J.*, 2010, **99**, 507.
40. R. M. A. Sullan, J. K. Li, G. C. Walker and S. Zou, *Biophys. J.*, 2010, **98**, 205A-205A.

Chapter 3

Quatsome membranes: AFM and AFM-FS study*

Liposomes (LPs) have emerged among the most promising supramolecular assemblies for nanomedicine, to be used as nanocarriers for the protection and delivery of active ingredients in pharmaceutical and cosmetic formulations. However, low membrane permeability is mainly achieved using gel-like state LPs, which rigidity represents a drawback for some applications that require a deformable nanovesicle, as the case of transdermal delivery. The search for alternative vesicular systems with enhanced properties compared to liposomes is then a greatly interesting field, especially when vesicle's mechanical properties are a critical issue. Quatsomes (QTs) are unilamellar nanovesicles constituted by quaternary ammonium surfactants and sterols, which fulfill the structural and physicochemical requirements to be a potential platform for the encapsulation of both therapeutic and diagnostic actives for site specific delivery. In this chapter, we characterize the morphology and the nanomechanics of QTs membranes for the first time by means of atomic force microscopy and spectroscopy.

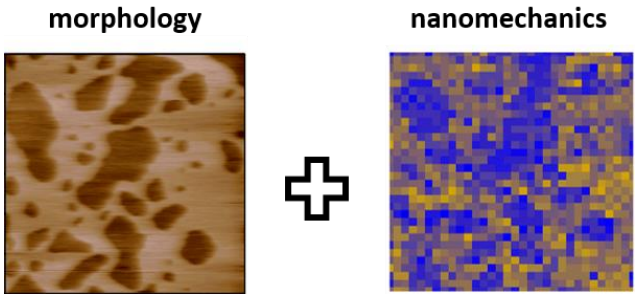

* This work has been performed in collaboration with the Nanomol and the Soft Matter Theory groups from the Institut de Ciència de Materials de Barcelona (ICMAB-CSIC), in Cerdanyola del Vallès (Spain) and with Nanomol Technologies SA, in Cerdanyola del Vallès (Spain).

3.1. Introduction

During the past decade, the application of nanotechnology to drug delivery has been widely expected to change the landscape of pharmaceutical and biotechnology industries.[1] Among the first nanotechnology drug delivery systems, liposomes (LPs) have emerged as one of the most promising tools for drug targeting in medical fields.[2-4] Advantages, such as biocompatibility, low toxicity and the possibility of trapping drugs into their aqueous core and/or in their bilayer, made LPs promising candidates to be used as nanocarriers for the protection and delivery of active ingredients in pharmaceutical and cosmetic formulations.[2, 5, 6] However, LPs have a high membrane permeability, causing leakage of the entrapped drugs, as well as poor colloidal and chemical stabilities, that lead LPs to aggregate.[3, 6, 7] Instead, the use of gel-like phospholipids lowers the permeability, but the vesicles become too rigid, drawback for some applications that require a deformable nanovesicle, as the case of transdermal delivery. In order to overcome these limitations, there has been a large interest on developing new systems that self-assemble into stable vesicles, satisfying the requirements for pharmaceutical formulations.[8-10] Non-liposomal structures composed by certain lipids that can self-assemble in appropriate conditions with surfactants,[11] polymers[12] or polypeptides,[13] among others, have been reported as a new generation of vesicular systems containing at least one natural or synthetic lipid. The composition of nanovesicle structures is then dependent on the required physicochemical properties (size, charge density, morphology, lamellarity and vesicle deformability) and efficiency to encapsulate drugs, considering the possibility of generating these nanocarriers with multiple functionalities.[1] For some specific applications, such as enhancement of skin penetration, it has been proposed that deformability of the carrier vesicles is not just a fundamentally interesting characteristic, but it is a key determinant of the nanovesicle ability to cross the skin barrier.[14]

Quatsomes (QTs) are unilamellar nanovesicles constituted by quaternary ammonium surfactants and sterols in equimolar proportion (figure 3.1).[6, 7, 15] These vesicular systems

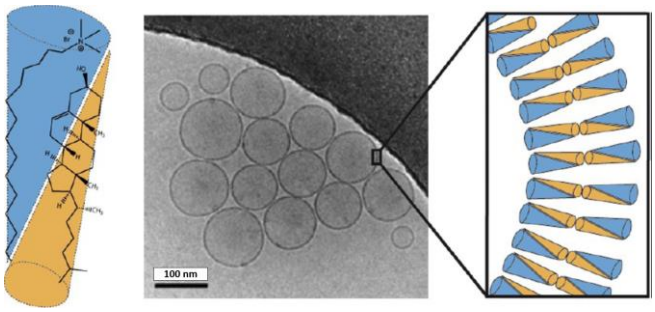

Figure 3.1 Scheme of the QT synthon composed by a cetyl trimethylammonium bromide (CTAB) and a cholesterol (Chol) molecules and a cryo-TEM image of QTs vesicles. Reprinted with permission from ref.[7]. Copyright © 2013. American Chemical Society.

are stable for several years and their morphologies do not change upon rising temperature or dilution, showing outstanding vesicle to vesicle homogeneity regarding size, lamellarity, and membrane supramolecular organization.[7, 16, 17] These properties make QTs as ideal systems for their membrane functionalization, which is very important for a robust and efficient drug targeting.[18, 19] QTs fulfill the structural and physicochemical requirements to be a potential platform for the encapsulation of both therapeutic and diagnostic actives for site specific delivery. According to the cationic surfactant and sterol, as well as the suspension media used to prepare the QTs, the mechanical properties of the QT bilayer and the flexibility of the entire vesicle may be tuned.

In this chapter, we used atomic force microscopy (AFM) and AFM-based force spectroscopy (AFM-FS) to characterize the membrane morphology and mechanics of QTs. We evaluated the effect of ions and temperature on the structure of the membrane lateral packing of these promising vesicular systems. We also provided preliminary elasticity measurements of entire QTs.

3.2. Experimental

Materials. Cholesterol (Chol) with 95% purity was obtained from Panreac (Barcelona, Spain), cetyl trimethylammonium bromide (CTAB) from Sigma Aldrich and 1,2-dioleoyl-*sn*-glycero-3-phosphocholine (DOPC) from Avanti Lipids. All the chemicals were used without further purification. The experiments were performed in ultrapure water (Milli-Q reverse osmosis system, 18.2 mΩ·cm resistivity) or in 94 mM NaCl, 3.1 mM Na_2HPO_4, 0.9 mM NaH_2PO_4 (pH 7.4) prepared with ultrapure water (phosphate-buffered saline or PBS buffer). For the AFM experiments the buffer solution was filtered before use employing a 0.22 μm pore size inorganic membrane filter.

Sample preparation. Quatsomes (QTs) were synthetized using the DELOS-SUSP method.[7, 20†] Briefly, a solution of Chol in ethanol was introduced into the reactor vessel. Then, the reactor vessel was pressurized with compressed CO_2, producing a volumetric expanded liquid solution, at a pressure of 115 bar and a temperature of 35 °C. After 60 minutes, the system was depressurized from the previous pressure to the atmospheric above an aqueous solution, either water or PBS buffer depending on the formulation. This solution contained CTAB dissolved above its critical micelle concentration (CMC) to get QTs (Chol:CTAB 1:1 molar ratio), or DOPC to get liposomes (LPs) of DOPC:Chol (4:1 molar ratio).

In order to remove the 10% of ethanol from the synthetized QTs as well as all the components which have not been integrated in their membrane, in some of the experiments the QT suspensions were finally purified by diafiltration (KrosFlo ® Diafiltrator by Spectrum

† The preparation of QT vesicles was performed at the Nanomol group from ICMAB-CSIC.

Lab, membrane MWCO 100 kDa and 20 cm2 surface area), even considering that none of the components (Chol or CTAB) can individually form vesicular systems.

Circular mica surfaces (Ted Pella, Redding, CA), previously glued onto Teflon discs using epoxy-based mountain glue, were employed as membrane substrate for the AFM experiments. Supported quatsomes membranes (SQMs) and supported lipid bilayers (SLBs) were obtained by direct fusion onto freshly cleaved mica surfaces, after depositing 100 µL of QT vesicles or LPs (2.75 mg/ml and 2.1 mg/ml, respectively) for 30 min at room temperature (*RT*). For the elasticity measurement on QT vesicles, 100 µL were deposited on a silicon substrate (Ted Pella, Redding, CA),[‡] for 10 min. Afterwards, the samples were rinsed several times with the desired buffer solution to get rid of unfused vesicles, although keeping the mica surfaces always hydrated.

Dynamic light scattering (DLS). Size distribution and zeta potential (ξ-pot) of QTs and LPs vesicles suspensions were analysed by DLS using a Zetasizer NanoS (Malvern Instruments, UK). Measurements were carried out on a minimum of two samples from three independent runs. The measurements were performed at room temperature (*RT*).

Cryogenic transmission electron microscopy (Cryo-TEM). The morphology of the distinct QTs was studied by Cryo-TEM using a JEOL JEM-2011 (JEOL Ltd., Tokyo, Japan) operating at 120 kV. The samples were frozen by plunge freezing in liquid ethane and stored in liquid nitrogen until loaded onto a cryogenic sample holder. The Cryo-TEM images were acquired below -175 ºC.

Atomic force microscopy (AFM) and AFM-based force spectroscopy (AFM-FS). AFM images and force spectroscopy experiments were performed using an MFP-3D atomic force microscope (Asylum Research, Santa Barbara, CA) using V-shaped Si_3N_4 cantilevers with Si_3N_4 tips and nominal spring constants of 0.35 $N \cdot m^{-1}$ and 0.24 $N \cdot m^{-1}$ (DNP, Bruker AFM Probes, Camarillo, CA). For the measurements under controlled temperature (*T*), we used a *T*-controlled sample stage (BioHeater, Asylum Research, Santa Barbara, CA), which allows heating the samples in liquid environment from *RT* up to 80 °C.

AFM images over a range of areas from 0.5 x 0.5 to 5 x 5 μm^2 were acquired in AC mode at *RT* and under liquid conditions (both ultrapure water and PBS buffer solution). After imaging the selected region, AFM-FS measurements were performed by approaching and retracting the AFM tip to the sample at a constant velocity of 1 $\mu m \cdot s^{-1}$. The force-separation curves were recorded by following an array of points from 20 x 20 to 30 x 30 (force map mode). A home-made Python program based on ref.[21] was used to analyze the force-separation curves from the grids and evaluate the breakthrough force (F_b) values.

[‡] The squared Si substrates were obtained from wafers and cleaned with piranha solution (7:3 H_2SO_4:H_2O_2 (30%)) before their use.

For the elasticity measurement on QT vesicles, the AFM measurements were performed using V-shaped Si_3N_4 cantilevers with Si_3N_4 tips and nominal spring constants of 0.03 $N \cdot m^{-1}$ (MSNL, Bruker AFM Probes, Camarillo, CA). After imaging an interesting area in AFM contact mode, force-separation curves were recorded in force-map mode approaching and retracting the tip at a constant 1 $\mu m \cdot s^{-1}$ velocity. Only the curves performed out of the center of the QT vesicle were analyzed.

Molecular dynamics (MD). MD simulations were performed using NAMD 2.11 software.[22] We defined a QT membrane made of 2 leaflets of 27 CTA^+ and 27 Chol molecules each and we simulated them in water as well as with 100 mM NaCl, to mimic the environmental conditions. In addition, the simulations were performed at different temperatures: 10º, 15º, 20º, 25º, 35º and 50º for QT in water and 15º, 25º, 30º, 35º, 40º and 50º for QT in water with 100 mM NaCl.

3.3. Results and discussions

3.3.1. QT vesicles: Structural characterization§

Prior to the membrane study, characterization of QTs vesicles suspension in different liquid environments was performed: QTs in ultrapure Milli-Q water (QT_H_2O) and QTs in PBS buffer (94 mM NaCl, 3.1 mM Na_2HPO_4, 0.9 mM NaH_2PO_4 (pH 7.4)) (QT_PBS). By means of DLS, we evaluated a higher hydrodynamic diameter of QT_PBS than QT_H_2O (table 3.1), with mean values of 152 nm and 90 nm, respectively. The same trend showed the polydispersity index (PDI) values, with 0.387 for QT_PBS and 0.232 for QT_H_2O. This discrepancy in the diameter might be attributed to the presence of ions in the PBS solution, affecting both geometric and hydrodynamic sizes, usually not equivalent. With ions present in the buffer, the interactions between Chol and CTAB can be affected, modifying the molecular orientation and/or the distance between the molecules, therefore increasing the vesicle size. In addition, the phosphate ions can interact with the CTAB after the QTs formation, leading to a larger and more interacting solvation shell and reducing the diffusion of the QTs vesicles in solution. As expected, the surface charge density of QTs is also affected

Table 3.1 Hydrodynamic diameter size, PDI and ζ-pot values of QTs in water and in PBS buffer before and after diafiltration.

	size (nm)	PDI	ζ-pot (mV)
QT_H_2O	90	0.232	85.0
QT_H_2O diaf.	93	0.200	73.0
QT_PBS	152	0.387	42.7
QT_PBS diaf.	126	0.400	37.0

§ The experiments showed in this section were performed by Natascia Grimaldi at Nanomol group from ICMAB-CSIC.

by the presence of the ions in the solution, reducing the ζ-pot from 85.0 mV to 42.7 mV (table 3.1), when in water or PBS buffer, respectively.

Size and ζ-pot measurements were also performed after diafiltration on QTs (QT_H_2O diaf. And QT_PBS diaf) (table 3.1). Considering the high PDI values, we observed that there is no significant difference in the hydrodynamic diameter between before and after the diafiltration process. However, a decrease on the ζ-pot values is detected when diafiltration is performed, with values of 73.0 mV and 37.0 mV for QT_H_2O and QT_PBS, respectively.

The morphology of the QTs vesicles in both water and PBS solutions was studied by means of Cryo-TEM (figure 3.2). In the case of QT_H_2O (figure 3.2(a)), circular vesicles of different sizes were observed. However, QT_PBS (figure 3.2(b)) showed more variety of geometries, from circular to more elongated ones, and generally bigger than QT_H_2O, agreeing with the results obtained by DLS.

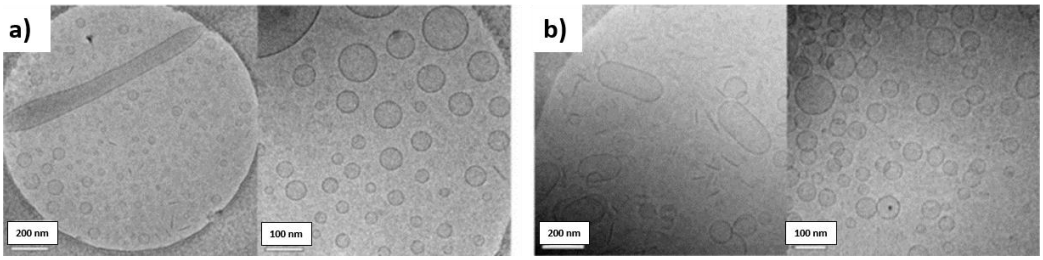

Figure 3.2 Comparison of the cryo-TEM images: a) QT_H_2O. b) QT_PBS.

3.3.2. QT membranes on mica: AFM topographical characterization.

When exposed to freshly cleaved mica, QT vesicles open and fuse onto the substrate forming supported QT membranes (SQM). This procedure is equivalent to the commonly known liposome rupture method,[23] based on the formation of an SLB by depositing a suspension of lipid vesicles onto a flat surface. The morphology of SQM can then be studied by means of AFM imaging.

As displayed in the AFM topographies shown in figure 3.3, QT_H_2O and QT_PBS membranes completely covered the mica surface. At the initiation of the AFM experiment (t_0) after depositing the QTs onto the mica surface for 30 min, segregation into domains was observed for SQMs in both liquid environments. The thickness of the different membrane domains was determined from the force-separation curves performed during the AFM-FS measurements: 4.7 ± 0.2 nm and 4.1 ± 0.3 nm for the higher and lower domains, respectively, for QT_H_2O membranes, and 5.3 ± 0.4 nm and 4.5 ± 0.4 nm for the higher and lower domains, respectively, for QT_PBS membranes, slightly higher than for SQM in ultrapure water.

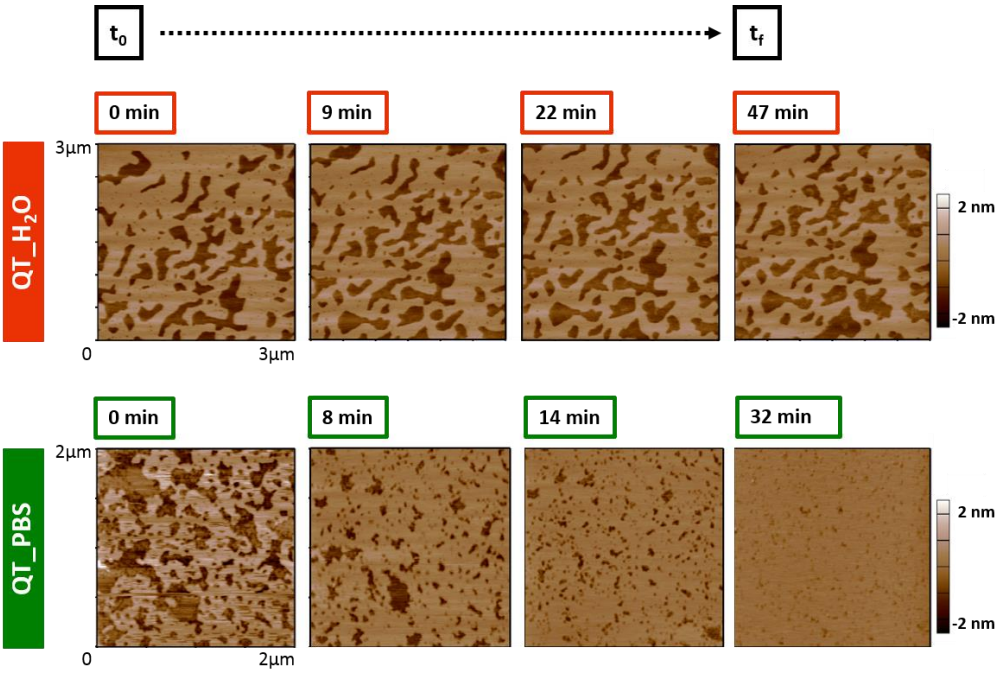

Figure 3.3 Consecutive AC AFM topographical images of QT_H_2O and QT_PBS SQM on mica and at *RT*.

Series of consecutive images were acquired in order to see the membrane behavior with time. A steady topography was observed for QT_H_2O (figure 3.3, top) after several minutes (t_f ~ 45 min). Conversely, the QT_PBS membrane showed a dynamic behavior, slowly becoming more homogeneous after few minutes (t_f ~ 30 min) of imaging. This is shown in the successive topographies of the same area of QT_PBS membrane presented in figure 3.3 (bottom), where it seems that the thicker phase is the one that prevails. To ensure that this homogeneous effect was taking place not only in the specific scanned region, other areas of the same sample, but previously unexplored, were also imaged after t_f and, as expected, the SQM in PBS was converting to a single phase all over the sample. The membrane at this state had a thickness of 4.9 ± 0.5 nm, determined from the force-separation curves carried out in the AFM-FS measurements.

To better understand the origin of the stability and the behavior of the domains in QT_H_2O and QT_PBS membranes, we also imaged the SQMs after performing the diafiltration process (figure 3.4). In the case of diafiltered QT_H_2O, the topography acquired by AFM was similar to the non-diafiltered sample (figure 3.3, top and figure 3.5(a), top), since different domains were also distinguished (figure 3.4, top). For diafiltered QT_PBS, the morphology was totally homogeneous from the beginning (figure 3.4, bottom), contrarily to what was initially observed for the non-diafiltered sample (figure 3.3, bottom and figure 3.5(a),

middle). Hence, diafiltered QT_PBS membranes can be compared to the non-diafiltered ones at t_f (figure 3.5, bottom), since both show a unique phase uniform layer. In both diafiltered QT_H_2O and QT_PBS, the membrane thickness barely variated compared to the SQM without diafiltration.

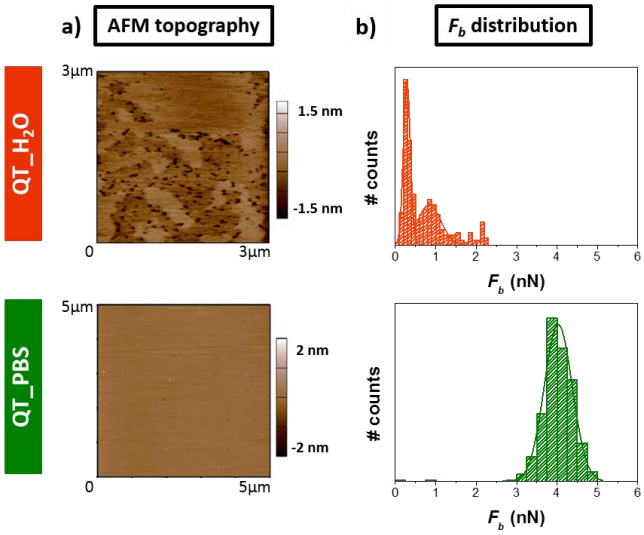

Figure 3.4 QT_H2O and QT_PBS SQMs on mica and at *RT* after diafiltration process. a) AFM topographical images. b) F_b distributions.

3.3.3. QT membranes on mica: AFM mechanical characterization.

As explained in the previous chapter, the lateral interactions between the molecules can be directly explored by measuring the maximum force a membrane is able to withstand before its rupture, the breakthrough force (F_b),[24, 25] as a result of an applied external pressure, *i.e.* the AFM tip breaking through the SQM. The F_b values were determined by performing several force-separation curves over an area of the SQM previously imaged (figure 3.5). Sharp discontinuities (breakthroughs) at low F_b values were observed for both QT_H_2O and QT_PBS membranes in the approach part of the force-separation (*F*-Sep) curves (figure 3.5(c)). These sharp breakthroughs at few nN are generally characteristic of fluid-like lipid bilayers.

For the heterogeneous membrane of QT_H_2O, the clear domains identified in the topography (figure 3.5(a), top) were also observed in the F_b map (figure 3.5(b), top). A correspondent bimodal F_b distribution (figure 3.5(d), top) was then obtained, with mean F_b values of 1.2 ± 0. 5 nN and 1.9 ± 0.9 nN for the lower and higher domains, respectively (figure 3.6). In QT_PBS SQM, the initial heterogeneous membrane topography (figure 3.5(a), middle) was also observed in the F_b map (figure 3.5(b), middle), as well as the resultant mean F_b values obtained from the bimodal distribution: 2.5 ± 0.8 nN and 6.3 ± 2.5 nN for the

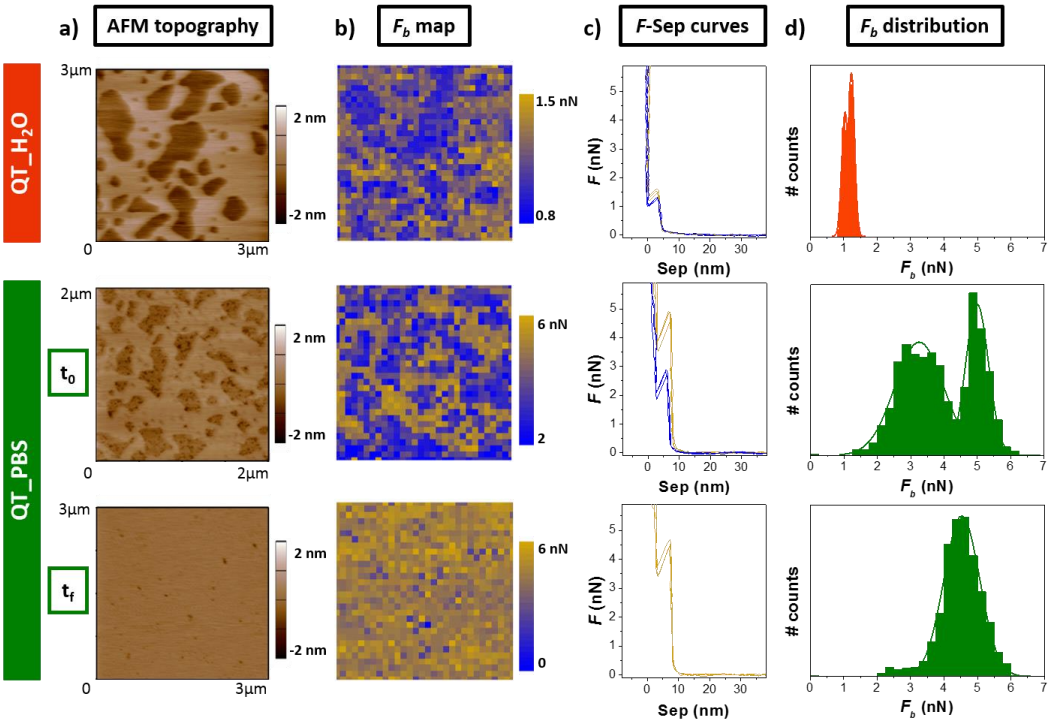

Figure 3.5 QT_H_2O and QT_PBS (at t_0 and t_f) SQMs on mica and at *RT*. a) AC AFM topographical images. b) F_b maps. c) *F*-Sep curves. d) F_b distributions.

lower and higher phases, respectively (figure 3.5(d), middle, and figure 3.6). When the QT_PBS became homogeneous at t_f (figure 3.5(a), bottom), a uniform F_b map (figure 3.5(b), bottom) associated to a unimodal distribution (figure 3.5(d), bottom) with mean F_b value of 6.2 ± 1.8 nN was observed (figure 3.6). This force value is close to the one obtained for the higher domain when the QT_PBS membrane was still heterogeneous. This fact agrees with the topographical characterization (figure 3.3, bottom), where the higher domains in the SQM in PBS seemed to prevail when the system became a single phase.

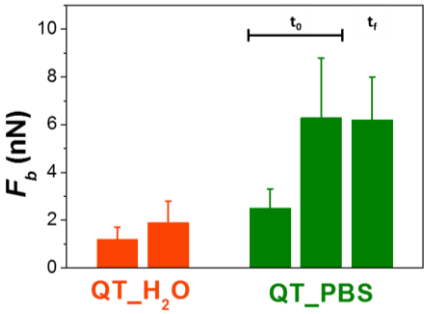

Figure 3.6 Mean F_b values of QT_H_2O and QT_PBS on mica and at *RT*.

QT_H_2O and QT_PBS were also characterized by AFM-FS after being diafiltered (figure 3.4). In both systems, a small decrease of the SQMs mechanical stability was observed, displaying F_b values slightly inferior than those ones obtained without the diafiltration process. For QT_H_2O, we obtained a bimodal F_b distribution with mean values of 0.7 ± 0.5 nN and 1.2 ± 0.5 nN for the lower and higher domains, respectively (figure 3.4, top), whereas for QT_PBS, a single F_b peak centered at 4.9 ± 0.7 nN was achieved (figure 3.4, bottom).

3.3.4. Effect of the ions on the SQM topography and mechanics.

As described in the previous section, QT_PBS SQMs display higher F_b values than QT_H_2O SQMs, indicating that they are mechanically more stable in PBS than in ultrapure water (figure 3.6). This is related to the presence of the ions in the PBS buffer, which are known to have an important contribution to the membrane mechanical resistance, by enhancing the lateral packing, translated into a higher F_b.[26]

To better understand the effect of ions into SQMs, we performed the topographical and mechanical study on QT_H_2O and, *in situ*, exchanged the medium to PBS buffer and characterized it again (figure 3.7). As expected, QT_H_2O membranes showed two different domains distinguished in the topographical AFM image (figure 3.7(a), top) and the F_b map (figure 3.7(b), top), with the corresponding bimodal distribution with low values of F_b (figure 3.7(c), top). After rinsing the sample several times with PBS buffer and repeating the same characterization procedure (figure 3.7, bottom), we observed that the mechanical

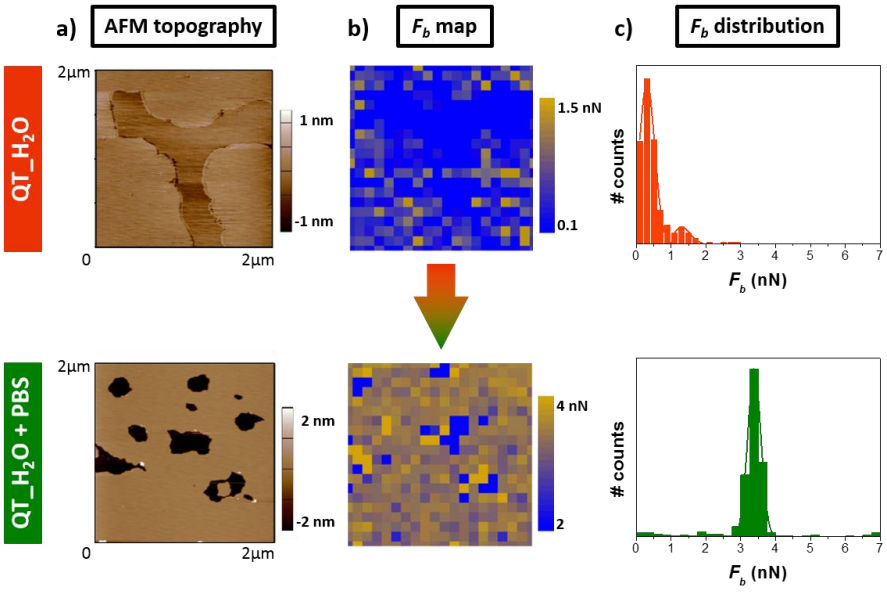

Figure 3.7 QT_H_2O and QT_H_2O + PBS (after changing the liquid medium to PBS + NaCl) SQMs on mica and at *RT*. a) AC AFM topographical images. b) F_b maps. c) F_b distributions.

stability of the system (QT_H_2O + PBS) significantly increased from about 1 nN to 3.4 ± 0.6 nN (figure 3.7(c), bottom), reaching F_b values in the order of those for QT_PBS membranes.

In addition, we acquired a series of consecutive images with time, once the solution was already exchanged to PBS buffer. As observed for QT_PBS membranes (figure 3.3, bottom), the initially phase segregated SQM became homogeneous, being again the higher domain the one that prevails (figure 3.8).

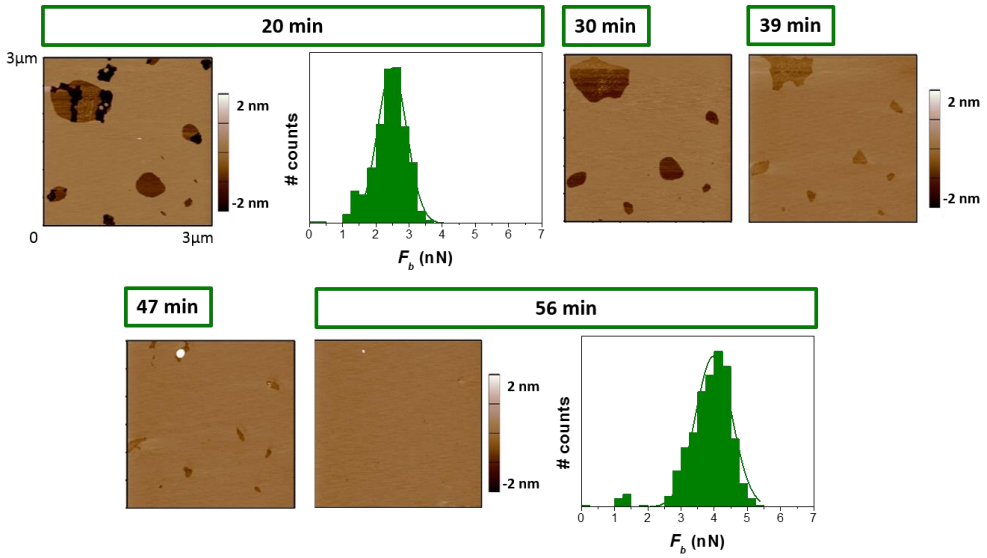

Figure 3.8 Consecutive AC AFM topographical images and F_b distributions for QT_H_2O + PBS SQM on mica at *RT*. The time described in the figure represents the minutes after the first PBS rinsing.

3.3.5. Effect of the temperature on the SQMs structure.

The previous nanomechanical characterization suggested that SQMs are in the fluid state at *RT*, from the low F_b values detected with AFM-FS, mechanical stability comparable to fluid state phospholipid bilayers. In addition, no thermal transition temperature was observed when performing DSC (differential scanning calorimetry) on QT vesicles throughout a large range of temperatures: from -50 ºC to 70 ºC. In this section, we evaluated the effect of the temperature on the morphology of QT_H_2O and QT_PBS membranes by means of AFM using a temperature (*T*)-control system in an attempt to determine the origin of the different domains observed in QT_H_2O.

In the case of the SQM in PBS, we let the system stabilize to the homogeneous phase at *RT* (~ 25 ºC), knowing its dynamic behavior at this *T*. Further increasing *T* up to 45 ºC showed no changes in the topographical images of the QT_PBS membrane (figure 3.9(b)).

Contrarily, for QT_H_2O, upon rising *T* from *RT* up to 42.5 ºC (figure 3.9(a), plot *T vs.* t), the heterogeneous morphology became homogeneous (figure 3.9(a)).

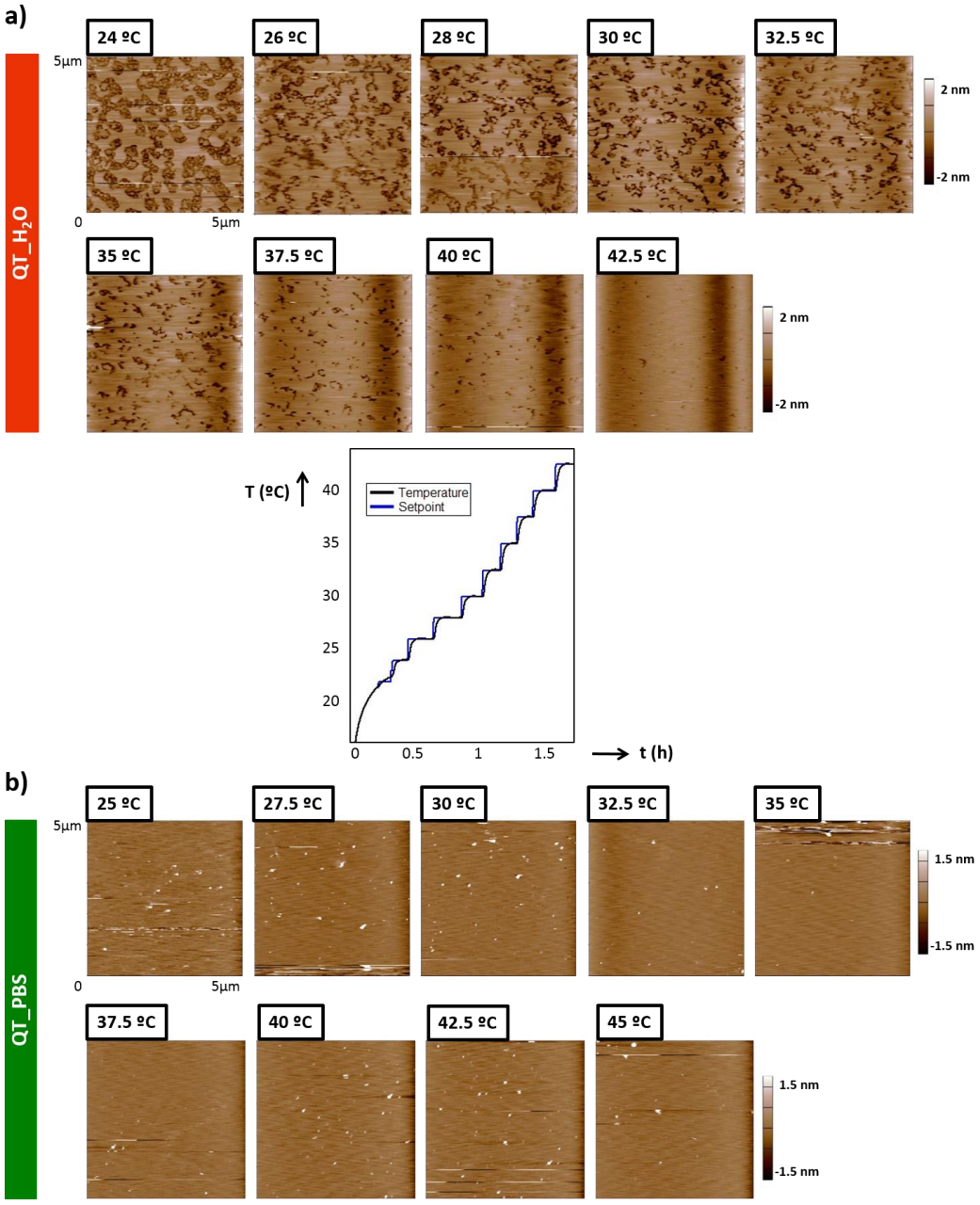

Figure 3.9 AC AFM topographical images for QT_H_2O (a) and QT_PBS (b) supported on mica in PBS pH 7.4 increasing the experimental temperature. *T vs.* t plot representing the different *T* steps for the experiment performed with QT_H_2O SQMs (a).

To more precisely determine this transition to a unique phase, we studied the QT_H_2O system considering bigger (*T*) and larger (t) steps (figure 3.10, plot *T vs.* t), letting the membrane adapt to each *T* for at least 30 min. As observed in figure 3.10, SQMs in water turned into a homogeneous phase when *T* was around 30 ºC.

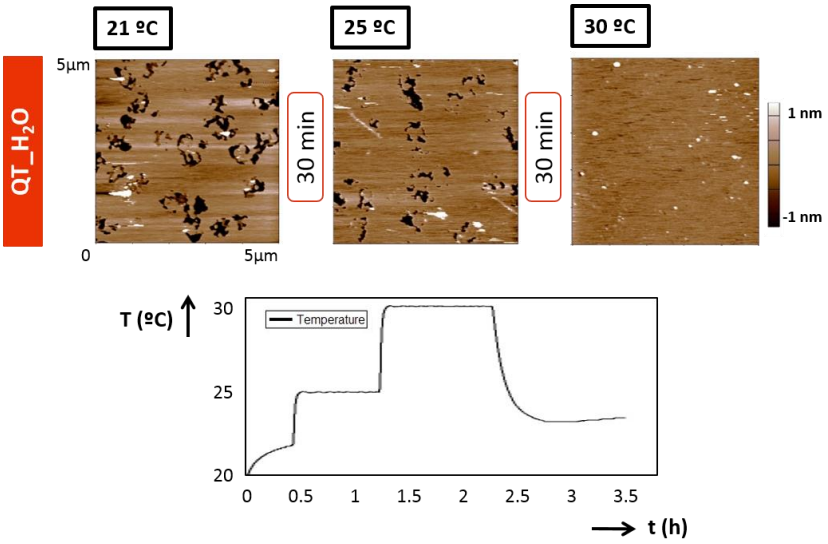

Figure 3.10 AC AFM topographical images for QT_H2O supported on mica in PBS pH 7.4 increasing the experimental temperature. *T vs.* t plot representing the different *T* steps.

Thanks to the collaboration with the Soft Matter Theory group from ICMAB-CSIC,** atomic molecular dynamic (MD) simulations were performed to better understand the behavior observed with the AFM for the QT_H_2O membranes, by analyzing the orientation of the molecules of each QT bilayer leaflet at the water/QT interface at different temperatures. We reported the average angle between nitrogen atoms of CTA^+ molecules and the QT interface as a function of time during the MD simulations (figure 3.11(a)). As observed (figure 3.11(a) and (b), top), the symmetry of the leaflets was broken at 10 ºC: while the layer B (blue) maintained its nearly vertical orientation, the layer A (orange) spontaneously adopted a substantial inclination. This suggests that QT components can be significantly inclined to the interface. On the other hand, at 50 ºC (figure 3.11(a) and (b), bottom) the relative inclination between the two leaflets disappeared, recovering again a symmetric configuration. At 25 ºC (figure 3.11, middle and 3.12), however, clear fluctuations from the stable configurations observed at 10 ºC and 50 ºC were obtained, explaining the possible coexistence of different thicknesses (domains) at *RT*.

** The MD simulations were performed by Sílvia Illa-Tusset and Dr. Jordi Faraudo (Soft Matter group, ICMAB-CSIC).

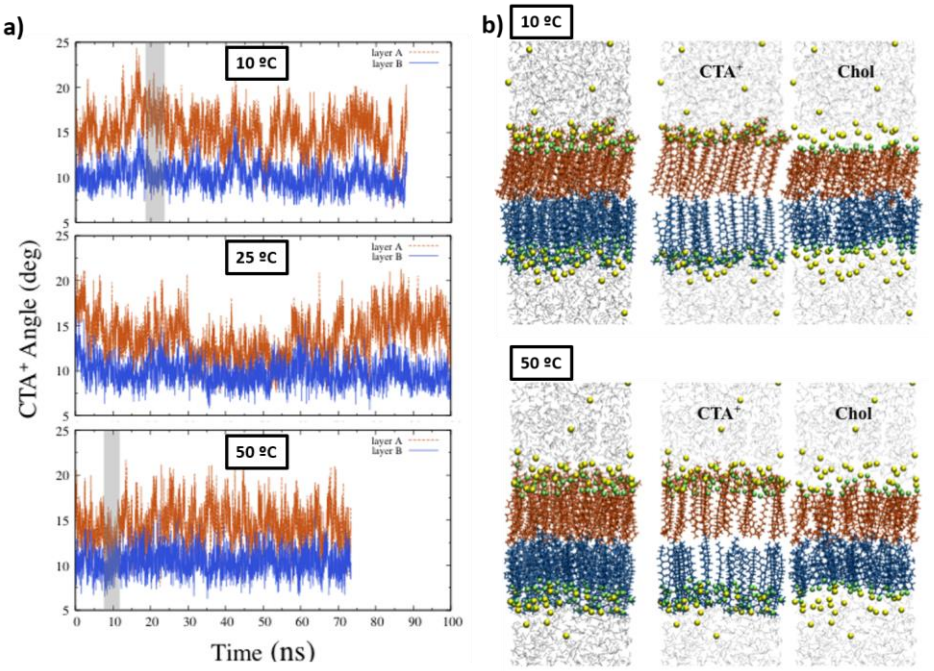

Figure 3.11 a) Inclination angle for CTA^+ molecules *vs*. time at 10 ºC, 25 ºC and 50 ºC for each leaflet (orange: layer A, blue: layer B). b) MD simulation frames of QT_H_2O showing the stable orientations of the bilayer (left) and for each QT component: CTA^+ (middle) and Chol (right) at 10 ºC and 50 ºC. The frames correspond to the grey bands at 10 ºC and 50 ºC showed in (a).

The same behaviour was observed when simulating the QT membrane with the presence of ions in the liquid medium (QT_PBS). However, the coexistence of configurations was detected at a temperature lower than *RT*. At *RT*, the system showed a stable symmetric configuration of the leaflets with MD and a homogeneous morphology with AFM.

We should take into account when interpreting and relating the AFM experimental results with the ones obtained from the MD simulations, that the systems simulated were of 15 – 16 nm^2 size. Thus, it is not possible to observe domains in the MD simulations, but throughout the simulations performed we could see how the system explored all the different equilibrium states. Considering the effect of the substrate on the AFM experiments, a shift in the domains transition to slightly different *T* values may be expected for SQMs. Still, these results agreed with the coexistence of different domains observed in AFM for QT_H_2O (figure 3.12).

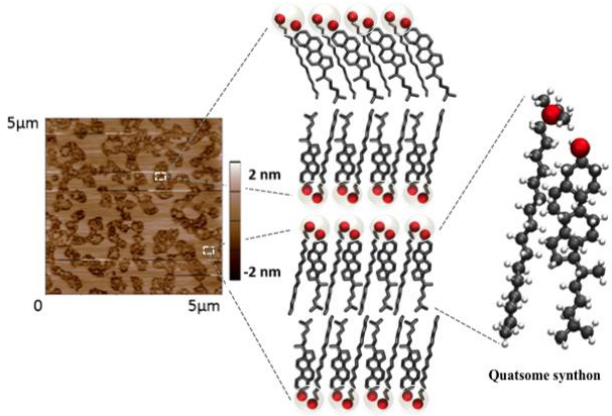

Figure 3.12 Correlation between the different topographical domains observed with AFM with the different orientations detected with MD simulations for a QT_H_2O membrane at 25 ºC.

3.3.6. Elasticity measurement on QT vesicles††

We finally assessed the elastic response of entire QTs deposited on silicon substrates. When studying vesicles on a flat substrate, it is not possible to prevent deformation of their architecture due to the adsorption. Hence, each vesicle can be described as a spherical cap, allowing then the estimation of the radius (R) of the exposed ''top'' regions of the spherical cap using the following equation 3.1:[27, 28]

$$R = \frac{0.25W^2 + h^2}{2h} \qquad \text{(equation 3.1)}$$

being W the width and h the height of the supported vesicle (figure 3.13(a)). In this section, we measured the geometrical parameters from QT_H_2O and QT_PBS vesicles deposited onto silicon substrates (figure 3.13(b)). W was extracted from contact mode topographical images by considering the 90 % of the distance between the two ends of the spherical cap obtained with the profile section, as a criterion to correct tip convolution effects. h was determined from the force-distance curves performed on the center of the QT vesicle, measuring from the start of the tip-QT mechanical contact until the tip-substrate contact (figure 3.13(b)).

Typically, an initial elastic response is expected for deformation on shells smaller than the thickness of the membrane, resulting in a linear dependence between the force and the indentation (Ind) (deformation) into the QT vesicle (figure 3.13(b), inset). According to the shell deformation theory, the slope of the *F vs*. Ind curve represents the stiffness of the

†† This section was performed in collaboration with José Antonio Durán, who performed the Master thesis at the Nanoprobes and Nanoswitches group in IBEC.

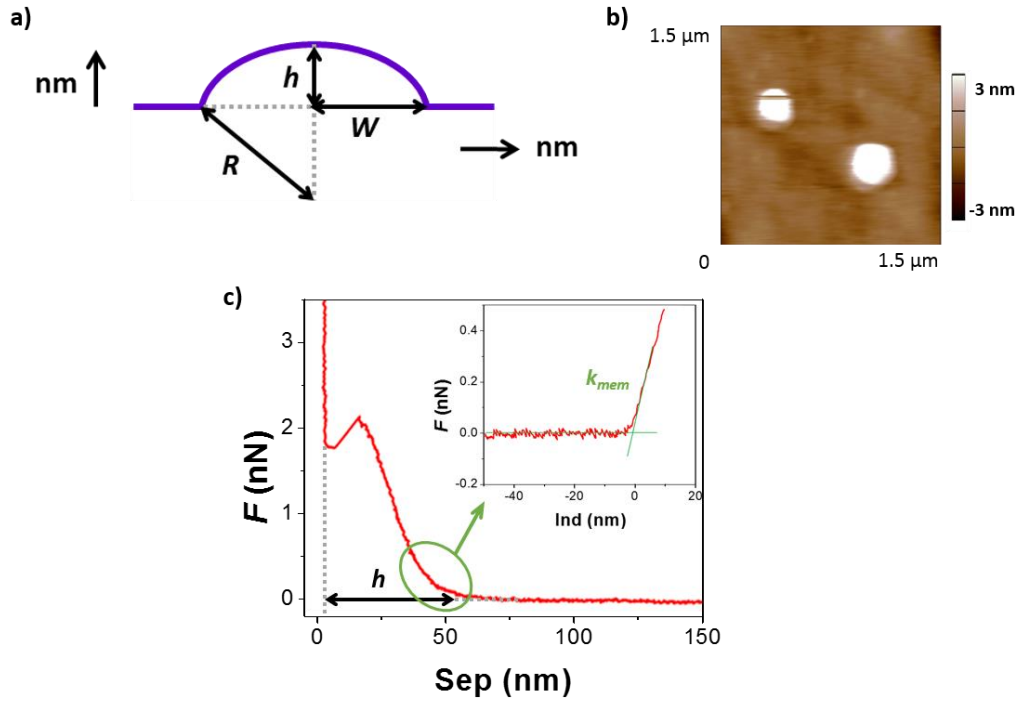

Figure 3.13 a) Diagram showing the geometrical parameters of a spherical cap. b) AC AFM topographical image QT_PBS vesicles supported on a silicon substrate and at *RT*. c) Force-separation curve performed in the center of a QT vesicle. Inset: zoom of the first tip-QT mechanical contact region.

vesicle membrane (k_{mem}), which can be expressed with equation 3.2.[29,30] Using then equation 3.1 to get R and k_{mem} from the AFM-FS measurements, we evaluated the Young modulus (E) of QT vesicles (equation 3.2):

$$k_{mem} = \frac{4E \cdot th^2}{R\sqrt{3(1-\nu^2)}} \rightarrow E = \frac{k_{mem} \cdot R\sqrt{3(1-\nu^2)}}{4 \cdot th^2} \qquad \text{(equation 3.2)}$$

being th the thickness of the QT membrane and ν the Poisson ratio. Here, we used the th values obtained in section 3.3.2, considering 4.4 nm[‡‡] and 4.9 nm for QT_H_2O and QT_PBS, respectively, and we assumed ν as 0.5, typical value employed for lipid vesicles.

From AFM-FS experiments performed in a minimum of three QT vesicles in both media (water and PBS), the obtained mean E values were: 55 ± 10 MPa for QT_H_2O and 74 ± 10 MPa for QT_PBS. Again, we observed the role of the ions on the nanomechanical behavior of

[‡‡] Since the QT_H_2O membrane is segregated into different domains we used the mean thickness obtained from the domains.

QT vesicles, by enhancing the rigidity of QT vesicles with the presence of salts in the environment. This result was in agreement with the previous F_b characterization presented in sections 3.3.3 and 3.3.4, and it is comparable to LPs composed of DOPC:Chol (80:20 molar ratio) (115 ± 15 MPa).

3.4. Conclusions

We characterized for the first time the morphology and the mechanical properties of supported QT membranes in different liquid environments and *T*. We determined that the QT membrane behaves as a typical fluid-like phospholipid bilayer. While a stable heterogeneous topography was observed for QT_H_2O, QT_PBS showed a dynamic behavior from segregation turning into a homogeneous SQM at *RT*.

By means of AFM-FS, we determined the effect of the presence of ions into the liquid media, which enhanced the lateral interactions between the membrane molecules, leading to higher F_b. We could also study the effect of the temperature on the SQMs, comparing the different morphologies of QT_H_2O and QT_PBS obtained by AFM with the stable configurations performed with MD at different *T*. We could determine a coexistence of different phases in the QT_H_2O membrane at *RT*, associated with different possible molecular orientations.

We finally evaluated the elasticity of entire vesicles deposited on silicon substrate, where again the ions of the buffer lead to higher nanomechanics, increasing the rigidity of the QT_PBS vesicles, compared with the QT_H_2O ones.

3.5. References

1. O. C. Farokhzad and R. Langer, *ACS Nano*, 2009, **3**, 16-20.
2. R. R. Sawant and V. P. Torchilin, *Soft Matter*, 2010, **6**, 4026-4044.
3. B. S. Pattni, V. V. Chupin and V. P. Torchilin, *Chem. Rev.*, 2015, **115**, 10938-10966.
4. F. Fernandez-Trillo, L. M. Grover, A. Stephenson-Brown, P. Harrison and P. M. Mendes, *Angew. Chem.-Int. Edit.*, 2017, **56**, 3142-3160.
5. G. Gregoriadis, *Trends Biotechnol.*, 1995, **13**, 527-537.
6. N. Grimaldi, F. Andrade, N. Segovia, L. Ferrer-Tasies, S. Sala, J. Veciana and N. Ventosa, *Chem. Soc. Rev.*, 2016, **45**, 6520-6545.
7. L. Ferrer-Tasies, E. Moreno-Calvo, M. Cano-Sarabia, M. Aguilella-Arzo, A. Angelova, S. Lesieur, S. Ricart, J. Faraudo, N. Ventosa and J. Veciana, *Langmuir*, 2013, **29**, 6519-6528.
8. M. Antonietti and S. Forster, *Adv. Mater.*, 2003, **15**, 1323-1333.
9. S. Geng, B. Yang, G. Wang, G. Qin, S. Wada and J. Y. Wang, *Nanotechnology*, 2014, **25**, 275103.
10. M. L. Immordino, F. Dosio and L. Cattel, *Int. J. Nanomed.*, 2006, **1**, 297-315.
11. C. Marianecci, L. Di Marzio, F. Rinaldi, C. Celia, D. Paolino, F. Alhaique, S. Esposito and M. Carafa, *Adv. Colloid Interfac.*, 2014, **205**, 187-206.
12. C. LoPresti, H. Lomas, M. Massignani, T. Smart and G. Battaglia, *J. Mater. Chem.*, 2009, **19**, 3576-3590.
13. S. Gudlur, P. Sukthankar, J. Gao, L. A. Avila, Y. Hiromasa, J. Chen, T. Iwamoto and J. M. Tomich, *PLOS ONE*, 2012, **7**, e45374.

14. A. Zeb, O. S. Qureshi, H. S. Kim, J. H. Cha and J. K. Kim, *Int. J. Nanomed.*, 2016, **11**, 3813-3824.
15. M. Cano-Sarabia, A. Angelova, N. Ventosa, S. Lesieur and J. Veciana, *J. Colloid Interfac.*, 2010, **350**, 10-15.
16. E. Elizondo, J. Larsen, N. S. Hatzakis, I. Cabrera, T. Bjornhorn, J. Veciana, D. Stamou and N. Ventosa, *J. Am. Chem. Soc.*, 2012, **134**, 1918-1921.
17. M. Cano-Sarabia, N. Ventosa, S. Sala, C. Patino, R. Arranz and J. Veciana, *Langmuir*, 2008, **24**, 2433-2437.
18. R. R. Sawant and V. P. Torchilin, *Aaps. J.*, 2012, **14**, 303-315.
19. S. Azarmi, W. H. Roa and R. Lobenberg, *Adv. Drug. Deliv. Rev.*, 2008, **60**, 863-875.
20. N. Ventosa, J. Veciana, S. Sala and M. Cano. Method for obtaining micro- and nano-disperse systems. *Patent WO/2006/079889*, 2006.
21. J. K. Li, R. M. A. Sullan and S. Zou, *Langmuir*, 2011, **27**, 1308-1313.
22. J. C. Phillips, R. Braun, W. Wang, J. Gumbart, E. Tajkhorshid, E. Villa, C. Chipot, R. D. Skeel, L. Kalé and K. Schulten, *J. Comput. Chem.*, 2005, **26**, 1781-1802.
23. M.-P. Mingeot-Leclercq, M. Deleu, R. Brasseur and Y. F. Dufrene, *Nat. Protoc.*, 2008, **3**, 1654-1659.
24. L. Redondo-Morata, M. I. Giannotti and F. Sanz, "Atomic Force Microscopy in Liquid", *Wiley-VCH Verlag GmbH & Co.KGaA*, Weinheim, Germany, In Press.
25. B. Gumi-Audenis, L. Costa, F. Carla, F. Comin, F. Sanz and M. I. Giannotti, *Membranes*, 2016, **6**.
26. L. Redondo-Morata, M. I. Giannotti and F. Sanz, *Mol. Membr. Biol.*, 2014, **31**, 17-28.
27. Q. Chen and G. J. Vancso, *Macromol. Rapid Comm.*, 2011, **32**, 1704-1709.
28. O. Et-Thakafy, N. Delorme, C. Gaillard, C. Meriadec, F. Artzner, C. Lopez and F. Guyomarc'h, *Langmuir*, 2017, **33**, 5117-5126.
29. A. Fery and R. Weinkamer, *Polymer*, 2007, **48**, 7221-7235.
30. N. Delorme and A. Fery, *Phys. Rev. E*, 2006, **74**, 030901.

Chapter 4

Pulling lipid tubes from model membranes

Cell processes like endocytosis, membrane resealing, signaling and transcription, involve conformational changes which depend on the chemical composition and the physicochemical properties of the lipid membrane. Thus, the better understanding of the mechanical role of the lipids in cell membrane force triggered mechanisms has recently become the focus of attention. In this chapter, we propose the use of pulling lipid tubes with an atomic force microscopy (AFM) tip out of model SLBs as a methodological approach to explore the nanomechanics of supported lipid bilayers through the evaluation of tube growing force (F_{tube}). We demonstrated that this approach allows to assess the contribution of the membrane composition as well as to evaluate the influence of the underlying substrate to the membrane mechanics.

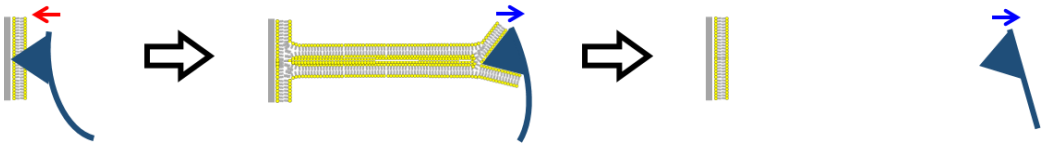

4.1. Introduction

Several cellular processes, including endocytosis, membrane resealing, signaling and transcription, among others, involve conformational changes such as bending, vesiculation and tubulation.[1] For instance, in endocytosis, the endocytic system needs to generate force enough to form an endocytic vesicle by bending the membrane bilayer.[2] Separation of a membrane segment from the cytoskeleton as well as strong membrane bending are both involved in these mechanisms, which are also associated with the membrane chemical composition and physicochemical properties.[1]

In vitro studies of the membrane mechanics have shown that subtle changes in the composition of the membrane affect the overall mechanical response. Micropipette aspiration is for instance one of the most used techniques to evaluate the elasticity of giant unilamellar vesicles (GUVs) at the mesoscopic scale.[3, 4] Nevertheless, the complex heterogeneous composition of the membranes, with domains in the micro and nanoscale, requires the use of local nanometric resolution techniques like atomic force microscopy (AFM) and, specifically, AFM-based force spectroscopy (AFM-FS) to study supported lipid bilayers (SLBs).[5, 6] As shown in previous chapters, in these experiments, the AFM tip is typically used as a force sensor and actuator that penetrates an individually SLB.

However, there is still the concern of the unknown effect of the supporting substrate on the measured mechanical properties as well as the impossibility of measuring the bilayer curvature due to its two-dimensional confinement. Indeed, as explained in the introductory chapter, alternative approaches, such as polymer-cushioned phospholipid bilayers[7, 8], pore spanning bilayers[9] and multilamellar membranes are proposed to overcome these limitations. Although these methods require complex protocols for sample preparation compared to simple SLBs, they allow the physical characterization of the bilayer decoupling the effect of the substrate.

AFM experiments have been also expanded to characterize the mechanics of live cells, to assess the cell elasticity,[10] including the contribution of the plasma membrane as well as the underlying cytoplasm and cytoskeleton,[11] or puncturing through the different membranes the AFM tip encounters. Moreover, the AFM probe can also be used to pull lipids from cells and membranes by applying a force orthogonal to a small membrane region,[2] processes that resemble the cell vesiculation and tubulation.

It has been reported that in a cell, the tube growing force (F_{tube}) depends on the membrane bending stiffness (κ), the in-plane membrane tension (σ) and the membrane-cytoskeleton adhesion (γ).[2] In regions where the membrane has separated from the cytoskeleton, what it is named as bleb or free membrane, F_{tube} is strictly dependent on the membrane properties, with the principal contributions being κ and σ as there is no direct interaction with the cytoskeleton.[12] However, the cytoskeleton adhesion and σ are in general

difficult terms to separate, so it has been proposed the so-called apparent membrane tension (σ_{app}), defining the membrane tension when considering the whole cell membrane and taking into account the adhesion contribution.[2] Hence, variations in the cytoskeleton-membrane adhesion term have a direct impact on F_{tube}.[12, 13]

In order to relate these membrane parameters, the following mathematical expression (equation 4.1) has been proposed:[14-17]

$$\sigma_{app} = \frac{F_{tube}^{\ 2}}{8\kappa\pi^2} = \sigma + \gamma \qquad \text{(equation 4.1)}$$

where γ is the adhesion energy parameter. Thus, determining F_{tube} from blebs ($F_{tube\ b}$), where $\gamma = 0$, will allow to separate adhesion and membrane tension. It is already reported that to evaluate γ, measurements from blebs and cytoskeleton supported cell regions ($\gamma \neq 0$) shown that $F_{tube\ b} < 0.5 \cdot F_{tube\ cyt}$, meaning that over 75% of σ_{app} is from adhesion.[2, 12]

A simplified but similar situation occurs when lipid tubes are pulled by AFM from an SLB. This approach combines the advantages of AFM to locally probe a sample with lateral resolution at the nanoscale and apply and sense force in the pN range, with the simplicity of the SLB preparation. In figure 4.1, we present a typical force-separation curve from an AFM-

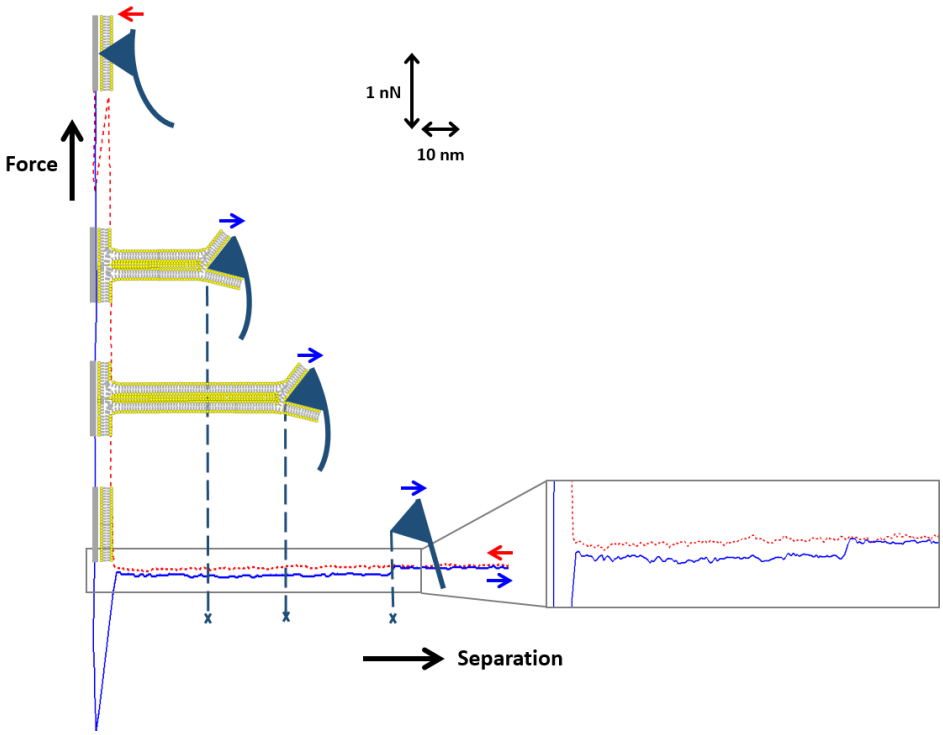

Figure 4.1 Scheme of a force-separation curve when pulling a membrane tube out of an SLB.

FS measurement on an SLB obtained by approaching (red doted curve) and retracting (blue curve) the AFM tip from the bilayer at a constant velocity. In the approach part, we observe the discontinuity defining the breakthrough force (F_b), when the AFM tip ruptures the bilayer.* When retracting the tip away from the sample, the tip remains connected to the surface through a lipid tube, that grows longer while the tip moves further away, up to a certain distance when it breaks and the cantilever returns to the equilibrium position. The lipid growing process occurs at a constant force F_{tube} and it is observed as a force plateau in the retract force-separation recordings, at several tens of pN.

In this chapter, we propose the use of pulling lipid tubes with an AFM tip out of model SLBs as a methodological approach to explore the nanomechanical properties of lipid membranes through the evaluation of F_{tube}. Studying SLBs with different compositions, we demonstrate that this approach allows to assess the contribution of the chemical composition to the membrane mechanics. In addition, we prove that the influence of the underlying substrate on the membrane mechanics can be determined, by comparing the tube growth from deposited vesicles and lipid bilayers supported onto different substrates.

4.2. Experimental

Materials. 1,2-dioleoyl-*sn*-glycero-3-phosphoethanolamine (DOPE), 1,2-dipalmitoyl-*sn*-glycero-3-phosphoethanolamine (DPPE), 1,2-dioleoyl-*sn*-glycero-3-phosphocholine (DOPC), 1,2-dipalmitoyl-*sn*-glycero-3-phosphoCholine (DPPC), 1,2-distearoyl-*sn*-glycero-3-phosphocholine (DSPC), 1,2- dioleoyl-*sn*-glycero-3-phospho-(1'-*rac*-glycerol) (DOPG), 1,2-dipalmitoyl-*sn*-glycero-3-phospho-(1'-*rac*-glycerol) (DPPG) and cholesterol (Chol) were purchased from Sigma-Aldrich (St. Louis, MO). The experiments were performed in 150 mM NaCl, 20 mM $MgCl_2$, 20 mM HEPES (4-(2-hydroxyethyl)-1-piperazineethanesulfonic acid) (pH 7.4) buffer solution or in 94 mM NaCl, 3.1 mM Na_2HPO_4, 0.9 mM NaH_2PO_4 (pH 7.4) buffer solution. Both buffers were prepared with ultrapure water (Milli-Q reverse osmosis system, 18.2 mΩ·cm resistivity) and filtered before use with an inorganic membrane filter (0.22 μm pore size Whatman International Ltd, England, UK).

Sample preparation. The different lipids were individually dissolved in chloroform:methanol (v:v 3:1) to give a final concentration of 3 mM. Aliquots of each phospholipid were poured into a falcon tube, evaporating then the solvent to dryness under nitrogen flow in order to achieve a thin film spread on the walls of the tube. The dried lipid films were then hydrated with buffer solution (150 mM NaCl, 20 mM $MgCl_2$, 20 mM HEPES, pH 7.4), previously heated above the transition temperature (T_m) of the phospholipid, until a final total concentration of 0.5 mM. The falcon tubes were later subjected to cycles of vortex mixing and heating to *ca.* 60ºC. The vesicles suspensions were placed in an

* For further details see introductory chapter or chapter 2.

ultrasounds bath for 30 min to finally obtain unilamellar vesicles.[18] The DOPC:Chol (80:20 molar ratio) were synthesized by DELOS-SUSP method[19] and suspended in 94 mM NaCl, 3.1 mM Na_2HPO_4, 0.9 mM NaH_2PO_4 (pH 7.4) buffer solution.†

Supported lipid bilayers (SLBs) were obtained by vesicles fusion method.[6] The vesicles suspensions were deposited onto circular freshly cleaved mica surfaces (Ted Pella, Redding, CA) and incubated for 30 min at a temperature above the phospholipid T_m. Afterwards, the samples were rinsed several times with buffer solution to avoid unfused vesicles, always keeping the substrates hydrated.

To study supported unfused vesicles, DOPC:Chol vesicles of 70 nm average diameter measured by dynamic light scattering (DLS) were used. Vesicles were deposited onto square silicon substrates (Ted Pella, Redding, CA),‡ incubated for 5 min at room temperature (*RT*) and then rinsed with the specific buffer solution. In this case, we obtained a combination of unfused vesicles with some bilayer patches onto the silicon substrate.

Atomic force microscopy-based force spectroscopy (AFM-FS). AFM-FS measurements were performed using an MFP-3D atomic force microscope (AFM) (Asylum Research, Santa Barbara, CA) at *RT* and under liquid conditions (buffer solution), on a sample region previously visualized using AC-mode for SLBs and contact mode for supported vesicles. We used V-shaped Si_3N_4 cantilevers having a nominal spring constant of 0.35 $N \cdot m^{-1}$: SNL, which has the tip made of silicon and with a nominal tip radius (r_{tip}) between 2 and 12 nm, and DNP, which has the tip made of silicon nitride and with a nominal r_{tip} between 20 and 60 nm (Bruker AFM Probes, Camarillo, CA). After having measured the sensitivity of the piezo ($V \cdot m^{-1}$), the cantilever spring constants were individually calibrated by using the equipartition theorem (thermal noise routine).[20] Force-distance curves were recorded by approaching and retracting the AFM cantilever tip at 1 $\mu m \cdot s^{-1}$ (unless specifically stated) and in the force map mode.[6, 18]

4.3. Results and discussions

4.3.1. Phospholipid headgroup and phase state

We first assessed the role of the lipid molecular structure on the tube growth process. We prepared and studied SLBs composed of different individual phospholipids, namely DOPE, DPPE, DOPC, DPPC, DOPG and DPPG. The chemical structures of these phospholipids are presented in figure 4.2. We chose phospholipids of constant chain length (both DO- or

† The DOPC:Chol (80:20 molar ratio) vesicles were provided by the Nanomol group of Institut de Ciència de Materials de Barcelona (ICMAB-CSIC), Cerdanyola del Vallès (Spain).
‡ The squared Si substrates were obtained from wafers and cleaned with piranha solution (7:3 H_2SO_4:H_2O_2 (30%)) before their use.

DP-, fluid or gel state at *RT*,[§] respectively) but changing the headgroup (phosphoethanolamine (PE), phosphocholine (PC) and phosphoglycerol (PG)).

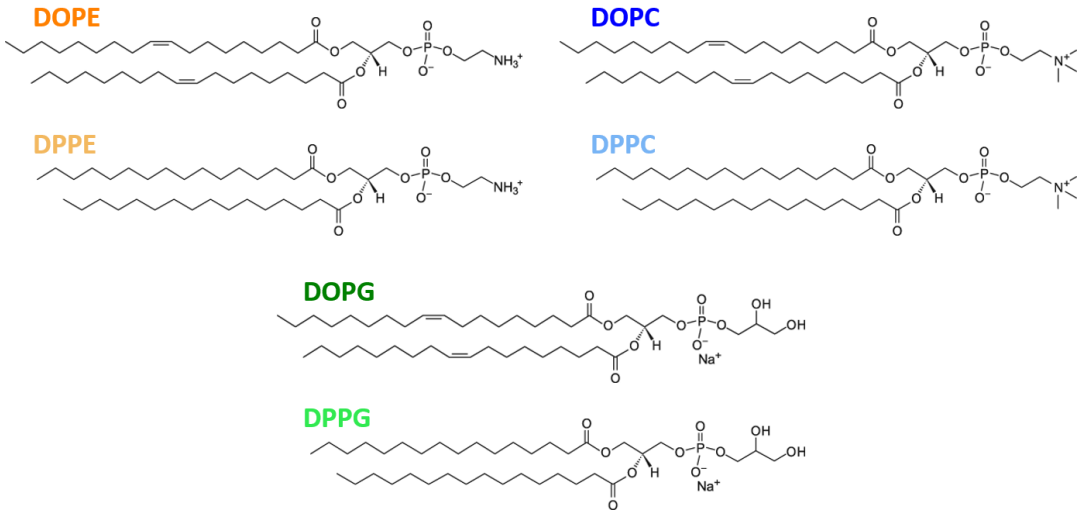

Figure 4.2 Chemical structures of DOPE, DPPE, DOPC, DPPC, DOPG and DPPG phospholipids.

After imaging the samples to locate bilayer patches, force-distance curves were recorded using sharp AFM tips (SNL, nominal r_{tip} between 2 and 12 nm). From the plateaus observed in the retract curves, the F_{tube} values along with the distance at which the tubes are ruptured or detached (d) were calculated. Figure 4.3 shows the F_{tube} and d distributions and F_{tube} *vs.* d plots grouped according to the headgroup (PE (a), PC (b) and PG (c)) as well as the F_{tube} mean values (d).

We observe that F_{tube} is smaller for fluid-like (or liquid-disordered, l_d) phospholipid bilayers (in the range of 70 pN) than for the gel-like (or solid-ordered, s_o) bilayers of the same headgroup (in the range of 100 pN). While in the l_d state the F_{tube} is nearly constant, with a slight increase from DOPE to DOPC (66 ± 2 pN for DOPE, 80 ± 3 pN for DOPC and 75 ± 3 pN for DOPG), it clearly increases when changing the headgroup for s_o bilayers from PE to PC and then to PG (92 ± 2 pN for DPPE, 104 ± 3 pN for DPPC and 112 ± 3 pN for DPPG).[**] These values are directly related to the molecular lateral packing and interaction with the substrate and surrounding solvent, mainly electrostatic nature.[6, 21] As a consequence, growing tubes from SLBs with the AFM occurs at higher force for PG SLBs, charged phospholipids that together with the ions from the buffer form strong lateral packing

[§]DOPE (T_m = -16 ºC), DOPC (T_m = -17 ºC) and DOPG (T_m = -18 ºC) are l_d SLBs, whereas DPPE (T_m = 63 ºC), DPPC (T_m = 41 ºC) and DPPG (T_m = 41 ºC) are s_o SLBs.

[**] The errors of these results are calculated evaluating the standard errors of the mean.

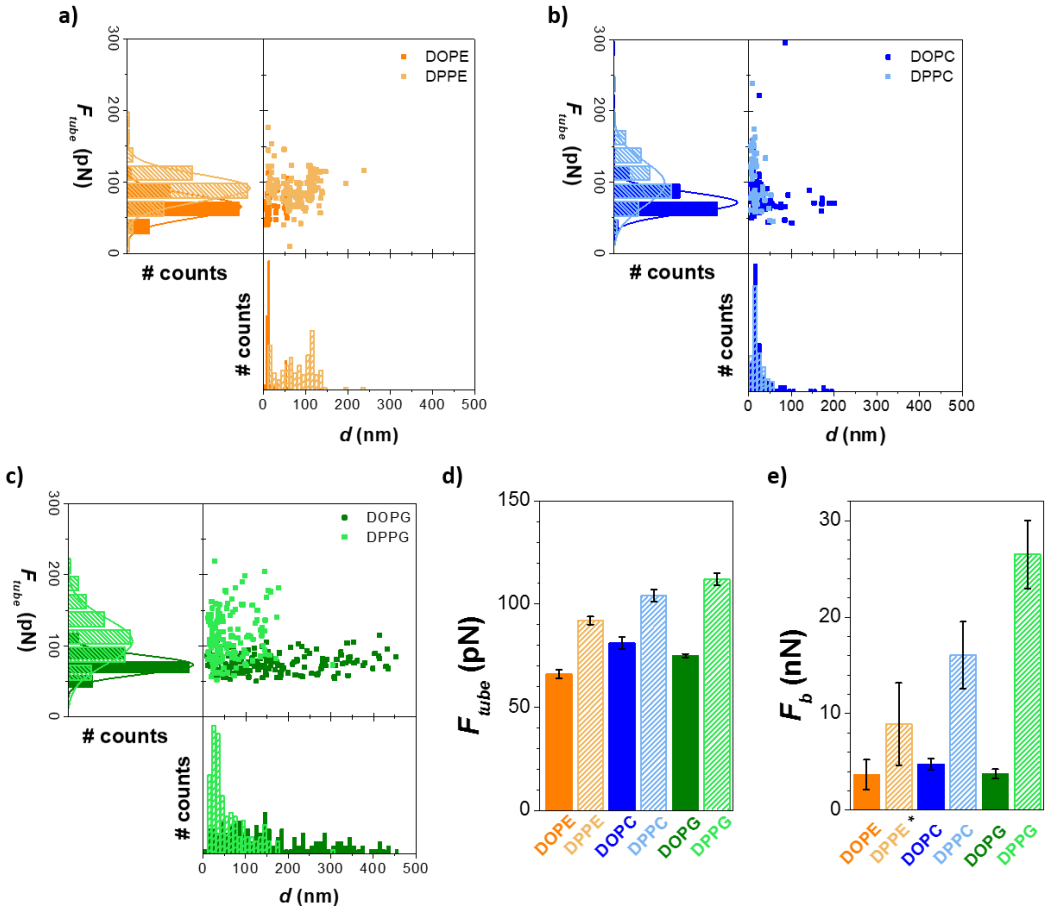

Figure 4.3 *F_{tube} vs. d* plots with F_{tube} and *d* histograms for all the phospholipid systems sorted by same headgroup: PE (a), PC (b) and PG (c) (n > 100). d) Mean F_{tube} values. e) Mean F_b values. *Value obtained from ref.[20] The experiments were performed in 150 mM NaCl, 20 mM $MgCl_2$, 20 mM HEPES (pH 7.4) buffer solution and at *RT*.

between the lipid headgroups and enhanced interactions with the substrate. This behavior corresponds well with the trend observed on the well-established F_b characterization approach for such bilayers (figure 4.3(e)),[21] where not only significantly lower F_b are obtained for l_d SLBs than for s_o bilayers, but also the values increase like PE < PC < PG (DOPE 3.7 ± 1.6 nN, DPPE 8.9 ± 4.3 nN, DOPC 4.8 ± 0.6 nN, DPPC 16.1 ± 3.4 nN, DOPG 3.8 ± 0.5 nN, DPPG 26.5 ± 3.5 nN).

Interestingly, when evaluating the tube growth on DSPC SLBs, no significant variation in F_{tube} (98 ± 1 pN) was observed, respect to DPPC bilayers (figure 4.4(a) and (b)). DSPC tails have the same number of carbons as DOPC in the chains (18) but fully saturated, meaning

that at *RT* the bilayer is in the gel state. This is two more carbons than DPPC, also in the gel state at *RT*.†† In contrast, this difference in tail length is related with an increase in the F_b, since the force needed to rupture a DSPC SLB (32.7 ± 2.0 nN) is significantly higher than for DPPC ones (figure 4.4(c)).

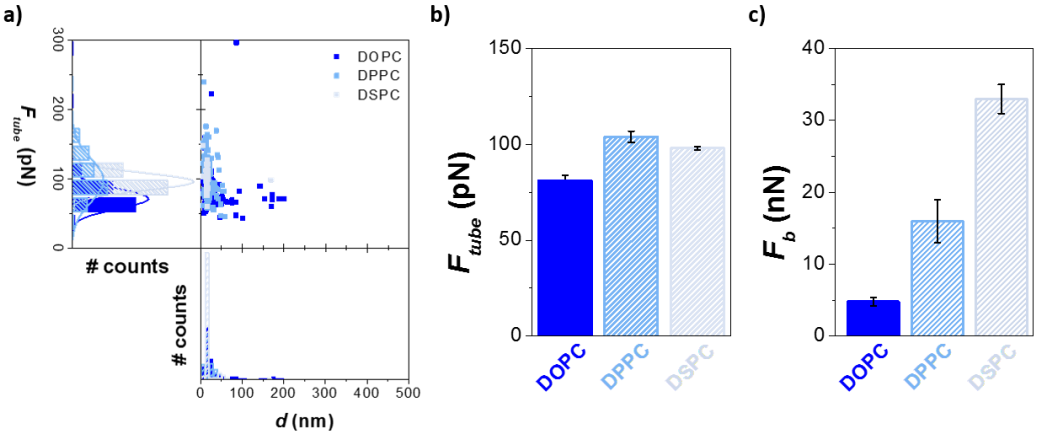

Figure 4.4 a) F_{tube} histograms for all the PC systems (n > 110). b) Mean F_{tube} values. c) Mean F_b values. The experiments were performed in 150 mM NaCl, 20 mM $MgCl_2$, 20 mM HEPES (pH 7.4) buffer solution and at *RT*.

In general, the distance at which the tube breaks or detaches from the tip was fairly constant when comparing the different phospholipid systems (figure 4.3(a-c)). Still, the tubes growing from DOPG bilayers normally extended to longer distances. This might be related to the charge of PG phospholipids, giving rise to higher interactions between the lipid molecules and the AFM tip.

From the resultant F_{tube} values, it is possible to estimate the apparent membrane tension σ_{app} according to equation 4.1. Focusing on DOPC membranes and considering κ as $17 k_B T$ (for T = 298 K) from reported X-ray studies on GUVs,[3, 22] we calculated a σ_{app} of 0.94 pN·nm^{-1}. This value agrees with reported studies performed on DOPC SLBs as well, in which using the same expression and knowing the tube radius and the surface tension of the bilayer, they estimate a similar F_{tube}.[23]

We demonstrate that the mechanical properties associated to the bilayer order and structure, such as bending stiffness and in-plane membrane tension, as evidenced from F_{tube}, depend not only on the phospholipid headgroup, but also on the phospholipid state of the bilayer.[21, 24]

††DOPC 18:1, DPPC 16:0 and DSPC 18:0 (T_m = 55 ºC).

4.3.2. Effect of the underlying substrate

As explained in the introductory section of this chapter, it is possible to estimate the adhesion parameter depending on the membrane support by using equation 4.1, by evaluating the apparent membrane tension of the SLBs and the membrane tension of free standing membranes. Thus, to study the influence of the underlying substrate on F_{tube} and σ, we compared the tube growth from DOPC:Chol (80:20 molar ratio) deposited vesicles, where the bilayer is not in direct interaction with the substrate, and bilayers supported onto silicon (with a native silicon oxide layer) and mica surfaces, as schematized in figure 4.5(a). In these experiments, vesicles are equivalent to free membranes (blebs), with $\gamma = 0$ in equation 4.1, and the bilayers as the systems comprising the adhesion term, with $\gamma \neq 0$ in equation 4.1. A topographical image of a vesicle supported onto a Si substrate in shown in figure 4.5(b).

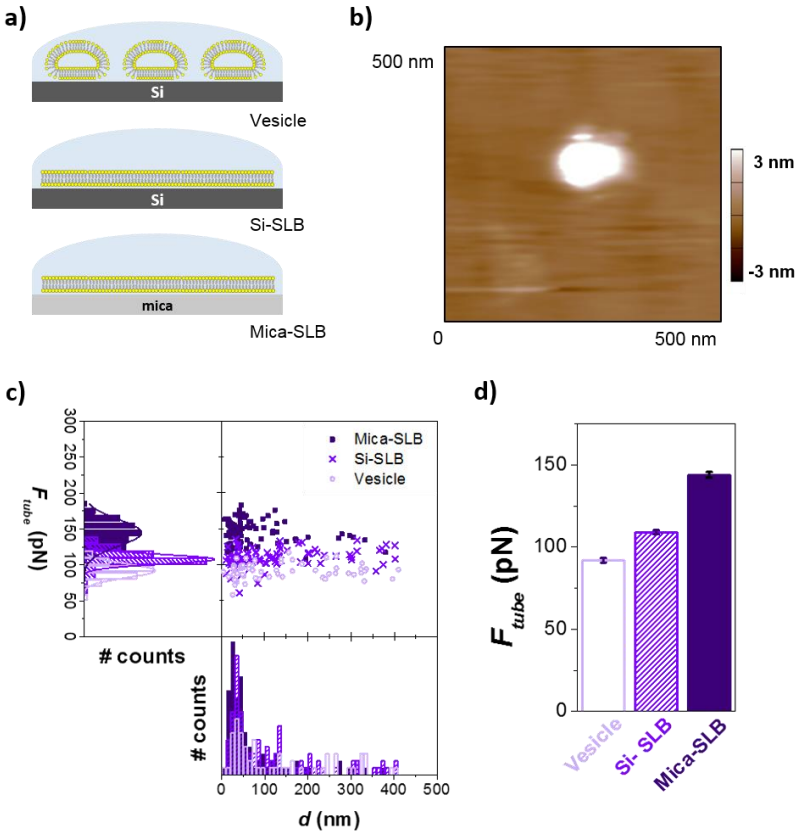

Figure 4.5 a) Scheme of the vesicles deposited onto Si, and the bilayers supported onto Si and mica. b) AFM topographical image from a vesicle of of DOPC:Chol (80:20 molar ratio). c) F_{tube} histograms (n > 65). c) F_{tube} *vs. d* plots with F_{tube} and *d* histograms. d) Mean F_{tube} values. The experiments were performed in 94 mM NaCl, 3.1 mM Na_2HPO_4, 0.9 mM NaH_2PO_4 (pH 7.4) buffer solution and at *RT*.

The resultant F_{tube} histograms and F_{tube} *vs. d* plots (figure 4.5(c) and (d)), demonstrate that the lowest F_{tube} is obtained for the vesicles ($F_{tube\ b}$ = 92 ± 2 pN), shifting to higher F_{tube} values for the SLB on silicon ($F_{tube\ Si}$ = 109 ± 2 pN), and on mica ($F_{tube\ mica}$ = 144 ± 2 pN). ‡‡

When comparing the different underlying substrates, we observe $F_{tube\ Si}$ as approximately 15% higher than for the vesicles ($F_{tube\ b}$) and $F_{tube\ mica}$ a 37% higher than $F_{tube\ b}$, equations 4.2 and 4.3.

$$F_{tube\ b} = 0.85 \cdot F_{tube\ Si} \qquad \text{(equation 4.2)}$$

$$F_{tube\ b} = 0.63 \cdot F_{tube\ mica} \qquad \text{(equation 4.3)}$$

Combining equation 4.1 with equations 4.2 and 4.3, we can then obtain the relations between the apparent membrane tensions concerning the different underlying substrates: σ_b for vesicles, and $\sigma_{app\ Si}$ and $\sigma_{app\ mica}$ for bilayers supported onto silicon or mica, respectively (equations 4.4 and 4.5).

$$\sigma_b = \frac{F_{tube\ b}{}^2}{8\kappa\pi^2} = \frac{(0.85 \cdot F_{tube\ Si})^2}{8\kappa\pi^2} = 0.72 \cdot \sigma_{app\ Si} \qquad \text{(equation 4.4)}$$

$$\sigma_b = \frac{F_{tube\ b}{}^2}{8\kappa\pi^2} = \frac{(0.63 \cdot F_{tube\ mica})^2}{8\kappa\pi^2} = 0.40 \cdot \sigma_{app\ mica} \qquad \text{(equation 4.5)}$$

Knowing that the sum of σ_b and the corresponding adhesion term γ defines σ_{app} (equations 4.1), we estimate γ for the bilayers supported onto silicon or mica, which stands for a 28% and 60% of the apparent supported membrane tensions ($\sigma_{app\ Si}$ and $\sigma_{app\ mica}$, respectively). This demonstrates that SLBs models represent an intermediate scenario between a bleb and a cytoskeleton supported membrane, when over 75% of the apparent membrane tension is from adhesion.[2] Nevertheless, it is important to take into account that changing the lipid composition of the membrane, for instance the phospholipid headgroup, this results would probably change the adhesion contribution due to the different electrostatic interaction with the underlying substrate.

It has been reported that contents up to 30 mol % of Chol do not significantly affect the mechanical properties of DOPC:Chol SLBs.[25, 26] This allows us to consider the same κ employed before for DOPC membranes (17 k_BT) as for DOPC:Chol (80:20) systems studied in this section. Using equation 4.1 for blebs and considering $F_{tube\ b}$, we obtain a σ_b of 1.53 pN·m^{-1}. Performing the same calculations for the Si or mica supported membranes, and by employing $F_{tube\ Si}$ and $F_{tube\ mica}$ with equations 4.6 and 4.7, we obtain the following values:

‡‡ The errors of these results are calculated evaluating the standard errors of the mean.

$$\sigma_{app\ Si} = \frac{{F_{tube\ Si}}^2}{8\kappa\pi^2} = 2.11\ pN \cdot nm^{-1} \quad \text{(equation 4.6)}$$

$$\sigma_{app\ mica} = \frac{{F_{tube\ mica}}^2}{8\kappa\pi^2} = 3.80\ pN \cdot nm^{-1} \quad \text{(equation 4.7)}$$

From these results and considering that the σ_{app} is defined as the sum of σ_b with γ, we can estimate that the adhesion contribution to the in-plane membrane tension from the substrates corresponds to 0.58 pN·m^{-1} and 2.27 pN·m^{-1} for the Si-SLBs and mica-SLBs, respectively.

4.3.3. F_{tube} does not depend on the AFM tip

In this section, we study the effect of the AFM tip properties (i.e. nominal r_{tip} or tip material) on the force values measured during the growth of the lipid tube. We first compared the results obtained when performing the experiments with two different tips that have the same specifications except for the tip material and its r_{tip}: SNL, with a tip made of silicon and its nominal r_{tip} between 2 and 12 nm, and DNP, with a tip made of silicon nitride and its nominal r_{tip} between 20 and 60 nm. We performed the experiments on DOPC bilayers onto mica where, as exposed in section 3.3.1, the F_{tube} value obtained using SNL tips was 80 ± 3 pN. Carrying out the same experiments with DNP tips, we obtained F_{tube} in the same range: 81 ± 3 pN. Still, we noticed that for higher r_{tip}, more tube growth events were detected in a force map measurement. In any case, we can conclude that even if a higher r_{tip} facilitates the tube growth events, it is does not affect the resultant F_{tube} value. In cells, a comparable scenario has been observed, where increasing r_{tip} leads the formation of multiple tethers, but no effect to the growing force even with different tip functionalizations.[27, 28]

We further evaluated the influence of the pulling velocity on the F_{tube} value. We chose DOPC and DSPC bilayers supported onto mica, representative of l_d and s_o SLBs, and determined F_{tube} from experiments performed at 1 μm·s^{-1} and 3 μm·s^{-1}. As shown in the histograms of figure 4.6, there is no significant change on F_{tube} when considering this range of speeds. The absence of correlation between the growth of the tube with the velocity of the AFM tip agrees with the literature, since it has been already reported that, within 0.5 μm·s^{-1} and 50 μm·s^{-1}, the measured F_{tube} seems to show a no speed dependency.[29] Once the tube is formed, its growth process occurs at a constant force, expected to be independent of the velocity, as the loading rate in here is zero.

4.4. Conclusions

In this chapter, we proposed a methodological approach based on the use of the AFM tip to pull lipid tubes out of model SLBs to evaluate the nanomechanical properties of lipid membranes. We established that the phase state of the SLB determines the tube growing

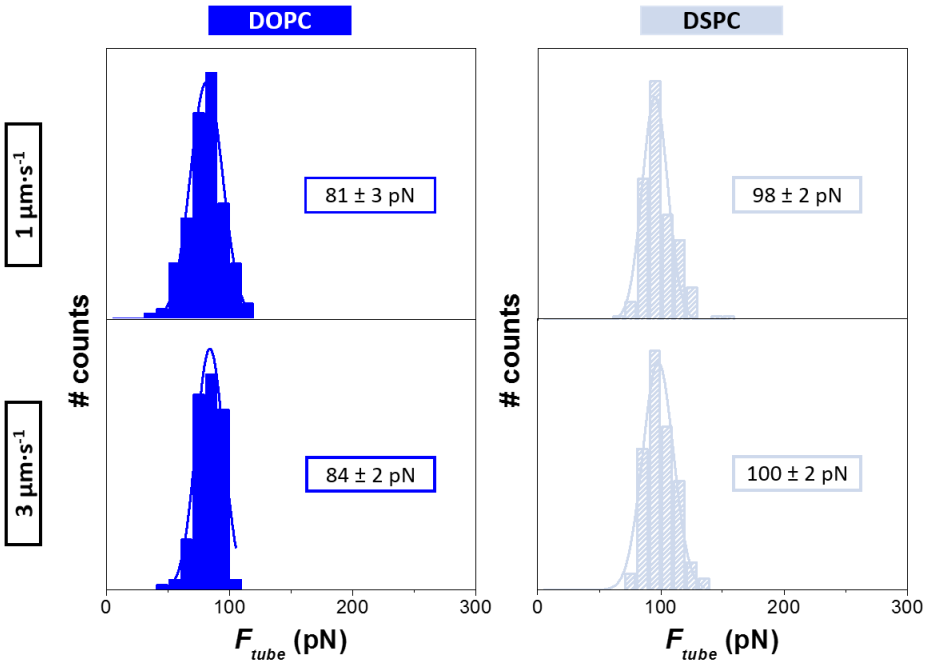

Figure 4.6 F_{tube} histograms for DOPC and DSPC SLBs approaching and retracting the tip at 1 and 3 µm·s^{-1} (n > 130). The experiments were performed in 150 mM NaCl, 20 mM $MgCl_2$, 20 mM HEPES (pH 7.4) buffer solution and at *RT*.

force, which in general is higher for s_o than for l_d bilayers. We exposed that F_{tube} also depends on the phospholipid headgroup, enhancing F_{tube} values from PE to PC and to PG bilayers, due to stronger interactions between the charged phospholipid headgroups (PG) and the ions from the buffer solution. This behavior is comparable to the one observed on the well-established F_b analysis.

In addition, we evaluated the influence of the underlying substrate on the tube growing force and membrane tension, comparing the tube growth from deposited vesicles and SLBs (silicon or mica). With this approach we were able to assess the contribution of the different substrates on the tubing growth process and we demonstrated that SLB model represents an intermediate scenario between a free membrane (blebs) and a cytoskeleton supported membrane, regarding the contribution to the overall membrane tension.

We finally confirmed that the tube growth is not dependent on the tip radius, nor on the velocity of the tip while retracting away from the sample in the studied range.

4.5. References

1. G. van Meer, D. R. Voelker and G. W. Feigenson, *Nat. Rev. Mol. Cell Bio.*, 2008, **9**, 112-124.
2. M. P. Sheetz, *Nat. Rev. Mol. Cell Bio.*, 2001, **2**, 392.

3. W. Rawicz, K. C. Olbrich, T. McIntosh, D. Needham and E. Evans, *Biophys. J.*, 2000, **79**, 328-339.
4. E. Evans, V. Heinrich, F. Ludwig and W. Rawicz, *Biophys. J.*, 2003, **85**, 2342-2350.
5. S. Garcia-Manyes and F. Sanz, *BBA - Biomembranes*, 2010, **1798**, 741-749.
6. L. Redondo-Morata, M. I. Giannotti and F. Sanz, *Mol. Membr. Biol.*, 2014, **31**, 17-28.
7. J. Majewski, J. Y. Wong, C. K. Park, M. Seitz, J. N. Israelachvili and G. S. Smith, *Biophys. J.*, 1998, **75**, 2363-2367.
8. H. L. Smith, M. S. Jablin, A. Vidyasagar, J. Saiz, E. Watkins, R. Toomey, A. J. Hurd and J. Majewski, *Phys. Rev. Lett.*, 2009, **102**.
9. I. Mey, M. Stephan, E. K. Schmitt, M. M. Mueller, M. Ben Amar, C. Steinem and A. Janshoff, *J. Am. Chem. Soc.*, 2009, **131**, 7031-7039.
10. K. Haase and A. E. Pelling, *J. R. Soc. Interface*, 2015, **12**.
11. E. Moeendarbary, L. Valon, M. Fritzsche, A. R. Harris, D. A. Moulding, A. J. Thrasher, E. Stride, L. Mahadevan and G. T. Charras, *Nat. Mater.*, 2013, **12**, 253-261.
12. J. Dai and M. P. Sheetz, *Biophys. J.*, 1999, **77**, 3363-3370.
13. D. Raucher, T. Stauffer, W. Chen, K. Shen, S. Guo, J. D. York, M. P. Sheetz and T. Meyer, *Cell*, 2000, **100**, 221-228.
14. P. B. Canham, *J. Theor. Biol.*, 1970, **26**, 61-81.
15. J. Daillant, E. Bellet-Amalric, A. Braslau, T. Charitat, G. Fragneto, F. Graner, S. Mora, F. Rieutord and B. Stidder, *P. Natl. Acad. Sci. USA*, 2005, **102**, 11639-11644.
16. A. Roux, *Soft Matter*, 2013, **9**, 6726-6736.
17. J. W. Armond, J. V. Macpherson and M. S. Turner, *Langmuir*, 2011, **27**, 8269-8274.
18. B. Gumi-Audenis, L. Costa, F. Carla, F. Comin, F. Sanz and M. I. Giannotti, *Membranes*, 2016, **6**, 58.
19. N. Ventosa, J. Veciana, S. Sala and M. Cano. Method for obtaining micro- and nano-disperse systems. *Patent WO/2006/079889*, 2006.
20. R. Proksch, T. E. Schaffer, J. P. Cleveland, R. C. Callahan and M. B. Viani, *Nanotechnology*, 2004, **15**, 1344-1350.
21. S. Garcia-Manyes, L. Redondo-Morata, G. Oncins and F. Sanz, *J. Am. Chem. Soc.*, 2010, **132**, 12874-12886.
22. J. F. Nagle, M. S. Jablin, S. Tristram-Nagle and K. Akabori, *Chem. Phys. Lipids*, 2015, **185**, 3-10.
23. I. Pera, R. Stark, M. Kappl, H. J. Butt and F. Benfenati, *Biophys. J.*, 2004, **87**, 2446-2455.
24. L. Picas, F. Rico and S. Scheuring, *Biophys. J.*, 2012, **102**, L1-L3.
25. L. Redondo-Morata, M. I. Giannotti and F. Sanz, *Langmuir*, 2012, **28**, 12851-12860.
26. R. Dimova, *Adv. Colloid Interfac.*, 2014, **208**, 225-234.
27. M. Sun, J. S. Graham, B. Hegedüs, F. Marga, Y. Zhang, G. Forgacs and M. Grandbois, *Biophys. J.*, 2005, **89**, 4320-4329.
28. G. Girdhar and J.-Y. Shao, *Biophys. J.*, 2004, **87**, 3561-3568.
29. N. Maeda, T. J. Senden and J.-M. di Meglio, *BBA - Biomembranes*, 2002, **1564**, 165-172.

Chapter 5

Effect of HNP1 defensin on model supported lipid bilayers

The cell membrane is the first line of defense against invading species. Its structural and physical properties are sometimes altered due to the membrane composition and the non-specific interactions with small molecules that play important roles in many biological events, including membrane fusion and lysis. In humans, human neutrophil peptide (HNPs) defensins contribute to the host defense by acting rapidly to kill and inactivate the microbes. However, the mechanisms by which microorganisms are killed by defensins are not fully understood, although in general it is believed that killing is a consequence of disruption of the microbial membrane. It becomes important to further deepen into the lipid specificity of these antimicrobial peptides and their influence into the integral properties of membranes, to better understand their activity towards mammalian or bacterial cells. In this chapter, we characterize the changes on the morphology and mechanics (atomic force microscopy and spectroscopy) as well as the electronic structure (X-ray reflectometry) of supported lipid bilayers with different composition before and upon the incubation of the HNP1 defensin.

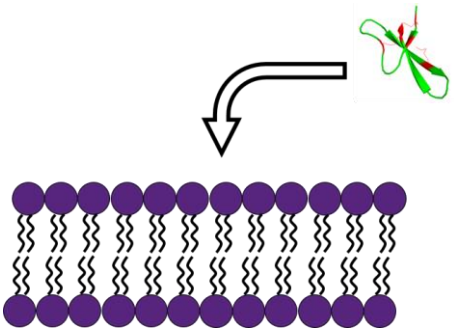

5.1. Introduction

The cell membrane is the first line of defense against invading species. Its composition and non-specific interaction with small molecules can alter its structural and physical properties, affecting the interactions between the membrane and the surrounding molecules. Membrane – peptide interactions play essential roles in a number of biological events, including membrane fusion and membrane lysis.[1] Examples of peptides that have been investigated so far include model peptides, antimicrobial peptides (AMPs), virus-derived peptides, cell-penetrating peptides and amyloid peptides.[2]

Defensins are 2-6 kDa, cysteine (Cys)-rich, cationic AMPs active against different bacteria (both gram-positive and negative), fungi, and enveloped viruses.[3] In humans, human neutrophil peptide (HNPs) defensins contribute to the host defense by acting rapidly to kill and inactivate the microbes.[4-6] However, the mechanisms by which microorganisms are killed by defensins are not fully understood, although in general it is believed that killing is a consequence of disruption of the microbial membrane.[7] Defensins are amphipathic molecules that have clusters of positively charged amino-acids and hydrophobic amino-acid side chains. This polar topology allows them to insert themselves into the phospholipid membrane in a way that their hydrophobic regions are buried within the interior of the lipid bilayer, whereas their charged regions, mostly cationic, interact with the anionic phospholipid headgroups and the water.[8] Several mechanisms, including pore formation (figure 5.1), membrane solubilization, peptide translocation and membrane thinning, have been proposed considering peptides of different length, hydrophobicity, charge and secondary structure.[9, 10] They seem to be initiated by surface association of the hydrophilic part of the peptide with the lipid headgroups, followed by membrane interruption at a threshold peptide concentration. Therefore, it becomes important to further deepen into the

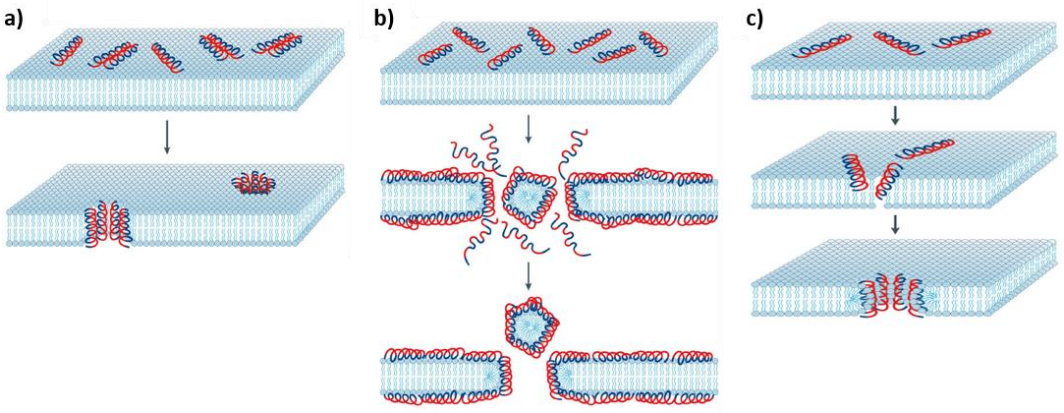

Figure 5.1 Some examples of mechanisms proposed for AMPs killing: a) Barrel-stave model. b) Carpet model. c) Toroidal model. Adapted by permission from Springer Nature: ref.[10]. Copyright © 2005.

lipid specificity of membrane-active AMPs and their influence into the integral properties of membranes, to better understand their activity against mammalian or bacterial cells.[9]

HNP1 is one of the most abundant forms of the α-defensins family, that is produced in the cytoplasmic azurophilic granules of neutrophils. This 30 amino-acids monomer is strongly stabilized by three Cys disulfide bridges (highlighted in red in figure 5.2(a)) that interconnect each β-sheet. It is known to be present as a dimer in solution, where each monomer presents a positive net charge equal to +3 (figure 5.2(c)),[11] conferred by four arginine residues (Arg5, Arg14, Arg15, and Arg24) and a negative glutamic acid (Glu13). Moreover, the lipid composition has been established to be determinant for the selectivity of HNP1 to interact with the membrane. Tryptophan (Trp)-26 (highlighted in purple in figure 5.2(b)) has been reported to be the the most critical residue in HNP1, contributing to the defensin function at multiple levels.[6, 12] Trp provides high binding energy due to its possibility of interacting with hydrophobic molecules, such as the bacterial membrane.[6] In addition, Trp-26 has a significant role in the stabilization of the structure of HNP1 dimers, which can lead to the formation of pores in the microbial membrane.[6]

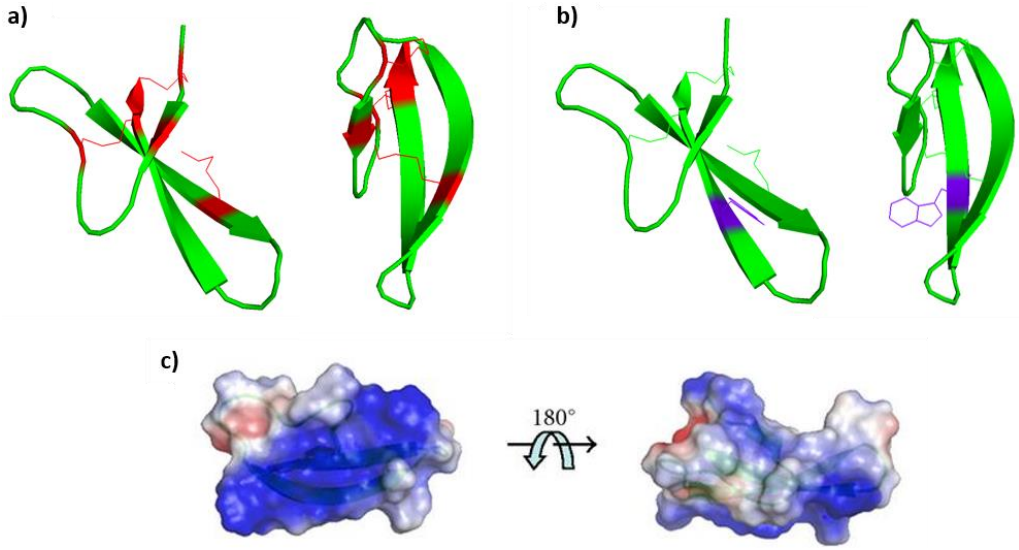

Figure 5.2 Two different orientation views of the structure of the HNP1 defensin. The β-sheets are structures are indicated by flat ribbons and arrows. a) Cys disulfide bridges highlighted in red. b) Trp highlighted in purple. c) Density electrostatic surface map of HNP-1 defensin: the positive charges (Arg residues) are shown in blue and the negative charge (Glu residue) in red. Reproduced with permission from ref.[11] Copyright © 2011.

In this chapter, we aim to evaluate the influence of the HNP1 defensin on supported lipid bilayers (SLBs) with different composition, representing simplified models including lipids found in both mammalian and bacterial membranes. We used atomic force microscopy (AFM) and AFM-base force spectroscopy (AFM-FS) to characterize the changes on the

morphology and the mechanical properties of the bilayers. In addition, we complemented the study by using X-ray reflectometry (XRR) to determine the electronic structure before and upon the addition of the peptide.

5.2. Experimental

Materials. The HNP1 peptide [ACYCRIPACIAGERRYGTCIYQGRLWAFCC] was purchased from Eurogenec (Belgium) and used without further purification. 1,2-dioleoyl-*sn*-glycero-3-phosphocholine (DOPC), 1,2-dipalmitoyl-*sn*-glycero-3-phosphoCholine (DPPC), 1,2-dioleoyl-*sn*-glycero-3-phosphoethanolamine (DOPE), 1,2- dioleoyl-*sn*-glycero-3-phospho-(1'-*rac*-glycerol) (DOPG) and 1,2-dipalmitoyl-*sn*-glycero-3-phospho-(1'-*rac*-glycerol) (DPPG) were purchased from Sigma-Aldrich (St. Louis, MO). All the buffer solutions were prepared with ultrapure water (Milli-Q reverse osmosis system, 18.2 mΩ·cm resistivity) and filtered before use with an inorganic membrane filter (0.22 μm pore size Whatman International Ltd, England, UK).

Sample preparation. The different lipids were individually dissolved in chloroform:methanol (v:v 3:1) to give a final concentration of 3 mM. Aliquots of each phospholipid were poured into a falcon tube, evaporating then the solvent to dryness under nitrogen flow in order to achieve a thin film spread on the walls of the tube. The dried lipid films were then hydrated with buffer solution (150 mM NaCl, 20 mM $MgCl_2$, 20 mM 4-(2-hydroxyethyl)-1-piperazineethanesulfonic acid (HEPES), pH 7.4), previously heated above the transition temperature (T_m) of the phospholipid, until a final total concentration of 0.5 mM. The falcon tubes were later subjected to cycles of vortex mixing and heating to *ca.* 60 ºC. The vesicles suspensions were placed in an ultrasounds bath for 30 min to finally obtain unilamellar vesicles.[13-15]

Supported lipid bilayers (SLBs) were obtained by the vesicles fusion method.[14, 16, 17] The vesicles suspensions were deposited onto the corresponding substrate depending on the experimental technique and incubated for 30 min at 70 ºC. Afterwards, the samples were rinsed several times with buffer solution (150 mM NaCl, 20 mM HEPES, pH 7.4)[18],* to avoid unfused vesicles, always keeping the substrates hydrated. The buffer solution covering the SLB was then replaced with the same buffer but containing the HNP1 defensin (10 and 15 μM). For the UV microscopy measurements, after incubating the defensin for 1 h, the samples were rinsed again several times to avoid background signal from the peptide in solution.

For the AFM experiments, circular mica surfaces (Ted Pella, Redding, CA) were used as support for the SLBs. In the case of XRR acquisitions, we employed 5 x 5 mm^2 square Si

* In this chapter the rinsing as well as the experiments were performed with the usual buffer but without $MgCl_2$ to prevent the loss of the peptide activity due to Mg^{2+}.

substrates (CrysTec) with orientation (100) ± 5º, polished (r.m.s. > 0.3 nm) and 275 µm thickness with its native oxide. They were cleaned with piranha solution (7:3 H_2SO_4:H_2O_2 (30%)) and then exposed to plasma (Expanded Plasma Cleaner PDC-002, Harrick Scientific Corporation) at high RF power level for 4 min to activate the hydrophilic bonding of the Si surfaces. For the UV microscopy measurements, a thin freshly cleaved mica substrate (~ 10 µm thick) attached to a Teflon ring was used.

Atomic force microscopy (AFM) and AFM-based force spectroscopy (AFM-FS). AFM images were performed using an MFP-3D AFM (Asylum Research, Santa Barbara, CA). All AFM images were acquired in AC mode at room temperature (*RT*) under liquid conditions (buffer solution) using V-shaped Si_3N_4 cantilevers with sharp silicon tips and having a nominal spring constant of 0.35 $N \cdot m^{-1}$ and a nominal tip radius (r_{tip}) between 2 and 12 nm (SNL, Bruker AFM Probes, Camarillo, CA). The AFM-FS measurements were performed using V-shaped Si_3N_4 cantilevers with a nominal spring constant of 0.12 $N \cdot m^{-1}$, 0.24 $N \cdot m^{-1}$ or 0.35 $N \cdot m^{-1}$ and a nominal r_{tip} between 20 and 60 nm (DNP, Bruker AFM Probes, Camarillo, CA). After having measured the sensitivity of the piezo ($V \cdot m^{-1}$), the cantilever spring constants were individually calibrated by using the equipartition theorem (thermal noise routine).[19] Force-distance curves were recorded by approaching and retracting the AFM cantilever tip at different speeds and in the force map mode.[13, 16]

To evaluate the Young modulus (*E*) of the SLBs, the force-distance curves performed at 1 $\mu m \cdot s^{-1}$ with DNP tips were fitted using the Derjaguin-Muller-Toporov (DMT) model.[20] The DMT model defining the indentation of a plane (bilayer) with a sphere (AFM tip) is composed of two parts (equation 5.1).[21, 22] The first one is the attractive part, where the tip is out of contact with the sample ($z > z_0$), and it is based on an attractive force (F_{att}). The second part corresponds to the repulsion, where the tip is already in contact with the sample ($z < z_0$), and it is described with the Hertz model contribution and a constant adhesion force (F_{adh}). In equation 5.1 the DMT model is expressed:†

$$F_{DMT} = \begin{cases} -|F_{att}(z)|, & z > z_0 \\ \frac{4}{3}\frac{\sqrt{r_{tip}} \cdot E}{(1-\nu^2)}\sqrt{(z_0 - z)^3} - |F_{adh}|, & z < z_0 \end{cases} \qquad \text{(equation 5.1)}$$

being z_0 the position of the tip-sample contact and ν the Poisson ratio (assumed as 0.5). In our case, the region fitted was the first tip-SLB contact up to indentations shorter than 1 nm. Knowing that the nominal r_{tip} for DNP tips ranges from 20 to 60 nm, we used r_{tip} as 40 nm to estimate *E*.

† It is important to consider that the DMT model can be written as in equation 5.1 since $E_{tip} >> E_{sample}$.

XR reflectometry (XRR). The XRR acquisitions were conducted at the soft interfaces and coherent scattering beamline (ID10) of the ESRF, the European Synchrotron, in Grenoble (France).‡ The beam energy was 30 keV, corresponding to a wavelength of 0.413 Å. The beam was focused at the sample position to a final size of 250 µm x 10 µm (horizontal x vertical).

The XRR intensities were measured over a range of angles by tilting the sample stage. The XRR data was treated employing the GenX software and modeling the interface with a four-slabs model,[23] after normalizing§ and performing the background subtraction** to the XRR curves. This model includes the upper phospholipid headgroups (H_{upp}), the hydrocarbon tails, the bottom phospholipid headgroups (H_{bot}) and a SiO_2 layer. A schematic representation of an ideal scattering length density (SLD) profile obtained by fitting an XRR curve of an SLB using the 4-slabs model shown in figure 5.3. Being dependent on the coverage characterizing each sample, the slabs defining the bilayer were then free

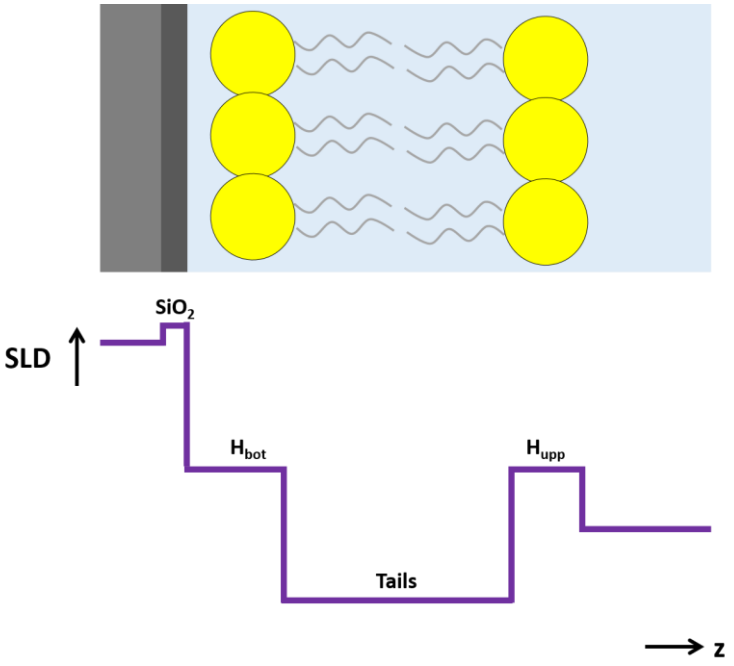

Figure 5.3 Schematic representation of an SLB section under liquid environment and an ideal SLD profile obtained by fitting an XRR curve from a bilayer using the 4-slabs model.

‡ The XR experiments were performed in the official synchrotron beamtime SC-4337 at ID10 beamline of the ESRF.
§ The normalization factor is given by the intensity of the direct XR beam at a fixed vertical position in absence of sample tilt.
** The background subtraction was performed by subtracting the XRR curves with another XRR curve acquired in the off-specular region (the intensity is collected at an angle that is asymmetric compared to the incident one, see introduction chapter for further details).

parameters to fit in the model, without imposing any symmetric condition for the electronic density or the roughness between H_{upp} and H_{bot}. All the XRR curves were fitted from $Q_{perpendicular}$ (Q_{perp}) = 0.1 $Å^{-1}$ because the beam footprint was larger than the size of the sample.

UV microscopy.†† UV microscopy images were obtained with a UVEX microscope (JAN Scientific, USA) equipped with 15X and 40X magnification objectives. In the UV microscope the sample is illuminated (exposition for 1 second) in an inversed configuration and the fluorescence is collected by the objective above the sample in an epifluorescence geometry. The use of a thin mica disk (~ 10 μm thick, obtained through careful manual cleavage with tweezers) glued on a Teflon ring permits the excitation light to be transmitted through mica and reach the membranes supported onto the outer mica surface. Before acquiring the UV fluorescence data, the samples were imaged by AFM to confirm the presence of bilayer. The UV fluorescence images were treated using the Gwyddyon software, by plotting the intensity pixel distribution comparing the membranes before and after incubation with the peptide (figure 5.4).

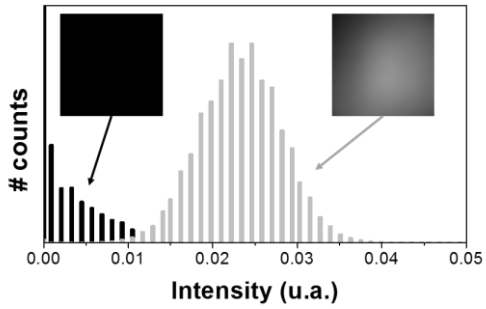

Figure 5.4 UV fluorescence intensity pixel distribution from images of an SLB before and after incubating the HNP1 defensin in 150 mM NaCl, 20 mM HEPES (pH 7.4) buffer solution and at *RT*.

5.3. Results and discussions

5.3.1. HNP1 defensin and phosphocholine (PC) bilayers

We evaluated the effect of the HNP1 defensin on pure DOPC and DPPC bilayers, major components found in mammalian membranes. Having a common headgroup, the difference between these phospholipids is the length of the tails as well as the number of unsaturation, leading to a different SLB phase state at *RT*.‡‡

First, to check if the peptide stayed in/on the membrane, we tested the UV fluorescence acquired before and after the peptide incubation (figure 5.4 and 5.5). These measurements

†† The measurements were performed at the Institut de Génomique Fonctionelle (IGF) in Montpellier, France.
‡‡DOPC 18:1 (T_m = -17 ºC, fluid state at *RT*) and DPPC 16:0 (T_m = 41 ºC, gel state at *RT*).

were possible thanks to the photophysical properties of Trp, which is the main determinant of the HNP1 defensin fluorescence. The peptide exhibits intrinsic fluorescence at 350 nm thanks to its Trp residue.[12, 24] As expected, we obtained a negligible signal for the pure PC membranes, while a clear intensity peak appears when the HNP1 defensin was incubated with the membrane, confirming its presence at the membrane level (figure 5.5).

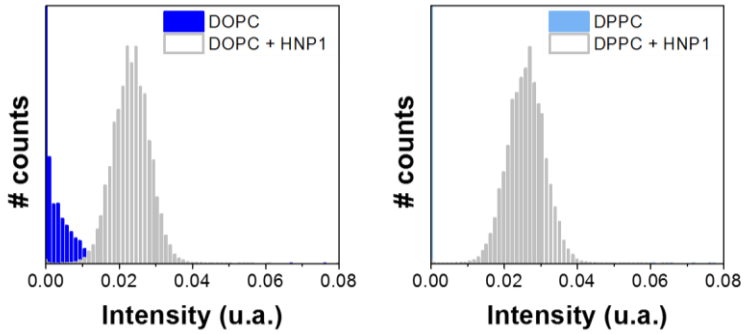

Figure 5.5 UV fluorescence intensity pixel distribution from DOPC and DPPC SLBs images before and after inserting the HNP1 defensin in 150 mM NaCl, 20 mM HEPES (pH 7.4) buffer solution and at *RT*.

5.3.1.1. HNP1 on DOPC SLBs.

We first assessed the morphology of DOPC SLBs, acquiring consecutive AFM images from the pure DOPC bilayer and after the addition of the HNP1 defensin (figure 5.6). We always performed a control experiment by inserting buffer solution instead of the one containing HNP1, to compare with the possible changes produced by the peptide. While no changes in the DOPC topography seemed to occur when performing the control experiment (figure 5.6(a)), the appearance of holes was observed approximately 45 min after the addition of the HNP1 (figure 5.6(b)). The small holes remained in the topography of the bilayer even after scanning the same region for more than 2 h. When leaving the sample with the peptide overnight, we still detected the presence of these holes, always after scanning the image for a couple times. Holes created in fluid-like phospholipid bilayers like DOPC at *RT* are expected to heal very fast. However, this did not happen after incubation of the HNP1, suggesting that the peptide was stabilizing the holes, probably generated by the AFM tip while imaging.

From the force-separation curves obtained by AFM-FS, information about the nanomechanical properties of the bilayers were evaluated. We performed the breakthrough force (F_b) characterization as well as on the Young modulus E, evaluated with equation 5.1, of the SLBs (figure 5.7(a)), assessing the nanomechanical stability and the stiffness of the SLBs, respectively. F_b appears as a discontinuity in the force-separation curve when approaching tip and bilayer, representing the maximum force the bilayer can stand before it is ruptured by the tip.[16, 25] We also explored the dependence of the mean F_b with the

approaching tip velocity by means of dynamic force spectroscopy (DFS).[§§] In addition, *E* was obtained from fitting the slope of the approaching curve in the first tip-SLB contact region using the DMT model,[20] frequently used for SLBs.[26]

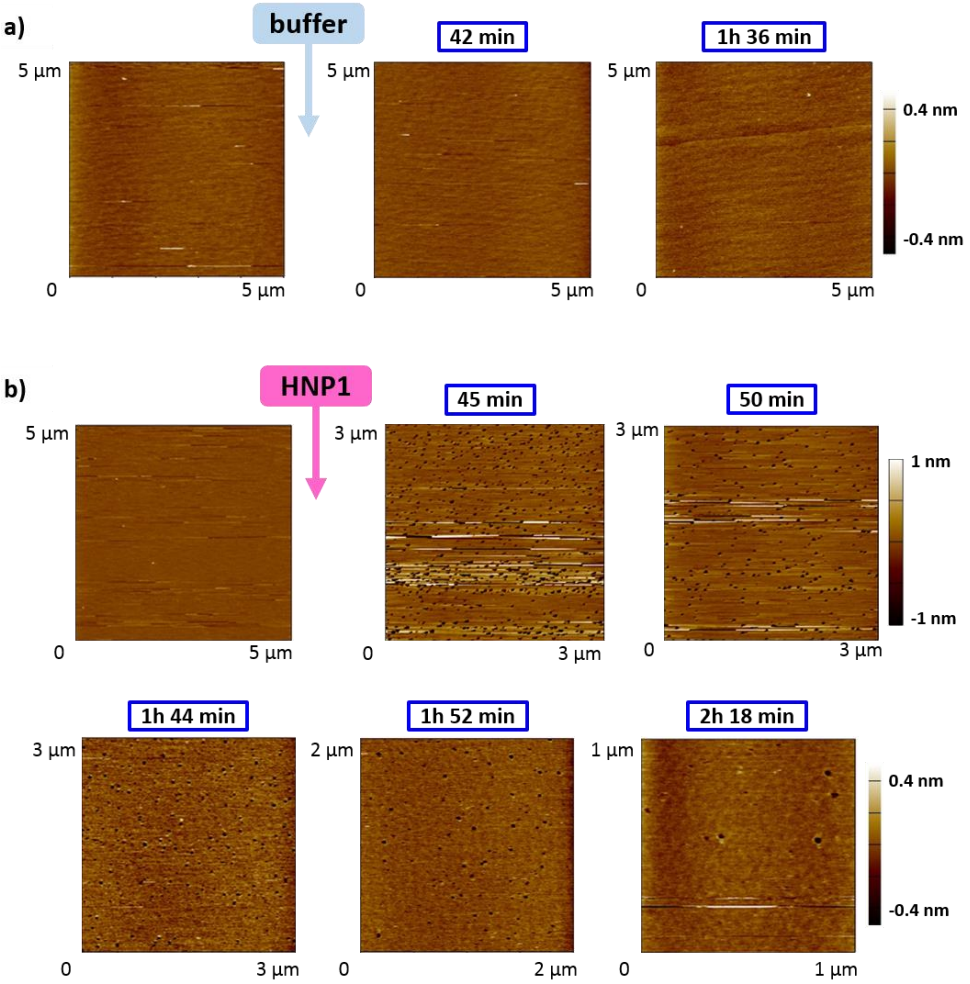

Figure 5.6 AC AFM topographical images of DOPC SLBs deposited on mica with time: a) Inserting buffer as a control. b) Inserting the HNP1 defensin. The experiments were performed in 150 mM NaCl, 20 mM HEPES (pH 7.4) buffer solution and at *RT*.

Before and after incubating the HNP1 defensin, we collected AFM-FS on DOPC SLBs at different velocities, ranging from 0.5 µm·s^{-1} and 3 µm·s^{-1} (figure 5.7(b)). No significance increase in F_b (from 5.7 nN to 8.1 nN) with the velocity was observed, as expected for the fluid-like SLBs. Besides, there was no relevant difference comparing the pure SLB with the

[§§] See chapter 2 for further details.

one containing the peptide. Concerning the Young modulus, we found that *E* decreased upon the insertion of the HNP1 from 168 ± 42 MPa to 113 ± 21 MPa, as shown in figure 5.7(c), suggesting a softer membrane.

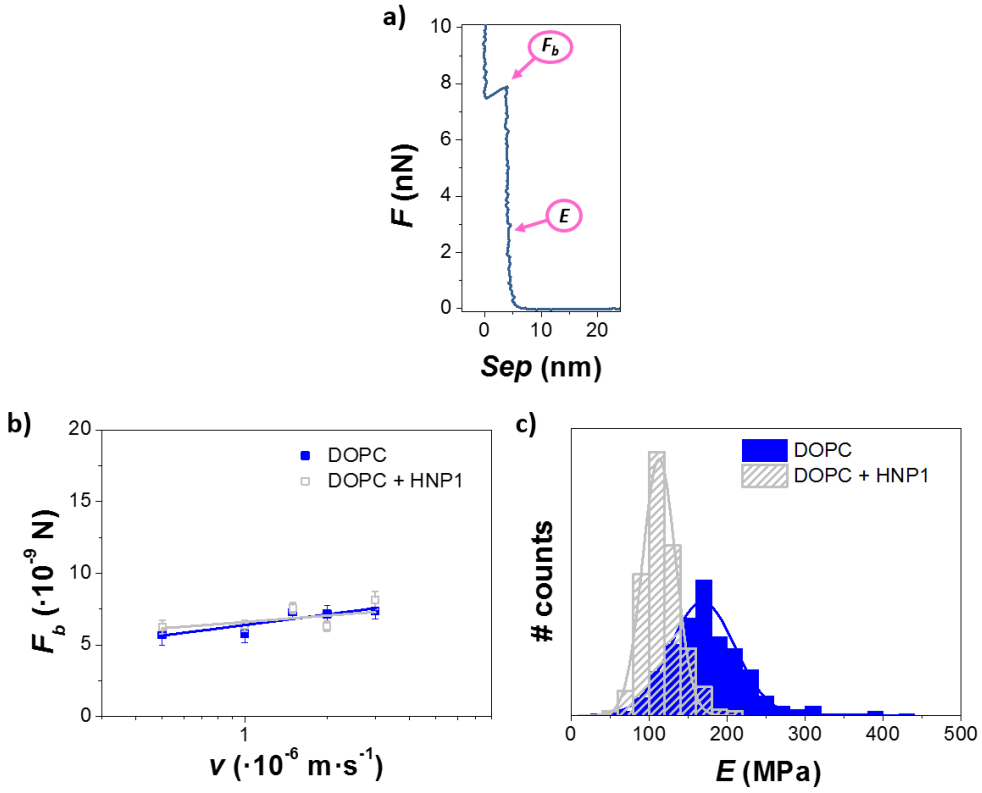

Figure 5.7 a) Approaching force-separation curve of a fluid-like DOPC SLB showing the F_b discontinuity and the contact region used to get *E* from fitting with the DMT model. b) F_b *vs*. tip velocity. c) Young modulus *E* distribution. The experiments were performed on DOPC SLBs deposited on mica before and after inserting the HNP1 defensin in 150 mM NaCl, 20 mM HEPES (pH 7.4) buffer solution and at *RT*.

XRR measurements allow to collect information on the electronic vertical structure of the SLB. The resultant SLD profiles obtained after fitting XRR curves from different regions of the SLB (figure 5.8(a) and (b)) with a 4-slabs model showed mainly an increase of the electronic density of the phospholipid tails upon the insertion of the HNP1 defensin, as well as a decrease of the upper heads density. This evidenced an increment of the disorder of the upper leaflet, and so a roughness enhancement, that can be related to the appearance of holes (or eventually a coverage decrease) on the bilayer, as observed on the AFM topographies (figure 5.6(b)). The first SLD (figure 5.8(a)) also suggests membrane thinning of few angstroms, small difference that could not be corroborated from the AFM-FS data.

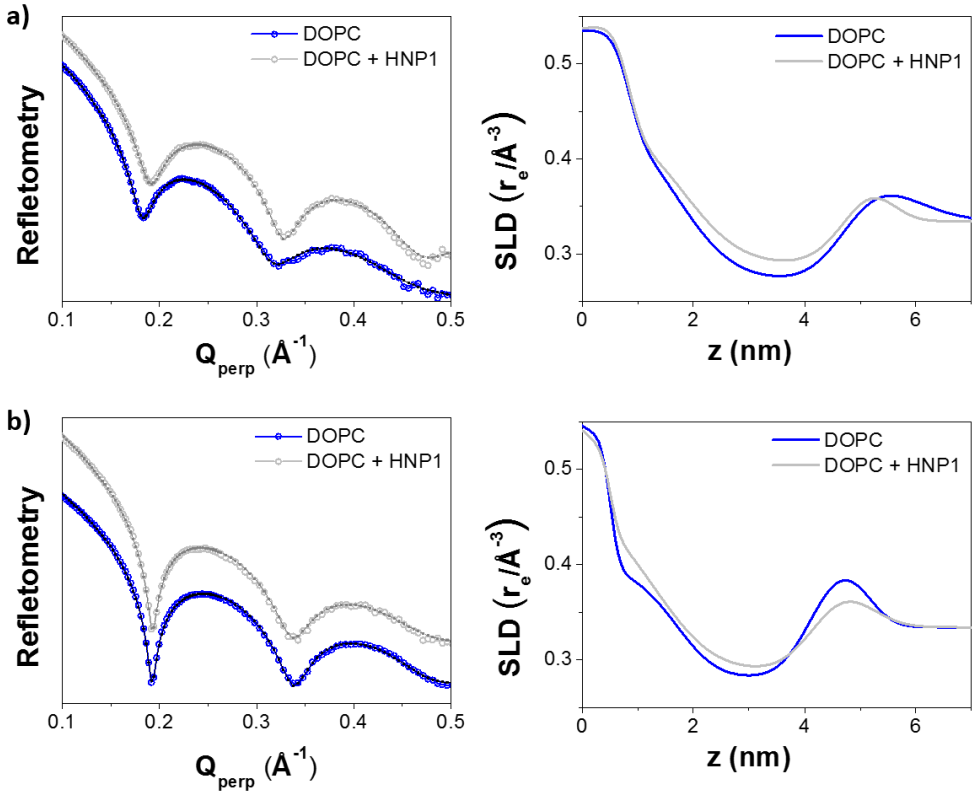

Figure 5.8 XRR reflectometry curves (shifted for better clarity) acquired and SLD profiles obtained from different areas (a and b) of a DOPC bilayer supported on Si before and after adding the HNP1 defensin, in 150 mM NaCl, 20 mM HEPES (pH 7.4) buffer solution and at *RT*.

5.3.1.2. HNP1 on DPPC SLBs.

We performed the same experiments onto DPPC bilayers. From the AFM topographical images (figure 5.9(a)), we mainly observed small dots on top of the DPPC SLB that appear approximately one hour after the peptide insertion. Interestingly, we obtained a similar timescale as for when the defensin has been incubated on DOPC, even though the resultant effect to the bilayer is different.

However, when performing AFM-FS experiments, the F_b significantly increased upon the addition of the HNP1 defensin (figure 5.9(b)), giving values of about 10 nN higher than for the pure DPPC bilayer (from 25.1 nN to 35.8 nN when the tip velocity was 1 $\mu m \cdot s^{-1}$). Moreover, the DFS measurements performed at different velocities ranging from 0.5 $\mu m \cdot s^{-1}$ and 5 $\mu m \cdot s^{-1}$ showed a clear increase of the mean F_b with the velocity of the AFM tip: from 25.1 nN to 37.3 nN for the pure DPPC SLB, and from 34.4 nN to 42.7 nN for the bilayer with the peptide (figure 5.9(b)). This trend allows to calculate the activation energy at zero F_b,

giving values of 10.2 k_BT and 15.8 k_BT for the DPPC bilayer before and after incubating the defensin.

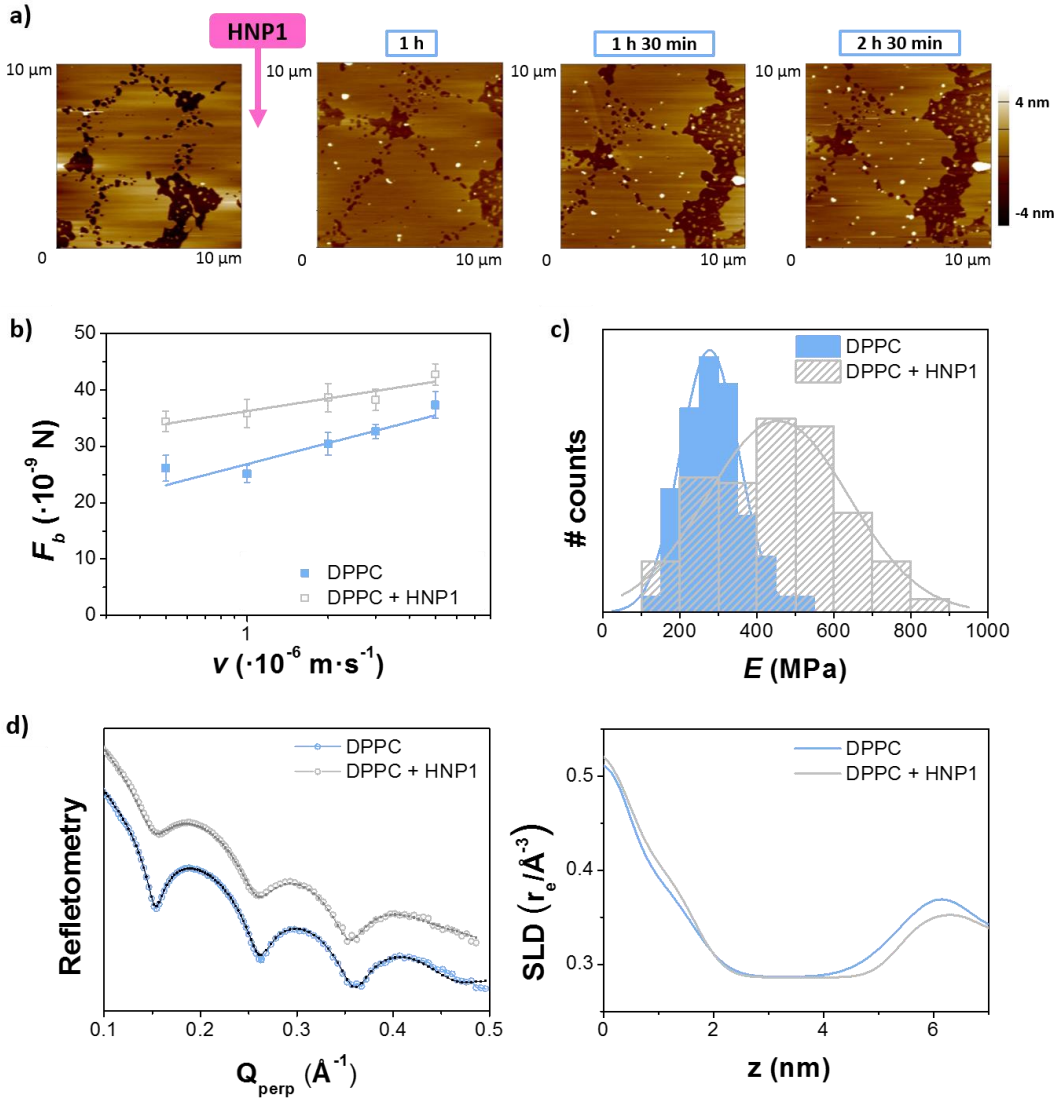

Figure 5.9 AFM, AFM-FS and XR experiments performed on DPPC SLBs deposited on mica before and after inserting the HNP1 defensin in 150 mM NaCl, 20 mM HEPES (pH 7.4) buffer solution and at *RT*. a) AC AFM topographical images with time. b) F_b *vs*. tip velocity. c) Young modulus E distribution. d) XRR reflectometry curves (shifted for better clarity) and SLD profiles.

When evaluating the Young modulus with the DMT model (figure 5.9(c)), we obtained an E of 277 ± 77 MPa for the pure DPPC SLB. Upon the addition of the peptide, a broader distribution shifted to higher E values is obtained, centred at 455 ± 184 MPa. This goes along

with the increment of the mechanical stability of the DPPC bilayer when containing the peptide.

From the XRR (figure 5.9(d)), an electronic density decrease on the heads from the upper leaflet was evidenced, suggesting that the peptide localizes preferably on the upper leaflet of the bilayer, inserted between the heads of the DPPC system. In addition, we observed a small increase of the membrane thickness.

Comparing the PC SLBs, we obtained a softer membrane together with appearance of holes due to the HNP1 defensin for the DOPC bilayer (figure 5.6 and 5.7), whereas the peptide significantly increased the mechanical stability when located on the DPPC SLBs (figure 5.9(a-c)). In accordance, XRR results suggested that the peptide was preferentially located in the upper leaflet, including heads and tails, of DOPC bilayers, but mainly between the upper heads of DPPC SLBs (figure 5.8 and 5.9(d)).

It is important to mention that the Young modulus values obtained in both PC bilayers are higher than the ones reported in literature.[26] This could be due to an underestimation of r_{tip}, to fitting the indentation for a too longer region or because of the influence of the substrate stiffness, leading to an overestimation of E. However, our interest was on evaluating the rigidity changes of the bilayer before and upon the insertion of the HNP1 defensin, giving rise to consider the resultant E values in relative terms.

5.3.2. HNP1 defensin and phosphoethanolamine (PE):phosphatidylglycerol (PG) bilayers

The major phospholipid species contained into bacterial membranes are PEs, PGs and cardiolipin (CL). Here, we evaluated the effect of the HNP1 defensin on model membranes composed of PEs and PGs. We first characterized pure DOPE SLBs, and we later mixed DOPE with DOPG or DPPG.[***]

We tested the UV fluorescence before and after the addition of the peptide to the buffer on the SLB, for the DOPE bilayer and the bilayer composed of DOPE:DOPG (25:75 molar ratio). In both cases (figure 5.10), we obtained a negligible signal for the pure phospholipid membranes and a clear intensity peak when the HNP1 defensin was present, confirming its presence on the SLBs.

5.3.2.1. HNP1 on DOPE SLBs.

From the AFM topographical images (figure 5.11(a)), we could not determine a significant effect of the HNP1 defensin to the DOPE morphology. There was evidence of peptide deposited into the mica surface not covered with bilayer, as well as few small dots

[***] DOPE 18:1 (T_m = -16 ºC, fluid state at *RT*), DOPG 18:1 (T_m = -18 ºC, fluid state at *RT*) and DPPG 16:0 (T_m = 41 ºC, gel state at *RT*).

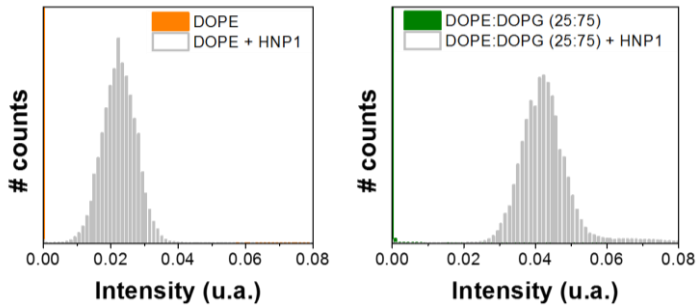

Figure 5.10 UV fluorescence intensity pixel distribution from DOPE and DOPE:DOPG (25:75 molar ratio) SLBs images before and after inserting the HNP1 defensin in 150 mM NaCl, 20 mM HEPES (pH 7.4) buffer solution and at *RT*.

that might be due to the HNP1 attached to the borders of the SLB patches. However, comparing the thickness of these topographies we could detect a thinning of the bilayer of about 0.5 nm when the membrane contained the peptide.

As expected for a fluid-like bilayer (see DOPC in section 5.3.1.1), DFS measurements performed in a range of velocities from 0.5 $\mu m \cdot s^{-1}$ to 3 $\mu m \cdot s^{-1}$ did not show a clear dependence of the mean F_b with the tip velocity (figure 5.11(b)). In addition, the trend of the bilayer containing the HNP1 defensin (from 6.4 nN to 7.0 nN) was similar to the pure DOPE (from 5.8 nN to 7.0 nN) SLB, suggesting no great influence on the lateral packing of the membrane. However, the Young modulus E (figure 5.11(c)), slightly decreased when the DOPE SLB contained the peptide from 129 ± 47 MPa to 97 ± 35 MPa.

From XRR (figure 5.11(d)), we clearly observed a thinning of the DOPE bilayer of about 0.5 nm when the peptide was inserted, in accordance with the difference in thickness noticed by AFM. In addition, we observed that the HNP1 defensin generally affected the headgroups of the DOPE SLB, with a consequent enhanced disorder.

5.3.2.2. HNP1 on DOPE:DOPG and DOPE:DPPG SLBs.

We then replaced 75 mol % of the DOPE content for PG phospholipids: DOPG, which has the same tails structure as DOPE but the PG headgroup, and DPPG, having two carbons less in the tails and no unsaturation.

The mixture DOPE:DOPG (25:75 molar ratio) forms a homogeneous fluid SLB, as observed in the first topographical image in figure 5.12(a). When the HNP1 defensin was incubated, no significant changes were observed on the AFM topographical images (figure 5.12(a)), and most of the peptide seemed to be located onto the mica surface. However, small dots on top of the bilayer seemed to appear occasionally, although this effect was not very reproducible.

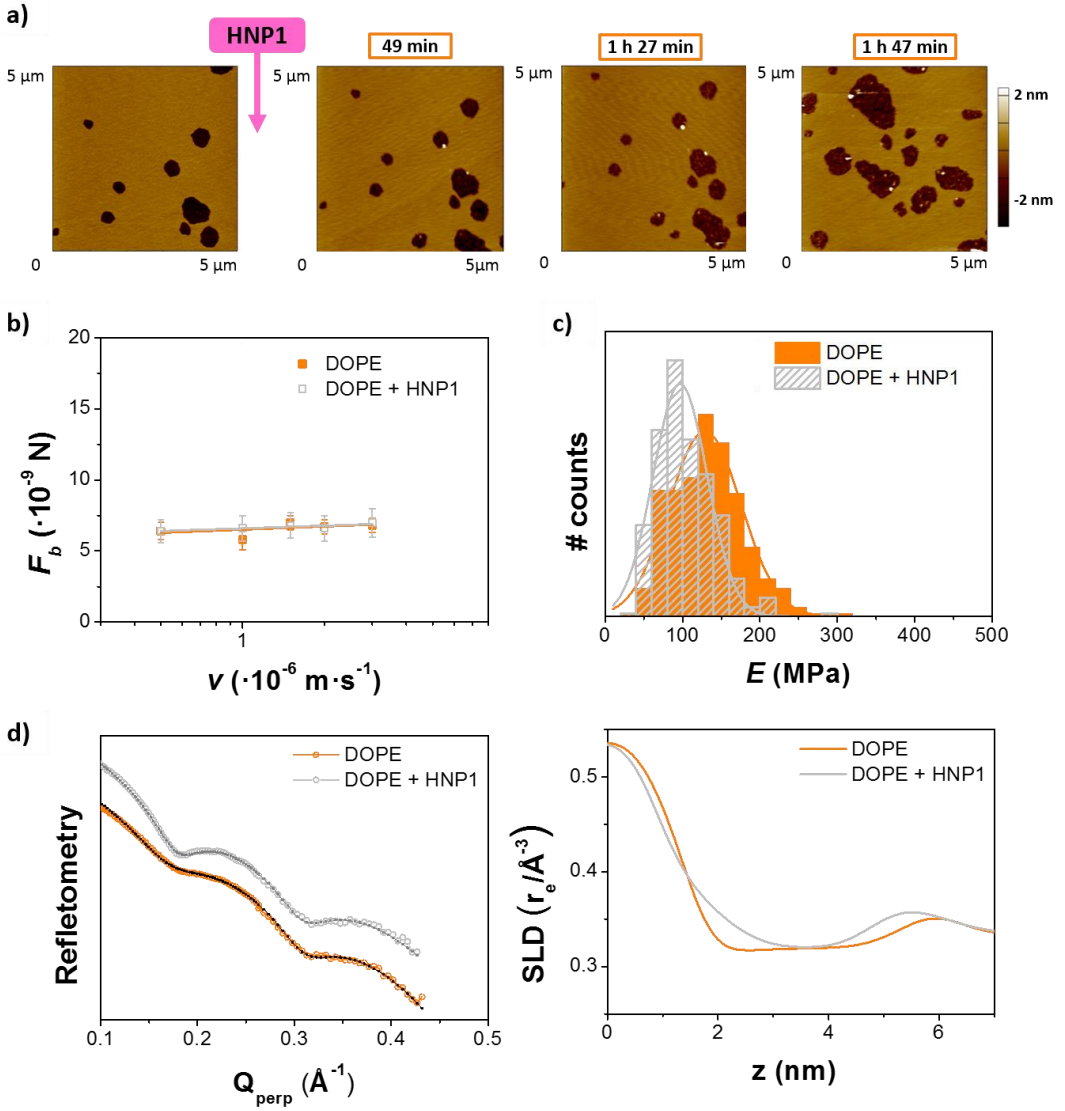

Figure 5.11 AFM, AFM-FS and XR experiments performed on DOPE SLBs deposited on mica before and after inserting the HNP1 defensin in 150 mM NaCl, 20 mM HEPES (pH 7.4) buffer solution and at *RT*. a) AC AFM topographical images with time. b) F_b *vs.* tip velocity. c) Young modulus *E* distribution. d) XRR reflectometry curves (shifted for better clarity) and SLD profiles.

AS observed for the previous fluid-like SLBs, F_b values did not show a dependence with the velocity ranging from 0.5 µm·s^{-1} and 3 µm·s^{-1} (figure 5.12(b)). In addition, no relevant effect onto the mechanics of the DOPE:DOPG system (from 5.3 nN to 6.8 nN) occurred upon the peptide incubation (from 5.5 nN to 5.8 nN). In this case, the evaluation of the bilayers

elasticity lead to a slight decrease in the Young modulus from pure to defensin-containing bilayer (figure 5.12(c)), with values of *E* of 93 ± 26 MPa and 82 ± 27 MPa, respectively.

However, as for DOPE SLBs, a thinning of the DOPE:DOPG bilayer was observed by means of the resultant SLD profiles obtained from the XRR curves (figure 5.12(d)). Nevertheless, in

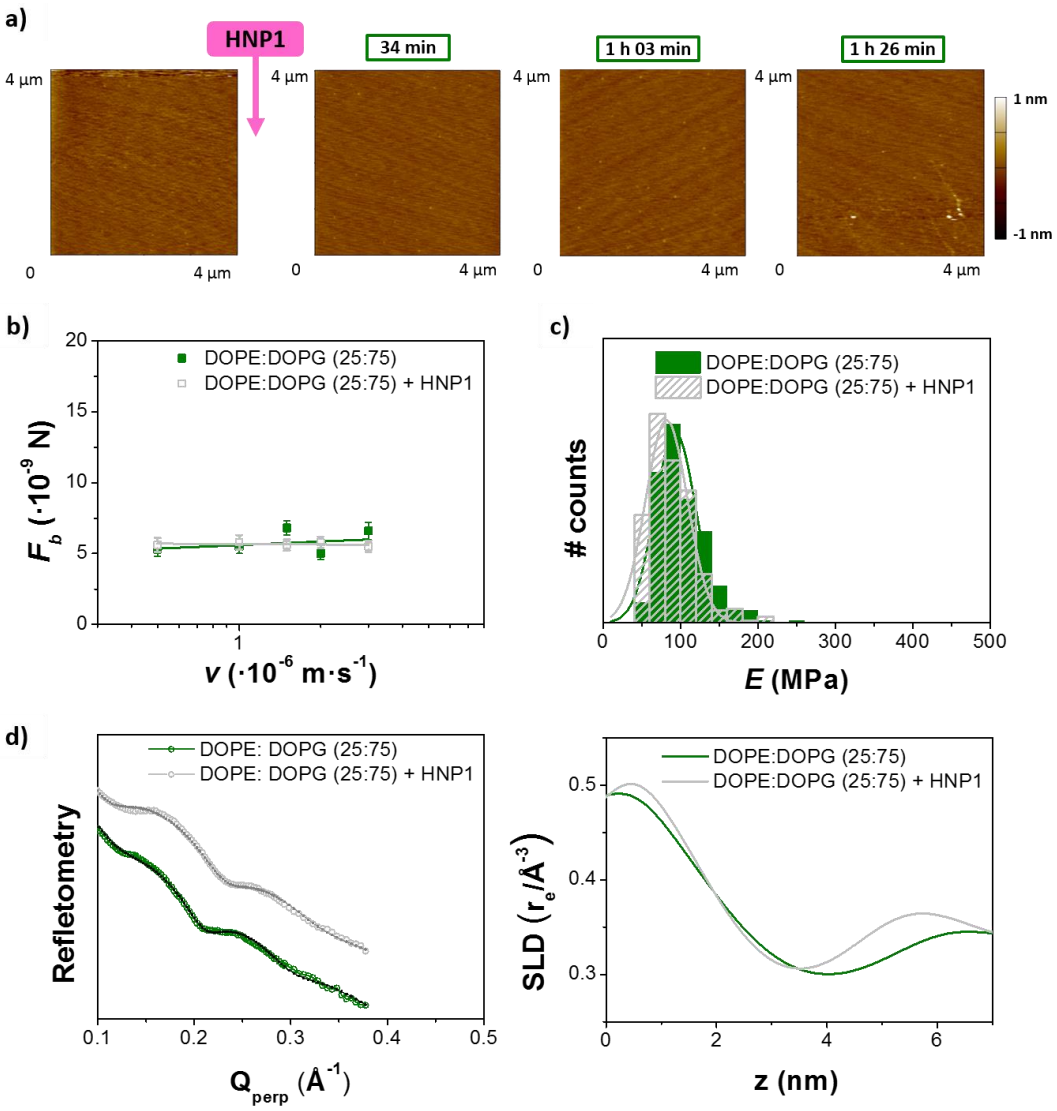

Figure 5.12 AFM, AFM-FS and XR experiments performed on DOPE:DOPG (25:75 molar ratio) SLBs deposited on mica before and after inserting the HNP1 defensin in 150 mM NaCl, 20 mM HEPES (pH 7.4) buffer solution and at *RT*. a) AC AFM topographical images with time. b) F_b *vs*. tip velocity. c) Young modulus *E* distribution. d) XRR reflectometry curves (shifted for better clarity) and SLD profiles.

this case the thinning was not observed by AFM. In addition, an increase of the electronic density for both upper heads and tails was determined.

Being DPPG a gel-state phospholipid, the mixture DOPE:DPPG (25:75 molar ratio) formed bilayers segregated into different domains, with a difference in height of about 0.8 nm (first image of figure 5.14(a)). When inserting the peptide, we observed the reduction in size of the higher domain and in some cases even disappearance, as demonstrated in the consecutive images displayed in figure 5.14(a). Changing the scanning region (figure 5.14(b)), we could also detect an increase of the membrane roughness. In this case, we did not perform XRR measurements due to the phase segregation in the bilayer, that makes more complicated the treatment of the XRR data, since a simple 4-slabs model does not describe properly a film with two domains.

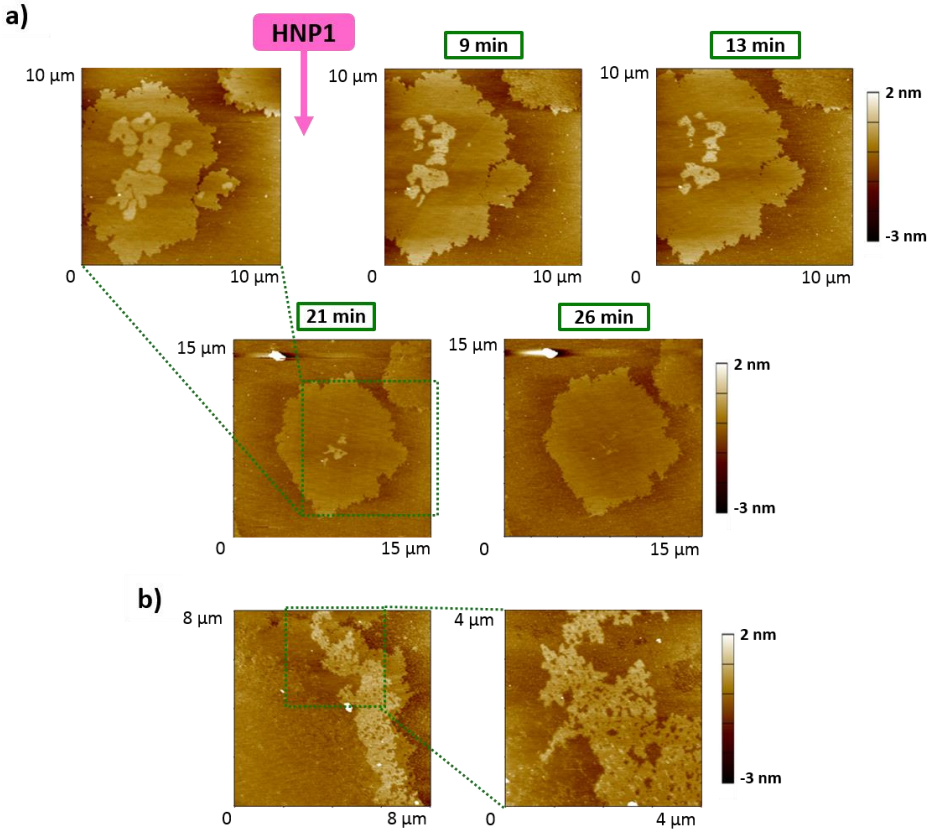

Figure 5.13 AC AFM topographical images performed on DOPE:DPPG (25:75 molar ratio) SLBs deposited on mica in 150 mM NaCl, 20 mM HEPES (pH 7.4) buffer solution and at *RT*. a) Images with time before and after inserting the HNP1 defensin. b) Images from a different region when the HNP1 defensin is already inserted.

5.4. Conclusions

We systematically evaluated the influence of the HNP1 defensin on the structural and nanomechanical properties of bilayers with different composition, including neutral and charged phospholipids. In general, we confirmed that the peptide affects PC SLBs more specifically and localized, whereas it disrupts the overall PE and PE:PG SLBs. It is important to point out that small peptides like HNP1 produce only subtle effects on the variables measured in this chapter, that are difficult to analyze and interpret.

From the AFM and XRR results in PC bilayers, we observed an increase on F_b leading to an enhanced packing of the upper DPPC headgroups, whereas the peptide seems to insert into the DOPC SLBs without causing a significant change on the bilayer resistance to be punctured by the AFM tip. On the other hand, this difference is detected in the DOPC elasticity when the HNP1 is inside the membrane, which facilitates the reorientation of the membrane by stabilizing the holes when rupturing with the AFM tip.

Concerning PE and PE:PG bilayers, we determined that the HNP1 defensin mostly produced a significant thinning of the membrane composed of pure DOPE observed from both AFM and XRR methodologies. When replacing 75 mol % of DOPE content for PG, no relevant changes were observed in the fluid-like mixture (DOPE:DOPG), whereas the peptide seems to dissolve the higher domains rich in DPPG as well as increase the roughness of the overall SLBs.

To better understand the influence observed on the studied model membranes upon the incubation of HNP1 defensins, we think that complementary experiments may be done. For instance, FRAP (fluorescence recovery after photobleaching) or FCS (fluorescence correlation spectroscopy) measurements could provide information about the effect of the peptide on the diffusion of the lipid molecules into the membrane, refining the elasticity results obtained in this work. In addition, high resolution AFM imaging could offer new insights on the membrane remodeling changes and local small defects produced by the peptide.

5.5. References

1. G. Fujii, M. E. Selsted and D. Eisenberg, *Protein Sci.*, 1993, **2**, 1301-1312.
2. A. A. Stromstedt, L. Ringstad, A. Schmidtchen and M. Malmsten, *Curr. Opin. Colloid In.*, 2010, **15**, 467-478.
3. T. Ganz, *Nat. Rev. Immunol.*, 2003, **3**, 710-720.
4. B. Ericksen, Z. Wu, W. Lu and R. I. Lehrer, *Antimicrob. Agents Ch.*, 2005, **49**, 269-275.
5. P. M. Silva, S. Goncalves and N. C. Santos, *Front. Microbiol.*, 2014, **5**, 97.
6. G. Wei, M. Pazgier, E. de Leeuw, M. Rajabi, J. Li, G. Zou, G. Jung, W. Yuan, W.-Y. Lu, R. I. Lehrer and W. Lu, *J. Biol. Chem.*, 2010, **285**, 16275-16285.
7. Y. Zhang, W. Lu and M. Hong, *Biochemistry-US*, 2010, **49**, 9770-9782.
8. A. Giuliani, G. Pirri and S. F. Nicoletto, *Cent. Eur. J. Biol.*, 2007, **2**, 1-33.
9. M. N. Melo, R. Ferre and M. A. R. B. Castanho, *Nat. Rev. Microbiol.*, 2009, **7**, 245.

10. K. A. Brogden, *Nat. Rev. Microbiol.*, 2005, **3**, 238.
11. E. Balducci, A. Bonucci, M. Picchianti, R. Pogni and E. Talluri, *Int. J. Pept.*, 2011, **2011**, 594723.
12. S. Goncalves, J. Abade, A. Teixeira and N. C. Santos, *Biopolymers*, 2012, **98**, 313-321.
13. B. Gumi-Audenis, L. Costa, F. Carla, F. Comin, F. Sanz and M. I. Giannotti, *Membranes*, 2016, **6**.
14. P. E. Milhiet, V. Vié, M.-C. Giocondi and C. Le Grimellec, *Single Mol.*, 2001, **2**, 109-112.
15. B. Gumi-Audenis, F. Sanz and M. I. Giannotti, *Soft Matter*, 2015, **11**, 5447-5454.
16. L. Redondo-Morata, M. I. Giannotti and F. Sanz, *Mol. Membr. Biol.*, 2014, **31**, 17-28.
17. L. Redondo-Morata, M. I. Giannotti and F. Sanz, *Langmuir*, 2012, **28**, 12851-12860.
18. J. Varkey and R. Nagaraj, *Antimicrob. Agents Ch.*, 2005, **49**, 4561-4566.
19. R. Proksch, T. E. Schaffer, J. P. Cleveland, R. C. Callahan and M. B. Viani, *Nanotechnology*, 2004, **15**, 1344-1350.
20. B. V. Derjaguin, V. M. Muller and Y. P. Toporov, *J. Colloid Int. Sci.*, 1975, **53**, 314-326.
21. J. N. Israelachvili, "Intermolecular and Surface Forces", *Academic Press*, London, 2nd edn., 1992.
22. X. Shi and Y.-P. Zhao, *J. Adhes. Sci. Technol.*, 2004, **18**, 55-68.
23. C. E. Miller, J. Majewski and T. L. Kuhl, *Colloid. Surface. A*, 2006, **284-285**, 434-439.
24. A. Bonucci, E. Balducci, M. Martinelli and R. Pogni, *Biophys. Chem.*, 2014, **190**, 32-40.
25. S. Garcia-Manyes and F. Sanz, *BBA - Biomembranes*, 2010, **1798**, 741-749.
26. L. Picas, F. Rico and S. Scheuring, *Biophys. J.*, 2012, **102**, L1-L3.

Chapter 6

In-plane molecular organization of hydrated single lipid bilayers: DPPC:Cholesterol*

Understanding the physical properties of the cholesterol (Chol)-phospholipid systems is essential to get a better knowledge on the function of each membrane constituent. The structural characterization of a single lipid membrane at the solid-liquid interface by grazing incidence X-ray diffraction (GIXD) is an extremely challenging task, and the only few successful GIXD studies on single hydrated bilayers reported so far have been using complex setups. In this chapter, we present a novel, simple and user-friendly setup that allows for straightforward GIXD characterization of hydrated individual supported lipid bilayers (SLBs). The setup is designed to minimize the scattering from the liquid and to allow the detection of the extremely weak diffracted signal of the lipid bilayer, enabling the differentiation of coexisting domains in phase-segregated membranes. We record GIXD patterns on 1,2-dipalmitoyl-*sn*-glycero-3-phosphoCholine (DPPC) single SLBs with various contents of Chol to help on further understanding the binary system that has been subject of a large number of studies with structural data.

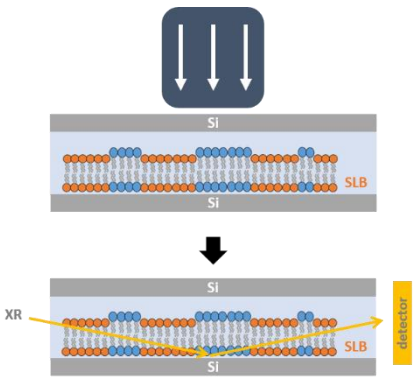

* This work has been published: B. Gumí-Audenis, L. Costa, L. Redondo-Morata, P. E. Milhiet, F. Sanz, R. Felici, M. I. Giannotti and F. Carlà. *Nanoscale,* 2018, **10**, 87 - 92.
This work has been performed in collaboration with ID03 beamline at the ESRF, the European Synchrotron, in Grenoble (France) and with the Centre de Biochimie Structurale (CBS) in Montpellier (France).

6.1. Introduction

Lateral segregation of membrane components into domains of lipids enriched in cholesterol (Chol) and sphingolipids are involved in many membrane functions, for instance signaling, remodeling and trafficking.[1, 2] Chol is responsible for controlling the phase behavior as well as the lipid organization, regulating the fluidity and permeability of the membrane while increasing its mechanical resistance.[3-8] It is then of high interest to understand the physical properties of the Chol-phospholipid systems at the molecular level to get a better knowledge on the role of Chol in the membrane.

Membranes comprising phospholipids and Chol have been extensively studied, including simplified models based on two components, as exposed for instance in chapter 2. In particular, temperature-composition phase diagrams of DPPC (1,2-dipalmitoyl-*sn*-glycero-3-phosphoCholine):Chol have been defined using different techniques such as nuclear magnetic resonance (NMR), differential scanning calorimetry (DSC), or neutron and X-ray (XR) scattering.[9-14] Yet, discrepancies on the determination of a complete phase diagram able to cover all compositional space and temperature range still remain. Atomic force microscopy (AFM) and AFM-based force spectroscopy (AFM-FS) have provided insights into the thermal transition of DPPC:Chol supported lipid bilayers (SLBs) at the nanometric scale, defining the coexistence of different domains, and facilitating the linking between the Chol content and the lateral organization of the membrane.[3, 4, 15, 16]

Information about phase segregation in lipid bilayers can also be gathered by XR scattering techniques, providing significantly higher resolution compared, for instance, to AFM. XR are very powerful, noninvasive techniques that have been extensively used in lipid bilayer studies to probe length scales ranging from angstroms to microns. A large part of the XR based experiments have been focused so far on determining the electronic vertical structure of lipid monolayers, bilayers and stacks of bilayers (or multi-bilayers), at the liquid/air and solid/liquid interfaces, respectively, by means of XR reflectivity (XRR), which is a well-established technique in the field.[17-21]

Knowledge about the lateral in-plane structure of such systems can be instead obtained by grazing incidence (GI) XR diffraction (GIXD). Nevertheless, the requirement of the wetting preservation to guarantee the stability of biological membranes at the solid/liquid interface makes the in-plane structural characterization of a single lipid bilayer extremely challenging. The presence of a wetting layer makes necessary the use of high energy XR to increase the transmission through the liquid, resulting in a weaker signal from the organic molecules.[19] Additionally, the scattering generated by the liquid environment increases the background level complicating the detection of the signal scattered by the bilayer structure. For this reason, most of the GIXD reported structural information relative to lipid membranes has been extrapolated from experiments conducted on multi-bilayers[22, 23] or on monolayers at the water/air interface.[24] However, lipid monolayers do not represent the

lamellar nature of the membrane, and the physico-chemical properties of multi-bilayers also differ from those of single bilayers. Because of their ease of formation and single lamellar arrangement, SLBs are among the most common model for biomembranes,[25] in addition to large and giant unilamellar vesicles (LUVs and GUVs, respectively). In this context, only few successful GIXD studies on single hydrated bilayers have been reported, achieving their goals by using complex methods and controlling humidity conditions during the XR measurements.[26-28].

In this chapter, we propose a novel user-friendly setup based on a thin layer cell configuration that allows the successful acquisition of GIXD data on hydrated SLBs. We characterize DPPC:Chol bilayers at different Chol composition to help on further understanding the binary system that has been subject of a large number of studies with structural data.[9-12] Finally, we present the morphologies of DPPC:Chol SLBs by means of AFM and fluorescence microscopy images, to complement the GIXD results.

6.2. Experimental

Materials. 1,2-dipalmitoyl-*sn*-glycero-3-phosphoCholine (DPPC) and cholesterol (Chol), were purchased from Sigma-Aldrich (St. Louis, MO). 1,2-dipalmitoyl-*sn*-glycero-3-phosphoethanolamine-*N*-(lissamine rhodamine B sulfonyl) (DPPE-Rh) was purchased from Avanti Polar Lipids Inc. All experiments were performed in buffer solution of 150 mM NaCl, 20 mM $MgCl_2$, 20 mM HEPES (4-(2-hydroxyethyl)-1-piperazineethanesulfonic acid) (pH 7.4) prepared with ultrapure water (Milli-Q reverse osmosis system, 18.2 mΩ·cm resistivity) and filtered before use with an inorganic membrane filter (0.22 μm pore size Whatman International Ltd, England, UK).

Sample preparation. DPPC and Chol were individually dissolved in chloroform:methanol (v:v 3:1) to give a final concentration of 3 mM. Aliquots of DPPC and Chol solutions were mixed and poured into a falcon tube to obtain the different compositions of DPPC:Chol (100:0, 90:10, 80:20, 60:40 and 50:50 molar ratio). For the fluorescence microscopy measurements, the DPPC:Chol solutions were subsequently mixed with DPPE-Rh to obtain a final DPPE-Rh molar fraction of 0.05 %. Next, the solvent was evaporated to dryness under nitrogen flow in order to achieve a thin film spread on the walls of the tube. The dried lipids films were then hydrated with buffer solution, previously heated above the transition temperature (T_m) of the phospholipid, until a final total concentration of 0.5 mM. The falcon tubes were later subjected to cycles of vortex mixing and heating to *ca.* 60ºC. The vesicles suspensions were placed in an ultrasounds bath for 30 min to finally obtain unilamellar vesicles.[3, 29, 30] For the fluorescence microscopy measurements, the vesicles were also extruded with a polycarbonate membrane filter (100 nm pore size, Whatman) purchased from Avanti Lipids.

Si wafers with orientation (100) ± 5º, polished (r.m.s. > 0.3 nm), 275 μm thickness with its native oxide and 50.8 mm diameter were purchased from CrysTec. Square substrates with approximate dimensions of 5 x 5 mm^2 were obtained from the wafers and cleaned with piranha solution (7:3 H_2SO_4:H_2O_2 (30%)). Then, they were exposed to plasma (Expanded Plasma Cleaner PDC-002, Harrick Scientific Corporation) at high RF power level for 4 min to activate the hydrophilic bonding of the Si surfaces. The circular glass coverslips (3.5 cm diameter, 180 μm thick, purchased from WilcoWells) were cleaned with piranha solution and exposed at high RF for 15 min.

Supported lipid bilayers (SLBs) were obtained by vesicles fusion method.[4, 29, 31] The vesicles suspensions were deposited onto the corresponding substrate depending on the experimental technique and incubated for 30 min at 70 ºC. Afterwards, the samples were rinsed several times with buffer solution to avoid unfused vesicles, always keeping the substrates hydrated.

Grazing incidence XR diffraction (GIXD). The GIXD experiments were conducted at the surface diffraction beamline (ID03) of the ESRF, the European Synchrotron, in Grenoble (France).† The beam energy was 24 keV, corresponding to a wavelength of 0.516 Å. The beam was focused at the sample position to a final size of 54 x 500 μm^2 (FWHM, vertical × horizontal). A MAXIPIX detector was installed on the diffractometer arm, 900 mm from the sample, with slits located 50 mm from the sample and with an opening of 4 mm x 2 mm (vertical x horizontal) to reduce the background level. The samples were directly mounted on the diffractometer stage. All the measurements were performed at room temperature (*RT*) in GI geometry with 0.05º incidence angle. To limit the exposure time and thus the possible beam damage during GIXD measurements, the scans were recorded by collecting a limited number of images in each scan. Typically, a scan from $2\theta = 4$ to $2\theta = 8$ was covered with 20 points. Raw data reduction was performed using the BINoculars code.[32] The data reported were obtained by summing the intensities of each pixel along the direction parallel to $Q_{perpendicular}$ (Q_{perp}) in an interval of Q_{perp} ranging from 0.02 to 0.15.

Atomic force microscopy (AFM). AFM images were performed using an MFP-3D AFM (Asylum Research, Santa Barbara, CA). All AFM images were acquired in AC mode at *RT* under liquid conditions (buffer solution) using V-shaped Si_3N_4 cantilevers with sharp silicon tips and having a nominal spring constant of 0.35 $N \cdot m^{-1}$ (SNL, Bruker AFM Probes, Camarillo, CA).

Fluorescence microscopy. Fluorescence microscopy images were obtained with a custom made inverted fluorescence microscope. We used an excitation wavelength of 525 nm and an emission filter centred at 605 nm (70 nm wide, CHROMA ET605/70).

† The XR experiments were performed in the following official synchrotron beamtimes at the ESRF: SC-4144 and IHSI-964 at ID03 beamline.

Fluorescence images were obtained with an externally-triggered iXon Ultra897 camera (Andor Technologies) with pulses of 100 ms period, resulting in an exposure time of 50 ms. Images were obtained by averaging over 20 single micrographs acquired in a row with ImageJ software. To reduce the background generated by the liquid environment, the Si substrate supporting the SLBs were turned upside down on top of a glass coverslip and imaged using of an inverted objective.

Correlative AFM-Fluorescence microscopy. We used an AFM-fluorescence microscope (Nanowizard 4 combined with fluorescence microscopy, JPK, Germany) to correlate the fluorescence image with the corresponding topographical information by AFM. All the measurements were performed at *RT* and under buffer conditions. The AFM images were acquired using V-shaped Si_3N_4 cantilevers with sharp silicon tips (SNL, Bruker AFM Probes, Camarillo, CA) and by means of quantitative imaging (QI) mode.

6.3. Results and discussions

6.3.1. Strategy of the setup

A schematic drawing of the setup used in this work is shown in figure 6.1(a). Hydrated SLBs were first prepared onto Si wafer substrates with orientation (100) by the vesicle rupture method (figure 6.1(a))[29, 31] and transferred onto the diffractometer stage with its surface covered by a droplet of buffer solution. The surface tilt, as well as its vertical position, was then aligned parallel to the incident XR beam by rocking the sample tilt while monitoring the reflected intensity (figure 6.1(b)-I). Once XR beam and surface were aligned, a second Si substrate was then positioned on top of the of the first Si wafer with its polished

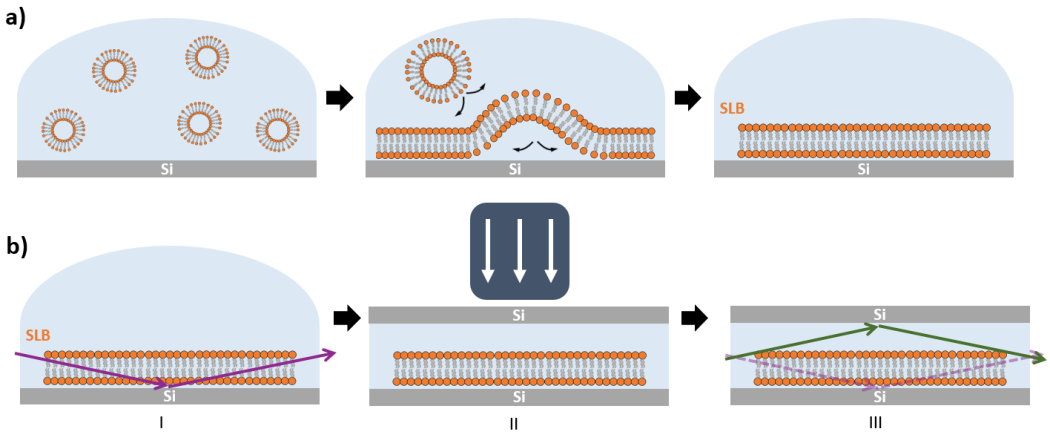

Figure 6.1 Schematics of the setup used. a) SLB deposition onto Si substrates via vesicle rupture method. b) Alignment of the sample with the XR beam and Si-SLB-Si configuration to perform the GIXD measurements.

surface facing the sample, and pressed against the sample with an external load (figure 6.1(b)-II). The liquid excess in the sample was spilled from the sides and carefully removed. This Si-SLB-Si arrangement allows the confinement of a thin layer of liquid between the sample and the flat Si surface. The lateral dimensions of the upper Si substrate were defined small enough to prevent the XR diffracted beam passing through this second Si before the detector, therefore avoiding any reflection or refraction (figure 6.1(b)-III).

The gap between the two Si substrates was estimated by measuring the transmitted intensity during a scan along the direction vertical to the sample surface (figure 6.2). It is worth noting that this method cannot be used for the exact determination of the gap size, because the value obtained in the transmission measure is a convolution of the gap width and XR beam size. The latter is too large to be used as a probe for an accurate estimation, but the measure still provides reliable information about the maximum value of the gap size. The peak corresponding to the gap between the Si wafers exposed in figure 6.2 has a width at the base of 50 μm which is comparable with the height of the incidence XR beam (54 μm). Considering the convolution between the XR beam and the gap size, we can conclude that, in the vertical scan, the sample is acting as a pinhole and the shape of the curve is in fact

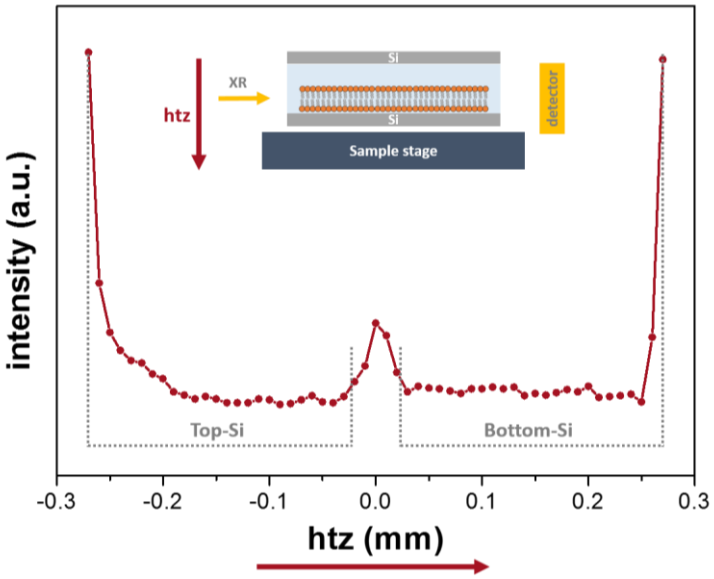

Figure 6.2 XR transmission scan along the direction vertical to the Si-SLB-Si sample surface (htz). The transmission of the Si wafers is lower than that of the buffer and the gap between the two Si wafers can be identified as a peak at the center of the plot. At the outer edges of the Si wafer the transmission increases again, as observed for the top-Si/air interface and the bottom-Si/sample stage gap on the left and right edges of the plot, respectively. The increase of the intensity at the Si/stage interface is due to the presence of an XR transparent adhesive tape used to fix the sample. The nominal thickness of the wafers is 275 μm.

determined by the XR beam size, while the gap between the two Si wafers must have a size considerably smaller than 50 μm, probably about few microns or less.

In this Si-SLB-Si configuration, the SLB is confined in a controlled geometry (figure 6.1(b)-III) and the thickness of the liquid layer is reduced enough to minimize the background signal generated by the liquid environment, allowing the detection of the diffracted signal of the bilayer. In figure 6.3 we can observe the effect of the liquid (buffer solution) on the GIXD background level. The presence of the buffer on a bare Si surface produces an increase of the background of about one order of magnitude compared to the Si/air interface (figure 6.3(a)). In this experimental configuration, it is basically impossible to detect any diffracted signal from an SLB, as observed in figure 6.3(b) (dark blue). However, when the second Si substrate is placed on top and pressed against the bottom Si-SLB system, the GIXD signal from the bilayer becomes visible (figure 6.3(b) light blue).

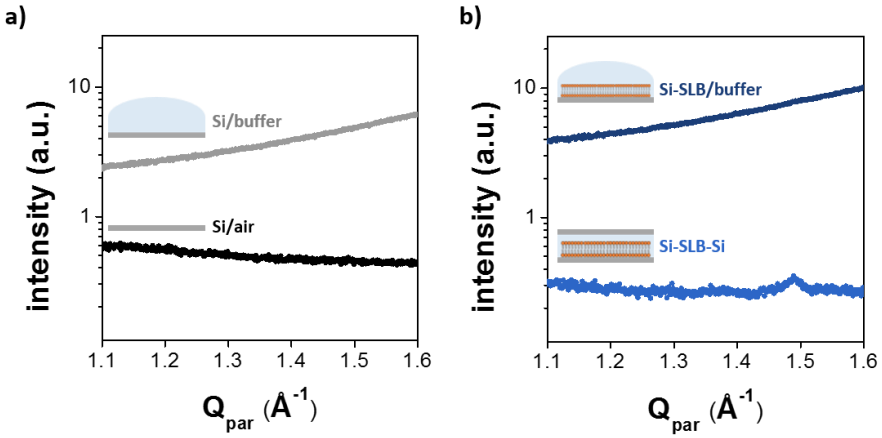

Figure 6.3 GIXD from: a) Si wafer without (black) and with (grey) buffer on the top. b) a DPPC SLB onto Si, in buffer solution, before (dark blue) and after (light blue) a second Si substrate was positioned on the top (Si-SLB-Si configuration). All measurements in buffer conditions were performed in 20 mM HEPES, 150 mM NaCl, 20 mM $MgCl_2$ buffer solution (pH 7.4) at *RT*.

It is worth to notice that, although the setup allows to access any $Q_{parallel}$ (Q_{par}) value, the access to high Q_{perp} values is limited by geometrical factors, such as the in-plane size of the two Si wafers (5 mm x 5 mm) and the distance between them (50 μm). Considering that the beam is hitting the system at the centre of the substrate, we can calculate that the maximum Q_{perp} accessible is ~ 0.19 $Å^{-1}$. This value could be probably augmented by increasing the distance between the wafers or reducing their size. The first option is not possible because it would lead to an increase of the thickness of the wetting layer and, thus, an increase in the background level. The reduction of the area of the wafers, for example by using rectangular samples with a shorter edge perpendicular to the direction of the beam, is a possibility that

could be explored in the future. However, there might be some issues related to the evaporation of the solution near the edge of the sample and the homogeneity of the sample in the region close to the edge.

6.3.2. GIXD on DPPC:Chol bilayers

Using this Si-SLB-Si configuration, we acquired GIXD patterns of single SLBs composed of DPPC and Chol at different molar ratios (DPPC:Chol: 100:0, 90:10, 80:20, 60:40 and 50:50) in 20 mM HEPES, 150 mM NaCl, 20 mM $MgCl_2$ buffer solution (pH 7.4) and at *RT*. All the GIXD measurements performed on the DPPC:Chol SLBs successfully revealed a 2D order, as exemplified in figure 6.4(a) for the DPPC:Chol 90:10 SLB. It is clearly visible that the diffracted intensity appears as two rods at Q_{par} 1.28 $Å^{-1}$ and 1.50 $Å^{-1}$ perpendicular to the substrate surface, indicating the 2D nature of the samples, that was verified by reflectometry. The XRR curve was performed without the upper Si wafer and with a buffer droplet on top, as in figure 6.1(b)-I.‡ In figure 6.4(b), we display an XRR curve of a pure DPPC SLB, that reveals a film thickness of 5.9 nm,§ comparable to a single gel-like state lipid bilayer,[3, 4] thus validating the absence of multi-bilayer structures.

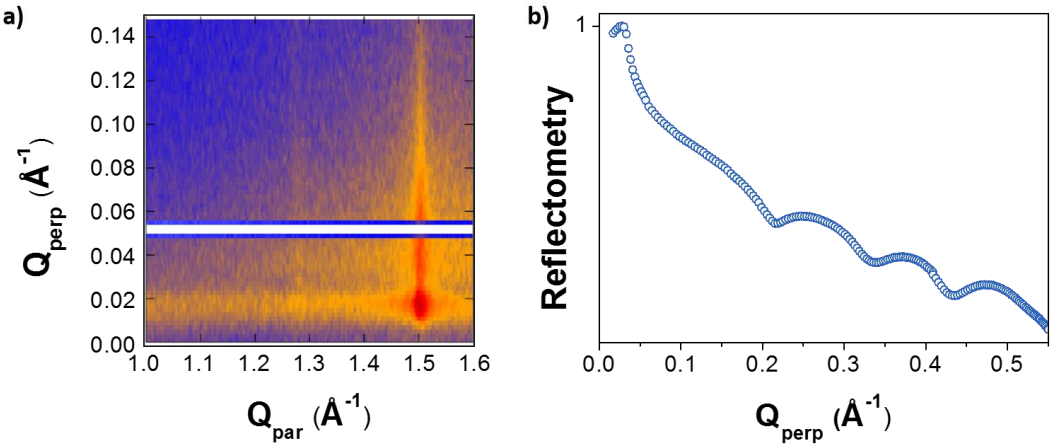

Figure 6.4 a) Diffracted intensity 2D contour plot for DPPC:Chol (90:10 molar ratio) SLB in Si-SLB-Si configuration. The white line parallel to Q_{par} originates from missing rows of pixels between the intersection of 2 chips of the area detector. b) XRR for DPPC SLB onto Si substrate. Both measurements were performed in 20 mM HEPES, 150 mM NaCl, 20 mM $MgCl_2$ buffer solution (pH 7.4) and at *RT*.

‡ For the acquisition of XRR scans, a set of attenuators was used to control the incident photon flux and limit the exposure of the sample to the XR.

§ The thickness of the bilayer was calculated from the XRR curve by measuring the Q_{perp} positions of two minimums and using the following expression:

$$thickness = \frac{2\pi}{\Delta Q_{perp}}$$

When integrated over Q_{perp}, the diffraction pattern obtained for pure DPPC SLBs presents one peak at Q_{par} = 1.50 $Å^{-1}$ (figure 6.5). Although the characterization method seems pretty robust and allows to determine correctly the position of the peaks along the Q_{par} direction, it is difficult to extract further information based on the intensity of the peaks. As matter of facts, the samples surface may not be perfectly homogeneous at the millimeter scale and this lack of homogeneity, originated by areas not covered by the SLB, influences the quality of the data and the intensities measured. In figure 6.6 a series of GIXD measures collected on a DPPC SLB by rotating the sample over an angle of 150 degrees in steps of 30 degrees is shown. While the intensity of the peak can vary significantly with the sample orientation, the single peak position in Q_{par} remains constant. This gives rise to the

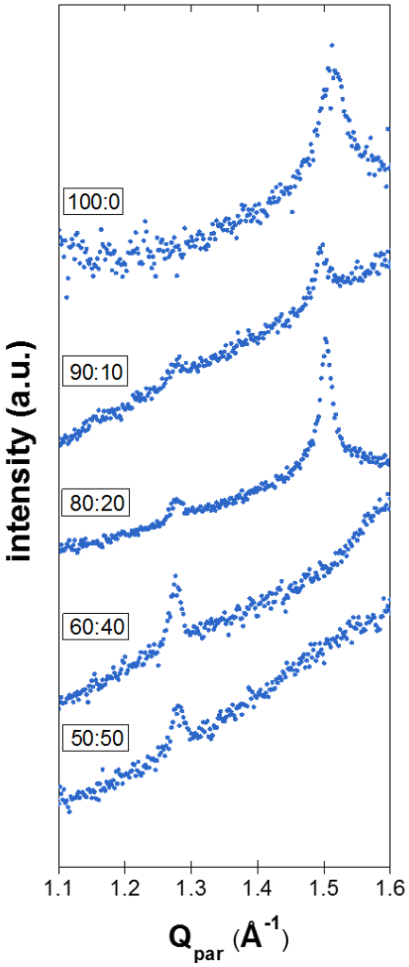

Figure 6.5 GIXD Q_{par} intensity (integrated over Q_{perp}) patterns from DPPC:Chol SLBs of 100:0, 90:10, 80:20, 60:40 and 50:50 molar ratios in Si-SLB-Si configuration, in 20 mM HEPES, 150 mM NaCl, 20 mM $MgCl_2$ buffer solution pH 7.4, at *RT*.

assumption of an hexagonal packing for the DPPC molecules on a Si-SLB in liquid conditions. In this context, a corresponding *d*-spacing of 0.48 nm was obtained.[33**]

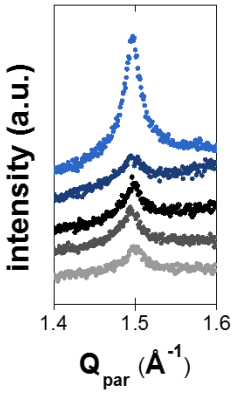

Figure 6.6 GIXD Q_{par} intensity (integrated over Q_{perp}) patterns from a pure DPPC SLB in Si-SLB-Si configuration, acquired over a rotation of 150 degrees in steps of 30 degrees, in 20 mM HEPES, 150 mM NaCl, 20 mM $MgCl_2$ buffer solution pH 7.4, at *RT*.

The molecular organization of DPPC has been reported by studying different DPPC configurations, *i.e.* monolayers at the liquid/air interface, or bilayers and stacks of bilayers at the solid/liquid interface. In general, both rectangular and hexagonal geometries have been assumed for DPPC packing. Some GIXD studies of pure DPPC monolayers at the liquid-air interface reported a rectangular geometry to define the packing, with values of 0.43 nm and 0.46 nm,[24, 27, 34] or a distorted hexagonal lattice with geometrical parameters between 0.51 and 0.50 nm depending on the lateral pressure.[35] Hexagonal packing for DPPC and DPPE SLBs in liquid environment has been identified using GIXD, with *d*-spacing of 0.50[35] and 0.48[28] nm, respectively, and using frequency modulation-AFM defining a lateral spacing of 0.49 nm.[36] The value extracted by the GIXD experiments in this work is then in good agreement with the literature.

The binary DPPC:Chol SLBs were also investigated for different compositions: 90:10, 80:20, 60:40 and 50:50 molar ratio. It is known that the Chol content in gel-like state membranes, such as DPPC SLBs at RT, determines the phase behavior into homogeneous or phase-segregated bilayers. In the presence of Chol, we identified a second peak at Q_{par} = 1.28 $Å^{-1}$ in the GIXD pattern for DPPC:Chol SLBs onto Si (figure 6.5). At low contents of Chol (10 and 20 mol %), this peak coexists with the one previously observed for pure DPPC SLBs, with no variation in the Q_{par} position within ± 0.02 $Å^{-1}$. Hence, considering two different

** The *d*-spacing for an hexagonal packing can be calculated using the following expression:

$$d = \frac{4\pi}{\sqrt{3} \cdot Q_{par}}$$

hexagonal packings, we obtain *d*-spacing of 0.57 and 0.48 nm from the Q_{par} values of 1.28 and 1.50 $Å^{-1}$, respectively. On the other hand, when Chol content is above 30 mol % (60:40 and 50:50 molar ratio), the GIXD patterns in figure 6.5 display only one peak: the peak corresponding to the DPPC-rich phase (high Q_{par}) is no longer visible, whereas the one at 1.28 $Å^{-1}$ (*d*-spacing of 0.57 nm) is still observable. These behaviors match with Chol intercalating between the DPPC molecules and increasing the average distance between DPPC moieties, in agreement with GIXD reports on DPPC:Chol monolayers at the liquid-air interface, that show an hexagonal packing displaying *d*-spacing values that depended on the amount of Chol, for more than 25 mol % Chol.[24]

Our observations are consistent with most phase diagrams for the binary mixture of DPPC:Chol,[9-12] where low contents of Chol up to 30 mol % lead to separation into two different phases that coexist at *RT*, and concentrations of Chol higher than 30 mol % appear to be a unique liquid ordered (l_o) phase at any temperature range studied. This condition has been also observed by means of temperature-controlled AFM on SLBs onto mica substrates, as well as with AFM-FS,[4] demonstrating an enhanced nanomechanical resistance of both the Chol-rich domains, for low Chol content bilayers, and the homogeneous l_o phase, for high Chol content bilayers. Such increase of nanomechanical resistance is associated to a strong lateral interaction mediated by Chol molecules placed between the DPPC ones, due to a highly stable structure with most probably an equimolar DPPC:Chol ratio. In addition, a fixed *d*-spacing, independent of Chol concentration, is also consistent with a well-defined interaction between DPPC and Chol, as suggested in the condensed complex model.[37]

6.3.3. AFM and fluorescence on DPPC:Chol bilayers

Although it is known that the underlying substrate may strongly affect the SLB order and the transition temperature range of the bilayer,[9, 38, 39] AFM and fluorescence microscopy measurements were used here to prove that the DPPC:Chol SLBs onto Si behave as observed on mica or in vesicles. AFM topographical images of the DPPC:Chol SLBs at the different Chol concentrations are shown in figure 6.7. From the pure DPPC SLB topography (100:0 molar ratio), a bilayer thickness of about 5 nm was determined from the section profile. This value is slightly lower than the one obtained by the XRR curve shown in figure 6.4(b) (5.9 nm), probably due to the membrane compression while scanning. On the other hand, fluorescence microscopy images of DPPC:Chol SLBs on Si, for 100:0, 90:10 and 60:40 molar ratio, are shown in figure 6.8, representing the different morphologies of the system.†† While the high roughness of the bare Si substrates (r.m.s. > 0.3 nm) makes difficult to detect the domains for the low Chol content bilayers (90:10 and 80:20 molar ratio) from the AFM topographies (figure 6.7), as they differ in height by ~0.2–0.3 nm, fluorescence images

†† The selected morphologies were: pure DPPC and DPPC:Chol 90:10 and 60:40, representative for bilayers with low and high Chol content, respectively.

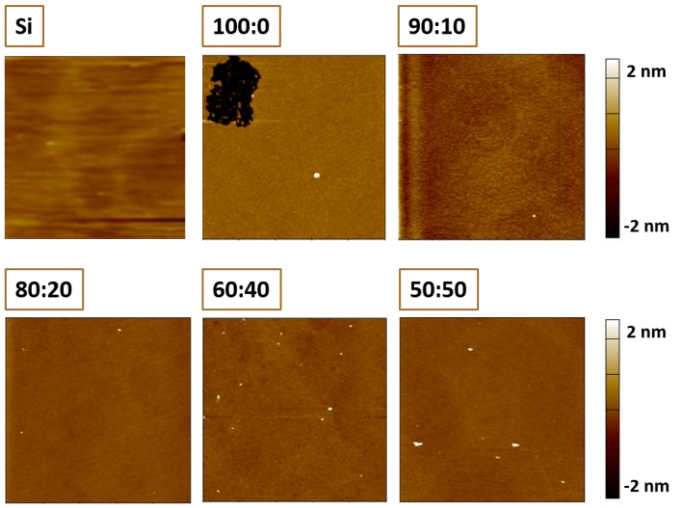

Figure 6.7 5 x 5 μm² AFM images from Si and DPPC:Chol SLBs (100:0, 90:10, 80:20, 60:40 and 50:50 molar ratios) on Si, in 20 mM HEPES, 150 mM NaCl, 20 mM $MgCl_2$ buffer solution pH 7.4, at *RT*.

evidenced domains on the DPPC:Chol 90:10 SLBs (figure 6.8). Conversely, both AFM and fluorescence measurements of DPPC:Chol SLBs with high concentrations of Chol (60:40 and 50:50 molar ratio) on Si substrates show homogeneous membranes (figures 6.7 and 6.8).

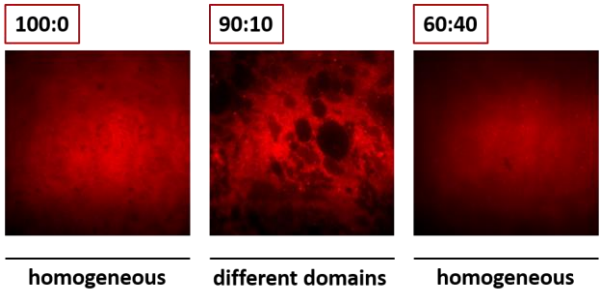

Figure 6.8 55 x 55 μm² fluorescence images (512 x 512 pixels) from DPPC:Chol mixed with 0.05 % DPPE-Rhodamine SLBs on Si, of 100:0, 90:10, and 60:40 molar ratios, in 20 mM HEPES, 150 mM NaCl, 20 mM $MgCl_2$ buffer solution pH 7.4, at *RT*.

Fluorescence is a good technique to visualize phase segregated membranes because of DPPE-Rh different partition into each phase. In order to determine the Chol-rich and Chol-poor areas, correlative AFM-fluorescence characterization of DPPC:Chol 90:10 SLBs onto a glass substrate allowed to perceive the coexistence of domains, by superposing low fluorescence intensity regions with higher topographical domains (figure 6.9), previously identified as enriched in Chol.[4] This coexistence, being observed in figure 6.8 and as an

equivalence in figure 6.9, corroborates that the phase behavior of DPPC:Chol SLBs on mica,[4, 8] vesicles in suspension,[7, 40] and described in many reported phase diagrams[9-12] also occurs on Si-SLBs. It consequently validates the GIXD data presented in figure 6.5.

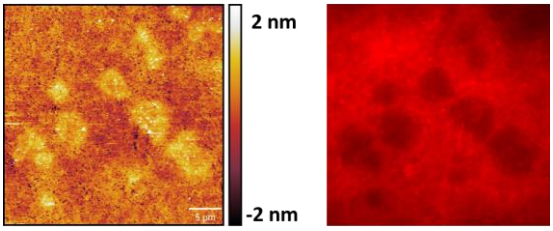

Figure 6.9 Correlative AFM-fluorescence images (35 x 35 µm²) of DPPC:Chol 90:10 SLBs on glass, in 20 mM HEPES, 150 mM NaCl, 20 mM $MgCl_2$ buffer solution pH 7.4, at *RT*.

6.4. Conclusions

The structural characterization of a single lipid membrane at the solid/liquid interface by GIXD is extremely challenging, and only few successful GIXD studies on single hydrated lipid bilayers have been reported,[26-28] where complex setups and controlled humidity conditions are required during the measurements. In this chapter, we presented a novel, simple and user-friendly setup that permits for straightforward GIXD characterization of hydrated individual SLBs, based on a Si-SLB-Si configuration. This allows reducing the scattering from the liquid and revealing the extremely weak diffracted signal of the lipid bilayer, capable of detecting different coexisting domains in phase-segregated membranes.

We recorded GIXD patterns on DPPC bilayers supported onto Si substrates with various contents of Chol, providing information about their structure at the submolecular level. Two *d*-spacing values were assigned to DPPC intermolecular distance of each phase in those phase-segregated bilayers (DPPC:Chol 90:10 and 80:20 molar ratios), while a single *d*-spacing value was obtained for homogeneous bilayers (DPPC and DPPC:Chol 60:40 and 50:50), in accordance to the phase diagram of this binary system.[4, 24, 36] The higher *d*-spacing corresponded to the Chol-enriched phase, where DPPC and Chol molecules may intercalate in a nearly stoichiometric ratio. This represents a reasonable scenario opening new avenues of research on the structure as well as dynamical processes of cell membranes in physiological environment.

6.5. References

1. G. van Meer, D. R. Voelker and G. W. Feigenson, *Nat. Rev. Mol. Cell Biol.*, 2008, **9**, 112-124.
2. D. Lingwood and K. Simons, *Science*, 2010, **327**, 46-50.
3. B. Gumi-Audenis, L. Costa, F. Carla, F. Comin, F. Sanz and M. I. Giannotti, *Membranes*, 2016, **6**.
4. L. Redondo-Morata, M. I. Giannotti and F. Sanz, *Langmuir*, 2012, **28**, 12851-12860.

5. T. Rog, M. Pasenkiewicz-Gierula, I. Vattulainen and M. Karttunen, *BBA-Biomembranes*, 2009, **1788**, 97-121.
6. W.-C. Hung, M.-T. Lee, F.-Y. Chen and H. W. Huang, *Biophys. J.*, 2007, **92**, 3960-3967.
7. J. J. Pan, S. Tristram-Nagle and J. F. Nagle, *Phys. Rev. E*, 2009, **80**.
8. P. E. Milhiet, M. C. Giocondi and C. Le Grimellec, *J. Biol. Chem.*, 2002, **277**, 875-878.
9. T. P. W. McMullen and R. N. McElhaney, *BBA-Biomembranes*, 1995, **1234**, 90-98.
10. S. Karmakar, V. A. Raghunathan and S. Mayor, *J. Phys. Condens. Matter*, 2005, **17**, S1177-S1182.
11. Y.-W. Chiang, A. J. Costa and J. H. Freed, *J. Phys. Chem. B*, 2007, **111**, 11260-11270.
12. D. Marsh, *BBA-Biomembranes*, 2010, **1798**, 688-699.
13. D. Marquardt, F. A. Heberle, J. D. Nickels, G. Pabst and J. Katsaras, *Soft Matter*, 2015, **11**, 9055-9072.
14. P. F. Almeida, *Biophys. J.*, 2011, **100**, 420-429.
15. S. Garcia-Manyes and F. Sanz, *BBA-Biomembranes*, 2010, **1798**, 741-749.
16. R. M. A. Sullan, J. K. Li, C. Hao, G. C. Walker and S. Zou, *Biophys. J.*, 2010, **99**, 507-516.
17. F. Evers, C. Jeworrek, K. Weise, M. Tolan and R. Winter, *Soft Matter*, 2012, **8**, 2170-2175.
18. B. Gumí-Audenis, F. Carlà, M. V. Vitorino, A. Panzarella, L. Porcar, M. Boilot, S. Guerber, P. Bernard, M. S. Rodrigues, F. Sanz, M. I. Giannotti and L. Costa, *J. Synchrotron Radiat.*, 2015, **22**, 1364–1371.
19. C. E. Miller, J. Majewski, T. Gog and T. L. Kuhl, *Phys. Rev. Lett.*, 2005, **94**.
20. E. Novakova, K. Giewekemeyer and T. Salditt, *Phys. Rev. E*, 2006, **74**.
21. J. Daillant, E. Bellet-Amalric, A. Braslau, T. Charitat, G. Fragneto, F. Graner, S. Mora, F. Rieutord and B. Stidder, *Proc. Natl. Acad. Sci. USA*, 2005, **102**, 11639-11644.
22. T. Salditt and G. Brotons, *Anal. Bioanal. Chem.*, 2004, **379**, 960-973.
23. M. A. Barrett, S. Zheng, L. A. Toppozini, R. J. Alsop, H. Dies, A. Wang, N. Jago, M. Moore and M. C. Rheinstadter, *Soft Matter*, 2013, **9**, 9342-9351.
24. A. Ivankin, I. Kuzmenko and D. Gidalevitz, *Phys. Rev. Lett.*, 2010, **104**, 108101.
25. E. T. Castellana and P. S. Cremer, *Surf. Sci. Rep.*, 2006, **61**, 429-444.
26. R. Ziblat, K. Kjaer, L. Leiserowitz and L. Addadi, *Angew. Chem. Int. Ed.*, 2009, **48**, 8958-8961.
27. R. Ziblat, L. Leiserowitz and L. Addadi, *J. Am. Chem. Soc.*, 2010, **132**, 9920-9927.
28. C. E. Miller, J. Majewski, E. B. Watkins, D. J. Mulder, T. Gog and T. L. Kuhl, *Phys. Rev. Lett.*, 2008, **100**, 058103.
29. P. E. Milhiet, V. Vié, M.-C. Giocondi and C. Le Grimellec, *Single Mol.*, 2001, **2**, 109-112.
30. B. Gumi-Audenis, F. Sanz and M. I. Giannotti, *Soft Matter*, 2015, **11**, 5447-5454.
31. L. Redondo-Morata, M. I. Giannotti and F. Sanz, *Mol. Membr. Biol.*, 2014, **31**, 17-28.
32. S. Roobol, W. Onderwaater, J. Drnec, R. Felici and J. Frenken, *J. Appl. Crystallogr.*, 2015, **48**, 1324-1329.
33. L. Costa, G. Li-Destri, N. H. Thomson, O. Konovalov and D. Pontoni, *Nano Lett.*, 2016, **16**, 5463-5468.
34. F. Neville, M. Cahuzac, O. Konovalov, Y. Ishitsuka, K. Y. C. Lee, I. Kuzmenko, G. M. Kale and D. Gidalevitz, *Biophys. J.*, 2006, **90**, 1275-1287.
35. E. B. Watkins, C. E. Miller, D. J. Mulder, T. L. Kuhl and J. Majewski, *Phys. Rev. Lett.*, 2009, **102**, 238101.
36. H. Asakawa and T. Fukuma, *Nanotechnology*, 2009, **20**.
37. H. M. McConnell and A. Radhakrishnan, *BBA - Biomembranes*, 2003, **1610**, 159-173.
38. Z. V. Leonenko, E. Finot, H. Ma, T. E. S. Dahms and D. T. Cramb, *Biophys. J.*, 2004, **86**, 3783-3793.
39. H. M. Seeger, A. Di Cerbo, A. Alessandrini and P. Facci, *J. Phys. Chem. B*, 2010, **114**, 8926-8933.
40. N. Kucerka, J. D. Perlmutter, J. Pan, S. Tristram-Nagle, J. Katsaras and J. N. Sachs, *Biophys. J.*, 2008, **95**, 2792-2805.

Chapter 7

Custom AFM for X-Ray beamlines*

A multimodal and correlative approach is often a requirement to better understand the mechanisms that govern the structure of biological membranes. In this chapter, we present the development of an atomic force microscope (AFM) that aims to correlate the AFM morphology and mechanics with the structural information gathered with grazing incidence X-ray (XR) experiments at solid/air and solid/liquid interfaces. The instrument allows a wide range of possible investigations, including soft and biological samples under physiological conditions (hydrated specimens). Besides, we expose the importance of a proper evaluation and characterization of the radiation damage effects induced by the XR beam on supported lipid bilayers. Finally, we detail the study of membrane phase transitions by means of the presented multimodal approach.

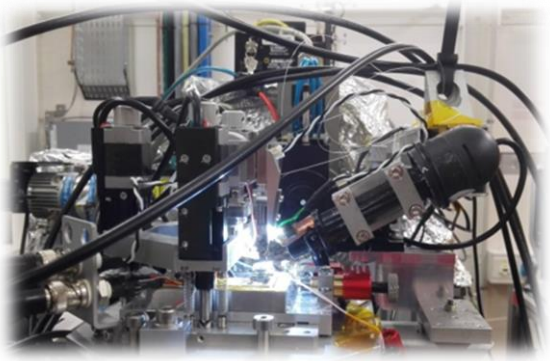

* This work has been published: B. Gumí-Audenis, F. Carlà, M. V. Vitorino, A. Panzarella, L. Porcar, M. Boilot, S. Guerber, P. Bernard, M. S. Rodrigues, F. Sanz, M. I. Giannotti and L. Costa, *J. Synchrotron Rad.*, 2015, **22**, 1364-1371; B. Gumí-Audenis, L. Costa, F. Carlà, F. Comin, F. Sanz and M. I. Giannotti, *Membranes*, 2016, **6**, 58.

7.1. Introduction

The understanding of the mechanisms that govern the structure of biological membranes, as well as the organization and dynamics of its constituents, requires a multimodal approach supported by diverse characterization tools, as highlighted in previous chapters. An instrumental development is often the first step of a multimodal and correlative approach. In this chapter, we expose an instrument development aimed to correlate the structural, morphological and mechanical changes occurring at the nano and mesoscale (figure 7.1), allowing the characterization of specific membrane remodeling effects. The development is focused on the simultaneous and correlative use of the atomic force microscopy (AFM) and synchrotron X-ray (XR) techniques (AFM-XR combination).

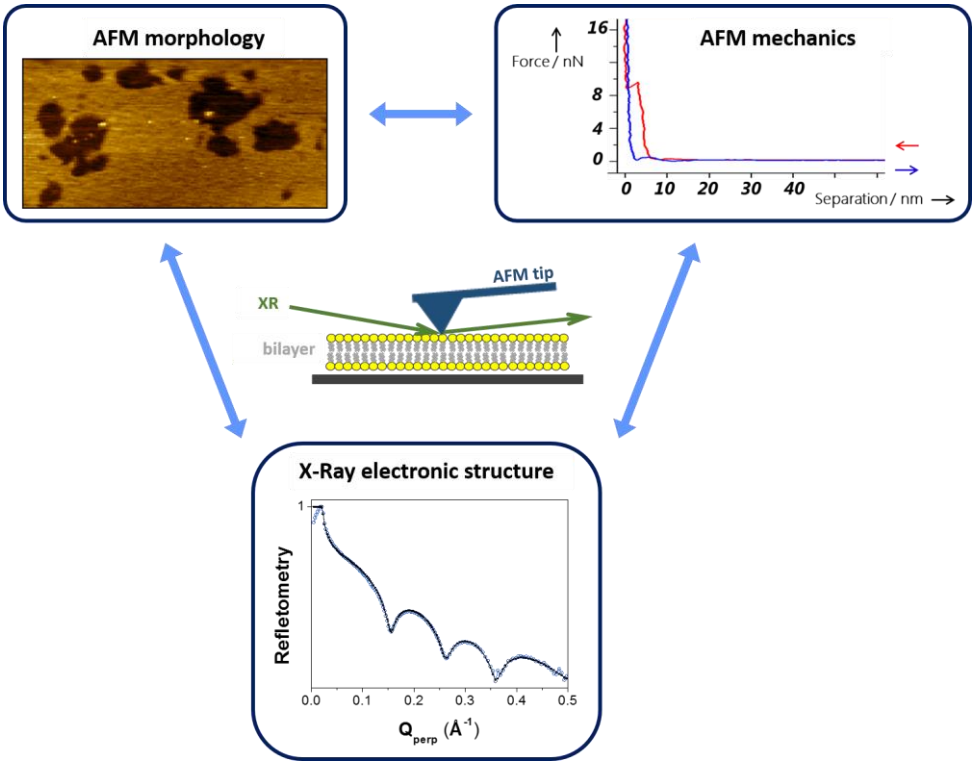

Figure 7.1 Scheme describing the aim of our instrument development: to correlate structural (XR), morphological and mechanical (AFM) information.

For several decades, grazing incidence (GI) XR techniques have been employed to characterize a large variety of samples, expanding our knowledge in many fields ranging from physics to biology and chemistry. In such types of experiments, the structural information provided through the interaction between the XR and the sample is usually averaged over the area illuminated by the beam footprint, which covers a surface larger than that accessible by means of AFM. Nevertheless, XR techniques do not involve any mechanical

interaction with the samples, preventing the direct evaluation of the mechanical properties. For these reasons, the combination of XR with the AFM local and nanomechanical information has become powerful during the last decade, introducing several operational schemes that have already been successfully tested.[1] In the first case reported, a conductive AFM tip was used as a local detector, either for collecting the total yield[2] or the XAFS–XEOL (XR absorption fine structure–XR excited optical luminescence) spectroscopy signal[3] in GI configuration, or to perform scanning transmission XR microscopy (STXM) in normal incidence.[4] A second line of experiments consisted of using the AFM as a mechanical indenter on nano-sized systems, while the XR beam was used to investigate the changes on the specimen lattice parameter.[5, 6]

In most of the previously referenced cases, some of the mechanical elements of the AFM limited the applications to the field of material science, preventing the possibility of exploring biological samples under liquid environment. We designed and built a custom fast AFM that can be installed as a sample holder for GI synchrotron radiation experiments, and tested it in few beamlines at the ESRF, the European Synchrotron, in Grenoble (France). This instrument extends the capabilities of the XR–AFM combination to experiments on soft and biological materials performed in hydrated conditions, allowing also the use of any commercially available AFM cantilever. In this way, local and temporal correlative AFM-XR can give insights of dynamic processes, such as membrane remodeling effects, phase transitions or chemical reactions. It can also make use of the AFM tip to apply an external force (mechanical, electric or magnetic) or to employ it to align a nano-object with the XR beam.

In addition, the AFM can also be used to evaluate the radiation damage induced by the XR beam in real time, since radiation damage limitation is a major challenge when using very intense XR beams on soft and biological samples. For instance, the formation of micrometric holes produced by an intense XR nanobeam on a semiconducting organic thin film has been recently observed by means of high speed AFM (HS-AFM).[7]

In this chapter, we first present the design structure and the commissioning of the custom AFM, that we developed at the Surface Science Lab (Scientific Infrastructure Group, Experiments Division) led by Dr. Fabio Comin at the ESRF, the European Synchrotron, in Grenoble (France). Next, we expose the importance of a proper evaluation and characterization of the radiation damage effects induced by the XR beam on supported lipid bilayers (SLBs). Finally, we detail the study of membrane phase transitions by means of correlative XR reflectometry (XRR), AFM and AFM-based force spectroscopy (AFM-FS).†

† All the XR experiments were performed in the following official synchrotron beamtimes at the ESRF: SC-4031, IHSI-928 and IHSI-929 at ID03 beamline, and SC-4237 at ID10 beamline.

7.2. Experimental

Materials. 1,2-distearoyl-*sn*-glycero-3-phosphoethanolamine (DSPE), 1,2-dipalmitoyl-*sn*-glycero-3-phosphocholine (DPPC), 1,2-dioleoyl-*sn*-glycero-3-phosphocoline (DOPC) and 1,2-dilauroyl-*sn*-glycero-3-phosphocholine (DLPC) were purchased from Sigma-Aldrich (St Louis, MO, USA). The experiments with DSPE monolayers were carried out at room temperature (*RT*) and at the solid/air interface. The experiments on DPPC, DOPC and DPPC:DLPC (1:1 molar ratio) bilayers were performed in buffer solution of 150 mM NaCl, 20 mM $MgCl_2$, 20 mM HEPES (4-(2-hydroxyethyl)-1-piperazineethanesulfonic acid) (pH 7.4) prepared with ultrapure water (Milli-Q reverse osmosis system, 18.2 mΩ·cm resistivity) and filtered before use with an inorganic membrane filter (0.1 μm pore size).

Sample preparation. DSPE was dissolved in chloroform to a final concentration of 0.13 mM. To obtain the DSPE monolayers, 10 μL of the solution were deposited onto 4 mm x 4 mm freshly cleaved mica substrates (Agar Scientific, UK) and left to dry under ambient conditions.

DPPC, DOPC and DLPC were individually dissolved in chloroform:methanol (v:v 3:1) to a final concentration of 3 mM. Afterwards, the solvent was evaporated to dryness under nitrogen flow in order to achieve a thin film on the walls of the tube. In the case of DPPC:DLPC (1:1 molar ratio), the desired concentration of phospholipid mixture was poured into the falcon tube before the solvent evaporation. Then, the dried films were hydrated with buffer solution, previously heated above the main transition temperature (T_m) of the phospholipid, until a final concentration of 0.5 mM. The falcon tubes were then subjected to cycles of vortex mixing and heating to *ca.* 60 ºC. The vesicles suspensions were placed in an ultrasound bath for 30 min to finally obtain unilamellar vesicles.[8, 9]

Silicon wafers with orientation (100) ± 5º, polished (r.m.s. < 0.5 nm), 275 μm thickness and 50.8 mm diameter were purchased from CrysTec. 4 mm x 4 mm square substrates were obtained from the wafers and subsequently exposed to plasma (Expanded Plasma Cleaner PDC-002, Harrick Scientific Corporation) at high RF power level for 5 min in order to activate the hydrophilic bonding of the Si surfaces.

SLBs were obtained by depositing 20 μL of the suspension of unilamellar vesicles onto the hydrophilic Si substrate for 20 min at a temperature above T_m of the phospholipid. Then, the samples were rinsed with buffer solution in order to remove the vesicles not fused, always keeping the Si substrate hydrated.

Differential Scanning Calorimetry (DSC): DSC measurements were performed using a MicroCal VP-DSC (MicroCal, Northhampton, MA). Approximately 600 μL of liposome suspensions (7 mM) were placed in the sample cell and the same volume of buffer solution was used as reference. With 0.5 ºC·min^{-1} heating and cooling rate, the measurements were performed in the temperature range of 25 to 70 ºC.

Atomic force microscopy (AFM) and AFM-based force spectroscopy (AFM-FS). The AFM experiments were all performed with the custom AFM described in section 7.3.1. The images were acquired in amplitude modulation AFM mode (AM mode) in large oscillation amplitude regime:[10] the free oscillation amplitude imposed to the tip ranged from 10 to 40 nm depending on the experiment.

For DSPE monolayers, the acquired AFM images were obtained at *RT* and in air conditions. We used AC55 cantilevers (Olympus, Japan) with nominal spring constant (k_s) of 85 $N \cdot m^{-1}$ and an optical fiber as a Fabry–Perot plate.[11] In the experiments where the XR beam was irradiating the sample, longer and softer NSC15 cantilevers (μmasch, Bulgaria) were used to facilitate the acquisition of the AFM images, since the level of vibrations present on the diffractometer was higher compared to the off-line configuration.

For DPPC, DOPC and DPPC:DLPC (1:1 molar ratio) bilayers, the images were acquired at *RT* and in liquid environment (buffer solution). We used V-shaped Si_3N_4 cantilevers with k_s of 0.35 $N \cdot m^{-1}$ (SNL, Bruker AFM Probes; Camarillo, CA) and an optical fiber as a Fabry–Perot plate. AFM-FS measurements were performed after imaging a region of interest characterized by large SLB areas. The force-distance curves were recorded by approaching and retracting the cantilever tip to the sample at constant velocity (300 $nm \cdot s^{-1}$) and in the force map mode.

For the temperature controlled experiments, a small Peltier element was placed below the sample to induce temperature dependent phase transitions of the specimen varying from 20 ºC to 47 ºC. In this case, some of the AFM images presented were acquired using a Cypher AFM (Asylum Research, Santa Barbara, CA).

XR reflectometry (XRR). We used high energy XR, 22.5 keV, corresponding to λ = 0.551 Å, required to penetrate through the liquid. The beam size was 300 μm x 30 μm (horizontal x vertical). A set of attenuators was used to control the incident photon flux and limit the exposure of the sample to XR. XRR curves were treated employing the GenX software and by modeling the interface with a seven-slabs model.[12, 13] This model includes the upper phospholipid headgroups (H_{upp}), the upper hydrocarbon tails (T_{upp}), the CH_3 groups, the bottom hydrocarbon tails (T_{bot}), the bottom phospholipid headgroups (H_{bot}), a layer of water molecules comprised between the substrate and H_{bot} and a SiO_2 layer. This Si substrate was kept as a fixed parameter. A schematic representation of an ideal scattering length density (SLD) profile obtained by fitting an XRR curve of an SLB using the 7-slabs model is shown in figure 7.2

7.3. Results and discussions

7.3.1. Design and development of the custom AFM

The custom AFM was designed to fulfill certain specific needs of XR GI experiments:

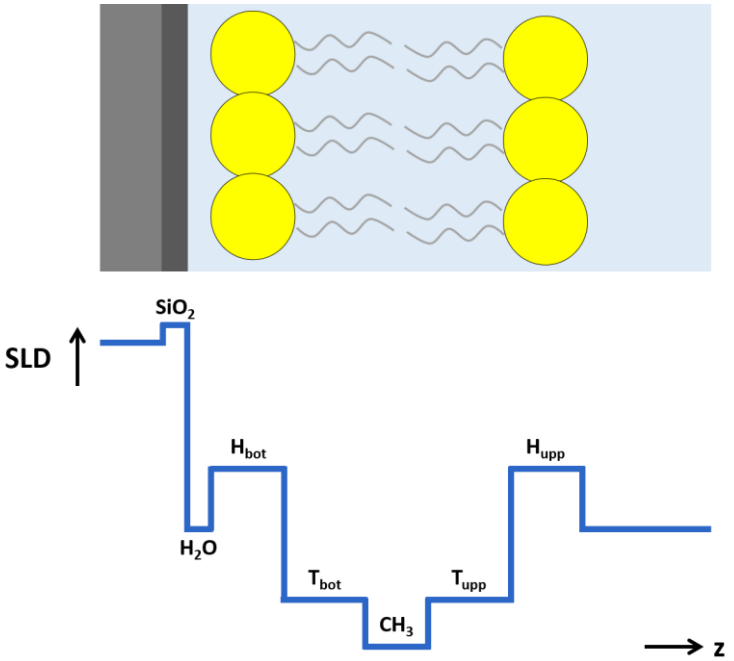

Figure 7.2 Schematic representation of an ideal SLD profile obtained by fitting an XRR curve from a bilayer using the 7-slabs model with a drawing of a supported SLB section under liquid environment.

I. Instrument weight significantly lower (1.35 kg) than commercial AFMs, to allow the installation of the instrument on top of several hexapods.

II. AFM still operational when rotated in-plane (up to 45º) and out-of-plane (up to 10º), to permit the alignment of the sample with the XR beam under GI conditions.

III. Favorable detection of the scattered beam out of the sample plane for XRR measurements and in the sample plane for surface scattering and diffraction experiments.

Different view plans of the design of the instrument structure are shown in figure 7.3(a), whereas in figure 7.3(b) pictures of the custom AFM already mounted on the hexapod of ID03 beamline at the ESRF are exposed. It has been designed to be a sample-scanning AFM, not displacing the AFM tip during the experiment. Consequently, the typical AFM-XR experiment geometry requires both the XR beam and the AFM tip to be aligned and fixed in space while the sample is being scanned. The custom AFM is composed of two separated parts made of aluminum: the microscope head and the microscope base. When the instrument is rotated out-of-plane, both AFM head and base are tilted, kept together thanks to six springs.

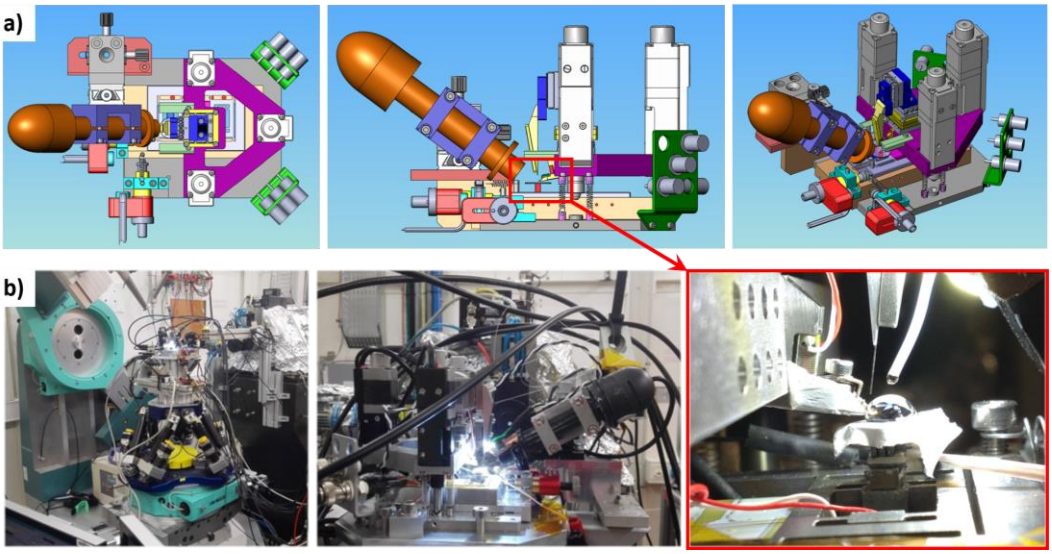

Figure 7.3 a) Design of the custom AFM structure in different view plans. b) Pictures of the custom AFM mounted on the hexapod of ID03 beamline at the ESRF, the European Synchrotron, in Grenoble (France).

In the microscope head, the cantilever holder can be easily inserted and removed through small magnets positioned both on the holder back side and the AFM head (figure 7.4(a)). This facilitates the exchange of the AFM cantilever chip, that is mechanically clamped inside the cantilever holder with a screw (figure 7.4(a)). Two versions of this holder have been fabricated depending on the experiment conditions. If the cantilever needs to be conductive, the Macor version is employed to detect the photoelectrons generated in the AFM tip by the incident XR beam. This allows the alignment between the AFM tip and the XR beam with a single micro or nanostructure. When this alignment is not necessary and so non-conductive cantilever is needed for the experiment, the aluminum version is then employed. In this context, the instrument makes possible the use of any commercially available AFM cantilever, permitting a wide range of experiments: from the study of soft and biological materials in liquid environment (soft cantilevers) to magnetic force microscopy (MFM) and electrostatic force microscopy (EFM) experiments (magnetic and conductive cantilevers). To acquire topographical images in AC mode, a piezoelectric element is employed to mechanically excite the cantilever at its resonance frequency.

The AFM tip position is measured with a Fabry-Perot or optical fiber-based interferometer (figure 7.4(b)),[11] which is a detection operational scheme that has already been employed for different experiments.[14, 15] A cleaved optical fiber with a diameter of 125 µm (Thorlabs) is brought to a distance of about 10 µm from the back side of the AFM cantilever using the stage composed of three inertial motors (SLC Smaract), that allow the movement of the optical fiber in X, Y and Z directions. The inertial motor which displaces the

fiber perpendicularly to the cantilever is then controlled in its linear dynamic range using a proportional-integral controller to keep the tip–fiber distance constant. The use of very small cantilevers with high resonance frequency is essential to achieve a fast imaging speed. However, an optical fiber with a diameter of 125 μm is not able to come close enough to the small cantilever due to the presence of the AFM cantilever chip. In this context, a SNOM (scanning near field optical microscopy) optical fiber has to be employed in the far-field regime: we used Lovalite pulled optical micro-tips with an apex radius of 100 nm. The laser employed is a 51nanoFI (red light, $\lambda \sim 650$ nm) and the coupler is a FBS-660-X, both from Shafter + Kirchhoff (figure 7.4(b)). The interference signal is converted into current by a photodetector and then converted into voltage with a FEMTO DHPCA-100 I/V converter. The microscope head is moved towards the microscope base with three long-range step-motors (8CMA06-13-15 Standa) and the final tip–sample approach is then completed using the scanner mounted on the microscope base.

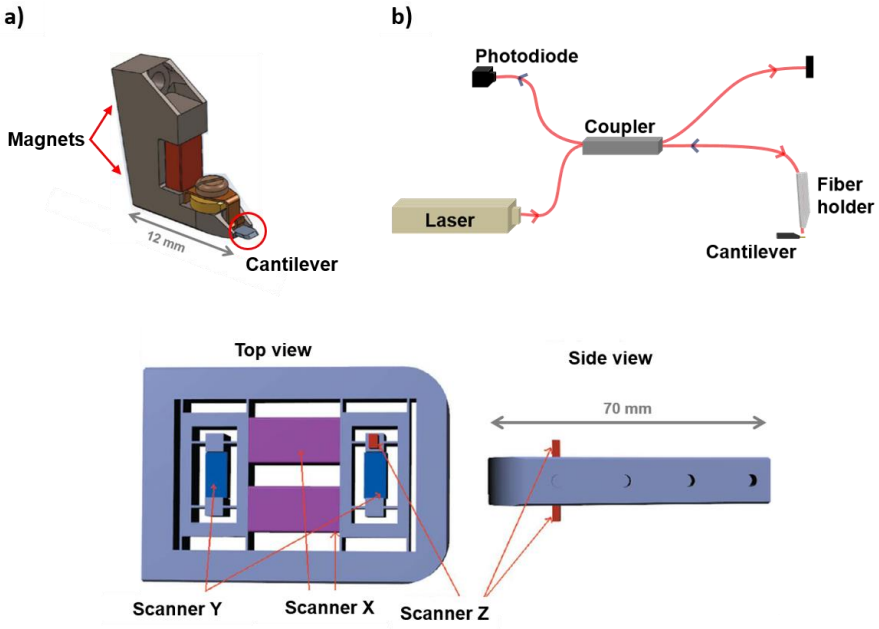

Figure 7.4 a) Cantilever holder. b) Optical fiber-based interferometry. c) Scanner.

Since official XR experiments in synchrotrons are limited in time, conventional AFM imaging acquisition time, usually in the order of tens of minutes, is a limitation. Therefore, we decided to design the instrument in such a way to get higher image acquisition rates. To get fast AFM imaging capabilities, not only small cantilevers are important, but also fast scanner and fast control electronics are essential. Accordingly, a custom-made scanner was built (figure 7.4(c)), inspired by the scanner structure of the high-speed AFM,[16] that allows the acquisition of several images per second of biological samples in physiological

conditions. The main characteristic of such a fast scanner is the insertion of second counterbalancing piezoelectric Z element, not displacing the center of mass of the structure while scanning. This permits the bandwidth of the system to be increased, allowing fast compensation for changes in the tip oscillation amplitude when in AC mode. The scanner was calibrated through the AFM characterization of standard calibration gratings and it provides a maximum scanning area of 12 μm (X) x 6 μm (Y) x 1 μm (Z). To acquire topographical images in various parts of the sample, the entire structure of the scanner can be displaced below the AFM tip using two picomotors.

The electronics driving the AFM are a complete Nanonis SPECS consisting of the modules RCS, SC4, OC4 and an HS4 power supply to drive the piezoelectric elements of the scanner. The AFM images and the AFM-FS measurements are acquired using the software included with the electronics. Two additional custom-made LabVIEW programs drive the step-motors, that control the long-range approach between the AFM head and its base, and the picomotors, which displace the scanner.

Samples are usually directly fixed on top of the scanner or, in the case of measurements at the solid/liquid interface, either on top of the aluminum sample holder disk covered with Teflon or on a Teflon cell used as sample holder. In addition, a small Peltier element can be placed below the sample to induce temperature dependent phase transitions of the specimen varying from 20 ºC to 47 ºC. In that case, the temperature is kept constant in a closed loop operational scheme and measured with a Pt100 resistance. Finally, an optical camera (Veho VMS-004) facilitates both fiber–cantilever and tip–sample alignments.

7.3.2. Commissioning of the custom AFM

The custom AFM was first tested off-line, on DSPE monolayers onto mica substrate in ambient conditions. The same 3 μm x 3 μm scanning area was imaged at different speeds (figure 7.5(a)), ranging from 26 seconds to 1 second per image. As observed, with the fastest speed it is possible to acquire images keeping an acceptable lateral and vertical resolution compared with the slow-scanned images. Nevertheless, when mounting the custom AFM on the hexapod of ID03 beamline (ESRF), the acquisition of high speed images (1 second per image) could not be reached due to the higher level of vibration of the beamline diffractometer stage. However, images of DSPE monolayers with a vertical resolution inferior to 1 nm and with a quality comparable to the ones obtained *ex-situ* were achieved (figure 7.5(b)), at 30 seconds per image and with the custom AFM on top of ID03 hexapod.

The second commissioning session was mainly focused on testing the custom AFM with samples that require liquid experimental conditions and proving that XR measurements are possible when the AFM is used as sample holder for GI XR experiments. To do that, SLBs onto Si substrates were characterized by means of AFM, AFM-FS and XRR under hydrated conditions using the buffer solution described in the Experimental section. To make sure

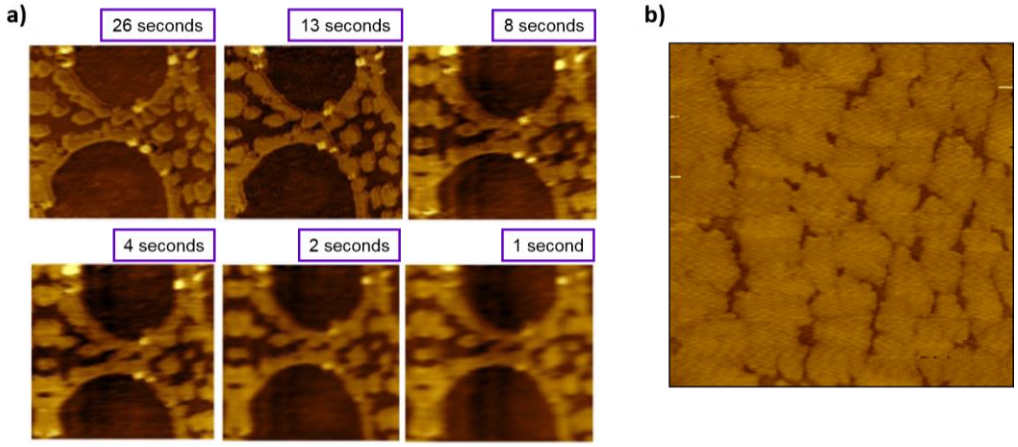

Figure 7.5 3 μm x 3 μm XR-AFM images of DSPE monolayers at the solid/air interface. a) The images were obtained off-line at different acquisition speeds. b) The image was acquired with the custom AFM mounted on the hexapod of ID03 beamline (ESRF).

that the AFM and XR measurements were carried out in the very same sample position, we aligned the AFM tip on top of the sample surface with the XR beam. We used STXM to measure the transmitted signal while scanning at different heights (figure 7.6(a)), determining then the exact position of the AFM cantilever, with an error of few tens of μm associated to the beam's vertical size, and permitting its alignment with the XR beam. Additionally, we measured the current flowing in the AFM cantilever once irradiated by the beam, suggesting that the entire cantilever and the tip were aligned with the XR beam, considering the size of the beam to be comparable to the size of the cantilever. In figure 7.6(b), we show the measurement of the current flowing in the AFM cantilever while being aligned with the XR beam and switching it on and off.

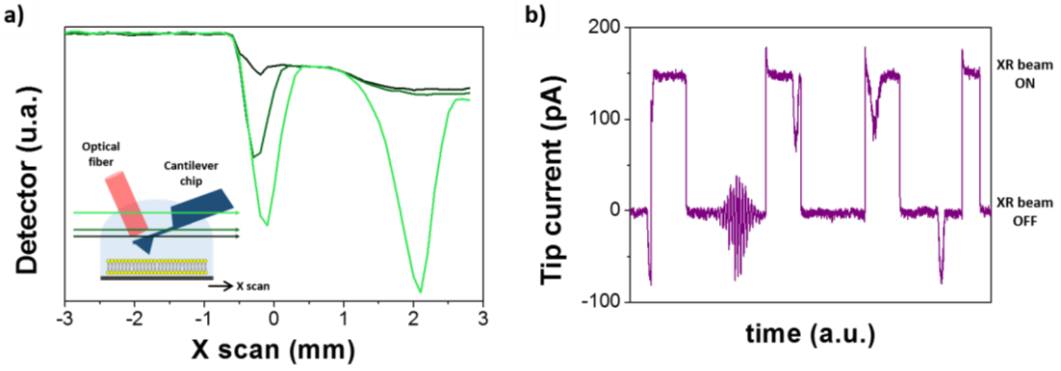

Figure 7.6 a) Transmitted XR beam scans measured along the X axis at different heights corresponding to different colors. Inset: pictorial scheme of the measurement set up. b) Current flowing in the AFM cantilever once aligned and irradiated by the XR beam.

An AFM image of a hydrated DPPC bilayer onto Si substrate is shown in figure 7.7, with the corresponding cantilever deflection-piezo motion curves performed in AFM-FS mode, enlightening (circles) the discontinuity that corresponds to the tip breaking through the bilayer, and the associated XRR curve with the resultant SLD profile. From the reflectometry data, a bilayer thickness of 5.5 nm is revealed,‡ whereas the morphological study of the AFM image provided an SLB thickness of 5.1 nm. This discrepancy can be explained as the underestimated thickness value obtained when imaging in AM mode, since compression of the phospholipid membranes is proved.

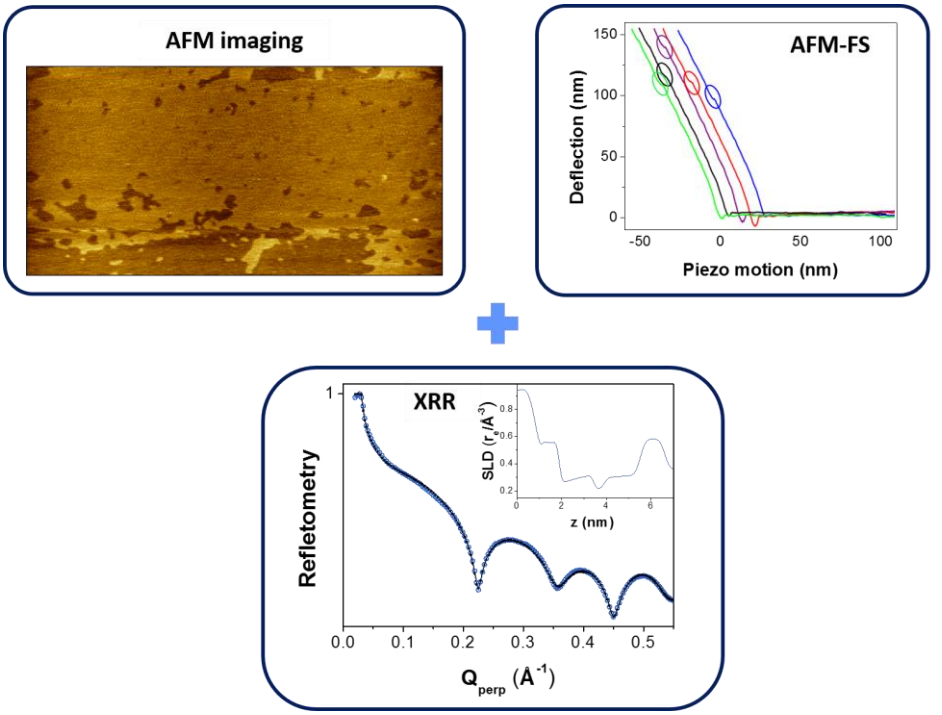

Figure 7.7 XR-AFM topographical image (12 μm x 6 μm), cantilever deflection-piezo motion curves in AFM-FS mode and XRR of DPPC bilayers supported onto Si substrate. The measurements were performed under buffer conditions (150 mM NaCl, 20 mM $MgCl_2$, 20mM HEPES (pH 7.4)) and at *RT*.

Besides getting topographical data on single SLBs (figure 7.7), we were able to perform AFM-FS measurements onto the bilayers. Evaluating the cantilever deflection–piezo motion curves registered, and considering the nominal k_s of the cantilever used (0.35 $N \cdot m^{-1}$), we estimated the breakthrough force (F_b) for the DPPC bilayers in the range of 35–45 nN. This

‡ The thickness of the bilayer can be calculated from the XRR curve by measuring the Q_{perp} positions of two minimums and applying the following expression:

$$thickness = \frac{2\pi}{\Delta Q_{perp}}$$

value is higher compared to the typical ones reported for DPPC SLBs (~ 20 nN).[17] However, this deviation may be attributed to the use of k_s, since it can consistently differ from the experimental spring constant, that was not calibrated in this specific experiment.

From treating each XRR curve, an SLD profile was achieved by modeling the interface with a seven-slabs model,[12, 13] including the layers detailed in the Experimental section. Evaluating the resultant SLD, we obtained structural parameters (thicknesses (*th*), electron density (ρ) and roughness (σ_{SLD})) of the bilayers. These structural parameters for the DPPC SLB are exposed in table 7.1. For the SiO_2 and the water molecules layers, only the roughness value is presented.

Table 7.1 Structural parameters obtained from the best XRR fit shown in figure 7.7 for the studied hydrated DPPC SLB.

Slab	*th* (nm)	ρ ($e^{-}\cdot Å^{-3}$)	σ_{SLD} (Å)
H_{upp}	1.09	0.55	1.82
T_{upp}	1.60	0.31	1.89
CH_3	0.49	0.23	1.34
T_{bot}	1.55	0.31	1.00
H_{bot}	0.77	0.58	1.00
H_2O	-	-	1.00
SiO_2	-	-	2.76

These measurements were essential for the commissioning of the custom AFM, especially to prove its ability of working at the solid/liquid interface. This AFM is considered to date, as the only one that can work in liquid environment inside an XR beamline. The instrument is unique, highly versatile and it can be used to address specific topics of different scientific disciplines, ranging from physics to chemistry and biology. On our side, we performed further investigations to evaluate the effect of the radiation damage on structural and mechanical properties of soft and biological samples, as well as studying the physical changes of those hydrated samples during dynamic processes, such as phase transitions or chemical reactions.

7.3.3. Radiation damage on phospholipid bilayers

XR can severely damage soft and biological materials as well as biomolecules, *i.e.* promoting the formation of radicals and charges.[18, 19] Being aware of how important can be the damage induced to a model membrane upon XR exposure after an XRR measurement, we decided to monitor the radiation damage induced by the beam on DOPC and DPPC SLBs during the acquisition of single XRR curves (figures 7.8 and 7.9). Particularly, AFM images before and after the XR beam exposure were acquired in the very same place of the sample. In both DOPC and DPPC SLBs, a decrease in the reflectometry intensity was first observed, finally leading to the disappearance of the XRR fringes (figures 7.8(a) and 7.9(a)). Nevertheless, the AFM images revealed a different behavior in the two samples.

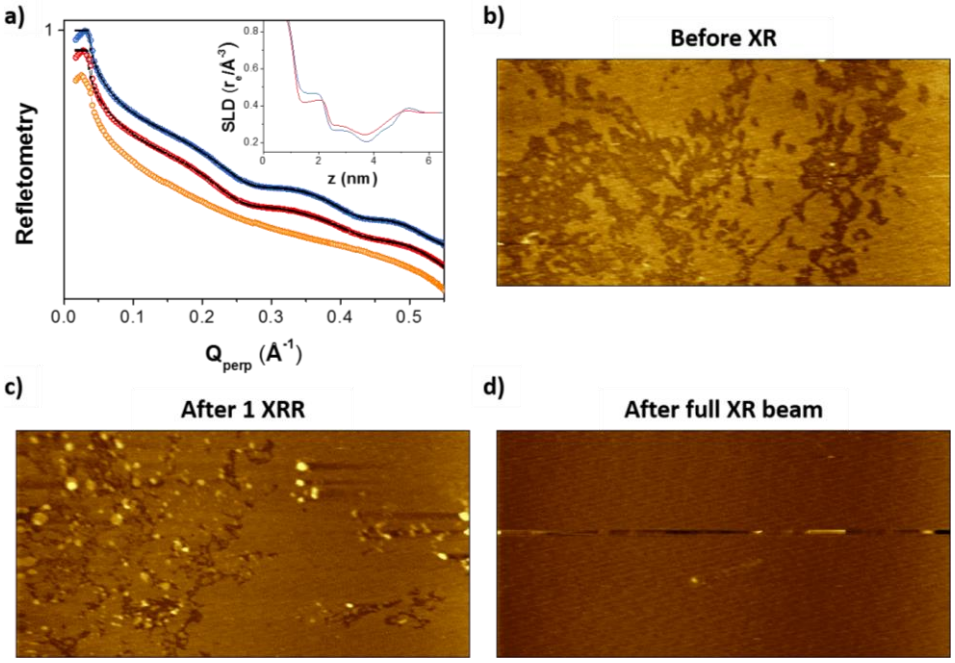

Figure 7.8 Radiation damage on DOPC bilayers in buffer conditions (150 mM NaCl, 20 mM $MgCl_2$, 20 mM HEPES (pH 7.4)) and at *RT*. a) Reflectometry: blue XRR curve and SLD profile (inset) acquired after AFM topography (b); red XRR curve and SLD profile (inset) acquired after AFM topography (c); orange XRR curve acquired after AFM topography (d). The XRR curves are shifted for better clarity. b) XR-AFM topography before XR exposure. c) XR-AFM topography after acquiring one XRR curve. d) XR-AFM topography after full XR beam exposure. The size of the AFM images is 12 µm x 6 µm.

Figure 7.8 shows the radiation damage effect obtained when performing XRR measurement on DOPC bilayers. After acquiring one reflectometry curve (figure 7.8(a), blue), deposition of lipid material on top of the main membrane can be easily noticed when comparing the AFM images presented in figures 7.8(b) and (c) before and after the XRR, respectively. Following the AFM image shown in figure 7.8(c), the second reflectometry curve was obtained (figure 7.8(a), red). The structural parameters obtained from the best fits as well as the roughness values for the SiO_2 and the water molecules layers are presented in table 7.2. Despite the similarity between these XRR curves, a change in the SLD profiles is observed, assigned to a modification on the bilayer density at the nanometric scale, in agreement with the morphological differences detected from the AFM images.

Finally, the same DOPC bilayer was investigated after a prolonged exposure of about 5 minutes in the absence of attenuation filters, at an incident angle of 0.1º. As observed in figure 7.8(d), the membrane has totally disappeared, correlating with the flat XRR curve represented in figure 7.8(a), orange.

Table 7.3 Structural parameters of the DOPC bilayers obtained from the best XRR fits corresponding to the blue and red data shown in figure 7.8(a).

	Blue data			Red data		
Slab	***th* (nm)**	**ρ ($e^{-}\cdot Å^{-3}$)**	**σ_{SLD} (Å)**	***th* (nm)**	**ρ ($e^{-}\cdot Å^{-3}$)**	**σ_{SLD} (Å)**
H_{upp}	0.55	0.39	1.45	0.75	0.37	1.94
T_{upp}	0.77	0.28	1.69	0.59	0.33	2.84
CH_3	0.79	0.21	2.07	0.85	0.25	2.82
T_{bot}	1.07	0.27	2.95	0.93	0.29	2.99
H_{bot}	1.18	0.47	1.64	1.19	0.42	1.01
H_2O	-	-	1.13	-	-	1.13
SiO_2	-	-	2.76	-	-	2.76

For the DPPC SLBs, the formation of holes in the bilayer structure at the micrometric and nanometric scale is clearly visible in the AFM images before and after (figure 7.9(c) and (d), respectively) acquiring the first XRR (figure 7.9(a), blue). This is reflected as an amplitude decrease in the fringes of the XRR curve (figure 7.9(a), red), confirming the coverage decrease and the increment of the roughness. The structural parameters obtained from the best fits as well as the roughness values for the SiO_2 and the water molecules layers are presented in table 7.3. As in the case of DOPC bilayers, a change in the SLD profile is observed after XR irradiation, related to the modification of the membrane density and coverage at the nanoscale.

Table 7.2 Structural parameters of the DPPC bilayers obtained from the best XRR fits corresponding to the blue and red data shown in figure 7.9(a).

	Blue data			Red data		
Slab	***th* (nm)**	**ρ ($e^{-}\cdot Å^{-3}$)**	**σ_{SLD} (Å)**	***th* (nm)**	**ρ ($e^{-}\cdot Å^{-3}$)**	**σ_{SLD} (Å)**
H_{upp}	1.11	0.46	3.00	1.10	0.45	1.57
T_{upp}	1.31	0.31	2.97	1.68	0.31	2.98
CH_3	0.80	0.24	3.00	0.32	0.29	2.95
T_{bot}	1.44	0.30	2.98	1.35	0.31	2.94
H_{bot}	0.89	0.44	1.02	0.92	0.38	1.04
H_2O	-	-	2.42	-	-	2.42
SiO_2	-	-	2.76	-	-	2.76

The reason why the DOPC and DPPC bilayers show different damage extent cannot be explained on the mere basis of the data collected during this experiment, but it is probably related with the double-bond on the phospholipid tail for DOPC, susceptible to interact with many radiolysis products. However, the XR irradiation at this specific energy (22.5 keV) seems to significantly modify the membrane density and coverage for both phospholipid systems. In this context, minimizing radiation damage is one of the key issues to reinforce the use of XR over neutron techniques, with higher resolution and faster measurements, to study biological films.[20] In this respect, it is worth to mention that we have recently

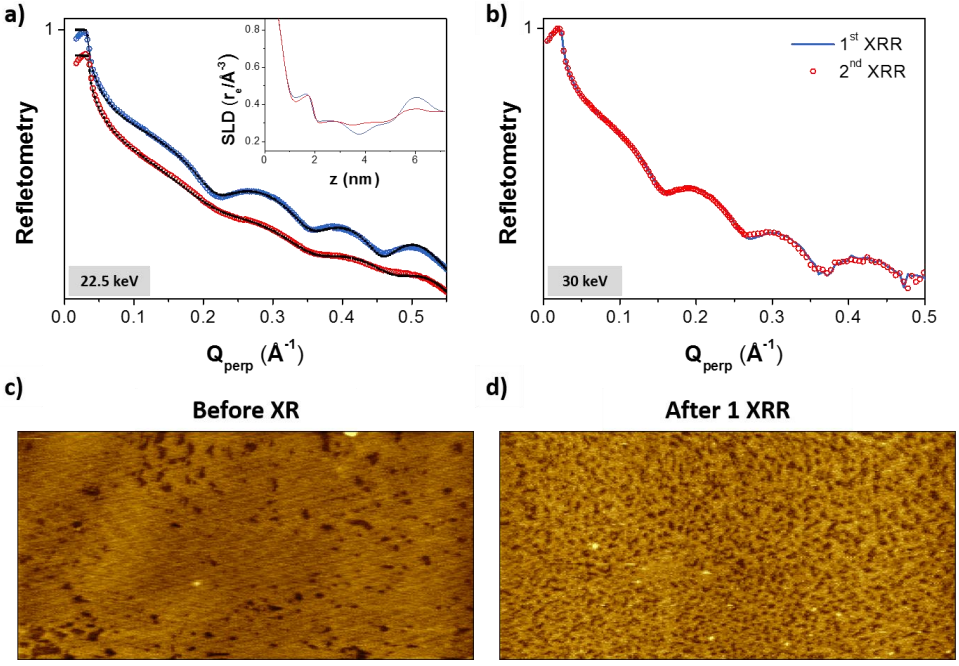

Figure 7.9 Radiation damage on DPPC bilayers in buffer conditions (150 mM NaCl, 20 mM $MgCl_2$, 20 mM HEPES (pH 7.4)) and at *RT*. a) Reflectometry at 22.5 keV: blue XRR curve and SLD profile (inset) acquired after AFM topography (c); red XRR curve and SLD profile (inset) acquired after AFM topography (d). The XRR curves are shifted for better clarity. b) Reflectometry at 30 keV. c) XR-AFM topography before XR exposure. d) XR-AFM topography after acquiring one XRR curve. The size of the AFM images is 12 μm x 6 μm.

discovered that when increasing the XR energy to 30 keV, the radiation damage on SLBs is minimized. This novel approach allowed us to acquire two consecutive XRR datasets in the very same sample region of a DPPC bilayer (figure 7.9(b)), without observing important radiation damage effects. While the use of a higher XR energy clearly permits to reduce the damage and increases the transmission through the liquid, still XRR data show enough resolution to characterize the structural parameters of DPPC molecules.[§] The use of higher XR energy represents an important advance towards radiation damage-free characterization XR experiments on soft or biological materials.

7.3.4. Dynamic processes: phase transitions on phospholipid bilayers

As previously shown (section 7.3.2), the combination of AFM and XR techniques permits the local characterization providing at once structural, morphological and mechanical information. The simultaneous characterization becomes then important in the case of membrane remodeling effects, since they are highly dynamic and affect the membrane at

[§] Further details explained in the introduction section of chapter 6.

different length scales: from the nano to the mesoscale. In this frame, we studied the remodeling effects occurring during the phase transition of phospholipid bilayers, correlating the structural and morphological variations with the change on the bilayer nanomechanics.

Before using the custom AFM, a Cypher AFM (Asylum Research, Santa Barbara, CA) was used to test a Peltier element placed in between the sample substrate and the sample stage of the AFM. We performed the study on DPPC:DLPC (1:1 molar ratio) bilayers. As DPPC T_m is at 41.9 ºC and DLPC at -2 ºC, we chose two temperatures: *RT*, which was around 27 ºC, and high temperature (*HT*), corresponding to 55 ºC. As observed in figure 7.10, at *RT* the SLB segregates into different domains, showing a continuous fluid phase enriched with DLPC and higher small domains associated to a DPPC-rich phase. When the *HT* is reached, the binary phospholipid system is homogeneous and fluid, since the DPPC overpassed the gel-to-fluid transition. After cooling and warming up again the system, the same behavior was observed (figure 7.10), showing reversibility.

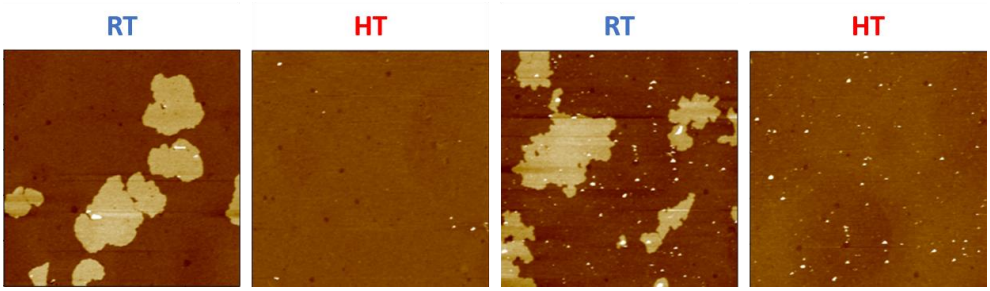

Figure 7. 10 5 µm x 5 µm AFM (commercial AFM) images of DPPC:DLPC (1:1 molar ratio) bilayers at *RT* (27 ºC) or *HT* (55 ºC) in buffer conditions (150 mM NaCl, 20 mM $MgCl_2$, 20 mM HEPES (pH 7.4)). All the images were acquired in the same sample region.

We then moved to the custom AFM and we performed the phase transition study on DPPC bilayers (figure 7.11), since we did not succeed to obtain data good enough for the mixture of DPPC:DLPC with the custom AFM. We carried out AFM and XRR measurements at 27 ºC (*RT*), where the DPPC bilayer is at gel-like state, and at 44 ºC, right after the main T_m of DPPC liposomes (see the DSC thermogram in figure 7.11(a)). At 44 ºC, the SLB shows coexistence of gel and fluid behaviors (figure 7.11(c)), as the thermal transition of a supported membrane is broader than in the liposome suspension due to the effect of the substrate.[21-23] Comparing the AFM images in figure 7.11(c) collected before and during the transition, we evaluate a membrane remodeling from the DPPC patches with an average thickness of 3.5 nm to coexistence of gel and fluid DPPC domains with a difference in thickness between them of 0.5 nm, both calculated from the AFM topographies. In addition, the local information provided by AFM permits to characterize the size of the domains, ranging from few tens to hundreds of nm^2. The simultaneous presence of two membrane

phases at 44 ºC is supported by the nanomechanical information collected by means of AFM-FS (figure 7.11(d)), since a bimodal F_b distribution is obtained, with higher F_b for the gel-like phase (18.6 ± 3.4 nN) compared to the fluid-like one (9.9± 2.2 nN).

Moreover, the membrane thinning due to the temperature raise is also evidenced by the increase of the oscillation periods in the XRR curves (figure 7.11(b)). This implies an increment of the phospholipid disorder in the DPPC during T_m, that clearly reduces F_b. Although not novel, these results are the first *in situ* observation reporting a connection between the disorder characterizing the dynamics of a membrane in the fluid phase with the decrease of its mechanical stability occurring during a dynamic phase transition process.

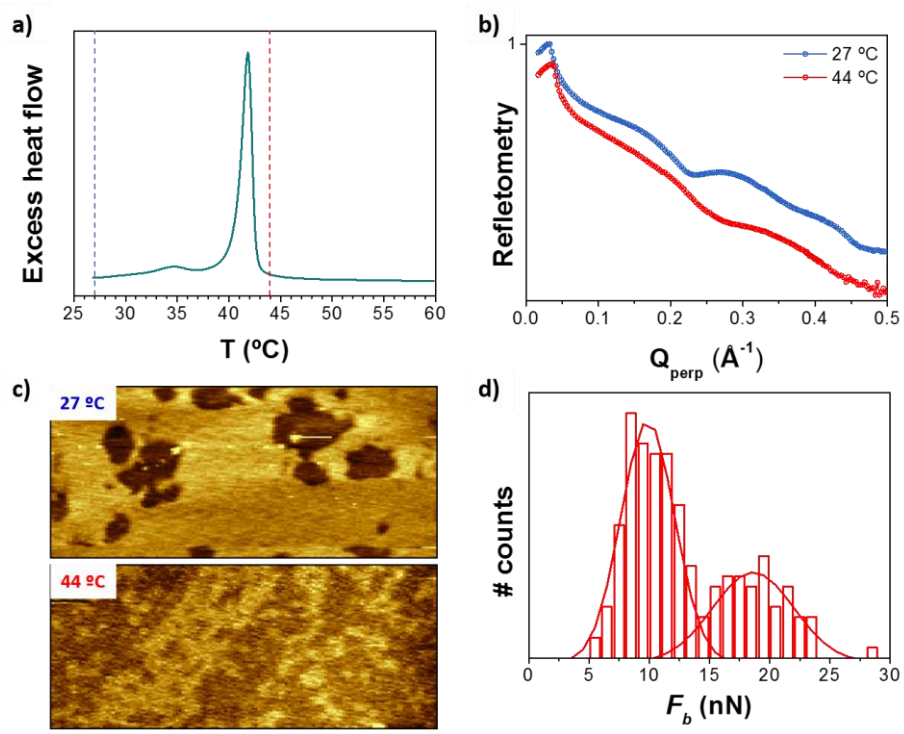

Figure 7.11 Phase transition of DPPC bilayers in 150 mM NaCl, 20 mM $MgCl_2$, 20 mM HEPES (pH 7.4) buffer solution. a) DSC thermogram of DPPC vesicles. b) XRR curves performed at 27 ºC (blue) and 44 ºC (red). c) 6 µm x 2.5 XR-AFM images at 27 ºC and 44 ºC. d) Bimodal F_b histogram performed at 44 ºC.

7.4. Conclusions

We showed that membrane remodeling effects can be characterized simultaneously by correlative XR, AFM and AFM-FS. To achieve this, we developed a custom AFM which can be integrated as a sample holder in the synchrotron XR beamlines, allowing GI XR experiments to be performed simultaneously in terms of time and with the local AFM topography and

mechanical characterization at the nanoscale. The commissioning of the instrument was successfully carried out at the ID03 beamline of the ESRF, by exploring phospholipid monolayers and bilayers at the solid/air and solid/liquid interfaces, respectively. For the case of hydrated SLBs, their structure together with their morphology and nanomechanical properties were characterized in the very same place and time, confirming the ability of our instrument to study soft and biological samples in liquid conditions while installed on top of an XR beamline hexapod.

We evidenced the radiation damage effects produced by the XR beam on DOPC and DPPC bilayers with both the custom AFM and XRR. We showed that a proper characterization of the radiation damage, frequently occurring when studying soft and biological materials and biomolecules, is needed to evaluate phospholipids structural parameters. We determined that the use of higher energy (30 keV) is more suitable compared to lower XR energies (≈ 20 keV), conventionally used and reported in the recent literature.

We showed that correlative XR, AFM and AFM-FS can be used to characterize *in situ* membrane remodeling effects such as phase transitions of model phospholipid membranes. We correlated the increase of disorder, characterizing a DPPC SLB from the gel to the fluid phase, with the decrease of the mechanical stability evaluated by means of AFM-FS during the phase transition.

7.5. References

1. L. Costa and M. S. Rodrigues, *Synchrotron Radiation News*, 2016, **29**, 3-7.
2. M. S. Rodrigues, O. Dhez, S. Le Denmat, J. Chevrier, R. Felici and F. Comin, *J. Instrum.*, 2008, **3**.
3. C. Fauquet, M. Dehlinger, F. Jandard, S. Ferrero, D. Pailharey, S. Larcheri, R. Graziola, J. Purans, A. Bjeoumikhov, A. Erko, I. Zizak, B. Dahmani and D. Tonneau, *Nanoscale Res. Lett.*, 2011, **6**, 308.
4. N. Pilet, J. Raabe, S. E. Stevenson, S. Romer, L. Bernard, C. R. McNeill, R. H. Fink, H. J. Hug and C. Quitmann, *Nanotechnology*, 2012, **23**.
5. T. Scheler, M. Rodrigues, T. W. Cornelius, C. Mocuta, A. Malachias, R. Magalhaes-Paniago, F. Comin, J. Chevrier and T. H. Metzger, *Appl. Phys. Lett.*, 2009, **94**.
6. Z. Ren, F. Mastropietro, A. Davydok, S. Langlais, M. I. Richard, J. J. Furter, O. Thomas, M. Dupraz, M. Verdier, G. Beutier, P. Boesecke and T. W. Cornelius, *J. Synchrotron Rad.*, 2014, **21**, 1128-1133.
7. M. V. Vitorino, Y. Fuchs, T. Dane, M. S. Rodrigues, M. Rosenthal, A. Panzarella, P. Bernard, O. Hignette, L. Dupuy, M. Burghammer and L. Costa, *J. Synchrotron Rad.*, 2016, **23**, 1110-1117.
8. S. J. Attwood, Y. Choi and Z. Leonenko, *Int. J. Mol. Sci.*, 2013, **14**, 3514-3539.
9. M.-P. Mingeot-Leclercq, M. Deleu, R. Brasseur and Y. F. Dufrene, *Nat. Protoc.*, 2008, **3**, 1654-1659.
10. R. García and R. Pérez, *Surf. Sci. Rep.*, 2002, **47**, 197-301.
11. D. Rugar, H. J. Mamin and P. Guethner, *Appl. Phys. Lett.*, 1989, **55**, 2588-2590.
12. E. Nováková, K. Giewekemeyer and T. Salditt, *Phys. Rev. E*, 2006, **74**, 051911.
13. J. Daillant, E. Bellet-Amalric, A. Braslau, T. Charitat, G. Fragneto, F. Graner, S. Mora, F. Rieutord and B. Stidder, *Proc. Nat. Acad. Sci. USA*, 2005, **102**, 11639-11644.
14. L. Costa, M. S. Rodrigues, N. Benseny-Cases, V. Mayeux, J. Chevrier and F. Comin, *Plos One*, 2014, **9**.
15. M. V. Vitorino, S. Carpentier, A. Panzarella, M. S. Rodrigues and L. Costa, *Sci. Rep.*, 2015, **5**, 7818.
16. A. Toshio, *Nanotechnology*, 2012, **23**, 062001.
17. B. Gumi-Audenis, F. Sanz and M. I. Giannotti, *Soft Matter*, 2015, **11**, 5447-5454.

18. L. Costa, A. Andriatis, M. Brennich, J.-M. Teulon, S.-w. W. Chen, J.-L. Pellequer and A. Round, *BMC Struct. Biol.*, 2016, **16**, 18.
19. Steve P. Meisburger, M. Warkentin, H. Chen, Jesse B. Hopkins, Richard E. Gillilan, L. Pollack and Robert E. Thorne, *Biophys. J.*, **104**, 227-236.
20. C. E. Miller, J. Majewski, T. Gog and T. L. Kuhl, *Phys. Rev. Lett.*, 2005, **94**.
21. H. M. Seeger, A. Di Cerbo, A. Alessandrini and P. Facci, *J. Phys. Chem. B*, 2010, **114**, 8926-8933.
22. Z. V. Leonenko, E. Finot, H. Ma, T. E. S. Dahms and D. T. Cramb, *Biophys. J.*, 2004, **86**, 3783-3793.
23. S. Garcia-Manyes, G. Oncins and F. Sanz, *Biophys. J.*, 2005, **89**, 4261-4274.

Chapter 8

General conclusions

We explored the physicochemical and structural properties of model lipid membranes combining AFM, AFM-FS and XR techniques. The AFM provided information about the morphology and mechanics of membranes, as a consequence of the diversity in the chemical composition of phospholipid and non-phospholipid bilayers. This multimodal AFM + XR approach allowed us to investigate the effect of small peptides in the membrane physical and structural properties. In addition, we exposed new advanced methodologies based on both AFM-FS and XR techniques independently and combined.

The specific conclusions for each chapter are:

- We assessed the phase behaviour and nanomechanical properties of SLBs by AFM and AFM-FS techniques, for SLBs of composition ranging from pure phospholipids to more complex ternary mixtures. We confirm that the phospholipid state at the working temperature is a defining parameter governing the behaviour of lipid bilayer mixtures, including Chol and GalCer.

  In general, we observed that amounts up to 20 mol % GalCer provoke an increase in the nanomechanical stability for both DLPC and DPPC SLBs. When studying the ternary systems, Chol appears to be determinant for the domain formation, GalCer distribution and enhanced nanomechanical properties of DPPC:Chol:GalCer SLBs, whereas GalCer dominates the phase behaviour and mechanical stability of DLPC:Chol:GalCer SLBs.

- We characterized for the first time the morphology and the mechanical properties of supported QT membranes in different liquid environments at *RT*, observing a stable heterogeneous topography for QT_H_2O, and a dynamic behavior from segregation turning into a homogeneous SQM for QT_PBS. We asserted that the QT membrane behaves as a typical fluid-like phospholipid bilayer.

  We determined that the presence of ions into the liquid media enhances the lateral interactions between the membrane molecules, leading to higher F_b and rigidity for QT_PBS SQMs and vesicles, respectively, compared with the QT_H_2O system. We studied also the effect of the temperature on the SQMs, associating the different AFM topographies of QT_H_2O and QT_PBS with the different molecular orientations recorded by MD simulations at different *T*.

- We presented a methodological approach based on pulling lipid tubes out of model SLBs in order to evaluate the nanomechanical properties of lipid membranes. This methodology represents an attractive strategy as it combines the advantages of the AFM to locally probe a sample with lateral resolution at the nanoscale and apply and sense force in the pN range, with the simplicity of the SLB preparation. We established that the phase state of the SLB as well as the charge of the phospholipid headgroups determined the tube growing force and the membrane tension.

This approach allowed to assess the contribution of different underlying substrates on the tube growing force and membrane tension, comparing the tube growth from deposited vesicles and SLBs (silicon or mica). We demonstrated that the SLB model represents an intermediate scenario between a free membrane and a cytoskeleton supported membrane, regarding the contribution to the overall membrane tension.

- We investigate how the HNP1 defensin affects the structural and nanomechanical properties of bilayers with different composition. In general, we confirmed that the peptide affects PC SLBs more specifically and localized, whereas it disrupts the overall PE and PE:PG SLBs, depending on the presence of unsaturation in the phospholipid tails.

  After incubating the HNP1 defensin, we detected an F_b increase, enhancing the lateral packing of the upper DPPC headgroups, whereas the peptide seems to insert into the DOPC SLBs without causing a significant change on the bilayer mechanics, although it affects to the DOPC elasticity. We determined that the HNP1 defensin mostly produced a significant thinning of the DOPE membrane, while the phase state of the replaced DOPE content for PG determined the resultant SLB morphology.

- We presented a novel, simple and user-friendly setup that permitted GIXD measurements of hydrated individual SLBs, based on a Si-SLB-Si configuration. The setup is able to reduce the scattering from the liquid and to reveal the weak diffracted signal of the SLB, allowing the detection of different domains in heterogeneous membranes.

  We recorded GIXD patterns on DPPC:Chol bilayers supported onto Si substrates. We successfully characterized their structure at the submolecular level, even for coexisting domains, that correlates with the phase diagram of this binary system.

- We built a custom AFM to be integrated as a sample holder in the synchrotron XR beamlines, for grazing incidence XR experiments. This allowed to obtain the AFM topographical and mechanical characterization together with the acquisition of the electronic structure by means of XRR in the very same place and time. We confirmed the ability of our instrument to study soft and biological samples in liquid conditions while installed on top of an XR beamline stage.

  With this multimodal approach, we evidenced the radiation damage effects produced by the XR beam on PC bilayers. We further showed that correlative XR, AFM and AFM-FS can be used to characterize *in situ* membrane remodeling effects such as phase transitions of model phospholipid membranes.

Appendix 1

Resum en català

1. Introducció

1.1. Membranes biològiques

1.1.1. La composició de les membranes biològiques

Les membranes biològiques (BMs) són fronteres autosegellants, que limiten les barreres permeables de les cèl·lules i els orgànuls i proporcionen els mitjans necessaris per compartir funcions. A part de ser crucials per l'estructura cel·lular, proporcionen una matriu de suport per a totes les proteïnes que es troben inserides a la cèl·lula, actuant com canals per l'intercanvi de massa, energia i informació amb l'exterior.[1-3] Al 1972, Singer i Nicolson van proposar el *fluid mosaic model*,[4] assignant el concepte de fluïdesa a la membrana (figura 1.1). Ells van definir la membrana cel·lular com un líquid bidimensional, on tots els lípids i proteïnes associats a ella presenten mobilitat lateral, la qual és una propietat essencial per a la seva funció. Tot i tenint en compte l'alta complexitat en composició de les membranes, els lípids són el component principal, a més de totes les proteïnes i els carbohidrats, construint l'estructura de la bicapa.[5] Milers d'espècies de lípids es troben en les BMs, incloent fosfolípids, esterols i esfingolípids (SLs). Experimentalment, s'ha demostrat que les BMs són capaces de separar lateralment els seus constituents, subcompartimentant-los en petits dominis (10 – 200 nm) coneguts com *lipid rafts*.[6, 7] Aquests *lipid rafts* són conjunts nanomètrics rics en colesterol (Chol) i SLs, la formació dels quals és impulsada per les interaccions lípid-lípid i proteïna-lípid.[8] Estan presents a les dues capes de les membranes cel·lulars asimètriques i tenen un paper important en rols biològics, regulant processos cel·lulars com ara la senyalització i el tràfic en la membrana.[6, 8, 9]

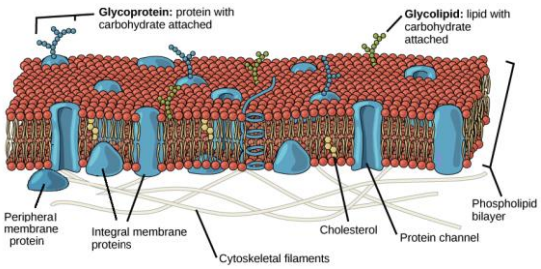

Figura 1.1 El *fluid mosaic model* de la membrana cel·lular.

1.1.2. La mecànica en les membranes biològiques

Les BMs intervenen en moltes funcions biològiques, com el tràfic, la divisió cel·lular, l'endocitosi i l'exocitosi, que exigeixen canvis conformacionals durs en la membrana lipídica com la fusió, la fissió o el creixement de tubs.[5] Aquests requeriments mecànics només són possibles degut a l'organització de la composició química dels lípids a la membrana de cada orgànul, la qual està directament relacionada amb la funció de l'orgànul.[10] Gràcies al seu comportament dinàmic, les forces laterals i transverses dins la membrana són significatives

i canvien ràpidament a mesura que la membrana es corba o s'estira, i quan nous components s'agreguen, es treuen o es modifiquen químicament. Diferències en l'estructura entre les dues capes i entre les diferents àrees de la bicapa poden estar associades a deformacions de la membrana per alterar-ne les activitats de les proteïnes d'unió a la membrana.[5, 11]

A més, els lípids dins la membrana actuen com un suport físic per a les integrines transmembrana, connectant la matriu extracel·lular amb el citoesquelet.[12] D'aquesta manera, la transmissió de senyals mecànics des de l'exterior de la cèl·lula cap al seu interior es produeix a través de la membrana plasmàtica, que determina el comportament d'aquelles cèl·lules.[13] Així doncs, és la correlació entre la composició i l'empaquetament dels lípid el que regeix les propietats fisicoquímiques de la membrana i la seva estructura mecànica.[14]

1.2. Sistemes de membranes model

Tenint en compte la complexa diversitat química de les BMs, sistemes de membranes model són utilitzats sovint per estudiar propietats de membrana i processos biològics. Per exemple, vesícules unilamel·lars gegants (GUVs) han esdevingut models essencials per imitar les BMs, quan s'estudia la dinàmica de dominis i la influència dels canvis de composició en les propietats físiques de tota la GUV.[15] Malgrat tot, degut a la micromètrica i nanomètrica mida dels dominis en les BMs i la conseqüent necessitat de tècniques locals per a explorar BMs a escala nanomètrica, sistemes de bicapes suportades, com les bicapes de lípids suportades (SLBs), s'han proposat com models, ja que són plataformes molt manejables, que conserven l'ordre bidimensional i la mobilitat lateral, i ofereixen ambients excel·lents per a la inserció de proteïnes de membrana.

D'entre tots els mètodes per a obtenir SLBs, el més popular i simple és el mètode de ruptura de liposomes, que consisteix en la fusió de vesícules unilamel·lars petites (SUVs) tan bon punt entren en contacte amb un substrat pla (figura 1.2).[16] De totes formes, la impossibilitat de separar les propietats de la bicapa del substrat que les suporta i de mesurar-ne la seva curvatura degut al seu confinament bidimensional són limitacions de l'enfoc de les SLBs. Per aquest motiu, altres sistemes de bicapa, com les bicapes de fosfolípids sobre polímers[17, 18] o les membranes multilamel·lars[19, 20] han estat proposats per a solvatar

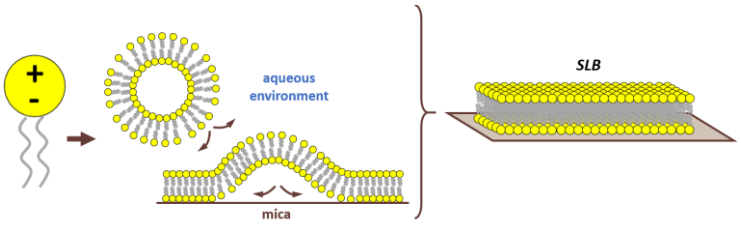

Figura 1.2 Diagrama esquemàtic mostrant la formació d'una SLB a través del mètode de ruptura de liposomes.

aquestes limitacions, ja que permeten la caracterització física de la bicapa sostraient l'efecte del substrat.

1.3. Caracterització física i estructural de les bicapes lipídiques

Diversos informes demostren la gran varietat de tècniques útils per estudiar membranes lipídiques suportades i sense suport. Gràcies a la possibilitat de treballar sota un ambient controlat i amb una resolució nanomètrica en distància i força, la microscòpia de forces atòmiques (AFM) és, avui en dia, una tècnica ben establerta tant per a obtenir una imatge de la morfologia com per mesurar les propietats locals físiques i mecàniques de les SLBs mitjançant modes d'espectroscòpia de forces.[21-25] De totes formes, la resolució que s'obté amb l'AFM és inferior a la que es pot obtenir amb tècniques de raigs X (XR) i neutrons.[26-29] En particular, les tècniques de XR com la reflectivitat de XR (XRR) o la difracció de XR amb incidència rasant (GIXD) són eines potents per caracteritzar superfícies a escala nanomètrica, proporcionant informació estructural a l'espai recíproc a través de la interacció dels XR amb l'estructura electrònica de la mostra.[30-34]

1.3.1. AFM: caracterització topogràfica i mecànica

El principal avantatge de l'AFM es basa en la possibilitat de controlar les condicions ambientals (composició del medi i temperatura) mentre s'apliquen i es detecten forces mínimes en el rang de pN a nN. Això permet operar en un entorn líquid en una gran varietat de mostres biològiques.[35, 36] L'AFM ha esdevingut una tècnica ben establerta per obtenir imatges de l'organització lateral de les membranes lipídiques que presenten morfologies homogènies o de fases separades.[22, 25]

Gràcies a l'habilitat d'aplicar i detectar forces amb alta precisió, l'AFM basat en l'espectroscòpia de forces (AFM-FS) s'ha convertit en una eina excel·lent per a estudiar les interaccions moleculars a nivell de molècula única.[37] Així doncs, durant les últimes dècades, l'AFM-FS ha permès realitzar estudis nanomecànics en un gran rang de sistemes, com pressionar en materials durs mentre la punta de l'AFM s'apropa a la superfície[38] o estirar macromolècules individuals[37, 39-42] mentre la punta de l'AFM es retira de la superfície. En el cas de les bicapes lipídiques, l'AFM-FS s'ha utilitzat per caracteritzar les propietats mecàniques a la nanoescala amb una alta resolució espacial i de forces.[23, 24, 43, 44]

Experimentalment, es localitza un tros de membrana després d'obtenir-ne una imatge amb l'AFM. Llavors, la punta de l'AFM s'apropa i es manté a força constant sobre la SLB (AFM basat en *force clamp*)[19, 20] o s'apropa i s'allunya a velocitat constant.[21, 23, 45] Després del contacte mecànic, la deflexió de la micropalanca augmenta i la punta de l'AFM comprimeix elàsticament la SLB fins que la trenca sobtadament, entrant en contacte directe amb el substrat (figura 1.3). El moment en que la punta de l'AFM trenca la bicapa es veu representat per a una discontinuïtat en la corba de força-separació d'apropament (corba vermella en la

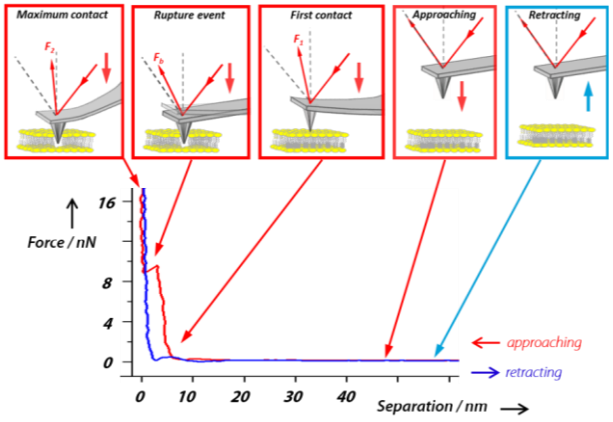

Figura 1.3 Esquema del procés de penetració d'una SLB utilitzant AFM-FS, mostrant una corba de força-separació típica que conté la discontinuïtat a la corba d'apropament quan la bicapa és trencada.

figura 1.3). La força vertical a la que ocorre la discontinuïtat correspon a la força màxima que la bicapa pot suportar fins que es trenca i es defineix com *breakthrough force* (F_b). La F_b acostuma a estar en el rang dels nN i és considerada com una mesura directa de les interaccions laterals entre les molècules de lípids. Informes previs demostren que la F_b es veu alterada per les variacions en l'estructura química dels fosfolípids[46, 47] i en l'entorn fisicoquímic (temperatura, pH o força iònica).[21, 46, 48, 49] És per això que la F_b es considera com l'empremta dactilar de l'estabilitat mecànica d'una bicapa concreta i en unes condicions ambientals específiques. En les SLBs de molts components, la F_b pot associar-se a la composició de la membrana de sistemes homogenis o de bicapes que presenten diferents dominis.[43, 50, 51]

1.3.2. Tècniques d'incidència rasant de XR: caracterització estructural

Les tècniques d'incidència rasant de XR s'han emprat per estudiar una gran varietat de mostres de molts camps diferents com la biologia, la química i la física, entre d'altres. Certament, les tècniques com XRR i GIXD (figura 1.4) s'han usat per caracteritzar les propietats estructurals de superfícies biològiques a escala nanomètrica.[32, 52, 53] Com s'ha comentat anteriorment, aquestes proporcionen informació sobre l'estructura de la mostra en l'espai recíproc, a través de la interacció entre els XR i la mostra. Les dades solen ser la mitjana de la informació obtinguda sota l'àrea il·luminada pel feix de XR, que va des dels centenars de micres fins als mil·límetres depenent de la mida del feix i de les condicions experimentals. Normalment les mesures es realitzen en sincrotrons, instal·lacions a gran escala amb feixos de XR d'alta brillantor. La radiació sincrotró permet investigar l'estructura dels materials que proporciona la densitat electrònica a alta resolució, permetent detectar escales de longitud que van dels àngstroms a les micres.

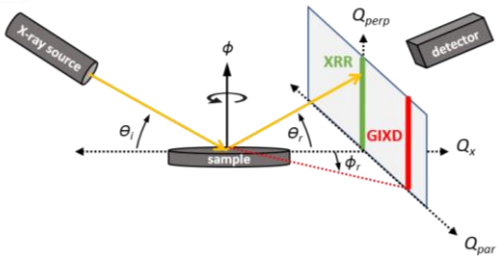

Figura 1.4 Diagrama de reflexió especular (θ_i i θ_r simètrics) i no-especular (θ_i i θ_r asimètrics) de XR, per adquisicions de XRR i GIXD, respectivament.

Malgrat tot, degut a que les tècniques de XR no requereixen d'una interacció mecànica amb la mostra, fa que les propietats mecàniques no puguin ser estudiades per XR. És per aquest motiu que la combinació dels XR amb la informació local i mecànica que s'obté amb l'AFM ha esdevingut important en l'última dècada.[54] Fins ara, la correlació *in situ* XR-AFM ha donat informació sobre processos dinàmics (reaccions químiques o transicions de fase), així com utilitzar la punta de l'AFM per a aplicar forces externes.

1.4. Objectius

L'objectiu general d'aquesta tesis és investigar les propietats fisicoquímiques i estructurals de membranes lipídiques model combinant tècniques de microscòpia i d'espectroscòpia de forces atòmiques (AFM i AFM-FS, respectivament) i de XR. L'AFM proporciona la informació morfològica i mecànica de les SLBs, mentre que els XR donen més coneixements en l'estructura electrònica de la bicapa. També proposem metodologies avançades basades en AFM-FS i XR, així com l'acoblament de les dues tècniques per dur a terme experiments locals *in situ*. Aquests processos tècnics ens permeten estudiar no només la diversitat en la composició química de les bicapes, sinó també la influència de molècules petites o pèptids en les propietats físiques i estructurals de la membrana. A més, amb AFM i AFM-FS també hem caracteritzat sistemes vesiculars que no contenen fosfolípids, els quals tenen una aplicació tecnològica: actuar com a nanotransportadors per al lliurament de fàrmacs.

En base a aquest objectiu general, els objectius específics són:

- Estudi de la nanomecànica per AFM i AFM-FS de SLBs de diferent composició (capítol 2) així com membranes de vesícules utilitzades en aplicacions biomèdiques (capítol 3).
- Avaluació de l'efecte de pèptids antimicrobians petits a les propietats estructurals i mecàniques de membranes model utilitzant tècniques d'AFM i XR (capítol 5).

- Establiment de metodologies avançades basades en les tècniques d'AFM-FS (capítol 4) i XR (capítol 6) per estudiar la mecànica i la organització lateral de SLBs, incloent el desenvolupament d'un AFM per utilitzar *in situ* durant mesures de sincrotró (capítol 7).

2. Bicapes de simples a complexes: estudi d'AFM i AFM-FS

Normalment, les propietats físiques de les BMs són difícils d'avaluar, incloent les que afecten als processos biològics mediats per la membrana.[1] A més, degut a que la composició de les membranes biològiques és tan complexa, ja que conté una gran quantitat de SLs junt amb Chol i glicerofosfolípids, fa que la seva caracterització fisicoquímica sigui encara més complicada. De fet, per a coordinar les seves funcions, la membrana és capaç de segregar lateralment petites agrupacions de lípids riques en Chol, SLs i proteïnes a la seva capa exterior,[6, 7] les quals tenen una influència important en funcions essencials dins de la senyalització i el tràfic en la membrana.[6, 9] Per aquest motiu, tècniques nanomètriques són necessàries per a explorar l'heterogeneïtat de les propietats físiques de les membranes biològiques.

Sistemes models de membrana, com les SLBs, s'utilitzen freqüentment per a mimetitzar BMs, permetent-ne la investigació de processos biològics que ocorren a nivell cel·lular i subcel·lular.[16, 22] Així doncs, l'ús de plataformes manejables de membrana en facilita la caracterització fisicoquímica, donant la possibilitat d'incrementar la complexitat de la bicapa, des d'un sol component, a d'altres que en continguin més d'un. Gràcies a la possibilitat de treballar en ambients controlats, la microscòpia de forces atòmiques (AFM) és avui en dia una tècnica ben establerta tant per a adquirir una imatge de morfologia com per a analitzar les propietats nanomecàniques locals de SLBs mitjançant modes d'espectroscòpia de forces.[21-25] En aquest treball (veure capítol 2), ens hem centrat en estudiar les propietats físiques de SLBs de fosfocolines (PC), abans i després d'incorporar Chol o/i un glicoesfingolípid (GSL), incrementant-ne la complexitat de la membrana.

El Chol pot arribar fins a concentracions del 50 % en molar de tot el lípid que conté la membrana plasmàtica de les cèl·lules. Certament, el Chol juga un paper essencial en la modulació de les propietats mecàniques, sent molt important en la funció i l'evolució de la membrana biològica.[5, 55] Regula la fluïditat de la membrana, controla l'organització i la fase dels lípids, i n'augmenta l'estabilitat mecànica.[21, 43, 56]

Dins la família dels SLs, els GSLs són comunicadors importants utilitzats per les cèl·lules, que actuen com a receptors en la senyalització, els processos d'adhesió microbiana i cel·lular, i exposen una identitat immunològica.[57, 58] Es considera que el Chol juga un paper essencial en els mecanismes relacionats amb la funció receptora dels GSLs,[59-62] regulant l'accessibilitat dels GSLs a través de configuracions de conformació directes dels grups del

cap dels fosfolípids. Aquí, ens hem centrat en les galactosilceramides (GalCer), les quals es troben normalment molt saturades en fonts naturals.[63, 64] Les GalCer es troben principalment en teixits neuronals i estan involucrades en una gran varietat d'activitats biològiques com ara interaccions entre cèl·lules, comunicacions intracel·lulars, desenvolupaments cel·lular i efectes antitumorals i citotòxics.[65] Les GalCer estan alineades en una manera compacta i tendeixen a acumular-se a la capa externa de la membrana junt amb el Chol.[64, 66] Per aquest motiu, és molt important entendre el comportament mecànic de les bicapes lipídiques i la funció física de cada component de la membrana.

En aquest treball (veure capítol 2), hem presentat l'ús de les tècniques ja ben establertes d'AFM i AFM-FS per caracteritzar el comportament de la fase i les propietats nanomecàniques de SLBs de PC, incorporant-ne després components (GalCer i/o Chol) per augmentar la complexitat dels sistemes. Hem confirmat que l'estat del fosfolípid (gel, en el cas de DPPC, o fluid, en el cas de DLPC) a la temperatura de treball és un paràmetre definitiu que governa el comportament de la mescla de lípids en la bicapa que inclou Chol i GalCer.

Un cop introduït el GalCer, no s'ha observat segregació de fases en les SLB de DPPC, mentre que separació en dominis s'ha manifestat en les SLBs de DLPC (figura 2.1). En general, quantitats fins a un 20 mol % de GalCer han provocat un augment en l'estabilitat nanomecànica pels dos sistemes (figura 2.2). Curiosament, els dominis segregats en la SLB de DLPC:GalCer tenen una estabilitat mecànica extremadament alta, mentre que augmentar la quantitat de GalCer confereix, per la fase continua rica en DLPC, característiques típiques

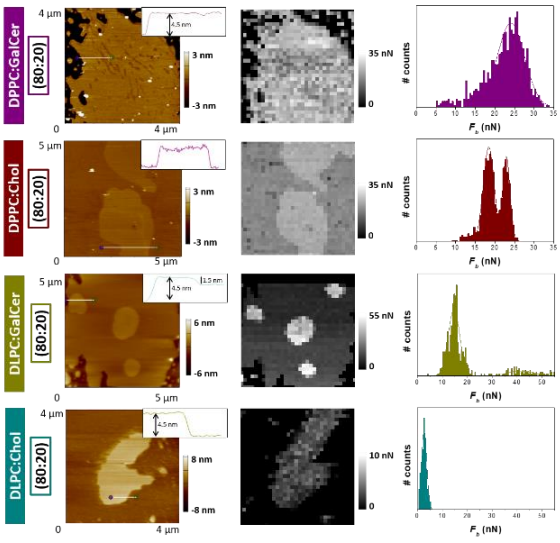

Figura 2.1. SLBs de DPPC:GalCer (80:20 en relació molar), DPPC:Chol (80:20 en relació molar), DLPC:GalCer (80:20 en relació molar) i DLPC:Chol (80:20 en relació molar) en mica en 150 mM NaCl, 20 mM $MgCl_2$, 20 mM HEPES (pH 7.4) i *RT*. a) Topografies i perfils obtinguts per AFM. b) Mapes de F_b. c) Distribucions de F_b.

d'una SLB en fase gel. Contràriament, 20 mol % de Chol ha provocat segregació de fases diferents i augment de la nanomecànica del sistema de DPPC, mentre que homogeneïtat i valors similars de F_b s'han obtingut per SLBs de DLPC (figures 2.1 i 2.2).

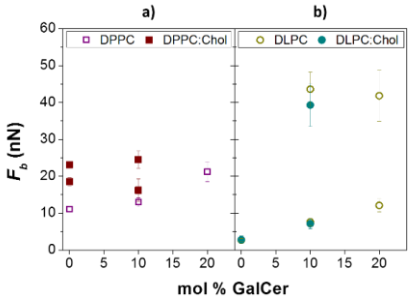

Figura 2.2. Valors de F_b de (a) sistemes de DPPC i DPPC:Chol (20 mol % Chol) i (b) sistemes de DLPC i DLPC:Chol (20 mol % Chol) en funció del contingut de GalCer. Tot els experiments s'han realitzat en 150 mM NaCl, 20 mM $MgCl_2$, 20 mM HEPES (pH 7.4) i a *RT*.

Quan hem estudiat les bicapes de 3 components, sembla que el Chol ha sigut determinant en la formació de dominis, en la distribució del GalCer i en augmentar les propietats mecàniques de les SLBs de DPPC:Chol:GalCer (figures 2.3 i 2.2). Per altra banda, per les SLBs de DLPC:Chol:GalCer, la fase i l'estabilitat mecànica han estat dominades per la immiscibilitat parcial del GalCer, mentre que el Chol gairebé no ha afectat a les bicapes de DLPC que contenen baixes quantitats de GalCer (figures 2.3 i 2.2).

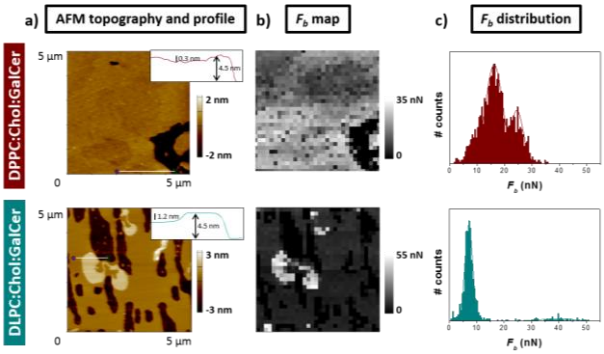

Figura 2.3. SLBs de DPPC:Chol_GalCer (70:20:10 en relació molar) i DLPC:Chol:GalCer (70:20:10 en relació molar) en mica en 150 mM NaCl, 20 mM $MgCl_2$, 20 mM HEPES (pH 7.4) i *RT*. a) Topografies i perfils obtinguts per AFM. b) Mapes de F_b. c) Distribucions de F_b.

3. Membranes de quatsomes: estudi d'AFM i AFM-FS

Durant l'última dècada, s'ha esperat que l'aplicació de la nanotecnologia al consum de medicaments canviés el panorama de les indústries farmacèutiques i biotecnològiques.[67] Entre els primers sistemes nanotecnològics de lliurament de fàrmacs, els liposomes (LPs)

han esdevingut una de les eines més prometedores per transportar drogues dins del camp de la medicina.[68-70] Avantatges com la biocompatibilitat, el baix nivell de toxicitat i la possibilitat d'encapsular drogues dins del seu nucli aquós i/o en la seva bicapa, fan que els LPs siguin candidats favorables per protegir i transportar components actius de formulacions farmacèutiques i cosmètiques.[68, 71, 72] Tanmateix, els LPs tenen una permeabilitat de membrana alta, provocant fugues de les drogues captades, així com també tenen estabilitats col·loïdals i químiques pobres, que en causen la seva agregació.[69, 72, 73] En canvi, l'ús de fosfolípids en estat gel disminueix la permeabilitat dels LPs, però les vesícules es tornen més rígides, el qual és un inconvenient per algunes de les aplicacions que requereixen de vesícules deformables, com ara el cas del lliurament transdèrmic. Per tal de superar aquestes limitacions, hi ha hagut un gran interès en desenvolupar nou sistemes que s'uneixin donant vesícules estables, complint els requeriments per les formulacions farmacèutiques.[74-76] Estructures no-liposomals compostes per alguns lípids que es poden unir en condicions específiques amb tensioactius,[77] polímers[78] o polipèptids,[79] entre d'altres, han estat reportats com una nova generació de sistemes vesiculars que contenen com a mínim un lípid natural o sintètic. La composició de les estructures vesiculars depèn llavors de les propietats fisicoquímiques (mida, densitat de càrrega, morfologia, lamel·laritat i deformabilitat vesicular) i de l'eficiència per encapsular drogues necessàries, considerant la possibilitat de generar aquest nanotransportadors amb funcionalitats múltiples.[67] En el cas d'algunes aplicacions específiques, com ara la millora en la penetració de la pell, s'ha proposat que la deformabilitat de les vesícules transportadores no és únicament un interès fonamental, sinó que és un paper clau en l'habilitat de la vesícula de travessar la barrera dèrmica.[80]

Els quatsomes (QTs) són nanovesícules unilamel·lars constituïdes per tensioactius d'amoni quaternari i esterols en proporció equimolar (figura 3.1).[72, 73, 81] Aquests sistemes vesiculars són estables durant molts anys i les seves morfologies no canvien al augmentar la temperatura o la dilució, mostrant una excepcional homogeneïtat vesícula a vesícula pel que fa a mida, lamel·laritat i organització supramolecular de membrana.[73, 82, 83] Aquestes propietats fan que els QTs siguin sistemes ideals per a funcionalitzar-ne la seva membrana, la qual cosa és molt important per aconseguir una direcció del fàrmac concreta, robusta i eficient.[84, 85] Els QTs compleixen els requisits estructurals i fisicoquímics com a plataformes

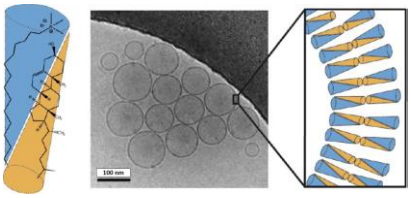

Figura 3.1 Esquema del sintó QT compost per molècules de *cetyl trimethylammonium bromide* (CTAB) i Chol i imatge de cryo-TEM de vesícules de QTs.

potents pel que fa a l'encapsulament de components actius terapèutics i de diagnosi que han de ser lliurats en un lloc específic. Segons el tensioactiu catiònic i l'esterol, així com el medi de suspensió utilitzat per a preparar els QTs, les propietats mecàniques de la bicapa dels QTs i la flexibilitat de la vesícula sencera poden ser ajustades.

En aquest treball (veure capítol 3), hem utilitzat les tècniques d'AFM i AFM-FS per caracteritzar per primera vegada la morfologia i les propietats mecàniques de membranes suportades de QTs (SQMs) en diferents medis líquids i *T* (figura 3.2). Mentre una topografia homogènia en el temps s'ha observat per la membrana de QTs en aigua (QT_H_2O), la membrana de QTs en PBS (QT_PBS) ha mostrat un comportament dinàmic passant d'una membrana amb separació de dominis a una SQM homogènia a *RT*. Amb l'AFM-FS hem determinat l'efecte de la presència de ions en el medi líquid, que ha causat l'augment de les interaccions laterals entre les molècules de la membrana, incrementant-ne la F_b.

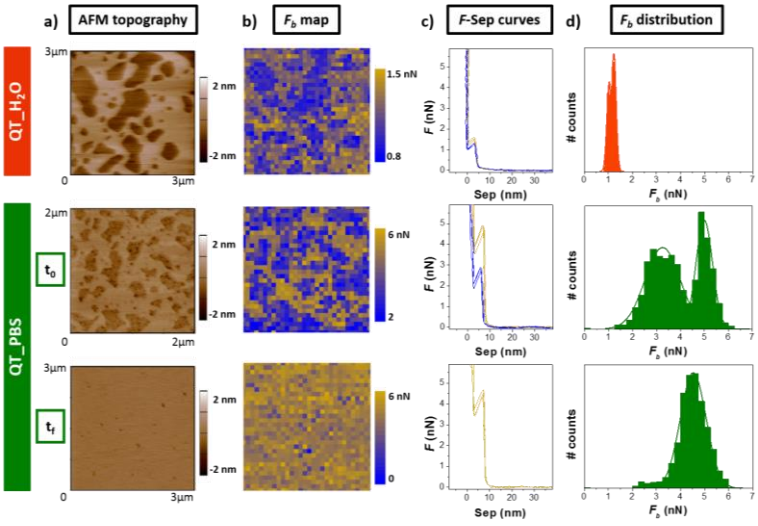

Figura 3.2 SQMs de QT_H_2O i QT_PBS (a t_0 i t_f) dipositades sobre mica i a *RT*. a) Imatges topogràfiques d'AFM. b) Mapes de F_b. c) Corbes de *F*-Sep. d) Distribucions de F_b.

També hem estudiat la influència de la temperatura a les SQMs, comparant les diferents morfologies de QT_H_2O i QT_PBS obtingudes amb l'AFM amb les simulacions de *Molecular Dynamics* (MD) realitzades a diferents *T*. Hem detectat que la simetria de les capes de la bicapa observada a 50 ºC es trenca als 10 ºC, i que la coexistència de les dues configuracions ocorre a una temperatura intermèdia, que coincideix amb els resultats observats amb l'AFM.

Finalment, hem avaluat l'elasticitat de vesícules senceres depositades sobre substrats de silici, on hem observat, un altre cop, que els ions en la solució tampó indueixen a una nanomecànica més alta, augmentant la rigidesa de les vesícules QT_PBS en relació a les QT_H_2O.

4. Extracció de tubs lipídics a partir de membranes model

Molts processos cel·lulars, incloent endocitosis, resegellar, senyalització i transcripció de membranes, entre d'altres, requereixen de canvis conformacionals com ara flexió, vesiculació i tubulació.[5] Per exemple, en la endocitosis, el sistema endocític necessita generar força suficient per a formar una vesícula endocítica doblant la bicapa de la membrana.[86] La separació d'un segment de membrana del citoesquelet així com la forta flexió de la membrana estan involucrats en aquests mecanismes, els quals també estan associats a la composició química de la membrana i a les seves propietats fisicoquímiques.[5]

Estudis *in vitro* de mecànica de membrana han mostrat que canvis subtils en la composició de la membrana afecten la resposta mecànica general. L'aspiració amb micropipeta és, per exemple, una de les tècniques més utilitzades per avaluar l'elasticitat de GUVs a escala mesoscòpica.[15, 87] De totes formes, la composició complexa i heterogènia de les membranes, amb dominis a la micro i nanoescala, requereix de tècniques locals amb resolució nanomètrica com l'AFM, o específicament l'AM-FS, per estudiar SLBs.[21, 23] En aquests experiments, la punta de l'AFM s'utilitza típicament com un sensor de forces que penetra una SLB individualment.

Malgrat tot, existeix encara la preocupació de l'efecte desconegut del substrat en les mesures de les propietats mecàniques, així com la impossibilitat de mesurar la curvatura de la bicapa degut al seu confinament bidimensional. En efecte, tal i com s'ha comentat en el capítol d'introducció, sistemes alternatius s'han proposat per a superar aquestes limitacions. Encara que aquests mètodes requereixen de protocols molt més complexes que el simple de SLBs pel que fa a la preparació de les mostres, permeten una caracterització física de la bicapa independent de l'efecte del substrat.

Els experiments d'AFM s'han expandit també en la caracterització de la mecànica de cèl·lules vives, permetent l'avaluació de l'elasticitat de la cèl·lula,[88] incloent la contribució de la membrana plasmàtica i del citoplasma i el citoesquelet de sota,[89] o inclús punxant a través de les diferents membranes amb la punta d'AFM. A més, la punta de l'AFM també és pot utilitzar per a estirar lípids des de cèl·lules i membranes mentre s'aplica una força ortogonal a una regió petita de la membrana,[86] procés que és molt similar al de vesiculació o tubulació de cèl·lules.

Una situació més simple però similar ocorre quan tubs de lípids són estirats per AFM des de SLBs. Aquest enfoc combina els avantatges de l'AFM de caracteritzar una mostra localment amb resolució lateral nanomètrica i aplicar i detectar forces en el rang dels pN, amb la simplicitat de la preparació de les SLBs. Així doncs, en la part d'apropament d'una corba força-separació (figura 4.1, corba vermella puntejada), observem la discontinuïtat que defineix la F_b un cop la punta d'AFM trenca la bicapa. Quan la punta s'allunya de la mostra (figura 4.1, corba blava), la punta es manté connectada a la superfície a través d'un tub de

lípids, que va creixent a mesura que la punta s'allunya fins a una certa distància en que es trenca i la micropalanca retorna a la posició d'equilibri. El procés de creixement del tub ocorre a una força constant F_{tube} i s'observa com un pla de força en l'allunyament dels enregistraments força-separació a poques desenes de pN.

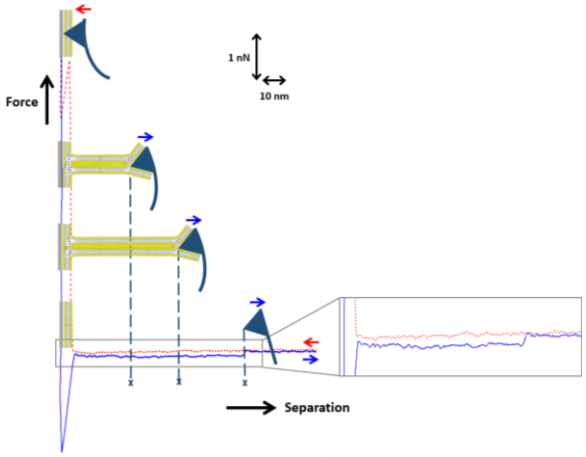

Figura 4.1 Esquema d'una corba de forca-separació mentre s'estira un tub des d'una SLB.

En aquest treball (capítol 4), proposem l'ús de la punta d'AFM per estirar tubs de lípids des de SLBs model com una estratègia metodològica per explorar les propietats mecàniques de membranes lipídiques mitjantçant l'avaluació de F_{tube} (figura 4.2). Estudiant SLBs de diferent composició, hem demostrat que aquesta estratègia permet estimar la contribució de la composició química a la mecànica de la membrana. Hem establert que l'estat del fosfolípid en la SLB determina la força del creixement del tub, que en general és més alta per bicapes s_o que per les l_d. Hem exposat que F_{tube} també depèn del grup del cap del fosfolípid, augmentant els valors des de les bicapes de PE a les de PC i després a les de PG, degut a les

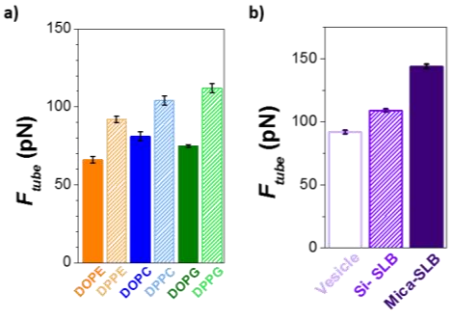

Figura 4.2 Valors de F_{tube} per: a) SLBs de DOPE, DPPE, DOPC, DPPC, DOPG i DPPG en 150 mM NaCl, 20 mM $MgCl_2$, 20 mM HEPES (pH 7.4) i a *RT*. b) Vesícules depositades sobre Si i bicapes suportades sobre Si i mica en 94 mM NaCl, 3.1 mM Na_2HPO_4, 0.9 mM NaH_2PO_4 (pH 7.4) i a *RT*.

interaccions més fortes entre els grups del cap dels fosfolípids carregats (PG) i els ions presents en la solució tampó (figura 4.2(a)). Aquest comportament és comparable al que s'observa amb la tècnica de F_b.

A més, hem mostrat que es pot determinar la influència del substrat en el valor de F_{tube}, comparant el creixement de tubs des de vesícules depositades i bicapes lipídiques suportades en diferents substrats (silici o mica) (figura 4.2(b)). Així doncs, hem demostrat que els models de SLB representen un escenari intermedi entre una membrana lliure i una membrana suportada pel citoesquelet.

5. Efecte de la defensina HNP1 en bicapes lipídiques suportades model

La membrana cel·lular és la primera línia de defensa contra espècies invasores. La seva composició i la interacció no-específica amb molècules petites poden alterar-ne les propietats estructurals i físiques, afectant les interaccions entre la membrana i les molècules que l'envolten. Les interaccions membrana-pèptid juguen un paper essencial en un gran nombre d'esdeveniments biològics, incloent fusió i lisis de membrana.[90] Exemples de pèptids que han estat investigats fins ara són els pèptids model, els pèptids antimicrobians (AMPs), els pèptids derivats de virus, els pèptids de penetració de cèl·lules i els pèptids amiloides.[91]

Les defensines són AMPs de 2-6 kDa, rics en cisteïnes (Cys), catiònics i actius contra diferents bacteris, fongs i virus.[92] En humans, les defensines *human neutrophil peptides* (HNPs) contribueixen a la defensa pròpia matant i desactivant ràpidament els microbis.[93-95] Malgrat tot, els mecanismes pels quals les defensines maten els microorganismes no es coneixen del tot, tot i que en general es creu que la matança és una conseqüència de la disrupció de la membrana micriobiana.[96] Les defensines són molècules amfipàtiques que tenen clústers d'aminoàcids carregats positivament i cadenes laterals d'aminoàcids hidrofòbics. Aquesta topologia polar els hi permet inserir-se dins la membrana fosfolipídica de manera que les seves regions hidrofòbiques queden enterrades a l'interior de la bicapa lipídica, mentre que les regions carregades, normalment catiòniques, interactuen amb els grups aniònics del cap dels fosfolípids i l'aigua.[97] Molts mecanismes, incloent formació de porus, solubilització de la membrana, translocació del pèptid i aprimament de la membrana, han estat proposats considerant pèptids de diferent longitud, hidrofobicitat, càrrega i estructura secundària.[98, 99] Sembla que es veuen iniciats per l'associació de la superfície de la part hidrofòbica amb els grups del cap del lípid, seguit de la irrupció de la membrana a un llindar concret de concentració del pèptid. És per això que és important aprofundir en l'especificitat lipídica dels AMPs actius de membrana i la seva influència en les propietats integrals de les membranes, per entendre millor la seva activitat en contra cèl·lules mamàries o bacterianes.[98]

L'HNP1 és una de les formes més abundants de la família de les α-defensines, produïda en els grànuls citoplàsmics azurilfàlics dels neutròfils. Aquest monòmer de 30 aminoàcids es troba fortament estabilitzat per tres ponts disulfúrics de Cys (senyalats en vermell a la figura 5.1(a)),[100] que interconnecten cada pla-β. És conegut per ser present com a dímer en solució, on cada monòmer presenta una càrrega positiva neta igual a +3 (figura 5.1(c)), atorgada per quatre residus d'arginina i un àcid glutàmic negatiu. A més, s'ha establert que la composició lipídica és determinant per la selectivitat del HNP1 per interactuar amb la membrana. El triptòfan (Trp)-26 (senyalat en lila a la figura 5.1(b)) ha estat reportat de ser el residu més crític del HNP1, contribuint a la funció de la defensina a nivells múltiples.[95, 101] El Trp proporciona una energia d'enllaç alta degut a la seva possibilitat d'interaccionar amb molècules hidrofòbiques, com la membrana bacteriana. A més, el Trp-26 té un rol significatiu en l'estabilització de l'estructura de dímers de HNP1, que provoquen la formació de porus en la membrana microbiana.[95]

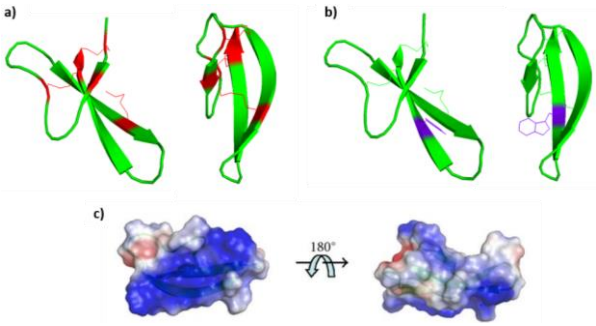

Figura 5.1 Dues orientacions de l'estructura de l'HNP1. a) Ponts disulfúrics i Cys senyalats en vermell. b) Trp senyalat en lila. c) Mapa de densitat electrostàtica de superfície de l'HNP1: càrregues negatives senyalades en blau I les negatives en vermell.

En aquest treball (veure capítol 5), hem avaluat sistemàticament la influència de la defensina HNP1 en les propietats estructurals i mecàniques de bicapes de diferent composició, incloent fosfolípids neutres i amb càrrega. En general, hem confirmat que el pèptid afecta a les SLBs de PC d'una manera més específica i localitzada, mentre que altera les SLBs de PE i PE:PG de forma general.

Dels resultats de AFM i XR en bicapes de PC, hem observat un augment de la F_b que provoca un empaquetament dels grups superiors dels caps de la SLB de DPPC, mentre que el pèptid sembla que s'insereix dins de la SLB de DOPC sense causar un canvi significatiu en la mecànica de la bicapa. Per altra banda, aquesta diferència és detectada en l'elasticitat de la SLB de DOPC quan l'HNP1 és dins la membrana, el qual facilita la reorientació de la membrana estabilitzant-ne els forats un cop punxada amb la punta de l'AFM.

Pel que fa a les bicapes de PE i PE:PG, hem determinat que la defensina HNP1 produeix generalment un aprimament de la membrana de DOPE, resultat observat per les dues

metodologies d'AFM i XRR. Després de substituir un 75 % en mols de DOPE per PG, no hem observat canvis rellevants pel que fa a la mescla fluida (DOPE:DOPG), mentre que el pèptid sembla que dissol els dominis alts rics en DPPG així com n'incrementa la rugositat general de la SLB.

6. Organització molecular en el pla d'una única bicapa lipídica hidratada: DPPC:Colesterol

Les membranes que contenen fosfolípids i Chol han estat àmpliament estudiades, incloent models simplificats basats en dos components. En particular, per a definir els diagrames de temperatura-composició del sistema DPPC:Chol s'han utilitzat diferents tècniques, com ara ressonància magnètica nuclear (NMR), calorimetria d'escaneig diferencial (DSC) o dispersió de neutrons i XR.[102-107] No obstant això, encara existeixen discrepàncies en la determinació d'un diagrama de fase complet capaç de cobrir tot el rang temperatura i l'espai de composicions. L'AFM i l'AFM-FS han proporcionat informació sobre la transició tèrmica de SLBs de DPPC:Chol a escala nanomètrica, definint la coexistència de diferents dominis i facilitant la relació entre el contingut de Chol i la organització lateral de la membrana.[23, 43, 45, 108]

Informació sobre segregació de fases en bicapes lipídiques també es pot obtenir mitjançant tècniques de dispersió de XR, proporcionant una resolució significativament més alta, per exemple, en comparació, amb l'AFM. Els XR són tècniques molt potents i no invasives que han estat àmpliament utilitzades en estudis sobre bicapes lipídiques, investigant en escales de longituds que van des dels àngstroms fins a les micres. Fins ara, una gran part dels experiments basats en XR s'han centrat en determinar l'estructura electrònica vertical de monocapes lipídiques, bicapes o conjunts de bicapes (també anomenats multi-bicapes) a les interfícies líquid/aire i sòlid/líquid, respectivament, per mitjà de XRR, que és una tècnica ben establerta en el camp.[30, 33, 34, 52, 109]

El coneixement sobre l'estructura lateral en el pla de membranes biològiques es pot obtenir a través de GIXD. Malgrat tot, la necessitat de preservar la mostra hidratada per garantir-ne l'estabilitat a la interfície sòlid/líquid fa que la caracterització estructural en el pla d'una única bicapa lipídica sigui tot un repte. La presència d'una capa hidratada requereix l'ús de XR d'alta energia per augmentar la transmissió a través del líquid, cosa que fa que les molècules orgàniques donin, com a conseqüència, un senyal més feble.[52] A més, la difracció generada per l'entorn líquid augmenta el nivell del fons, que complica la detecció del senyal difractat per l'estructura de la bicapa. Per aquesta raó, la majoria d'informació estructural relativa a membranes lipídiques obtinguda per GIXD s'ha extrapolat d'experiments realitzats en multi-bicapes[110, 111] o en monocapes a la interfície líquid/aire.[112] De totes formes, les monocapes de lípids no representen la naturalesa laminar d'una membrana i les propietats físico-químiques de les multi-bicapes també difereixen de les

d'una bicapa única. Degut a la facilitat de formació i d'arranjament laminar únic, les SLBs són dels models més comuns per representar BMs,[113] a més de vesícules uni-laminars grans i gegants. Per aquest motiu, només pocs estudis de GIXD sobre bicapes úniques hidratades s'han arribat a publicar amb èxit, els quals han requerit de configuracions complexes i condicions d'humitat controlada durant les mesures.[32, 114, 115]

En aquest treball (veure capítol 6), hem presentat una configuració nova, senzilla i de fàcil ús (figura 6.1(a)) basada en una cel·la de capa fina (Si-SLB-Si), que permet l'adquisició amb èxit de dades de GIXD en SLBs individuals i hidratades (figura 6.2(b)). Això permet reduir la dispersió del líquid i revelar el senyal extremadament feble difractat per la membrana lipídica, capaç de detectar la coexistència de diferents dominis en membranes que presenten segregació de fases.

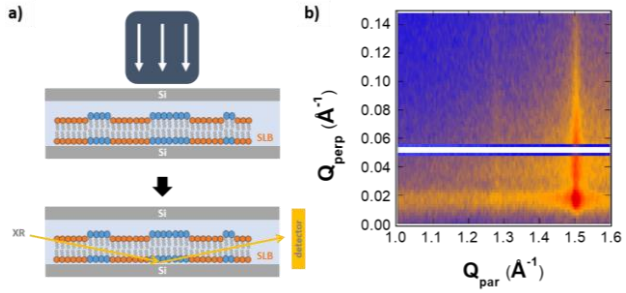

Figura 6.1. a) Esquema de la configuració utilitzada per les mesures de GIXD, mostrant l'arranjament Si-SLB-Si. b) Gràfic 2D de la intensitat difractada per a una SLB de DPPC:Chol (90:10 en relació molar) en la configuració Si-SLB-Si.

Hem registrat patrons de GIXD de bicapes de DPPC suportades en substrats de Si que contenen diferents quantitats de Chol, i hem proporcionat informació sobre la seva estructura a nivell submolecular (figura 6.2). Per les bicapes que presenten segregació de fases (DPPC:Chol 90:10 i 80:20 en relació molar) s'han assignat dos valors de distància intermolecular pel DPPC en cada fase, mentre que per les bicapes homogènies (DPPC:Chol 60:40 i 50:50 en relació molar), s'ha obtingut únicament un sol valor, resultats que estan en acord amb el diagrama de fases d'aquest sistema binari.[43, 112, 116] El valor més alt de distància correspon a la fase rica en Chol, on les molècules de DPPC i Chol podrien estar intercalades en una proporció gairebé estequiomètrica. Això representa un escenari raonable per a obrir noves vies d'investigació en l'estructura i processos dinàmics de membranes cel·lulars en ambients fisiològics.

7. AFM adaptat per línies de sincrotró XR

La comprensió dels mecanismes que governen l'estructura de les membranes biològiques, així com la organització i la dinàmica dels seus constituents, requereixen d'un

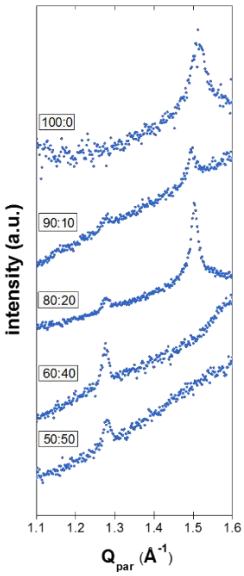

Figura 6.2. Patrons de Q_{par} i intensitat GIXD (integrada sobre Q_{perp}) de bicapes de DPPC:Chol en relació molar 100:0, 90:10, 80:20, 60:40 and 50:50 i configuració Si-SLB-Si. Les mesures estan realitzades en una solució tampó de 20 mM HEPES, 150 mM NaCl, 20 mM $MgCl_2$ (pH 7.4) i a *RT*.

enfocament multimodal recolzat per vàries tècniques de caracterització. Sovint, un desenvolupament instrumental sol ser el primer pas d'aquest enfocament multimodal i correlatiu. En aquest treball, exposem el desenvolupament d'un instrument que té com a objectiu correlacionar els canvis estructurals, morfològics i mecànics que passen a la nanoescala i mesoescala (figura 7.1), permetent caracteritzar efectes específics de remodelació de la membrana. El desenvolupament es centra en l'ús simultani i correlatiu de tècniques de AFM i XR de sincrotró (combinació AFM-XR).

Durant moltes dècades, les tècniques de XR amb incidència rasant han estat utilitzades per caracteritzar una gran varietat de mostres, ampliant el coneixement a molts camps des de la física a la biologia i la química. En aquest tipus d'experiments, la informació estructural obtinguda a través de la interacció entre els XR i la mostra sol ser la mitjana de tota la informació adquirida sota l'àrea il·luminada pel feix, que cobreix una superfície molt més gran que l'accessible amb l'AFM. De totes formes, degut a que les tècniques de XR no interaccionen mecànicament amb les mostres, no és possible avaluar-ne les propietats mecàniques. Per aquesta raó, la combinació dels XR amb la informació local i nanomecànica que es pot obtenir amb AFM ha esdevingut molt potent en l'última dècada, introduint molts esquemes operacionals amb els quals ja s'han arribat a obtenir resultats satisfactoris.[117-120] No obstant això, alguns dels elements mecànics de l'AFM han limitat les aplicacions al camp de ciència de materials, impedint l'exploració de mostres biològiques en ambient líquid.

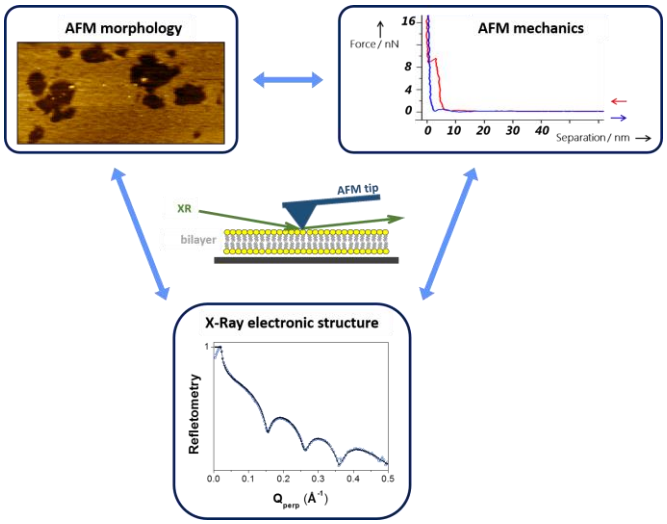

Figure 7.1 Esquema que descriu l'objectiu del desenvolupament del nostre instrument: correlacionar la informació estructural (XR), morfològica (AFM) i mecànica (AFM-FS).

En aquest treball (veure capítol 7), hem presentat el disseny de l'estructura d'un AFM (figura 7.2) que s'ha construït per a ser instal·lat en línies de sincrotró, permetent realitzar experiments de XR d'incidència rasant simultàniament amb la caracterització a la nanoescala de la topografia i la mecànica obtinguda per AFM. La posada en marxa de l'instrument s'ha dut a terme a la línia ID03 del sincrotró ESRF de Grenoble, explorant monocapes i bicapes lipídiques a les interfícies sòlid/aire i sòlid/líquid, respectivament. En el cas de les SLBs hidratades, tant l'estructura com la morfologia i les propietats mecàniques s'han caracteritzat en el mateix temps i lloc de la mostra. Això confirma la capacitat de l'instrument d'estudiar mostres toves i biològiques en entorn líquid, tot i estant instal·lat sobre l'hexàpode d'una línia de sincrotró.

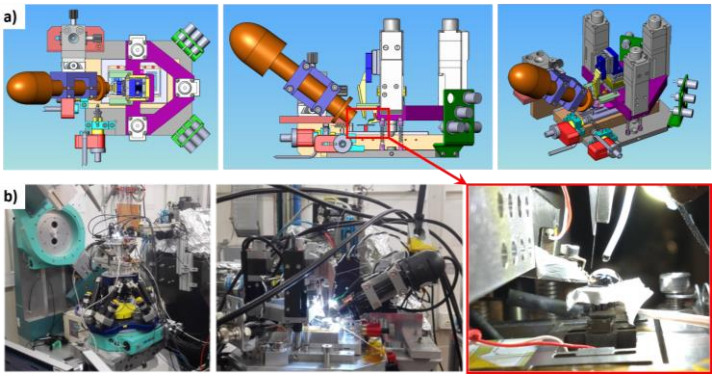

Figure 7.2 a) Disseny de l'estructura de l'AFM des de diferents plans. b) Fotografies de l'AFM muntat sobre l'hexàpode de la línia ID03 del sincrotró ESRF de Grenoble (França).

Se sap que la limitació pel dany de radiació és un repte important quan s'utilitzen feixos de XR intensos en mostres toves o biològiques.[121] En el capítol 7, hem evidenciat els efectes induïts pel feix de XR a temps real en bicapes de DOPC i DPPC tant per AFM com per XRR. Hem mostrat que és necessària la caracterització del dany per radiació per a poder avaluar els paràmetres estructurals dels fosfolípids. Hem establert que l'ús de XR d'alta energia (30 keV) és més adequat en comparació amb energies inferiors (≈ 20 keV), les quals han estat convencionalment utilitzades en la literatura recent.

Finalment, hem mostrat que els XR, l'AFM i l'AFM-FS correlatius poder ser utilitzats per caracteritzar *in situ* els efectes de remodelació de la membrana, com ara transicions de fase de membranes fosfolipídiques models. Hem correlacionat l'augment del desordre, caracteritzant una SLB de DPPC passant de fase gel a fluida, amb la disminució de l'estabilitat mecànica avaluada per AFM-FS durant la transició de fase.

8. Conclusions

Hem explorat les propietats fisicoquímiques i estructurals de models de membranes lipídiques combinant les tècniques d'AFM, AFM-FS i XR. L'AFM ens ha proporcionat la informació sobre la morfologia i la mecànica de les membranes, com a conseqüència de la diversitat en la composició química de bicapes compostes o no de fosfolípids. Aquest enfoc multimodal d'AFM + XR ens ha permès investigar la influència de pèptids petits en les propietats físiques i estructurals de les membranes. A més, hem exposat un avanç en noves metodologies basades en ambdues tècniques d'AFM-FS i XR de forma independent, així com la combinació de les dues.

9. Referències

1. W. Dowhan, *Annu. Rev. Biochem*, 1997, **66**, 199-232.
2. O. Mouritsen and L. Bagatolli, "Life - As a Matter of Fat", *Springer International Publishing AG*, 2015.
3. P. L. Yeagle, "The Membranes of Cells", *Academic Press*, Boston, 2016, pp. 1-25.
4. S. J. Singer and G. L. Nicolson, *Science*, 1972, **175**, 720.
5. G. van Meer, D. R. Voelker and G. W. Feigenson, *Nat. Rev. Mol. Cell Bio.*, 2008, **9**, 112-124.
6. D. Lingwood and K. Simons, *Science*, 2010, **327**, 46-50.
7. K. Simons and W. L. C. Vaz, *Annu. Rev. Biophy. Biom.*, 2004, **33**, 269-295.
8. E. Sezgin, I. Levental, S. Mayor and C. Eggeling, *Nat. Rev. Mol. Cell Bio.*, 2017, **18**, 361.
9. S. Chiantia, N. Kahya and P. Schwille, *Langmuir*, 2007, **23**, 7659-7665.
10. J. C. M. Holthuis and T. P. Levine, *Nat. Rev. Mol. Cell Bio.*, 2005, **6**, 209.
11. P. A. Janmey and P. K. J. Kinnunen, *Trends Cell Biol.*, 2006, **16**, 538-546.
12. E. Hohenester, *Curr. Opin. Struc. Biol.*, 2014, **29**, 10-16.
13. P. Roca-Cusachs, T. Iskratsch and M. P. Sheetz, *J. Cell Sci.*, 2012, **125**, 3025.
14. A. E. M. Beedle, A. Williams, J. Relat-Goberna and S. Garcia-Manyes, *Curr. Opin. Chem. Biol.*, 2015, **29**, 87-93.
15. E. Evans, V. Heinrich, F. Ludwig and W. Rawicz, *Biophys. J.*, 2003, **85**, 2342-2350.
16. M.-P. Mingeot-Leclercq, M. Deleu, R. Brasseur and Y. F. Dufrene, *Nat. Protoc.*, 2008, **3**, 1654-1659.

17. J. Majewski, J. Y. Wong, C. K. Park, M. Seitz, J. N. Israelachvili and G. S. Smith, *Biophys. J.*, 1998, **75**, 2363-2367.
18. H. L. Smith, M. S. Jablin, A. Vidyasagar, J. Saiz, E. Watkins, R. Toomey, A. J. Hurd and J. Majewski, *Phys. Rev. Lett.*, 2009, **102**.
19. L. Redondo-Morata, M. I. Giannotti and F. Sanz, *Langmuir*, 2012, **28**, 6403-6410.
20. J. Relat-Goberna, A. E. M. Beedle and S. Garcia-Manyes, *Small*, 2017, **13**, 1700147-n/a.
21. L. Redondo-Morata, M. I. Giannotti and F. Sanz, *Mol. Membr. Biol.*, 2014, **31**, 17-28.
22. L. Redondo-Morata, M. I. Giannotti and F. Sanz, "Atomic Force Microscopy in Liquid", *Wiley-VCH Verlag GmbH & Co.KGaA*, Weinheim, Germany, 2012.
23. S. Garcia-Manyes and F. Sanz, *BBA - Biomembranes*, 2010, **1798**, 741-749.
24. L. Picas, P. E. Milhiet and J. Hernandez-Borrell, *Chem. Phys. Lipids*, 2012, **165**, 845-860.
25. K. El Kirat, S. Morandat and Y. F. Dufrene, *BBA - Biomembranes*, 2010, **1798**, 750-765.
26. G. Fragneto, T. Charitat and J. Daillant, *Eur. Biophys. J. Biophy.*, 2012, **41**, 863-874.
27. G. Fragneto, *Eur. Phys. J. – Spec. Top.*, 2012, **213**, 327-342.
28. N. Kucerka, F. A. Heberle, J. J. Pan and J. Katsaras, *Membranes*, 2015, **5**, 454-472.
29. J. F. Nagle and S. Tristram-Nagle, *BBA – Rev. Biomembranes*, 2000, **1469**, 159-195.
30. F. Evers, C. Jeworrek, K. Weise, M. Tolan and R. Winter, *Soft Matter*, 2012, **8**, 2170-2175.
31. C. E. Miller, J. Majewski, T. Gog and T. L. Kuhl, *Phys. Rev. Lett.*, 2005, **94**, 238104.
32. C. E. Miller, J. Majewski, E. B. Watkins, D. J. Mulder, T. Gog and T. L. Kuhl, *Phys. Rev. Lett.*, 2008, **100**, 058103.
33. E. Novakova, K. Giewekemeyer and T. Salditt, *Phys. Rev. E*, 2006, **74**.
34. J. Daillant, E. Bellet-Amalric, A. Braslau, T. Charitat, G. Fragneto, F. Graner, S. Mora, F. Rieutord and B. Stidder, *P. Natl. Acad. Sci. USA*, 2005, **102**, 11639-11644.
35. Y. F. Dufrene, T. Ando, R. Garcia, D. Alsteens, D. Martinez-Martin, A. Engel, C. Gerber and D. J. Muller, *Nat. Nano.*, 2017, **12**, 295-307.
36. P. Parot, Y. F. Dufrene, P. Hinterdorfer, C. Le Grimellee, D. Navajas, J. L. Pellequer and S. Scheuring, *J. Mol. Recognit.*, 2007, **20**, 418-431.
37. M. I. Giannotti and G. J. Vancso, *Chem. Phys. Chem.*, 2007, **8**, 2290-2307.
38. S. G. Corcoran, R. J. Colton, E. T. Lilleodden and W. W. Gerberich, *Phys. Rev. B*, 1997, **55**, 16057-16060.
39. M. I. Giannotti, M. Rinaudo and G. J. Vancso, *Biomacromolecules*, 2007, **8**, 2648-2652.
40. M. I. Giannotti, I. C. de Vaca, J. M. Artes, F. Sanz, V. Guallar and P. Gorostiza, *J. Phys. Chem. B*, 2015, **119**, 12050-12058.
41. F. Rico, L. Gonzalez, I. Casuso, M. Puig-Vidal and S. Scheuring, *Science*, 2013, **342**, 741-743.
42. T. E. Fisher, A. F. Oberhauser, M. Carrion-Vazquez, P. E. Marszalek and J. M. Fernandez, *Trends Biochem. Sci.*, 1999, **24**, 379-384.
43. L. Redondo-Morata, M. I. Giannotti and F. Sanz, *Langmuir*, 2012, **28**, 12851-12860.
44. A. Alessandrini and P. Facci, *Micron.*, 2012, **43**, 1212-1223.
45. B. Gumi-Audenis, L. Costa, F. Carla, F. Comin, F. Sanz and M. I. Giannotti, *Membranes*, 2016, **6**.
46. S. Garcia-Manyes, G. Oncins and F. Sanz, *Biophys. J.*, 2005, **89**, 1812-1826.
47. S. Garcia-Manyes, L. Redondo-Morata, G. Oncins and F. Sanz, *J. Am. Chem. Soc.*, 2010, **132**, 12874-12886.
48. S. Garcia-Manyes, G. Oncins and F. Sanz, *Biophys. J.*, 2005, **89**, 4261-4274.
49. S. Garcia-Manyes, G. Oncins and F. Sanz, *Electrochim. Acta*, 2006, **51**, 5029-5036.
50. J. K. Li, R. M. A. Sullan and S. Zou, *Langmuir*, 2011, **27**, 1308-1313.
51. M. H. Abdulreda and V. T. Moy, *Biophys. J.*, 2007, **92**, 4369-4378.
52. C. E. Miller, J. Majewski, T. Gog and T. L. Kuhl, *Phys. Rev. Lett.*, 2005, **94**.
53. E. Nováková, K. Giewekemeyer and T. Salditt, *Phys. Rev. E*, 2006, **74**, 051911.
54. B. Gumi-Audenis, F. Carla, M. V. Vitorino, A. Panzarella, L. Porcar, M. Boilot, S. Guerber, P. Bernard, M. S. Rodrigues, F. Sanz, M. I. Giannotti and L. Costa, *J. Synchrotron Radiat.*, 2015, **22**, 1364-1371.
55. J. Henriksen, A. C. Rowat, E. Brief, Y. W. Hsueh, J. L. Thewalt, M. J. Zuckermann and J. H. Ipsen, *Biophys. J.*, 2006, **90**, 1639-1649.

56. J. J. Pan, T. T. Mills, S. Tristram-Nagle and J. F. Nagle, *Phys. Rev. Lett.*, 2008, **100**.
57. S.-i. Hakomori, *BBA – Gen. Subjects*, 2008, **1780**, 325.
58. R. Malhotra, *Biochem. Anal. Biochem.* , 2012, **1**, 1000108.
59. D. Lingwood, B. Binnington, T. Róg, I. Vattulainen, M. Grzybek, Ü. Coskun, C. A. Lingwood and K. Simons, *Nat. Chem. Biol.*, 2011, **7**, 260.
60. N. Yahi, A. Aulas and J. Fantini, *PLoS ONE*, 2010, **5**, e9079.
61. J. Fantini, N. Yahi and N. Garmy, *Front. Physiol.*, 2013, **4**, 120.
62. T. Róg and I. Vattulainen, *Chem. Phys. Lipids*, 2014, **184**, 82.
63. X. L. Han and H. Cheng, *J. Lipid Res.*, 2005, **46**, 163-175.
64. M. L. Longo and C. D. Blanchette, *BBA - Biomembranes*, 2010, **1798**, 1357-1367.
65. X. Zhou, L. Tang and Y. Liu, *Lipids*, 2009, **44**, 759-763.
66. C. D. Blanchette, W. C. Lin, T. V. Ratto and M. L. Longo, *Biophys. J.*, 2006, **90**, 4466-4478.
67. O. C. Farokhzad and R. Langer, *ACS Nano*, 2009, **3**, 16-20.
68. R. R. Sawant and V. P. Torchilin, *Soft Matter*, 2010, **6**, 4026-4044.
69. B. S. Pattni, V. V. Chupin and V. P. Torchilin, *Chem. Rev.*, 2015, **115**, 10938-10966.
70. F. Fernandez-Trillo, L. M. Grover, A. Stephenson-Brown, P. Harrison and P. M. Mendes, *Angew. Chem.-Int. Edit.*, 2017, **56**, 3142-3160.
71. G. Gregoriadis, *Trends Biotechnol.*, 1995, **13**, 527-537.
72. N. Grimaldi, F. Andrade, N. Segovia, L. Ferrer-Tasies, S. Sala, J. Veciana and N. Ventosa, *Chem. Soc. Rev.*, 2016, **45**, 6520-6545.
73. L. Ferrer-Tasies, E. Moreno-Calvo, M. Cano-Sarabia, M. Aguilella-Arzo, A. Angelova, S. Lesieur, S. Ricart, J. Faraudo, N. Ventosa and J. Veciana, *Langmuir*, 2013, **29**, 6519-6528.
74. M. Antonietti and S. Forster, *Adv. Mater.*, 2003, **15**, 1323-1333.
75. S. Geng, B. Yang, G. Wang, G. Qin, S. Wada and J. Y. Wang, *Nanotechnology*, 2014, **25**, 275103.
76. M. L. Immordino, F. Dosio and L. Cattel, *Int. J. Nanomed.*, 2006, **1**, 297-315.
77. C. Marianecci, L. Di Marzio, F. Rinaldi, C. Celia, D. Paolino, F. Alhaique, S. Esposito and M. Carafa, *Adv. Colloid Interfac.*, 2014, **205**, 187-206.
78. C. LoPresti, H. Lomas, M. Massignani, T. Smart and G. Battaglia, *J. Mater. Chem.*, 2009, **19**, 3576-3590.
79. S. Gudlur, P. Sukthankar, J. Gao, L. A. Avila, Y. Hiromasa, J. Chen, T. Iwamoto and J. M. Tomich, *PLoS ONE*, 2012, **7**, e45374.
80. A. Zeb, O. S. Qureshi, H. S. Kim, J. H. Cha and J. K. Kim, *Int. J. Nanomed.*, 2016, **11**, 3813-3824.
81. M. Cano-Sarabia, A. Angelova, N. Ventosa, S. Lesieur and J. Veciana, *J. Colloid Interfac.*, 2010, **350**, 10-15.
82. E. Elizondo, J. Larsen, N. S. Hatzakis, I. Cabrera, T. Bjornhorn, J. Veciana, D. Stamou and N. Ventosa, *J. Am. Chem. Soc.*, 2012, **134**, 1918-1921.
83. M. Cano-Sarabia, N. Ventosa, S. Sala, C. Patino, R. Arranz and J. Veciana, *Langmuir*, 2008, **24**, 2433-2437.
84. R. R. Sawant and V. P. Torchilin, *Aaps. J.*, 2012, **14**, 303-315.
85. S. Azarmi, W. H. Roa and R. Lobenberg, *Adv. Drug Deliv. Rev.*, 2008, **60**, 863-875.
86. M. P. Sheetz, *Nat. Rev. Mol. Cell Bio.,* 2001, **2**, 392.
87. W. Rawicz, K. C. Olbrich, T. McIntosh, D. Needham and E. Evans, *Biophys. J.*, 2000, **79**, 328-339.
88. K. Haase and A. E. Pelling, *J. R. Soc. Interface*, 2015, **12**.
89. E. Moeendarbary, L. Valon, M. Fritzsche, A. R. Harris, D. A. Moulding, A. J. Thrasher, E. Stride, L. Mahadevan and G. T. Charras, *Nat. Mater.*, 2013, **12**, 253-261.
90. G. Fujii, M. E. Selsted and D. Eisenberg, *Protein Sci.*, 1993, **2**, 1301-1312.
91. A. A. Stromstedt, L. Ringstad, A. Schmidtchen and M. Malmsten, *Curr. Opin. Colloid In.*, 2010, **15**, 467-478.
92. T. Ganz, *Nat. Rev. Immunol.*, 2003, **3**, 710-720.
93. B. Ericksen, Z. Wu, W. Lu and R. I. Lehrer, *Antimicrob. Agents Ch.*, 2005, **49**, 269-275.
94. P. M. Silva, S. Goncalves and N. C. Santos, *Front. Microbiol.*, 2014, **5**, 97.

95. G. Wei, M. Pazgier, E. de Leeuw, M. Rajabi, J. Li, G. Zou, G. Jung, W. Yuan, W.-Y. Lu, R. I. Lehrer and W. Lu, *J. Biol. Chem.*, 2010, **285**, 16275-16285.
96. Y. Zhang, W. Lu and M. Hong, *Biochemistry-US*, 2010, **49**, 9770-9782.
97. A. Giuliani, G. Pirri and S. F. Nicoletto, *Cent. Eur. J. Biol.*, 2007, **2**, 1-33.
98. M. N. Melo, R. Ferre and M. A. R. B. Castanho, *Nat. Rev. Microbiol.*, 2009, **7**, 245.
99. K. A. Brogden, *Nat. Rev. Microbiol.*, 2005, **3**, 238.
100. E. Balducci, A. Bonucci, M. Picchianti, R. Pogni and E. Talluri, *Int. J. Pept.*, 2011, **2011**, 594723.
101. S. Goncalves, J. Abade, A. Teixeira and N. C. Santos, *Biopolymers*, 2012, **98**, 313-321.
102. T. P. W. McMullen and R. N. McElhaney, *BBA - Biomembranes*, 1995, **1234**, 90-98.
103. S. Karmakar, V. A. Raghunathan and S. Mayor, *J. Phys. Condens. Matter*, 2005, **17**, S1177-S1182.
104. Y.-W. Chiang, A. J. Costa and J. H. Freed, *J. Phys. Chem. B*, 2007, **111**, 11260-11270.
105. D. Marsh, *BBA - Biomembranes*, 2010, **1798**, 688-699.
106. D. Marquardt, F. A. Heberle, J. D. Nickels, G. Pabst and J. Katsaras, *Soft Matter*, 2015, **11**, 9055-9072.
107. P. F. Almeida, *Biophys. J.*, 2011, **100**, 420-429.
108. R. M. A. Sullan, J. K. Li, C. Hao, G. C. Walker and S. Zou, *Biophys. J.*, 2010, **99**, 507-516.
109. B. . Gumí-Audenis, F. Carlà, M. V. Vitorino, A. Panzarella, L. Porcar, M. Boilot, S. Guerber, P. Bernard, M. S. Rodrigues, F. Sanz, M. I. Giannotti and L. Costa, *J. Synchrotron Radiat.*, 2015, **22**, 1364–1371.
110. T. Salditt and G. Brotons, *Anal. Bioanal. Chem.*, 2004, **379**, 960-973.
111. M. A. Barrett, S. Zheng, L. A. Toppozini, R. J. Alsop, H. Dies, A. Wang, N. Jago, M. Moore and M. C. Rheinstadter, *Soft Matter*, 2013, **9**, 9342-9351.
112. A. Ivankin, I. Kuzmenko and D. Gidalevitz, *Phys. Rev. Lett.*, 2010, **104**, 108101.
113. E. T. Castellana and P. S. Cremer, *Surf. Sci. Rep.*, 2006, **61**, 429-444.
114. R. Ziblat, K. Kjaer, L. Leiserowitz and L. Addadi, *Angew. Chem. Int. Ed.*, 2009, **48**, 8958-8961.
115. R. Ziblat, L. Leiserowitz and L. Addadi, *J. Am. Chem. Soc.*, 2010, **132**, 9920-9927.
116. H. Asakawa and T. Fukuma, *Nanotechnology*, 2009, **20**.
117. L. Costa and M. S. Rodrigues, *Synchrotron Radiation News*, 2016, **29**, 3-7.
118. M. S. Rodrigues, O. Dhez, S. Le Denmat, J. Chevrier, R. Felici and F. Comin, *J. Instrum.*, 2008, **3**.
119. T. Scheler, M. Rodrigues, T. W. Cornelius, C. Mocuta, A. Malachias, R. Magalhaes-Paniago, F. Comin, J. Chevrier and T. H. Metzger, *Appl. Phys. Lett.*, 2009, **94**.
120. Z. Ren, F. Mastropietro, A. Davydok, S. Langlais, M. I. Richard, J. J. Furter, O. Thomas, M. Dupraz, M. Verdier, G. Beutier, P. Boesecke and T. W. Cornelius, *J. Synchrotron Rad.*, 2014, **21**, 1128-1133.
121. M. V. Vitorino, Y. Fuchs, T. Dane, M. S. Rodrigues, M. Rosenthal, A. Panzarella, P. Bernard, O. Hignette, L. Dupuy, M. Burghammer and L. Costa, *J. Synchrotron Rad.*, 2016, **23**, 1110-1117.

Appendix 2

Symbols and acronyms

A	Frequency at which the AFM tip attempts to penetrate the bilayer
AC mode	Intermittent contact mode
AFM	Atomic force microscopy
AFM-FC	Atomic force microscopy based force clamp
AFM-FS	Atomic force microscopy based force spectroscopy
AM mode	Amplitude modulation
AMP	Antimicrobial peptide
Arg	Arginine
BAM	Brewster angle microscopy
BM	Biological membrane
Cer	Ceramide
Chol	Cholesterol
CMC	Critical micelle concentration
Cryo-TEM	Cryogenic transmission electron microscopy
CTAB	Cetyl trimethylammonium bromide
Cys	Cysteine
d	Distance at which the tubes are ruptured or detached
DFS	Dynamic force spectroscopy
DLPC	1,2-dilauroyl-*sn*-glycero-3-phosphocholine
DLS	Dynamic light scattering
DMPC	1,2-dimyristoyl-*sn*-glycero-3-phosphocholine
DMT	Derjaguin-Muller-Toporov
DOPC	1,2-dioleoyl-*sn*-glycero-3-phosphocoline
DOPE	1,2-dioleoyl-*sn*-glycero-3-phosphoethanolamine
DOPG	1,2-dielaidoyl-*sn*-glycero-3-phospho-(1'-*rac*-glycerol)
DPPC	1,2-dipalmitoyl-*sn*-glycero-3-phosphocholine
DPPE	1,2-dipalmitoyl-*sn*-glycero-3-phosphoethanolamine
DPPE-Rh	1,2-dipalmitoyl-*sn*-glycero-3-phosphoethanolamine-*N*-(lissamine rhodamine B sulfonyl)
DPPG	1,2-dipalmitoyl-*sn*-glycero-3-phospho-(1'-*rac*-glycerol)
DSC	Differential scanning calorimetry
DSPC	1,2-distearoyl-*sn*-glycero-3-phosphocholine
DSPE	1,2-distearoyl-*sn*-glycero-3-phosphoethanolamine
E	Young modulus
EFM	Electrostatic force microscopy
F	Force
F_{adh}	Adhesion force
F_{att}	Attractive force
F_b	Breakthrough force

FCS	Fluorescence correlation spectroscopy
FRAP	Fluorescence recovering after photobleaching
F_{tube}	Tube growing force
$F_{tube\ b}$	Tube growing force from a bleb
$F_{tube\ cyt}$	Tube growing force from a cytoskeleton supported bilayer
$F_{tube\ mica}$	Tube growing force from a mica supported bilayer
$F_{tube\ Si}$	Tube growing force from a silicon supported bilayer
FWHM	Full width at half maximum
GalCer	Galactosylceramides
GI	Grazing incidence
GISAXS	Grazing incidence small-angle X-ray scattering
GIXD	Grazing incidence X-xay diffraction
GlcCer	Glucosylceramide
Glu	Glutamic acid
GPMV	Giant plasma membrane vesicle
GSL	Glycosphingolipid
GUV	Giant unilamellar vesicle
h	Height of a vesicle
H_{bot}	Bottom headgroups
HEPES	4-(2-hydroxyethyl)-1-piperazineethanesulfonic acid
HNP	Human neutrophil peptide
HS-AFM	High speed atomic force microscopy
HT	High temperature
H_{upp}	Upper headgroups
Ind	Indentation
k_B	Boltzmann factor
k_{mem}	Stiffness of the vesicle membrane
k_s	Nominal spring constant of the cantilever
LB	Langmuir-Blodgett
l_d	Liquid-disordered
LP	Liposome
LUV	Large unilamellar vesicle
MD	Molecular dynamics
MFM	Magnetic force microscopy
NMR	Nuclear magnetic resonance
PBS	Phosphate-buffered saline solution
PC	Phosphocholine
PDI	Polydispersity index
PE	Phosphoethanolamine

PG	Phosphoglycerol
PSL	Phosphosphingolipid
P_β	Rippled gel phase
QI	Quantitative imaging
Q_{par}	Q parallel
Q_{perp}	Q perpendicular
QT	Quatsome
QT_H_2O	Quatsome in water
QT_PBS	Quatsome in phosphate-buffered saline solution
r	Loading rate
R	Radius of the top regions of a spherical cap
r.m.s.	Root mean square
RF	Radiofrequency
RT	Room temperature
r_{tip}	Tip radius
Sep	Separation
SL	Sphingolipid
SLB	Supported lipid bilayer
SLD	Scattering length density
SM	Sphingomyelin
SNOM	Scanning near field optical microscopy
s_o	Solid-ordered
SPB	Supported planar bilayer
SQM	Supported quatsome membrane
STXM	Scanning transmission XR microscopy
SUV	Small unilamellar vesicle
t	time
T	Absolute temperature
t_0	Initial time
T_{bot}	Bottom hydrocarbon tails
t_f	Final time
th	Thickness
T_m	Main transition temperature
Trp	Tryptophan
T_{upp}	Upper hydrocarbon tails
UV	Ultraviolet
v	Velocity
W	Width of a vesicle
XAFS	X-ray absorption fine structure

XEOL	X-ray excited optical luminescence
XR	X-ray
XRR	X-ray reflectometry
z_0	Tip-sample contact position
γ	Adhesion energy parameter
ΔE	Activation energy of the bilayer rupture
ΔE_0	Activation energy of the bilayer rupture in absence of an external force
ΔF	Interval of force
ζ-pot	Zeta potential
θ_i	Incident angle
θ_r	Reflected angle
κ	Membrane bending stiffness
λ	Wavelength
ρ	Electron density
σ	In-plane membrane tension
σ_{app}	Apparent membrane tension
$\sigma_{app\ cyt}$	Apparent cytoskeleton supported membrane tension
$\sigma_{app\ mica}$	Apparent mica supported membrane tension
$\sigma_{app\ Si}$	Apparent silicon supported membrane tension
σ_b	Apparent bleb tension
σ_{SLD}	Roughness

Appendix 3

Publications and communications

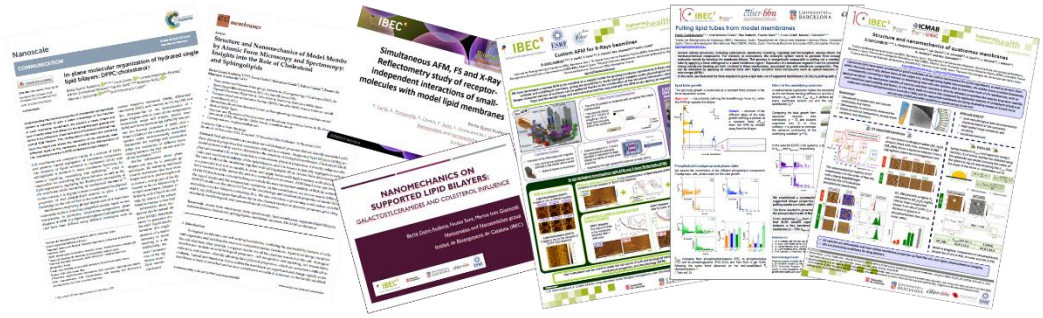

Publications:

Pulling lipid tubes from model membranes. *In preparation*.

HNP1 defensin effect on the structure and mechanics of model membranes. *In preparation*.

Structure and nanomechanics of quatsome membranes. *In preparation*.

B. Gumí-Audenis, L. Costa, L. Redondo-Morata, P.E. Milhiet, F. Sanz, R. Felici, M.I. Giannotti and F. Carlà. In-plane molecular organization of hydrated single lipid bilayers: DPPC:cholesterol. *Nanoscale,* **2018**, 10, 87-92

B. Gumí-Audenis, L. Costa, F. Carlà, F. Comin, F. Sanz and M.I. Giannotti. Structure and Nanomechanics of Model Membranes by Atomic Force Microscopy and Spectroscopy: Insights into the Role of Cholesterol and Sphingolipids. *Membranes*, **2016**, 6(4), 58

B. Gumí-Audenis, F. Carlá, M. Vargas-Vitorino, A. Panzarella, L. Porcar, M.Boilot, S. Guerber, B. Pascal, M.S. Rodrigues, F. Sanz, M.I. Giannotti, and L. Costa. Adapted AFM for beamlines: in-situ biological investigations under physiological conditions. *J. Synchrotron Rad.*, **2015**, 22(6), 1364-1371

B. Gumí-Audenis, F. Sanz and M.I. Giannotti. Impact of Galactosylceramide on the nanomechanical properties of lipid bilayer models: AFM-force spectroscopy study. *Soft Matter*, **2015**, 11, 5447-5454

Oral communications:

B. Gumí-Audenis, J.A. Durán, B. Barberà, F. Sanz, L. Costa and M.I. Giannotti. Pulling lipid tubes from model membranes. *Meeting of the Membrane Section of the German Biophysical Society "Membrane Models for Biophysics"*. **March 2018** Drübeck, Germany.

B. Gumí-Audenis. Nanomechanical and structural properties of supported lipid bilayers. *IBEC PhD discussion*. **Oct. 2017** Barcelona, Spain.

B. Gumí-Audenis, F. Carlá, F. Sanz, F. Comin, M.I. Giannotti and L. Costa. Custom AFM for X-Ray beamlines: *in situ* characterization of lipid bilayers. *VI Jornades de la Societat Catalana de Biofísica*. **Dec. 2016** Barcelona, Spain.

B. Gumí-Audenis, F. Sanz and M.I. Giannotti. Nanomechanics on supported lipid bilayers: galactosylceramides and cholesterol influence. *Fuerzas y Túnel Conference*. **Sep. 2016** Girona, Spain.

B. Gumí-Audenis and M. López-Martínez. Let's go to the nano: Scanning Probe Microscopies. *JIPI (Jornada d'Investigadors Predoctorals Interdisciplinària)* **Feb. 2016** Barcelona, Spain.

L. Costa, M. V. Vitorino, B. Gumí-Audenis, A. Panzarella and F. Comin. May the force be with you: high-speed atomic force microscopes for Synchrotron sample holders. *Synchrotron Radiation Instrumentation 2015 (SRI 2015)* **July 2015**, New York, USA.

B. Gumí-Audenis. Morphological and mechanical study of Supported Lipid Bilayers by AFM and X-Rays Reflectivity. *Soft Matter Meeting ESRF-ILL* **May 2015** Grenoble, France.

Flash oral and poster communications:

B. Gumí-Audenis, F. Carlá, F. Sanz, F. Comin, M.I. Giannotti and L. Costa. Custom AFM for X-Rays beamlines. *Fuerzas y Túnel Conference*. **Sep. 2016** Girona, Spain.

B. Gumí-Audenis, F. Carlá, A. Panzarella, F. Sanz, M.I. Giannotti, F. Comin and L. Costa. Characterization of model lipid membranes by simultaneous X-Ray Reflectometry and AFM at ID03. *ESRF Science and Student Days*. **Oct. 2015** Val Cenis – Lanslebourg, France.

B. Gumí-Audenis, F. Carlá, A. Panzarella, F. Comin, F. Sanz, L. Costa and M.I. Giannotti. Simultaneous AFM, FS and X-Ray Reflectometry study of receptor-independent interactions of small-molecules with model lipid membranes. *8th IBEC Symposium. Bioengineering for Regenerative Therapies.* **Sep. 2015** Barcelona, Spain.

Poster communications:

B. Gumí-Audenis, J.A. Durán, B. Barberà, F. Sanz, L. Costa and M.I. Giannotti. Pulling lipid tubes from model membranes. *XX Annual Linz Winter Workshop: Advances in Single-Molecule Research for Biology & Nanoscience.* **Feb. 2018** Linz, Austria.

S. Ortíz, B. Gumí-Audenis, A. Guerra-Castellano, M.A. De la Rosa, I. Díaz-Moreno, J. Samitier, P. Gorostiza and M.I. Giannotti. Redox partner proteins interaction forces. *XX Annual Linz Winter Workshop: Advances in Single-Molecule Research for Biology & Nanoscience*. **Feb. 2018** Linz, Austria.

B. Gumí-Audenis, L. Pasquina-Lemonche, N. Grimaldi, F. Sanz, J. Veciana, I. Ratera, N. Ventosa and and M.I. Giannotti. Structure and nanomechanics of quatsomes membranes. *Jornadas Anuales CIBER-BBN.* **Nov. 2017** Santander, Spain.

B. Gumí-Audenis, F. Comin, F. Sanz, L. Costa and M.I. Giannotti. Effect of defensins on the physical and structural properties of biomimetic membranes. *7th International Colloids Conference*. **June 2017** Sitges, Spain.

A. Crespo-Villanueva, B. Gumí-Audenis, F. Sanz, C. Lopez, M.I. Giannotti and Fanny Guyomarc'h. Protein interaction with lipid membranes: are the phase state or charge density

of the phospholipids affecting protein adsorption? *7th International Colloids Conference*. **June 2017** Sitges, Spain.

B. Gumí-Audenis, L. Pasquina-Lemonche, J.A. Durán, N. Grimaldi, F. Sanz, J. Veciana, I. Ratera, N. Ventosa and and M.I. Giannotti. Structure and nanomechanics of quatsomes membranes. *10th IBEC Symposium. Bioengineering for future medicine*. **June 2017** Barcelona, Spain.

M.I. Giannotti, B. Gumí-Audenis, F. Sanz and P. Gorostiza. Nanomechanics of model membranes and single molecules. *Jornadas Anuales CIBER-BBN*. **Nov. 2016** Sevilla, Spain.

B. Gumí-Audenis, F. Carlá, F. Comin, F. Sanz, L. Costa and M.I. Giannotti. Small molecules' interaction with model lipid membranes: AFM and X-Rays Reflectometry. *9th IBEC Symposium. Bioengineering for active aging*. **June 2016** Barcelona, Spain.

B. Gumí-Audenis, F. Carlá, F. Comin, F. Sanz, L. Costa and M.I. Giannotti. Structural and nanomechanical properties of model lipid membranes. *AFM BioMed Conference*. **April 2016** Porto, Portugal.

B. Gumí-Audenis, F. Carlá, F. Comin, F. Sanz, L. Costa and M.I. Giannotti. Study of small-molecules and peptide interactions with model lipid membranes by combining X-Ray Reflectometry and AFM. *Hercules school*. **April 2016**. Grenoble, France.

L. Costa, M.V. Vitorino, B. Gumí-Audenis, M. Boilot, P. Bernard, A.Panzarella, M.S. Rodrigues and F. Comin. High Speed Atomic Force Microscopies for SR techniques. *European XFEL Users' Meeting*. **Jan. 2015** Hamburg, Germany.

B. Gumí-Audenis, L. Redondo-Morata, F. Sanz and M.I. Giannotti. Nanomechianics on Model Lipid Membranes: Galactosylceramides and Cholesterol Effect. *AFM Beyond Imaging. Nanoscale Characterization of Functional Materials Workshop*. **Jan. 2015** Bellaterra, Spain.

B. Gumí-Audenis, F. Sanz and M.I. Giannotti. Galactosylceramides and Cholesterol Effect on the Nanomechanical Stability of Model Lipid Membranes. *3rd Workshop on Nanomedicine UAB (Universitat Autònoma de Barcelona)*. **Nov. 2014** Bellaterra, Spain.

B. Gumí-Audenis, F. Sanz and M.I. Giannotti. The Effect of Galactosylceramides on the Nanomechanical Stability of Model Lipid Membranes. *7th IBEC Symposium. Bioengineering for Future Medicine*. **Sep. 2014** Barcelona, Spain.

B. Gumí-Audenis, M. Boilot, P. Bernard, A.Panzarella, L. Costa, M.S. Rodrigues and F. Comin. High Speed X-Atomic Force Microscope for Beamlines. *ESRF Science and Student Days.* **Oct. 2013** Val Cenis – Lanslebourg, France.

Acknowledgments

Aquesta tesi l'he realitzada al grup de *Nanoprobes and Nanoswitches* de l'Institut de Bioenginyeria de Catalunya (IBEC) i al departament de Ciència dels Materials i Química Física de la Universitat de Barcelona sota supervisió de la Dra. Marina I. Giannotti i el Prof. Fausto Sanz. A més, en el transcurs de la tesi he fet vàries estades en un total de més de set mesos al *Surface Science Lab* (SSL) del sincrotró ESRF de Grenoble (França), sota la supervisió del Dr. Fabio Comin i el Dr. Luca Costa.

És increïble adonar-se de tota la gent que t'ha estat fent costat durant tots aquests mesos, no només en l'àmbit acadèmic i de treball, sinó també a nivell personal. M'encantaria poder agrair a tothom sense deixar-me a ningú, tot i que crec que és impossible mencionar a totes aquelles persones que han posat el seu granet de sorra en ajudar-me i donar-me suport durant aquests tres anys i mig de doctorat. Simplement MOLTES GRÀCIES a tots!

En primer lloc, agrair a tots i cada un dels membres del grup de *Nanoprobes and Nanoswitches*, tan els que ja no hi formen part com els que encara hi són. Al Fausto, per donar-me la oportunitat de començar com a estudiant de màster fa quasi cinc anys, i després confiar en mi, junt amb el Pau, per a continuar amb el doctorat. Infinitas gracias a Marina, mi directora de tesis. No sé ni por dónde empezar... Me adoptaste como tu estudiante de máster y seguí de tu manita durante todo el doctorado. Me has ayudado día a día siempre que lo he necesitado, tanto a nivel científico como a nivel personal, has estado a mi lado en momentos muy buenos, al igual que en alguno más complicado, hemos compartido ratos de beamtimes comiendo stroopwafels a las 4 de la mañana o esquivando conejos para volver a la guesthouse, nos hemos llenado a *haribo*s mientras discutíamos resultados en el despacho, entre mil otras más historias y anécdotas que han pasado. No sé ni como agradecerte todo lo que me has ayudado y aconsejado durante todo este tiempo. Y que por mucho que me vaya, siempre voy a ser, con el permiso de Michel ☺, tu hija adoptiva junto con Lorena, a la qual també li haig de donar mil gràcies, ja que, malgrat no haguem compartit laboratori en (quasi) cap moment, sempre has tingut un ratet per ajudar-nos i donar-nos la teva opinió. I a la resta del grup de *Nanoprobes and Nanoswitches*, tant els de l'hèlix, com els del chem space, els de Bellvitge o els de QF. Especialmente a Montse y a Marta, que por mucho que ya terminaron hace unos meses, ellas me acogieron cuando llegué al lab y me ayudaron en todo cuando yo, en mis inicios, estaba perdidísima. Montse, gracias por todo y más, por cada uno de los momentos en los que me has aconsejado, por todos los que hemos reído tanto como llorado, por los desayunos, cafés, cines, cenas, y miles de otras cosas. I a la Marta, merci per fer-me riure a totes hores, per donar-me consells, però sobretot, per ocupar-me tota la taula amb els teus post-its i notetes en els quals descrivies les grans veritats (SC, RT, …). Pero también me gustaría decir algo a los que aún estáis en el grupo. A Davia, por los momentos que hemos pasado juntas en el lab, especialmente durante el último año, y por ser mi mejor

compañera de “shopping”. A Fabio, por todas las largas charlas que hemos tenido y los miles de consejos y ánimos que me has dado desde que viniste al lab. Siempre serás el bambino del grupo. Y a Manu, que por muy papa frita que te autodigas, contigo he tenido grandes conversaciones tanto científicas como de otros temas. Y evidentemente no me gustaría dejarme a ninguna de las personas que han ido pasando temporalmente por el grupo, como Vero, o todos los estudiantes de máster y grado con los que he trabajado: Laia, Tony, Adri, Sthefy, Blai y Sara.

M’agradaria també mencionar a tota la gent que està a l’IBEC però que no són del grup com la Natàlia, el Macià, l’Albert, el Martí, la Maider, entre molts d’altres, amb els quals he tingut converses dins i fora del PCB, cafès, meetings del phd committee, dinars, laser tags, i fins a classes de dansa. No em voldria deixar tampoc als compis de la sala del 3r pis, que m’han acompanyat durant tot el procés d’escriptura de la tesi.

I would also like to thank a lot to Fabio and Luca, for giving me the opportunity to start my scientific career at *SSL* and introducing me to the AFM+XR field while building *Anita*. Thanks Fabio for all the scientific conversations we had as well as all the advises you gave me during all the stays I did in your lab. Luca, thanks a lot for all your help during all these years, for teaching me and explaining me every time (including drawings, that by the way, I keep them all) I was lost or I was not understanding something, for encouraging me always with a “dai Ber!”, for all the music, sometimes the same song in “repeat-mode”, you put in the lab or during the beamtimes, for reminding me every day your love for your city (as well as for the food of the canteen ☺), and a long etcetera of things. Regarding your new lab in Montpellier, I would like to acknowledge to Pierre-Emmanuel as well, for all the advises concerning fluorescence measurements. I would also like to mention the rest of the people I met at the *SSL*: Chris, Miguel, Anny, Leo, but specially Alain, who was always available to help me in the lab. In addition, I would like to acknowledge all the people from the beamlines ID03, ID10, SpLine and BM05, who helped me during the synchrotron experiments. In particular, thanks a lot to Fra, for all the advises and help you gave me during or concerning the beamtimes. To Roberto, for all the scientific conversations at ID03, to Oleg, for the big help you gave us concerning XR data treatment, and to Yuri and Irena from ILL, for the many discussions we had concerning XRR. I would like also to make reference to all the people that was involved in the design and mounting of *Anita*, the custom XR-AFM. Y evidentemente, no me quiero dejar a Sara, gracias por todos los gordi-cafés, las largas charlas, paseos y mil otras cosas, así como a toda la gente que conocí en Grenoble.

M’agradaria també donar les gràcies a tota la gent de l’ICMAB amb la que hem col·laborat durant aquest temps: a la Nora, a l’Imma, al Jaume, a la Lídia i al Jordi. Mencionar especialmente a Natascia, ya que ella era con la que me comunicába a menudo por todo el tema de QT y me pasaba toda la información que necesitaba. I no em puc deixar per res del món a la pez Sílvia! Qui ens diria que del jardí de Llívia passaríem a treballar juntes! No

oblidaré el moment en que ens vam adonar, de casualitat mentre sopàvem amb l'altra pez, que col·laboràvem en un mateix projecte. Gràcies per tota l'ajuda i ànims que m'has donat, especialment durant aquestes últimes setmanes.

Agrair també a tota la gent de fora del lab, els quals han fet que tota aquesta etapa fos més agradable: als meus estimats físics, a les nenes (o animalons) del cole, als de dansa, als de música, als de Llívia, a la Montse, a l'Anna, al Pau, a la Raquel... M'agradaria especialment mencionar a la Carla, per haver sigut una compi estupenda durant aquests dos anys en el cuquipis, i a la Mar, perquè sempre has estat al meu costat en tot moment.

A la meva família, que evidentment res hauria sigut possible sense el suport diari dels meus pares, que han fet sempre tot el que estava al seu abast per donar-me un cop de mà. Gràcies per aconsellar-me, per entendre'm i per fer-me costat en tot moment. Òbviament, mil gràcies a la meva sis A, que sempre ha tingut històries a explicar que m'han fet treure un somriure i perquè per molt que digui que "no entén res del que faig" sempre ha estat allà.

Finally, I would like to give infinite thanks to Bas, since the PhD period wouldn't have been the same without you close to me. Thanks for everything, for being there always, and especially for reminding me that *distance means nothing, when someone means so much*. Dankjewel dear!

Gràcies a tots!

Berta